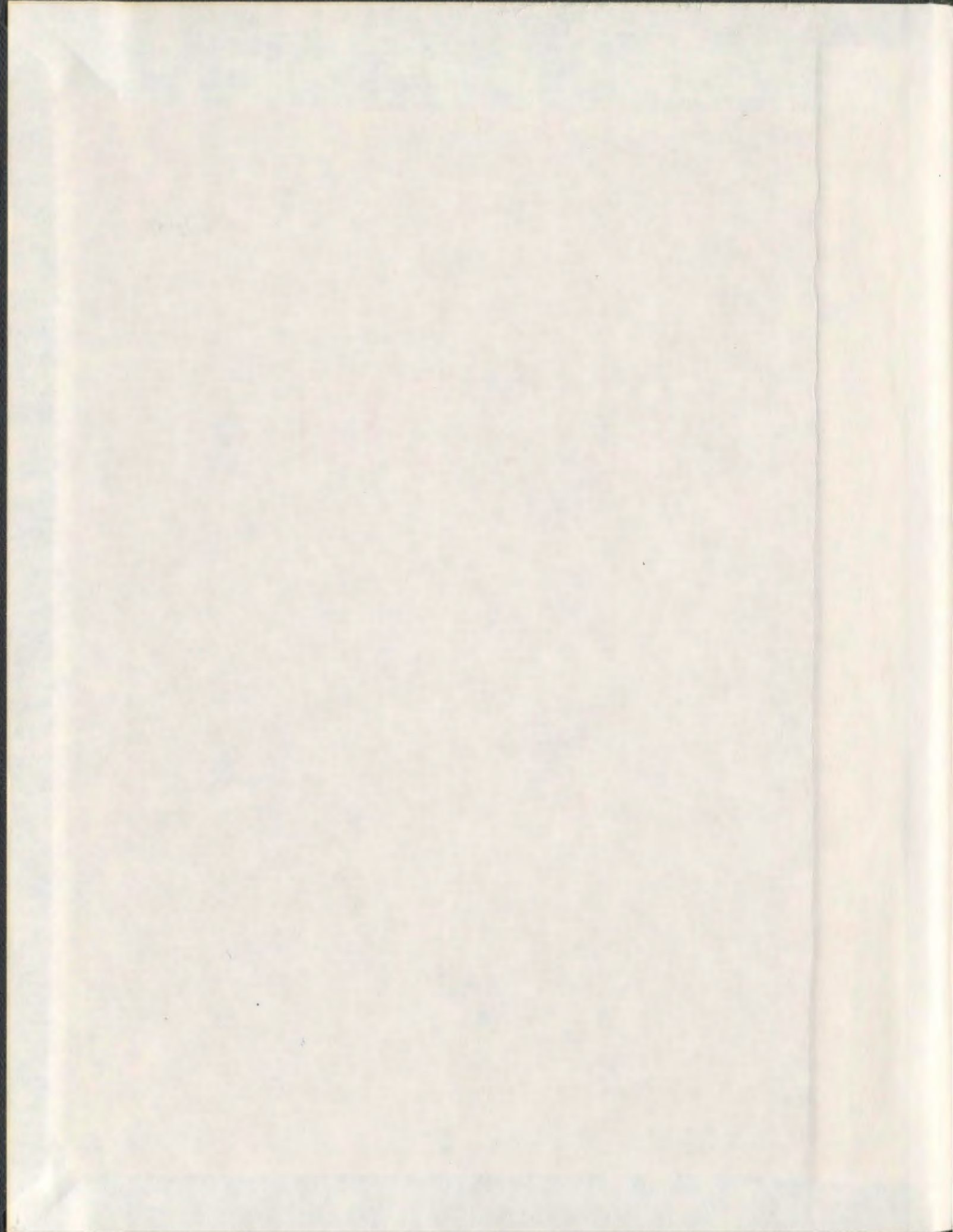


**BRILLOUIN SCATTERING STUDIES OF POROUS
SILICON-BASED ONE-DIMENSIONAL HYPERSONIC
PHONONIC-PHOTONIC CRYSTALS**

LANCE C. PARSONS



Brillouin Scattering Studies of Porous Silicon-Based One-Dimensional Hypersonic Phononic-Photonic Crystals

by

Lance C. Parsons

A Thesis Submitted in Partial Fulfilment of
the Requirements for the Degree of

Doctor of Philosophy

Department of Physics and Physical Oceanography
Memorial University of Newfoundland

January, 2013

St. John's

Newfoundland

Abstract

Brillouin light scattering spectroscopy and optical reflectance measurements were used to characterize the acoustic phononic band structure and the photonic band structure, respectively, of binary periodic mesoporous silicon superlattices with a repeated porosity sequence of $\sim 55\%$ ($\sim 45\%$) and modulation wavelengths of the order of 100 nm. The samples exhibited visible-range forbidden photon frequency bands, or photonic band gaps, for photons propagating along the modulation axis of the superlattice. This manifested as a peak in the near-normal incidence broadband optical reflectance spectrum. Using a combination of pseudo-reflection geometry Brillouin spectroscopy and near-normal incidence 180° -backscattering geometry Brillouin spectroscopy, a portion of the bulk acoustic band structure directed approximately along the superlattice periodicity was mapped for a series of samples. The obtained agreement between the data and calculations based on a one-dimensional elastic/electromagnetic continuum model suggested that the longitudinal bulk acoustic phonon dispersion curve had undergone zone-folding into the mini-Brillouin zone corresponding to the artificial periodicity. In particular, two peaks associated with folded bands of the longitudinal band structure were observed in the Brillouin spectra. For the transverse bulk acoustic mode, on the other hand, the Brillouin spectra showed evidence of a single band. Analysis of the Brillouin peaks associated with the longitudinal modes suggested that phonon attenuation in porous silicon was several

orders of magnitude larger than that observed in bulk crystalline silicon. It was, therefore, suggested that the film porosity played a significant role in the phonon attenuation. Additionally, another peak, attributed to a surface-localized mode with a frequency within a hypersonic phononic band gap in the longitudinal bulk mode band structure centered at ~ 16 GHz, was also observed. This surface-localized mode was a manifestation of the hypersonic phononic band gap. Taking into account the Brillouin scattering results along with those obtained through the optical reflectance measurements, it was inferred that the π -Si superlattices were one-dimensional hypersonic phononic-photonics crystals.

Oblique acoustic phonon propagation was also characterized using oblique 180° -backscattering geometry Brillouin scattering. The frequency of the probed folded longitudinal acoustic phonon modes depended on the phonon propagation direction. No evidence of coupling between the folded longitudinal bulk acoustic bands and the transverse bulk acoustic band was obtained. In addition to the bulk acoustic modes, peaks ascribed due to a Rayleigh surface mode and a pseudo-surface mode were observed in the oblique 180° -backscattering geometry Brillouin spectra. These surface modes were dispersive, with the phonon velocity increasing with phonon wavelength. This surface mode dispersion appeared to be an artefact of the periodic structure of the probed samples.

Co-Authorship Statement

The thesis author (L.C. Parsons) was the main contributor to all of the proceeding manuscripts, sharing authorship with Dr. G. Todd Andrews, the faculty supervisor for this graduate project. This work resulted in four manuscripts: one entitled “Observation of hypersonic phononic crystal effects in porous silicon superlattices”, another entitled “Probing near-normally propagating bulk acoustic waves using pseudo-reflection geometry Brillouin spectroscopy”, a third paper called “Brillouin scattering from porous silicon-based optical Bragg mirrors”, and a fourth entitled “Oblique acoustic phonon propagation in porous silicon superlattices”. For all four studies, the first three of which have already been published, Dr. Andrews assisted with sample fabrication as well as manuscript preparation. Aside from the first article, for which the writing responsibilities were shared from the outset of writing the document, the majority of Dr. Andrews input came once an initial draft of a given manuscript was completed. While the thesis author guided all the studies, completing most experiments and data analysis independently, discussions with Dr. Andrews provided invaluable insight and assistance throughout the course of the work.

Acknowledgments

First of all, a “thank you” goes to my supervisor, Dr. Todd Andrews, for providing an abundance of guidance and inspiration throughout this project. I would also like to acknowledge my colleagues within the Andrews research group (my π -Si brethren): Ania Harlick, Jordan Peckham, and Brendan Harvey. As well, I would like to thank the faculty, staff and fellow graduate students in the Memorial University of Newfoundland Dept. of Physics and Physical Oceanography. In particular, “thanks” goes to Dr. Oktay Aktas and Dr. Maynard Clouter for the insightful conversations regarding Brillouin light scattering spectroscopy. Additionally, a great deal of appreciation goes to Dr. Anand Yethiraj, Dr. Kris Poduska, Dr. Qiyang Chen, Dr. Stephanie Curnoe and Dr. Veerle Keppens for providing helpful feedback throughout the various stages of writing this thesis. I would also like to express my gratitude to the Natural Sciences and Engineering Research Council of Canada and Memorial University’s School of Graduate Studies for supplying financial support during my PhD program.

A great deal of appreciation goes to my friends and family, who have exhibited an enormous amount of support and patience throughout this whole process. Specifically, I would like to acknowledge: my parents, Tony and Carol; my sister, Dawn; my brother-in-law, Brian; my grandparents, John and Jean; the extended King family (Derm, Brenda, Alyson, Dave and J.D.); and my guitar-playing cohort, Shawn. Last

but certainly not least, I would like to thank Heather, who keeps me grounded even when my head is in the clouds.

List of Symbols

a - subscript used to denote light polarization (either p- or s-polarization)

α - angle between probed bulk phonon direction and the sample surface normal

α_{BS} - angle for bulk phonon probed using 180° -backscattering geometry

α_{PR} - angle for bulk phonon probed using pseudo-reflection scattering geometry

b - order of phononic band gap; transmission order of a Fabry-Perot etalon

β - wavevector of a surface-localized phonon

c - speed of light in vacuum

c_j - speed of light in superlattice constituent layer j

C - a constant related to the photon/phonon attenuation coefficient

χ - attenuation coefficient

d_j - thickness of superlattice constituent layer j

D - superlattice modulation wavelength

$\Delta\nu$ - full-width-at-half maximum of a Brillouin peak

η - number of modulations in a superlattice

f - photon frequency

F - material parameter related to the acoustic/elastic mismatch in a superlattice

γ - exponent for frequency dependence of attenuation coefficient

h - propagation distance of a bulk acoustic phonon; (integer) Bragg peak order

H - overall porous silicon film thickness

I - etch current

J - etch current density; subscript denoting the superlattice constituent layer

J_{crit} - critical current density

k_i - incident photon wavevector outside probed material

K_j - photon wavevector in superlattice constituent layer j

k_s - scattered photon wavevector outside probed material

K_i - incident photon wavevector inside the probed material

K_s - scattered photon wavevector inside the probed material

κ - photonic Bloch wavevector

l - (integer) folding order of the phonon band structure

λ - wavelength of light

λ_o - wavelength of probing laser beam

m - mass; integer denoting the unit cell of a superlattice

n - refractive index

n_{eff} - effective refractive index

n_{ave} - average refractive index

N - refractive index of crystalline silicon

ν - frequency of phonon

ν_{BS} - frequency of phonon probed using a 180° -backscattering geometry

ν_L - frequency of longitudinal bulk acoustic phonon

ν_{PR} - frequency of phonon probed using a pseudo-reflection geometry

ν_S - frequency of surface-localized acoustic phonon

ν_{SW} - frequency of surface-propagating acoustic phonon

ν_T - frequency of transverse bulk phonon

ω - angular frequency of photon

ω_i - angular frequency of incident light

ω_s - angular frequency of scattered light

Ω - angular frequency of phonon

Ω_{BS} - angular frequency of phonon probed using a 180° -backscattering geometry

Ω_{PR} - angular frequency of phonon probed using a pseudo-reflection geometry

Ω_S - angular frequency of a surface-localized phonon

\wp - light power deduced using a silicon photodiode power meter

P - material parameter related to the electromagnetic mismatch in a superlattices

P_a - polarization-dependent parameter related to electromagnetic mismatch

P_p - parameter related to electromagnetic mismatch (p-polarization)

P_s - parameter related to electromagnetic mismatch (s-polarization)

ϕ - empirical parameter related to porosity-dependence of sound velocities

ψ - angular offset between optical cavities of a tandem Fabry-Pérot interferometer

q - phonon wavevector

q_{BS} - phonon wavevector accessed using a 180° -backscattering geometry

q_{PR} - phonon wavevector accessed using a pseudo-reflection geometry

q_{SW} - phonon wavevector of a probed surface-propagating acoustic phonon

Q - phonon Bloch wavevector

r_y - porous silicon etch rate for the y - th applied etch current

R_{abs} - absolute optical reflectance

R_{rel} - relative optical reflectance

R_{ob} - optical reflectance at oblique angles

ρ - mass density

ρ_{c-si} - mass density of bulk crystalline silicon

t - (integer) order of optical Bragg peak

t_y - porous silicon etch time for the y - th applied etch current

τ - (integer) difference between zone-folding orders

V - sound velocity

$V_{L,eff}$ - effective longitudinal bulk mode velocity

$V_{T,eff}$ - effective transverse bulk mode velocity

w - photon wavenumber

Z - elastic impedance

ζ - porosity

List of Abbreviations

A - aperture

AW - acoustic wave

BS - 180°-backscattering geometry: beam-splitter

BLS - Brillouin light scattering

c-Si - crystalline silicon

CL - collection lens

DL - diode laser

F - filter

FO - optical fiber

FPI - Fabry-Pérot interferometer

FSR - free-spectral range

HWP - half-wave plate

IL - incident lens

L - lens: longitudinal bulk acoustic modes

M - mirror

MB - micrometer-adjustable bracket

π -Si - porous silicon

P - prism

PM - power meter

POL - optical polarizer

PR - pseudo-reflection scattering geometry

PRO - fiber optical reflectance probe

PS - pseudo-surface mode

R - Rayleigh wave

S - sample; surface-localized mode

SEM - scanning electron microscopy

SL - superlattice

SW - surface wave

T - transverse bulk acoustic modes

VNDF - variable neutral density filter

Contents

List of Tables	xvii
List of Figures	xxiii
1 Introduction	1
1.1 Porous Silicon	1
1.2 Porous Silicon-Based Photonic Crystals	7
1.3 Phononic Crystals	11
1.4 Brillouin Light Scattering from Phononic Crystals	13
1.5 Phononic Crystal Behaviour in Silicon-Based Structures	15
1.6 Surface-Localized Acoustic Phonons in One-Dimensional Phononic Crystals	17
1.7 Acoustic Phonon Propagation in Porous Silicon	18
1.8 Present Work	23
Chapter 1 References	26
2 Theory	40
2.1 Phonon and Photon Propagation in a Superlattice	40
2.1.1 Overview	40
2.1.2 Normal-Incidence Phonon Propagation in an Infinite Superlattice	42
2.1.3 Normal-Incidence Phonon Propagation in a Semi-Infinite Superlattice	48
2.1.4 Oblique-Incidence Photon Propagation in an Infinite Superlattice	51
2.2 Brillouin Light Scattering	58
2.2.1 Overview	58
2.2.2 180°-Backscattering and Pseudo-Reflection Brillouin Light Scattering Geometries	62
Chapter 2 References	66

3	Methods and Materials	68
3.1	Sample Preparation	68
3.2	Determination of Film Thickness	75
3.3	Determination of the Porosity, Mass Density, and Refractive Index of a Single-Layer Film	81
3.4	Optical Reflectance Spectroscopy	83
3.4.1	Broad-Band Optical Reflectance Setup and Method	83
3.4.2	Optical Reflectance from a Freestanding Multilayered π -Si Film	86
3.5	Brillouin Spectroscopy Setup	89
3.5.1	180°-Backscattering Geometry	89
3.5.2	Pseudo-Reflection Scattering Geometry	92
3.5.3	Tandem Fabry-Perot Interferometer	96
3.5.4	Brillouin Scattering from a Liquid	100
3.5.5	Analysis of Brillouin Spectra	102
3.6	Determination of the Longitudinal and Transverse Bulk Acoustic Phonon Velocities of a Single-Layer Film	105
3.7	Oblique Angle Reflectance Setup	106
3.8	Comments on Each Study	108
3.8.1	Observation of Hypersonic Phononic Crystal Effects in Porous Silicon Superlattices	108
3.8.2	Probing Near-Normally Propagating Bulk Acoustic Waves using Pseudo-Reflection Geometry Brillouin Spectroscopy	109
3.8.3	Brillouin Scattering from Porous Silicon-Based Optical Bragg Mirrors	110
3.8.4	Oblique Acoustic Phonon Propagation in Porous Silicon Superlattices	111
	Chapter 3 References	112
4	Observation of Hypersonic Phononic Crystal Effects in Porous Silicon Superlattices	115
4.1	Abstract	115
4.2	Introduction	116
4.3	Experimental Details	116
4.4	Theory	120
4.5	Results and Discussion	122
4.6	Conclusions	126
	Chapter 4 References	127
5	Probing Near-Normally Propagating Bulk Acoustic Waves using Pseudo-Reflection Geometry Brillouin Spectroscopy	128
5.1	Abstract	128
5.2	Introduction	129

5.3	Theory	131
5.3.1	Pseudo-Reflection Brillouin Scattering	131
5.3.2	Scattering from an Elastically Homogeneous Material	137
5.3.3	Error Analysis	138
5.4	Experimental Details	143
5.5	Results and Discussion	145
5.6	Conclusions	153
	Chapter 5 References	154
6	Brillouin Scattering from Porous Silicon-Based Optical Bragg Mirrors	158
6.1	Abstract	158
6.2	Introduction	159
6.3	Theory	162
6.3.1	Acoustic Phonon Propagation along the Modulation Axis of an Infinite Superlattice	162
6.3.2	Acoustic Phonon Propagation along the Modulation Axis of a Semi-Infinite Superlattice	164
6.3.3	Photon Propagation at Oblique Angles to the Modulation Axis of an Infinite Superlattice	165
6.3.4	Brillouin Scattering from a Semi-Infinite Superlattice	167
6.4	Experimental Details	170
6.5	Results and Discussion	174
6.5.1	Optical Reflectance	174
6.5.2	Brillouin Light Scattering	176
6.5.3	Comparison to Theory	181
6.6	Conclusions	186
	Chapter 6 References	188
7	Off-Axis Phonon Propagation in Porous Silicon Superlattices	194
7.1	Abstract	194
7.2	Introduction	195
7.3	Experimental Details	197
7.4	Theory	201
7.4.1	Phonon Propagation in an Infinite Superlattice	201
7.4.2	Oblique Angle Photon Propagation in an Infinite Superlattice	205
7.4.3	Brillouin Scattering from a Superlattice	207
7.4.4	Brillouin Linewidth	211
7.5	Results and Discussion	213
7.5.1	Optical Reflectance	213
7.5.2	Pseudo-Reflection Geometry Brillouin Scattering	217
7.5.3	Bulk Longitudinal Mode Linewidths	225

7.5.4	Oblique 180°-Backscattering Geometry Brillouin Scattering . . .	230
7.6	Conclusions	239
	Chapter 7 References	241
8	Summary	246
8.1	Current Results	246
8.2	Future Work	250
	Chapter 8 References	255
A	Raw Data from Experiments on Single-Layer Porous Silicon Films	257
	Appendix A References	267
B	Raw Data for Chapters 4 and 6	268
C	Raw Data for Chapter 5	330
D	Raw Data for Chapter 7	338

List of Tables

3.1	Anodization current densities used to make single-layer and multilayered porous silicon films.	73
3.2	Anodization etch rates and gravimetrically-deduced porosity values for samples made using a 1:1 (49% wt. HF: 98% wt. ethanol) electrolyte.	78
3.3	Bulk transverse phonon velocity, V_T , and bulk longitudinal phonon velocity, V_L , for single-layer π -Si films made using a 1:1 (49% wt. HF: 98% wt. ethanol) by volume electrolyte.	106
4.1	Porosity, refractive index and bulk acoustic phonon velocities for single layer porous silicon films.	120
5.1	Refractive index and bulk acoustic velocities for fused quartz, GaP, water, and porous silicon (π -Si) determined using pseudo-reflection Brillouin spectroscopy.	149
5.2	Ranges of k_m and corresponding q_{PR} probed in fused quartz, GaP, water and porous silicon films.	151
6.1	Porosity, refractive index and bulk acoustic phonon velocities for single-layer porous silicon films.	184
7.1	π -Si superlattice etch times, the modulation wavelength value as determined using the estimated etch rates with the given etch times, and the modulation wavelength value as determined from cross-sectional scanning electron microscope images.	199
7.2	Spectral positions of the first-order photonic band gaps, w_{gap} , the wavenumber ratio w_{λ_o}/w_{gap} , and the superlattice effective refractive index deduced using from the oblique reflectance measurements, $n_{\text{eff}}^{ob}(w_{\lambda_o})$	217
7.3	Porous silicon SL effective refractive index n_{eff} , effective bulk acoustic longitudinal mode velocity $V_{L,\text{eff}}$, effective bulk acoustic transverse mode velocity $V_{T,\text{eff}}$, and modulation wavelength D	224

7.4	The peak positions, the fitted linewidths, the attenuation exponent value, the associated folded bulk longitudinal mode attenuation coefficients, and the corresponding propagation distances of the phonons for the probed SLs.	229
A.1	Fabrication date as well as the frequencies of the BLS-probed transverse mode and the BLS-probed longitudinal mode for single-layer π -Si films made using an etch current of $I_{high} = 230$ mA.	261
A.2	Fabrication date as well as the frequencies of the BLS-probed transverse mode and the BLS-probed longitudinal mode for single-layer π -Si films made using an etch current of $I_{low} = 142$ mA.	264
A.3	Fabrication date as well as the gravimetrically-deduced porosity value for single-layer π -Si films made using an etch current of $I_{high} = 230$ mA.	264
A.4	Fabrication date as well as the gravimetrically-deduced porosity value for single-layer π -Si films made using an etch current of $I_{high} = 142$ mA.	265
A.5	Average porosity value obtained through statistical analysis of the data in Tables A.3 and A.4, $\zeta_{current}$; corresponding porosity values obtained in a previous study conducted in this laboratory, $\zeta_{polomska}$; the average of $\zeta_{current}$ and $\zeta_{polomska}$; the film refractive index at the Brillouin laser line; the average probed transverse and longitudinal phonon frequencies; and the transverse and longitudinal phonon velocities for single-layer π -Si samples made with etch currents $I_{high} = 230$ mA and $I_{high} = 142$ mA.	266
B.1	The θ_i value, the Brillouin spectrum collection date, and the observed phonon modes and corresponding frequencies obtained for sample PSi2.6#1, a binary periodic multilayered π -Si film.	271
B.2	The θ_i value, the Brillouin spectrum collection date, and the observed phonon modes and corresponding frequencies obtained for sample PSi2.12#9, a binary periodic multilayered π -Si film.	272
B.3	The θ_i value, the Brillouin spectrum collection date, and the observed phonon modes and corresponding frequencies obtained for sample PSi2.11#11, a binary periodic multilayered π -Si film.	274
B.4	The θ_i value, the Brillouin spectrum collection date, and the observed phonon modes and corresponding frequencies obtained for sample PSi2.12#11, a binary periodic multilayered π -Si film.	275
B.5	The θ_i value, the Brillouin spectrum collection date, and the observed phonon modes and corresponding frequencies obtained for sample PSi2.12#12, a binary periodic multilayered π -Si film.	277
B.6	The θ_i value, the Brillouin spectrum collection date, and the observed phonon modes and corresponding frequencies obtained for sample PSi2.12#13, a binary periodic multilayered π -Si film.	278

B.7	The θ_i value, the Brillouin spectrum collection date, and the observed phonon modes and corresponding frequencies obtained for sample P <i>Si</i> 2.13#11, a binary periodic multilayered π - <i>Si</i> film.	280
B.8	The θ_i value, the Brillouin spectrum collection date, and the observed phonon modes and corresponding frequencies obtained for sample P <i>Si</i> 2.13#12, a binary periodic multilayered π - <i>Si</i> film.	282
B.9	The θ_i value, the Brillouin spectrum collection date, and the observed phonon modes and corresponding frequencies obtained for sample P <i>Si</i> 2.14A#1, a binary periodic multilayered π - <i>Si</i> film.	284
B.10	The θ_i value, the Brillouin spectrum collection date, and the observed phonon modes and corresponding frequencies obtained for sample P <i>Si</i> 2.17#1, a binary periodic multilayered π - <i>Si</i> film.	285
B.11	The θ_i value, the Brillouin spectrum collection date, and the observed phonon modes and corresponding frequencies obtained for sample P <i>Si</i> 2.17#3, a binary periodic multilayered π - <i>Si</i> film.	286
B.12	The θ_i value, the Brillouin spectrum collection date, and the observed phonon modes and corresponding frequencies obtained for sample P <i>Si</i> 2.17#4, a binary periodic multilayered π - <i>Si</i> film.	287
B.13	The θ_i value, the Brillouin spectrum collection date, and the observed phonon modes and corresponding frequencies obtained for sample P <i>Si</i> 2.18#12, a binary periodic multilayered π - <i>Si</i> film.	289
B.14	The θ_i value, the Brillouin spectrum collection date, and the observed phonon modes and corresponding frequencies obtained for sample P <i>Si</i> 2.18#13, a binary periodic multilayered π - <i>Si</i> film.	291
B.15	The θ_i value, the Brillouin spectrum collection date, and the observed phonon modes and corresponding frequencies obtained for sample P <i>Si</i> 2.18#14, a binary periodic multilayered π - <i>Si</i> film.	293
B.16	The θ_i value, the Brillouin spectrum collection date, and the observed phonon modes and corresponding frequencies obtained for sample P <i>Si</i> 2.18#15, a binary periodic multilayered π - <i>Si</i> film.	295
B.17	The θ_i value, the Brillouin spectrum collection date, and the observed phonon modes and corresponding frequencies obtained for sample P <i>Si</i> 2.18#17, a binary periodic multilayered π - <i>Si</i> film.	296
B.18	The anodization times per cycle, the SL modulation wavelength and the spectral position of the observed first-order optical Bragg peak, for a series of binary periodic multilayered π - <i>Si</i> films.	300
B.19	The θ_i value, the Brillouin spectrum collection date, and the observed phonon modes and corresponding frequencies obtained for sample P <i>Si</i> 4.13#10, a binary periodic multilayered π - <i>Si</i> film.	301
B.20	The θ_i value, the Brillouin spectrum collection date, and the observed phonon modes and corresponding frequencies obtained for sample P <i>Si</i> 4.13#12, a binary periodic multilayered π - <i>Si</i> film.	302

B.22	The θ_i value, the Brillouin spectrum collection date, and the observed phonon modes and corresponding frequencies obtained for sample P <i>Si</i> 4.13#9, a binary periodic multilayered π -Si film.	303
B.23	The θ_i value, the Brillouin spectrum collection date, and the observed phonon modes and corresponding frequencies obtained for sample P <i>Si</i> 4.13#2, a binary periodic multilayered π -Si film.	305
B.24	The θ_i value, the Brillouin spectrum collection date, and the observed phonon modes and corresponding frequencies obtained for sample P <i>Si</i> 4.13#5, a binary periodic multilayered π -Si film.	306
B.25	The θ_i value, the collection date, and the observed phonon modes and corresponding frequencies obtained for sample P <i>Si</i> 2.12#5, a binary periodic multilayered π -Si film.	308
B.26	Angle θ_i , angle θ_s , the corresponding θ_m value, the date of data collection, and the frequencies of the bulk acoustic phonons probed in the pseudo-reflection geometry Brillouin scattering measurements done on sample P <i>Si</i> 2.12#5.	308
B.27	The θ_i value, the collection date, and the observed phonon modes and corresponding frequencies obtained for sample P <i>Si</i> 2.14A#2, a binary periodic multilayered π -Si film.	312
B.28	Angle θ_i , angle θ_s , the corresponding θ_m value, the date of data collection, and the frequencies of the bulk acoustic phonons probed in the pseudo-reflection geometry Brillouin scattering measurements done on sample P <i>Si</i> 2.14A#2.	313
B.29	The θ_i value, the collection date, and the observed phonon modes and corresponding frequencies obtained for sample P <i>Si</i> 2.20#8, a binary periodic multilayered π -Si film.	315
B.30	Angle θ_i , angle θ_s , the corresponding θ_m value, the date of data collection, and the frequencies of the bulk acoustic phonons probed in the pseudo-reflection geometry Brillouin scattering measurements done on sample P <i>Si</i> 2.20#8.	318
B.31	The θ_i value, the collection date, and the observed phonon modes and corresponding frequencies obtained for sample P <i>Si</i> 2.20#10, a binary periodic multilayered π -Si film.	321
B.32	Angle θ_i , angle θ_s , the corresponding θ_m value, the date of data collection, and the frequencies of the bulk acoustic phonons probed in the pseudo-reflection geometry Brillouin scattering measurements done on sample P <i>Si</i> 2.20#10.	324
B.33	The θ_i value, the collection date, and the observed phonon modes and corresponding frequencies obtained for sample P <i>Si</i> 4.9#9, a binary periodic multilayered π -Si film.	326

B.34	Angle θ_i , angle θ_s , the corresponding θ_m value, the date of data collection, and the frequencies of the bulk acoustic phonons probed in the pseudo-reflection geometry Brillouin scattering measurements done on sample PSi4.9#9.	328
C.1	Angle θ_i , angle θ_s , the corresponding θ_m value, the date of data collection, and the frequencies of the bulk acoustic phonons probed in the pseudo-reflection geometry Brillouin scattering measurements taken from sample PSi4.7#3.	331
C.2	Angle θ_i , angle θ_s , the corresponding θ_m value, the date of data collection, and the frequencies of the bulk acoustic phonons probed in the pseudo-reflection geometry Brillouin scattering measurements taken from sample PSi4.7#2.	333
C.3	Angle θ_i , angle θ_s , the corresponding θ_m value, the date of data collection, and the frequencies of the bulk acoustic phonons probed in the pseudo-reflection geometry Brillouin scattering measurements taken from a sample of fused quartz.	334
C.4	Angle θ_i , angle θ_s , the corresponding θ_m value, the date of data collection, and the frequencies of the bulk acoustic phonons probed in the pseudo-reflection geometry Brillouin scattering measurements taken from a sample of gallium phosphide.	334
C.5	Angle θ_i , angle θ_s , the corresponding θ_m value, the date of data collection, and the frequencies of the bulk acoustic phonons probed in the pseudo-reflection geometry Brillouin scattering measurements taken from a sample of water	337
D.1	Spectral positions of the first-order optical Bragg peaks observed for samples PSi2.3#15 and PSi2.6#4.	339
D.2	A set of incident angle-dependent optical reflectance data collected from sample PSi2.315, a binary periodic multilayered π -Si film.	340
D.3	Another set of incident angle-dependent optical reflectance data collected from sample PSi2.315, a binary periodic multilayered π -Si film.	341
D.4	Incident angle-dependent optical reflectance data collected from sample PSi2.64, a binary periodic multilayered π -Si film.	342
D.5	The θ_i value, the collection date, and the observed phonon modes and corresponding frequencies obtained for sample PSi2.3#15, a binary periodic multilayered π -Si film.	344
D.6	The θ_i value, the collection date, and the observed phonon modes and corresponding frequencies obtained for sample PSi2.3#15 in the second set of 180° -backscattering geometry Brillouin measurements.	346

D.7	The θ_i value, the collection date, and the observed phonon modes and corresponding frequencies obtained for sample P <i>Si</i> 2.3#15 in the third and fourth sets of 180°-backscattering geometry Brillouin measurements.	349
D.8	Angle θ_i , angle θ_s , the corresponding θ_m value, the date of data collection, and the frequencies of the bulk acoustic phonons probed in the pseudo-reflection geometry Brillouin scattering measurements done on sample P <i>Si</i> 2.3#15.	352
D.9	The θ_i value, the collection date, and the observed phonon modes and corresponding frequencies obtained for sample P <i>Si</i> 6#4, a binary periodic multilayered π -Si film.	355
D.10	The θ_i value, the collection date, and the observed phonon modes and corresponding frequencies obtained for sample P <i>Si</i> 6#4 in the second collection of 180°-backscattering Brillouin measurements.	357
D.11	The θ_i value, the collection date, and the observed phonon modes and corresponding frequencies obtained for sample P <i>Si</i> 6#4 in the third collection of 180°-backscattering Brillouin measurements.	359
D.12	Angle θ_i , angle θ_s , the corresponding θ_m value, the date of data collection, and the frequencies of the bulk acoustic phonons probed in the pseudo-reflection geometry Brillouin scattering measurements done on sample P <i>Si</i> 2.6#4.	361

List of Figures

1.1	Cross-sectional scanning electron micrograph of a supported mesoporous silicon film.	2
1.2	Illustration of the photonic band structure in a composite material with a binary periodicity in the optical parameters.	8
1.3	Electromagnetic standing waves in an optically periodic structure. . .	10
2.1	(a) Infinite and (b) semi-infinite two-component superlattices.	41
2.2	Schematic of the phononic band structure for propagation along the modulation axis of an infinite binary periodic superlattice.	45
2.3	Schematic of the photonic band structure for propagation along the modulation axis of an infinite binary periodic superlattice.	59
2.4	Schematic of a Brillouin spectrum.	61
2.5	(a) 180°-backscattering and (b) pseudo-reflection Brillouin light scattering geometries.	63
3.1	Cross-section of the electrolytic cell used for sample fabrication. . . .	71
3.2	Fabrication setup.	71
3.3	Cross-sections of (a) the freestanding film retrieval setup and (b) the sample holder.	76
3.4	Top-down image of a supported π -Si multilayered film.	79
3.5	Cross-sectional scanning electron micrograph of a freestanding single-layer π -Si film.	79
3.6	Cross-sectional scanning electron micrograph of a supported single-layer π -Si film.	80
3.7	Cross-sectional scanning electron micrograph of a supported multilayered π -Si film.	80
3.8	Broad-band optical reflectance spectroscopy setup.	84
3.9	The absolute reflectance spectrum of a broad-band dielectric mirror. .	85
3.10	Optical reflectance spectrum of GaP.	87

3.11	Optical reflectance spectra collected from the surfaces of a freestanding multilayered π -Si film.	88
3.12	180°-backscattering geometry Brillouin light scattering setup.	90
3.13	Procedure for setting up a pseudo-reflection Brillouin light scattering geometry.	92
3.14	Pseudo-reflection geometry Brillouin light scattering spectra collected at a large angle of incidence.	96
3.15	A tandem Fabry-Perot interferometer.	99
3.16	Sample mount used to probe water.	101
3.17	An example of a collected Brillouin light scattering spectrum.	103
3.18	Examples of (a) a Brillouin peak and (b) a center peak due to the reference beam.	104
3.19	Experimental setup to measure oblique angle reflectance.	108
4.1	(a) Cross-sectional scanning electron micrograph of a $D = 500$ nm superlattice (SL). (b) Scattering geometry.	118
4.2	Spectra collected from (a) a $D = 61$ nm 0.59/0.52 superlattice, (b) a $D = 98$ nm 0.59/0.52 superlattice, (c) a $D = 123$ nm 0.59/0.52 superlattice, and (d) a $D = 167$ nm 0.56/0.46 superlattice.	121
4.3	Phonon frequency versus modulation wavelength for superlattices with constituent layer porosities of (a) 0.59 and 0.52 and (b) 0.56 and 0.46.	124
5.1	Brillouin scattering geometries: (a) pseudo-reflection and (b) 180°-backscattering.	132
5.2	Dependence of α_{PR} on θ_m and refractive index for (a) $\theta_d = 3^\circ$ and (b) $\theta_d = 5^\circ$	135
5.3	Dependence of error in the sound velocity on angle of propagation within the (001)-plane of GaP.	142
5.4	Brillouin spectra of (a) fused quartz, (b) (100)-oriented GaP, (c) deionized water, and (d) a 58% porous silicon film for different values of θ_m	146
5.5	Acoustic wave frequency versus k_m for (a) fused quartz, (b) GaP, (c) water, and (d) 50% (diamonds) and 58% (circles) porous silicon.	148
5.6	Acoustic wave frequency versus q_{PR} for fused quartz.	152
6.1	(a) Infinite and (b) semi-infinite superlattices containing a two-layer unit cell.	163
6.2	(a) 180°-backscattering and (b) pseudo-reflection geometries.	168
6.3	(a) Optical reflectance spectra collected from $D = 145$ nm, $D = 166$ nm, and $D = 172$ nm porous silicon superlattices.	175
6.4	(a) Brillouin spectra collected from a $D = 99$ nm porous silicon superlattice at different angles of incidence.	178
6.5	Polarized Brillouin spectra collected from a $D = 166$ nm porous silicon superlattice at $\theta_m = 54^\circ$	179

6.6	(a) Near-normal incidence 180°-backscattering geometry Brillouin spectrum collected from a $D = 151$ nm sample.	180
6.7	(a) Near-normal incidence 180°-backscattering geometry Brillouin spectrum collected from two $D \sim 150$ nm superlattices, one with the lower elastic impedance (<i>i.e.</i> , higher porosity) layer adjacent to air and the other vice-versa.	182
6.8	Dependence of νD on qD for the porous silicon superlattices.	183
7.1	Schematic of the bulk acoustic phononic band structure along the modulation axis of a binary-periodic superlattice.	203
7.2	(a) pseudo-reflection and (b) 180°-backscattering geometries.	209
7.3	Optical reflectance spectra collected from (a) sample 1 and (b) sample 2.	216
7.4	Optical reflectance versus incident angle for (a) sample 1 and (b) sample 2 with $\lambda_o = 532$ nm.	218
7.5	Brillouin spectra collected from (a) sample 1 and (b) sample 2 at different angles of incidence.	220
7.6	Polarized Brillouin spectra collected from the sample 1 at $\theta_m = 53^\circ$	221
7.7	Dependence of bulk longitudinal and transverse mode frequency on k_m^2 for (a) sample 1 and (b) sample 2.	223
7.8	(a) Anti-Stokes portion of the near-normal incidence 180°-backscattering spectrum collected from sample 1. (b) The corresponding near-normal incidence 180°-backscattering spectrum with the shoulder contribution removed.	226
7.9	Oblique 180°-backscattering Brillouin spectra collected from (a) sample 1 and (b) sample 2 with $\theta_i = 70^\circ$ and 50° , respectively.	232
7.10	Oblique 180°-backscattering Brillouin spectra focusing on spectral features from bulk modes in (a) sample 1 and (b) sample 2.	233
7.11	Dependence of bulk mode frequency on $q_{ }^2$ for (a) sample 1 and (b) sample 2.	235
7.12	Oblique 180°-backscattering Brillouin spectra focusing on the θ_i -dependence of spectral features attributed to surface-propagating modes in (a) sample 1 and (b) sample 2.	237
7.13	Surface mode velocity versus $q_{ }D$ for the Rayleigh and a pseudo-surface in sample 1 and sample 2.	238
A.1	(a) Near-normal incidence 180°-backscattering geometry Brillouin spectrum and (b) near-normal incidence broadband optical reflectance spectrum collected from sample PSi2.20#3, a single-layer π -Si film.	259
A.2	(a) Near-normal incidence 180°-backscattering geometry Brillouin spectrum and (b) near-normal incidence broadband optical reflectance spectrum collected from sample PSi4.3#8, a single-layer π -Si film.	259

A.3	(a) Near-normal incidence 180° -backscattering geometry Brillouin spectrum and (b) near-normal incidence broadband optical reflectance spectrum collected from sample P <i>Si</i> 4.6#1, a single-layer π -Si film.	260
A.4	(a) Near-normal incidence 180° -backscattering geometry Brillouin spectrum and (b) near-normal incidence broadband optical reflectance spectrum collected from sample P <i>Si</i> 4.7#3, a single-layer π -Si film.	260
A.5	(a) Near-normal incidence 180° -backscattering geometry Brillouin spectrum and (b) near-normal incidence broadband optical reflectance spectrum collected from sample P <i>Si</i> 4.8#8, a single-layer π -Si film.	261
A.6	(a) Near-normal incidence 180° -backscattering geometry Brillouin spectrum and (b) near-normal incidence broadband optical reflectance spectrum collected from sample P <i>Si</i> 2.20#4, a single-layer π -Si film.	262
A.7	(a) Near-normal incidence 180° -backscattering geometry Brillouin spectrum and (b) near-normal incidence broadband optical reflectance spectrum collected from sample P <i>Si</i> 4.4#1, a single-layer π -Si film.	262
A.8	(a) Near-normal incidence 180° -backscattering geometry Brillouin spectrum and (b) near-normal incidence broadband optical reflectance spectrum collected from sample P <i>Si</i> 4.6#2, a single-layer π -Si film.	263
A.9	(a) Near-normal incidence 180° -backscattering geometry Brillouin spectrum and (b) near-normal incidence broadband optical reflectance spectrum collected from sample P <i>Si</i> 4.7#2, a single-layer π -Si film.	263
B.1	(a)-(b) Near-normal incidence 180° -backscattering geometry Brillouin spectra and (c) near-normal incidence broadband optical reflectance spectrum collected from sample P <i>Si</i> 2.6#1, a binary periodic multilayered π -Si film.	270
B.2	(a) Near-normal incidence 180° -backscattering geometry Brillouin spectrum and (b) near-normal incidence broadband optical reflectance spectrum collected from sample P <i>Si</i> 2.12#9, a binary periodic multilayered π -Si film.	272
B.3	(a)-(b) Near-normal incidence 180° -backscattering geometry Brillouin spectra and (c) near-normal incidence broadband optical reflectance spectrum collected from sample P <i>Si</i> 2.11#11, a binary periodic multilayered π -Si film.	273
B.4	(a) Near-normal incidence 180° -backscattering geometry Brillouin spectrum and (b) near-normal incidence broadband optical reflectance spectrum collected from sample P <i>Si</i> 2.12#11, a binary periodic multilayered π -Si film.	275
B.5	(a)-(b) Near-normal incidence 180° -backscattering geometry Brillouin spectra and (c) near-normal incidence broadband optical reflectance spectrum collected from sample P <i>Si</i> 2.12#12, a binary periodic multilayered π -Si film.	276

B.6	(a) Near-normal incidence 180° -backscattering geometry Brillouin spectrum and (b) near-normal incidence broadband optical reflectance spectrum collected from sample P <i>Si</i> 2.12#13, a binary periodic multilayered π -Si film.	278
B.7	(a)-(b) Near-normal incidence 180° -backscattering geometry Brillouin spectra and (c) near-normal incidence broadband optical reflectance spectrum collected from sample P <i>Si</i> 2.13#11, a binary periodic multilayered π -Si film.	279
B.8	(a)-(b) Near-normal incidence 180° -backscattering geometry Brillouin spectra and (c) near-normal incidence broadband optical reflectance spectrum collected from sample P <i>Si</i> 2.13#12, a binary periodic multilayered π -Si film.	281
B.9	(a)-(b) Near-normal incidence 180° -backscattering geometry Brillouin spectra and (c) near-normal incidence broadband optical reflectance spectrum collected from sample P <i>Si</i> 2.14A#1, a binary periodic multilayered π -Si film.	283
B.10	(a) Near-normal incidence 180° -backscattering geometry Brillouin spectrum and (b) near-normal incidence broadband optical reflectance spectrum collected from sample P <i>Si</i> 2.17#1, a binary periodic multilayered π -Si film.	285
B.11	(a) Near-normal incidence 180° -backscattering geometry Brillouin spectrum and (b) near-normal incidence broadband optical reflectance spectrum collected from sample P <i>Si</i> 2.17#3, a binary periodic multilayered π -Si film.	286
B.12	(a) Near-normal incidence 180° -backscattering geometry Brillouin spectrum and (b) near-normal incidence broadband optical reflectance spectrum collected from sample P <i>Si</i> 2.17#4, a binary periodic multilayered π -Si film.	287
B.13	(a)-(b) Near-normal incidence 180° -backscattering geometry Brillouin spectra and (c) near-normal incidence broadband optical reflectance spectrum collected from sample P <i>Si</i> 2.18#12, a binary periodic multilayered π -Si film.	288
B.14	(a)-(b) Near-normal incidence 180° -backscattering geometry Brillouin spectra and (c) near-normal incidence broadband optical reflectance spectrum collected from sample P <i>Si</i> 2.18#13, a binary periodic multilayered π -Si film.	290
B.15	(a)-(b) Near-normal incidence 180° -backscattering geometry Brillouin spectra and (c) near-normal incidence broadband optical reflectance spectrum collected from sample P <i>Si</i> 2.18#14, a binary periodic multilayered π -Si film.	292
B.16	Cross-sectional scanning electron micrograph of P <i>Si</i> 2.18#14.	294

B.17 (a) Near-normal incidence 180°-backscattering geometry Brillouin spectrum and (b) near-normal incidence broadband optical reflectance spectrum collected from sample P <i>Si</i> 2.18#15, a binary periodic multilayered π - <i>Si</i> film.	295
B.18 (a) Near-normal incidence 180°-backscattering geometry Brillouin spectrum and (b) near-normal incidence broadband optical reflectance spectrum collected from sample P <i>Si</i> 2.18#17, a binary periodic multilayered π - <i>Si</i> film.	296
B.19 Cross-sectional scanning electron micrograph of P <i>Si</i> 2.18#17.	297
B.20 Near-normal incidence broadband optical reflectance spectrum from sample P <i>Si</i> 2.20#7, a binary periodic multilayered π - <i>Si</i> film.	298
B.21 Near-normal incidence broadband optical reflectance spectrum from sample P <i>Si</i> 2.20#9, a binary periodic multilayered π - <i>Si</i> film.	298
B.22 Near-normal incidence broadband optical reflectance spectrum from sample P <i>Si</i> 2.18#7, a binary periodic multilayered π - <i>Si</i> film.	299
B.23 Near-normal incidence broadband optical reflectance spectrum from sample P <i>Si</i> 2.18#8, a binary periodic multilayered π - <i>Si</i> film.	299
B.24 Near-normal incidence broadband optical reflectance spectrum from sample P <i>Si</i> 2.18#9, a binary periodic multilayered π - <i>Si</i> film.	300
B.25 (a) Near-normal incidence 180°-backscattering geometry Brillouin spectrum and (b) near-normal incidence broadband optical reflectance spectrum collected from sample P <i>Si</i> 4.13#10, a binary periodic multilayered π - <i>Si</i> film with the higher porosity constituent layer at the air-film interface.	301
B.26 (a) Near-normal incidence 180°-backscattering geometry Brillouin spectrum and (b) near-normal incidence broadband optical reflectance spectrum collected from sample P <i>Si</i> 4.13#12, a binary periodic multilayered π - <i>Si</i> film with the lower porosity constituent layer at the air-film interface.	302
B.27 (a) Near-normal incidence 180°-backscattering geometry Brillouin spectrum and (b) near-normal incidence broadband optical reflectance spectrum collected from sample P <i>Si</i> 4.13#9, a binary periodic multilayered π - <i>Si</i> film with the lower porosity constituent layer at the air-film interface.	303
B.28 (a) Near-normal incidence 180°-backscattering geometry Brillouin spectrum, (b) oblique incidence 180°-backscattering geometry Brillouin spectrum, and (c) near-normal incidence broadband optical reflectance spectrum collected from sample P <i>Si</i> 4.13#2, a binary periodic multilayered π - <i>Si</i> film with the higher porosity constituent layer at the air-film interface.	304
B.29 Near-normal incidence 180°-backscattering geometry Brillouin spectrum collected from sample P <i>Si</i> 4.13#5, a binary periodic multilayered π - <i>Si</i> film with the lower porosity constituent layer at the air-film interface.	306

B.30 (a)-(b) Near-normal incidence 180° -backscattering geometry Brillouin spectra and (c) near-normal incidence broadband optical reflectance spectrum collected from sample PSi2.12#5, a binary periodic multilayered π -Si film.	307
B.31 Pseudo-reflection geometry Brillouin scattering spectra collected from sample PSi2.12#5, a binary periodic multilayered π -Si film.	309
B.32 Cross-sectional scanning electron micrograph of PSi2.12#15.	310
B.33 (a)-(b) Near-normal incidence 180° -backscattering geometry Brillouin spectra, (c) 180° -backscattering geometry Brillouin spectrum collected at unknown angle, and (d) near-normal incidence broadband optical reflectance spectrum collected from sample PSi2.14A#2, a binary periodic multilayered π -Si film.	311
B.34 Pseudo-reflection geometry Brillouin scattering spectra collected from sample PSi2.14A#2, a binary periodic multilayered π -Si film.	312
B.35 (a)-(c) Near-normal incidence 180° -backscattering geometry Brillouin spectra and (d) near-normal incidence broadband optical reflectance spectrum collected from sample PSi2.20#8, a binary periodic multilayered π -Si film.	314
B.36 A collection of pseudo-reflection geometry Brillouin scattering spectra collected from sample PSi2.20#8, a binary periodic multilayered π -Si film.	316
B.37 Another collection of pseudo-reflection geometry Brillouin scattering spectra collected from sample PSi2.20#8, a binary periodic multilayered π -Si film.	317
B.38 Cross-sectional scanning electron micrograph of PSi2.20#8.	319
B.39 (a)-(b) Near-normal incidence 180° -backscattering geometry Brillouin spectra and (c) near-normal incidence broadband optical reflectance spectrum collected from sample PSi2.20#10, a binary periodic multilayered π -Si film.	320
B.40 A collection of pseudo-reflection geometry Brillouin scattering spectra collected from sample PSi2.20#10, a binary periodic multilayered π -Si film.	322
B.41 Another collection of pseudo-reflection geometry Brillouin scattering spectra collected from sample PSi2.20#10, a binary periodic multilayered π -Si film.	323
B.42 Cross-sectional scanning electron micrograph of PSi2.20#10.	325
B.43 (a) Near-normal incidence 180° -backscattering geometry Brillouin spectrum and (b) near-normal incidence broadband optical reflectance spectrum collected from sample PSi4.9#9, a binary periodic multilayered π -Si film.	326

B.44	A collection of pseudo-reflection geometry Brillouin scattering spectra collected from sample P <i>Si</i> 4.9#9, a binary periodic multilayered π -Si film.	327
B.45	Cross-sectional scanning electron micrograph of P <i>Si</i> 4.9#9.	329
C.1	Pseudo-reflection geometry Brillouin scattering spectra collected from sample P <i>Si</i> 4.73, a single-layer π -Si film.	331
C.2	Pseudo-reflection geometry Brillouin scattering spectra collected from sample P <i>Si</i> 4.72, a single-layer π -Si film.	332
C.3	Pseudo-reflection geometry Brillouin scattering spectra collected from a sample of fused quartz.	333
C.4	Pseudo-reflection geometry Brillouin scattering spectra collected from a sample of gallium phosphide.	335
C.5	Pseudo-reflection geometry Brillouin scattering spectra collected from a sample of water.	336
D.1	A collection of oblique incidence 180°-backscattering geometry Brillouin spectra collected from sample P <i>Si</i> 2.3#15, a binary periodic multilayered π -Si film.	343
D.2	Another collection of oblique incidence 180°-backscattering geometry Brillouin spectra collected from sample P <i>Si</i> 2.3#15, a binary periodic multilayered π -Si film.	345
D.3	A third collection of oblique incidence 180°-backscattering geometry Brillouin spectra collected from sample P <i>Si</i> 2.3#15, a binary periodic multilayered π -Si film.	347
D.4	A fourth collection of oblique incidence 180°-backscattering geometry Brillouin spectra collected from sample P <i>Si</i> 2.3#15, a binary periodic multilayered π -Si film.	348
D.5	A collection of pseudo-reflection geometry Brillouin scattering spectra collected from sample P <i>Si</i> 2.3#15, a binary periodic multilayered π -Si film.	350
D.6	Another collection of pseudo-reflection geometry Brillouin scattering spectra collected from sample P <i>Si</i> 2.3#15, a binary periodic multilayered π -Si film.	351
D.7	Cross-sectional scanning electron micrograph of P <i>Si</i> 2.3#15.	353
D.8	A collection of oblique incidence 180°-backscattering geometry Brillouin spectra collected from sample P <i>Si</i> 2.6#4, a binary periodic multilayered π -Si film.	354
D.9	Another collection of oblique incidence 180°-backscattering geometry Brillouin spectra collected from sample P <i>Si</i> 2.6#4.	356
D.10	A third collection of oblique incidence 180°-backscattering geometry Brillouin spectra collected from sample P <i>Si</i> 2.6#4.	358

D.11 A collection of pseudo-reflection geometry Brillouin scattering spectra collected from sample PSi2.6#4. a binary periodic multilayered π -Si film.	360
D.12 Cross-sectional scanning electron micrograph of PSi2.6#4.	362

Chapter 1

Introduction

1.1 Porous Silicon

Porous silicon (π -Si) was discovered accidentally by Uhlir in 1956 during an experimental study on the use of electrochemical etching for shaping both silicon and germanium [1]. A brown film was observed on silicon samples which had been subjected to certain etch conditions and, at the time, it was mistakenly thought to be due to the formation of silicon suboxide on the sample surface. It was not until the 1970s that this brown film was properly recognized as a porous silicon nanostructure [2]. Figure 1.1 shows a cross-sectional scanning electron micrograph of a supported π -Si film.

While it is possible to obtain π -Si films by way of either chemical or light-assisted chemical (*i.e.*, photochemical) etching of bulk crystalline silicon with certain etchants [3], the most versatile and widely used method for fabrication is by electrochemical anodization of crystalline silicon in hydrofluoric acid-based electrolytes.

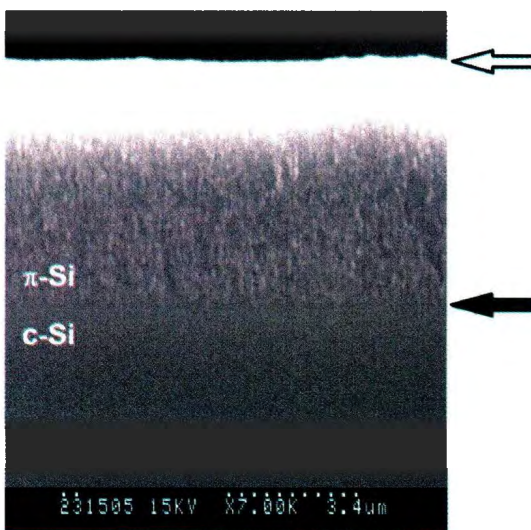


Figure 1.1: Cross-sectional scanning electron micrograph of a supported mesoporous silicon film. Empty (filled) arrows denote the film-air (substrate-film) interface. Image was post-processed in order to increase the contrast between the film and the substrate. The bright region at the film-air interface is thought to be due to electron charging effects which occur during the scanning electron imaging process.

Under the appropriate etching conditions, pores nucleate at the silicon-electrolyte interface and proceed to grow down into the silicon wafer. This results in the formation of a π -Si layer on a crystalline silicon substrate. The physical nature of the formed π -Si film is drastically different from that of the parent bulk crystalline silicon, a visibly opaque semiconductor with an indirect band gap of 1.12 eV [4]. This change in physical behaviour is a manifestation of the porous structure and, in turn, is governed by the pore morphology (a term used to identify properties like the shape, orientation, and interaction of the pores [5]), the pore geometry (which identifies the pore diameter and the distance between pores [5]), and the porosity (*i.e.*, the volume fraction of voids in the porous region, denoted by ζ). In addition to the dopant type

and concentration in the parent crystalline silicon wafer, the resulting morphology, geometry, and porosity of the π -Si film depend on the etch parameters, which include the applied current density, the electrolyte composition, the etch time, the intensity and wavelength of surface illumination during the etch [6], and the temperature [3]. Thus, the physical characteristics of a π -Si film are defined, in part, by the etch conditions under which it is made.

Studies on π -Si formation have garnered films with vastly different pore structures. Following the standard set by the International Union of Pure and Applied Chemistry, π -Si samples are typically distinguished according to pore geometry. Samples with geometries less than 10 nm are categorized as microporous while those with geometries greater than 50 nm are categorized as macroporous; between 10 nm and 50 nm, the film is said to be mesoporous [2, 5]. While this is a reasonable first step at differentiating between samples, it does not account for differences in morphology and, thus, π -Si films falling within the same categorization may have very different pore structures. This is illustrated in a study done by Ronnebeck *et al.* [7] on the formation of macroporous silicon by anodization of *n*-type silicon subjected to backside illumination (*i.e.*, the back of the substrate, opposite the electrolyte-silicon interface, was illuminated); it was found that the macropore orientation relative to the sample surface (*i.e.*, the pore morphology) was dependent on the crystal orientation of the parent silicon wafer. Additionally, other studies have reported more complex structures involving two different pore geometries, as in the case of macropores in *p*-type

silicon which have microporous structure in the pore walls [8]. While many different techniques and recipes have been used to fabricate various π -Si samples, some of the most widely studied structures include micropores formed in p -type silicon [3], mesopores formed in p^+ -type and n^+ -type silicon [9], and macropores formed in n -type silicon under backside illumination [5]. All of the aforementioned structures are made by anodization with simple hydrofluoric acid (HF) electrolytes.

Porous silicon is known to exhibit a number of novel physical attributes including room-temperature visible photoluminescence [10], electroluminescence [11], a high level of biocompatibility (*i.e.*, the ability of a material to interface with a natural substance without causing a natural response [12]) and bioactivity (*i.e.*, the ability of a material to promote direct interaction with a natural substance [13]) [14–16] as well as a very large internal surface area (of the order of $500 \text{ m}^2/\text{cm}^3$) [17]. Moreover, both the optical [18] and elastic [19] properties of π -Si depend on the pore characteristics and, thus, can be tuned by an appropriate choice of the etch conditions. These novel features, coupled with the fact that π -Si can be readily integrated into existing silicon-based technology, make this material of great interest from both a fundamental standpoint as well as for its potential use in both existing and new technological applications. Some of these include solar cells, photodectors, and light-emitting diodes [20], chemical and gas sensors [21–26], biological sensors [27–30] and implants [12, 13, 31, 32] as well as hydrogen energy cells [33, 34].

In order to fully appreciate the physical behaviour of π -Si, one must first have an understanding of how this material is made. Exposing bulk silicon to a HF solution in the absence of both an anodic current and light leads to a very slow (< 0.1 nm/min), isotropic etch of the silicon surface [35]: HF dissolves silicon dioxide, which forms naturally on silicon, and leaves the surface hydrogen-terminated. Additionally, it is known that holes are consumed in the dissolution of silicon. Therefore, by anodically biasing the silicon wafer and, in the case of n -type silicon and semi-insulating p -type silicon, illuminating the sample, more holes are supplied to the silicon-electrolyte interface, hence, changing the etch process [6]. Above a critical current density, J_{crit} (defined for a given experiment by the aforementioned conditions such as sample doping and electrolyte composition), an abundance of holes build up at the silicon-electrolyte interface and, in turn, the reaction is limited by the supply of HF in the solution. Due to better exposure to the electrolyte, hillocks on the silicon surface will dissolve more quickly than depressions. Consequently, this leads to flattening, or electropolishing, of the sample surface. Below J_{crit} , the etch process is limited by the number of available holes. In this regime, due to a higher accessibility to holes in the bulk of the silicon wafer, depressions etch faster than hillocks and, thus, pores form in the silicon wafer [36]. Upon nucleation, the walls of the pores grow until depleted of holes. Pore growth then proceeds into the bulk of the silicon sample, toward the source of the holes, via the pore tip [6]. Furthermore, due to the depletion of holes, the resulting porous silicon nanostructure has a relatively high resistivity comparable to

that of intrinsic silicon [37] and, therefore, is inert to further electrochemical etching. While the π -Si film is still susceptible to chemical dissolution, which may cause further erosion of the upper region of the porous structure [6, 38], this effect is typically slow relative to the electrochemical process and, hence, π -Si formation can be treated as a self-limiting process [6]. That is, further anodization of an as-formed π -Si film will have negligible effects on the existing porous region and etching will proceed at the pore tip.

While the above phenomenological description gives a general overview of the key features of π -Si formation, it says nothing about how the etch parameters influence structural characteristics such as pore morphology, pore geometry, and porosity. Due to the complexity of the system, a complete theory which successfully accounts for all the possible pore structures has yet to be formulated. Thus, the current state of the art involves resorting to different models and mechanisms depending on the nanostructure which is to be considered. It is generally thought that pore initiation is brought on by nonuniform dissolution of silicon due to surface defects and, therefore, form randomly on the silicon surface [2]. Since the pores grow in size until the walls are depleted of holes, the hole depletion mechanism, along with the charge transfer mechanism across the silicon-electrolyte interface, plays a major role in determining pore geometry [6]. Commonly invoked models for π -Si formation include a quantum confinement treatment for microporous structures [39] as well as an electric field-depletion mechanism for meso- and macroporous structures [40].

As stated earlier, the passivity of the pore walls against further etching ensures that π -Si formation is a self-limiting process. Therefore, once a π -Si layer is formed, electrochemical anodization of that layer stops. Subsequent etching occurs at the pore tip and, thus, by careful variation of the etch conditions during π -Si formation, the depth profile of the porous structure can be tuned in a controllable way [6]. In practice, variation in the etch conditions is typically achieved either by applying a time-varied current density profile to a homogeneously doped silicon wafer (while keeping all the other parameters constant) [41], or by applying fixed etch parameters to a wafer which has an inhomogeneous doping profile with depth [42]. These methods have been used to fabricate various π -Si multilayered structures such as superlattices. Additionally, due to the self-limiting nature of the pore formation, π -Si films can be easily removed from the crystalline silicon substrate. Subjecting a π -Si sample to electropolishing conditions leads to complete electrochemical dissolution at the film-substrate interface. Hence, freestanding π -Si films can be made [43].

1.2 Porous Silicon-Based Photonic Crystals

A photonic crystal is a composite material characterized by a spatial periodicity in the optical parameters (*i.e.*, dielectric constant) which leads to the formation of forbidden photon frequency bands, or photonic band gaps. Figure 1.2 illustrates the photonic band structure of a binary-periodic composite material. Light waves with frequencies within these band gaps cannot propagate in the material [44]. In general,

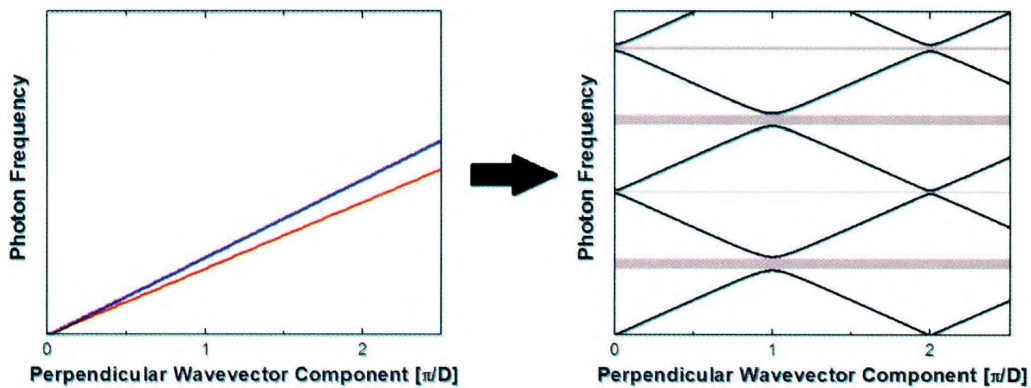


Figure 1.2: Illustration of the photonic band structure in a composite material with a binary periodicity in the optical parameters. The constituent layers are assumed to be non-dispersive, as depicted by the two linear dispersion curves in the left photon frequency versus wavevector plot. The photonic band structure of the resulting composite material exhibits a number of photonic band gaps, marked in gray on the right photon frequency versus wavevector plot. Parameter D denotes the modulation wavelength of the composite structure.

the width of the band gaps increase as the amplitude of the modulation in the optical parameters increases. Moreover, the center frequencies of the gaps tend to increase with decreasing modulation length. In turn, the photonic band structure can be tailored by the choice of constituent materials in the composite structure as well as the modulation length of the periodicity. Extensive research has been done on these structures, leading to the realization of photonic crystal-based devices such as optical mirrors, Fabry-Perot etalons [6], and waveguides [45, 46].

The origin of the photonic band gaps can be understood as follows. For an infinitely large structure with a periodic modulation in the dielectric constant, the wavevector for light propagating along the periodicity exhibits translational invariance to changes in magnitude equal to the reciprocal lattice vector related to said

periodicity. There is a discrete degeneracy in the frequency spectrum and the photon dispersion curve folds into mini-Brillouin zones corresponding to the artificial modulation. That is, photon dispersion within the artificially periodic structure is marked by a series of bands which are zone-folded according to the reciprocal lattice vector of the structure [44]. In particular, light with wavevectors at the edge and center of a given mini-Brillouin zone are equal to odd integer multiples of half the artificial reciprocal lattice vector and even integer multiples of half the artificial reciprocal lattice vector, respectively; the resulting standing waves have a group velocity of zero. Thus, at the zone edge and center, the slope of the dispersion curve is zero. Furthermore, for each wavelength value associated with the zone edge or center, two standing waves are possible (see Fig. 1.3). These standing waves are subject to slightly different effective refractive indices in the material and, therefore, have different frequencies. Hence, there is a splitting of the zone-folded photon bands at the zone edge and center, resulting in photonic band gaps in the photon spectrum [44, 47]. Again, this is shown in Fig. 1.2. Similar effects have been found in other physical systems such as magnons in magnetically periodic materials [48] and phonons in elastically periodic materials [49].

Through careful tailoring of the pore structure, porous silicon-based one- and two-dimensional photonic crystals have been made. In the latter case, macropores etched in [100]-oriented *n*-type silicon under backside illumination have been used. By patterning the crystalline silicon surface with a lithographic mask prior to anodization,

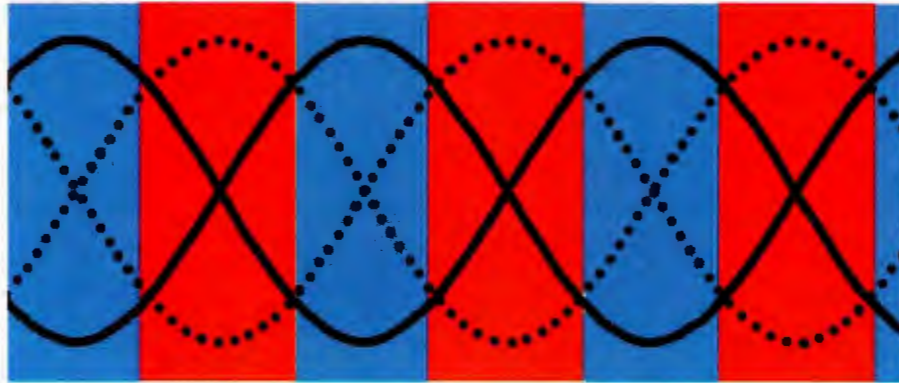


Figure 1.3: Standing waves in an optically periodic structure. The composite structure is composed of two homogeneous materials which have different optical properties. The standing waves have wavelengths equal to twice the periodicity (*i.e.*, the largest wavelength standing wave possible).

the nucleation sites of the pores were predetermined. Furthermore, the pore diameter is controlled by the illumination intensity. As a result, a two-dimensional hexagonal arrangement of highly columnar macropores in a silicon background may be fabricated [50, 51]. Thus, there is a periodic variation of the optical parameters in the plane perpendicular to the pores, with the dielectric constant alternating between that of silicon and that of air (or whatever material that may be filling the voids). This leads to the formation of two-dimensional photonic band gaps in the sample. Moreover, by changing the pore diameter and pore-to-pore spacing, the band gaps can be tuned over a wavelength range from $1.3 \mu\text{m}$ to $20 \mu\text{m}$ [50]. With regard to one-dimensional photonic crystals, both meso- and microporous silicon superlattices have been utilized. Since the pores in these particular nanostructures are much smaller than the wavelength of light being considered, each layer in the superlattice can be

treated as an effective medium with a refractive index lying between that of silicon and that of the fluid in the voids [18]. In fact, for air-filled voids, the effective refractive index decreases as the porosity increases [6]. Hence, a π -Si superlattice with a two-layer unit-cell has a periodicity in the dielectric constant and, therefore, may exhibit photonic band gaps along the sample surface normal. Porous silicon-based one-dimensional photonic crystals with stop bands in the visible [42, 52, 53] and infrared [18, 38, 41, 54, 55] spectral ranges have been made. Additionally, introducing defects into the periodicity of the structure has led to the realization of various optical cavities [6, 56–59].

1.3 Phononic Crystals

The acoustic analogue of a photonic crystal is the so-called phononic crystal. That is, a phononic crystal is a composite material characterized by a periodicity in the elastic/acoustic properties which causes the acoustic wave dispersion curve to fold into distinct bands in a manner similar to the electronic band structure of a semiconductor [60, 61]. This is accompanied by the formation of forbidden frequency bands over which acoustic waves cannot propagate within the material, also known as phononic band gaps [62]. One should note that within the current context, “acoustic waves” is also meant to refer to elastic or sound waves in solids.

As alluded to above, dispersion curve zone-folding occurs for excitations which have wavelengths comparable to the artificial periodicity. Hence, the spectral posi-

tion of the forbidden frequency bands depend on the period length of the modulation in the elastic/acoustic properties. Furthermore, these structures are categorized according to the frequency position of the phononic band gaps: systems with gaps in the kilohertz, megahertz, and gigahertz frequency ranges are called sonic, ultrasonic, and hypersonic phononic crystals, respectively [62].

Hypersonic phononic crystals are of particular interest because the band gaps affect the long wavelength (*i.e.*, > 10 nm [63]) thermal acoustic phonons. The resulting phonon band structure is qualitatively similar to the photon band structure shown in Fig. 1.2. The presence of the hypersonic phononic band gaps influence physical properties such as thermal conductivity and heat capacity. In turn, this has led to the proposal of a number of novel devices such as thermal barriers [64] and the saser [65], the acoustic analog of a laser. In addition, due to the length scale of the spatial periodicity, these systems may also exhibit photonic band gaps [66].

While the term “phononic crystal” came into use within the last two decades [61] (around the time sonic-frequency stop bands were observed in a sculpture consisting of a periodic array of cylindrical pipes [67]), studies on zone-folded acoustic waves and band gaps in periodic structures date as far back as the 1940s and '50s [68, 69]. Beginning in the late 1970s, extensive work has been done on the study of folded acoustic and optical phonons in semiconductor superlattices. In particular, both Raman light scattering spectroscopy, an inelastic light scattering technique used to characterize high-frequency, long-wavelength phonons, and phonon transmission

measurements have been used to study the acoustic phononic band structure of bi-layer superlattices with constituent layers composed of materials such as GaAs and AlAs [70–75], $\text{Al}_x\text{Ga}_{1-x}\text{As}$ and $\text{Al}_y\text{Ga}_{1-y}\text{As}$ [76], Si and $\text{Si}_x\text{Ge}_{1-x}$ [75, 77–79], CdTe and MgTe [80], GaSb and AlSb [81], amorphous Si and amorphous Ge [82], amorphous Si and amorphous SiN_x [83, 84] as well as InSb and $\text{In}_x\text{Al}_{1-x}\text{Sb}$ [85]. Typically, the artificial modulation length was of the order of a nanometer and, therefore, the center frequencies of the acoustic phononic band gaps were of the order of hundreds of gigahertz. In turn, the corresponding folded acoustic phononic band structure could be mapped using Raman spectroscopy, while the phononic band gaps could be accessed through the phonon transmission measurements. In each study, the obtained results showed evidence of folded acoustic phonons and, in some instances, one-dimensional hypersonic phononic band gaps along the direction of periodicity in the probed samples.

1.4 Brillouin Light Scattering from Phononic Crystals

More recent studies have reported evidence of hypersonic phononic crystal-behaviour in material systems such as ordered block and diblock copolymer solutions [86, 87], polymer superlattices [88], arrays of cylindrical holes in an epoxy film [64, 89], colloidal crystals [90–92], surface-structured polyurethane films [93], and SiO_2 /poly-(methyl methacrylate) superlattices [94, 95]. Most of these experiments were done using Brillouin light scattering spectroscopy (BLS) [64, 86, 87, 89–91, 93–95], an in-

elastic light scattering technique which has a much higher spectral resolution than Raman spectroscopy, enabling the study of excitations with frequencies as small as a few gigahertz. BLS is an appropriate method to probe the folded phononic band structure of these samples because the artificial modulation wavelengths were of the order of 100 nm and, therefore, the acoustic phononic band gaps of interest were in the gigahertz frequency range.

One particularly compelling study was carried out on faced-centred-cubic colloidal crystals formed by self-assembly of polystyrene nanoparticles with subsequent fluid infiltration [90]. Results collected through BLS experiments confirmed the presence of a hypersonic phononic band gap in these samples. This band gap manifested itself as a double-peak feature in the BLS spectra, with the two peaks attributed to two adjacent bands of the zone-folded longitudinal acoustic mode. The frequency difference between these two peaks represented the width of the phononic band gap at the edge of the mini-Brillouin zone corresponding to the artificial periodicity. Furthermore, it was found that this gap could be tuned by changing the size of the colloid particles and/or type of infiltrating fluid.

In another study, BLS was used to probe along the [10] direction of two-dimensional single crystalline arrays of cylindrical holes patterned in epoxy [89]. In this direction, the structure exhibited a hypersonic phononic band gap in the longitudinal acoustic phonon dispersion curve between 1.21 GHz and 1.57 GHz. Again, evidence of the

band gap was observed as a double-peak spectral feature which was attributed to folded phonon branches at the edge of the mini-Brillouin zone.

In yet another BLS study, spectra collected along the surface-normal of SiO₂/poly-(methyl methacrylate) multi-layers also showed peak doublets which were due to folded longitudinal acoustic phonons [94]. The observed one-dimensional hypersonic phononic band gap was centered at ~ 15 GHz and had a width of ~ 4.5 GHz. In a subsequent study done on these superlattices [95], phonon propagation at oblique angles to the modulation axis was studied and, in particular, it was shown that the position and width of the phononic gap changed with propagation direction.

Another notable experimental study was carried out on self-assembled block copolymer photonic crystals which had photonic band gaps in the visible spectral region [86]. The collected BLS spectra contained three peaks, two of which were attributed to branches of the folded bulk longitudinal acoustic phononic band structure. While zone-folding of the longitudinal acoustic phonon was observed, no evidence of a hypersonic phononic band gap was obtained. That is, spectra collected at wavevectors corresponding to the edge of the mini-Brillouin zone did not contain spectral peak doublets indicative of a phononic band gap.

1.5 Phononic Crystal Behaviour in Silicon-Based Structures

A number of studies have reported evidence of phononic band gaps in patterned crystalline silicon. In the work done by Dutcher *et al.* [96], results obtained through

BLS experiments found that Rayleigh surface phonons propagating in an ion-milled holographic grating on the surface of a [100]-oriented silicon wafer underwent zone-folding into the mini-Brillouin zone corresponding to the grating periodicity. This zone-folding was accompanied by a band gap in the Rayleigh surface phonon dispersion which was centered at ~ 10 GHz with a width of 0.5 GHz. Furthermore, double peak features observed in spectra collected at wavevectors within the interior of the mini-Brillouin zone suggested that a 0.8 GHz-wide, ~ 12 GHz-centered hybridization band gap had formed due to coupling between the Rayleigh surface mode and the so-called longitudinal resonance mode (*i.e.*, a leaky, longitudinally-polarized, surface mode which is weakly coupled to the surface and which radiates into the bulk longitudinal mode).

Additionally, theoretical and experimental results obtained by Mohammadi *et al.* [97, 98] found that by tailoring the geometrical parameters of a hexagonal array of air holes in a silicon plate, the structure can exhibit a two-dimensional phononic band gap in the plane perpendicular to the holes. In particular, phonon transmission experiments were done on an array of holes in a $15\ \mu\text{m}$ -thick silicon plate which had a nearest hole center-to-center distance of $15\ \mu\text{m}$ and a hole radius of $6.4\ \mu\text{m}$ (these samples were formed using lithographic patterning and deep plasma etching). An observed dip in phonon transmission between 119 MHz and 150 MHz along the ΓK direction of the hexagonal lattice provided evidence for the presence of a phononic band gap. These experimental results were in agreement with the theory.

1.6 Surface-Localized Acoustic Phonons in One-Dimensional Phononic Crystals

Since material systems in nature are not infinite in extent, a rigorous treatment of phonon propagation in superlattices must account for the fact that the layers terminate at interfaces with other materials. It is known that for binary periodic systems with a sufficiently large number of modulation repeats, bulk mode propagation is typically well-modeled assuming that the material structures are infinite superlattices. Due to the presence of interfaces between the finite superlattice and the external environment, however, there is a possibility of additional modes which are localized at these interfaces. It turns out that these surface-localized modes are evanescent modes with frequencies within phononic band gaps in the bulk mode band structures.

Since the early 80s, extensive theoretical [99–104] and experimental [105–112] work has been done to study these localized excitations. Binary-periodic superlattices with unit-cells of amorphous Ge and amorphous Si [105], Ge and SiO₂ [106], Al and Au [107], Cu and W [108, 109], Mo and Si [110, 111], Be and Mo [111] as well as Au and Al₂O₃ [112] have been studied. Furthermore, the observed surface-localized modes ranged in frequency from tens to hundreds of gigahertz, lying within band gaps in the bulk longitudinal dispersion curves. While Raman light scattering has been used [106], with the surface-localized mode manifesting as a Raman peak located between two peaks associated with adjacent folded bulk longitudinal mode bands,

much of the experimental work has relied on the use of picosecond ultrasonics to probe these modes. One should note that the picosecond ultrasonic experiments are based on a pump-probe laser system, in which a picosecond pulsed laser excites acoustic excitations on the surface of a material that, in turn, manifest as measurable changes in the reflectance experienced by a second, probing laser.

1.7 Acoustic Phonon Propagation in Porous Silicon

The elastic properties of single-layer π -Si films have been experimentally investigated using nano-indentation [113], acoustic microscopy [114, 115], phonon transmission techniques [19] as well as BLS [116–126]. It was found that for given sample morphology, the phonon velocities decreased as the porosity increased [19, 115, 120, 125]. Moreover, these velocities are dependent on the pore morphology, which is itself strongly dependent on the doping condition of the parent bulk crystalline silicon wafer [19, 123]. For example, phonon velocities in a film made from lightly doped p -type silicon are typically a factor smaller than those in p^+ -type film of the same porosity. Additionally, BLS experiments have shown that films made from p -type silicon are elastically isotropic [120], while studies done on samples fabricated using [111]-oriented [116] and [100]-oriented [125] p^+ -type silicon suggest that there is a slight cubic anisotropy in the elastic parameters in these films.

Since the π -Si phonon velocities and mass density (equal to the density of crystalline silicon multiplied by the volume fraction of silicon remaining in the porous

structure) decrease as the porosity increases, so too does the elastic impedance (*i.e.*, the product of the phonon velocity and the density [19]). In turn, π -Si superlattices exhibit a modulation in the elastic impedance which makes them an excellent candidate for one-dimensional phononic crystals.

In fact, theoretical work by Kiuchi *et al.* [127] has shown that π -Si superlattices with micron-length spatial modulations of the porosity exhibit one-dimensional acoustic phononic band gaps in the megahertz frequency range. An elastic continuum model was used to calculate the phononic band structure of the multi-layered system and, in particular, each constituent layer was treated as an elastic continuum for the long-wavelength acoustic phonons. The frequency position and width of the predicted band gaps were found to depend on both the porosity and the superlattice spatial period. Aiev and Snow [128] extended this work by applying a similar elastic continuum model to π -Si multi-layered films with modulations in the nanometer length-scale. Unlike the earlier study, acoustic attenuation was accounted for in these calculations (it was assumed that the acoustic attenuation coefficient increased parabolically with phonon frequency, as is typical of semiconductors). These proposed structures exhibited band gaps in the gigahertz frequency range. Moreover, it was found that acoustic attenuation caused the expected band gaps to shrink or, in the case of higher-order gaps, to close up altogether.

Reinhardt and Snow [129] used a scattering matrix method [130] to calculate the acoustic reflectance spectrum of both porous silicon-based acoustic Bragg mirrors

(*i.e.*, binary periodic multi-layer samples) and acoustic rugate filters (*i.e.*, structures with a sinusoidal variation in the porosity and, therefore, the elastic impedance). These structures, which had porosity modulations over hundreds of nanometers, displayed sub-10 GHz hypersonic phononic band gaps, as evidenced by sharp peaks in the acoustic reflectance spectrum. It was reported that the width of the band gaps increased as the elastic impedance mismatch between the constituent layers increased.

Experimentally, Alicv *et al.* [131] reported that phonon transmission and optical reflectance experiments conducted on a supported mesoporous silicon binary periodic multi-layered film fabricated from [100]-oriented p^+ -type silicon showed evidence of both one-dimensional hypersonic longitudinal acoustic phononic band gaps and infrared photonic band gaps. The sample consisted of 24 repeats of a unit-cell containing a 2.2 μm -thick 0.47 porous layer and a 1.7 μm -thick 0.61 porous layer. Specifically, the phonon transmittance spectrum contained a ~ 0.25 GHz-wide, ~ 50 dB dip and a ~ 0.10 MHz-wide, ~ 30 dB dip centered at 0.65 GHz and 1.3 GHz, respectively. These gaps in the phonon transmission corresponded to the first- and second-order longitudinal acoustic stop bands. In addition, introducing a 2.7 μm -thick 0.57 porous layer defect into an otherwise periodically multi-layered sample (containing alternations between a 1.38 μm -thick 0.57 porous layer and a 1.53 μm -thick 0.40 porous layer) led to the realization of an acoustic phonon microcavity. A transmission spike within the observed ~ 0.40 GHz-wide, ~ 1.00 GHz-centered phonon stop band was indicative of a

longitudinal acoustic phonon transmission mode stemming from localization around the defect.

In a study done by Thomas *et al.* [132], longitudinal acoustic phonon transmission experiments done on π -Si rugate filters with a sinusoidal variation in the porosity showed evidence of a 0.2 GHz-wide phononic band gap centered at about 1 GHz with 40 dB rejection. Rugate filters with modulation wavelengths of 3.70 μm and 2.42 μm , made by etching p^+ -type silicon, were examined together with π -Si Bragg mirrors with modulations of $\sim 3.5 \mu\text{m}$. Comparison between results found that higher-order phononic band gaps were suppressed in the rugate filter while the first-order band in the rugate filters was of similar quality to that of the Bragg mirrors.

Upon conducting Raman spectroscopy experiments on a p^- -type π -Si superlattice, Wu *et al.* [133] reported the observation of three spectral peak doublets which were attributed to folded longitudinal acoustic phonon modes at the second-, third-, and fourth-order band gaps. The three peak features were centered, respectively, at 39.3 cm^{-1} , 59.7 cm^{-1} , and 79.7 cm^{-1} and were in excellent agreement with calculations based on an elastic continuum model. The authors, however, did not properly take into account the porosity-dependence of the phonon velocities in p^- -type π -Si [115, 120]. Moreover, given the structure of the sample (which had a superlattice unit-cell consisting of layers with thicknesses of $\sim 8.6 \text{ nm}$ and $\sim 36 \text{ nm}$ and porosities of ~ 0.65 and ~ 0.78 , respectively), it appears that the spectral positions of the

double-peak features were too high in frequency to be due to the suggested phononic band gaps. Hence, the validity of these results is questionable.

While BLS has also been used to probe phonon propagation in supported multi-layer π -Si films, no evidence of phononic crystal-effects were reported. In the work by Andrews *et al.* [123], [100]-oriented p^+ -type mesoporous silicon multi-layer films with constituent layer porosity sequences of 0.65/0.40/0.65/0.40/0.65 were probed. The layer thicknesses were equal at 250 nm. While the focus of this study was the characterization of the Rayleigh surface phonon which propagated perpendicular to the direction of the artificial periodicity, additional peaks of unknown origin were observed in the collected spectra. Since the frequencies of these other modes were independent of the magnitude of the in-plane component of the transfer wavevector, it was unlikely that they were surface phonons.

In addition, BLS studies by Polomska and Andrews [124, 126] were carried out on [100]-oriented p^+ -type mesoporous silicon superlattices with modulation lengths as large as ~ 30 nm. In this case, the wavelength of the probed phonon was much longer than the superlattice period. Spectra collected from these films contained four peaks: one due to a quasi-transverse acoustic bulk phonon, one due to a quasi-longitudinal acoustic bulk phonon, and two due to surface phonons. Treating the multi-layered structure as an effective elastic medium, elastic constants were obtained through analysis of the collected spectra data and the resulting values were compared to those determined using the Grimsditch-Nizzoli effective elastic medium model for a semi-

conductor superlattice. There was only partial agreement between the experimentally determined values and those given by the model, with the best results obtained when assuming a cubic symmetry of the constituent layers.

1.8 Present Work

In the current work, Brillouin light scattering spectroscopy and optical reflectance measurements were done on binary periodic multi-layered mesoporous silicon films, with repeated porosity sequences of about 0.55/0.45, in an attempt to determine the potential of these structures as both one-dimensional hypersonic phononic crystals and visible-range photonic crystals. The modulation lengths of the superlattices, which ranged from ~ 40 nm to ~ 170 nm, were chosen such that the resulting acoustic path length over a single unit-cell was comparable to the wavelength of the acoustic phonons probed in the BLS experiments (which was used to map the phononic dispersion curve). Fabricating appropriate superlattices required *a priori* knowledge of the relationship between the etch parameters and the physical nature (*i.e.*, the growth-rate, elastic parameters, and optical parameters) of the resulting constituent layers. To facilitate this, single-layer π -Si films were made and characterized using BLS, optical reflectance measurements, and scanning electron microscopy.

Normal-incidence broadband optical reflectance measurements taken from these superlattices showed evidence of an optical Bragg peak, corresponding to a one-dimensional photonic band gap in the visible spectral range. Good agreement was

obtained between the experimental data and calculations based on a one-dimensional optical continuum model. Since the constituent layer thicknesses and refractive indices served as input parameters into the model, the results confirmed that the superlattices were fabricated as expected.

In order to map the acoustic phononic band structure along the modulation axis of these superlattices, a methodology for so-called pseudo-reflection geometry Brillouin scattering was developed and then validated through experiments on various well-known materials (*i.e.*, fused quartz, gallium phosphide, water). Probing approximately along the surface-normal of the π -Si superlattice samples, evidence of zone-folding of the bulk longitudinal acoustic mode band structure manifested through the appearance of a second longitudinal mode in the collected Brillouin spectra. Further, a surface-localized mode lying within a bulk longitudinal mode band gap centered at ~ 16 GHz was also observed, thus proving that the samples were hypersonic phononic crystals. The collected experimental acoustic phonon dispersion data showed good agreement with a one-dimensional phononic-photon continuum model similar to that described in [134]. It should be noted that this theoretical model required the input of both the optical and elastic constants of the constituent layers.

In a further study, off-axis acoustic phonon propagation in similar π -Si superlattices was probed using oblique angle 180° -backscattering geometry Brillouin scattering. The frequency of the probed folded longitudinal acoustic phonon was found to be strongly dependent of the propagation direction and this behaviour was theoretic-

cally treated using a simplified one-dimensional phononic-photonic continuum model. Analysis of the Brillouin peaks associated with the longitudinal modes suggested that the corresponding phonon attenuation in π -Si was orders of magnitude larger than that of bulk crystalline silicon, implying that the porosity had a strong effect on phonon attenuation. Finally, a Rayleigh surface mode and a pseudo-surface mode was observed in each film. In particular, these surface modes were dispersive, with the velocity increasing with phonon wavelength.

The significance of this work is twofold. Firstly, structures which exhibit both phononic and photonic band gaps are of fundamental interest due to the possibility of novel phonon-photon interactions such as optical cooling [66]. Here, an understanding of phonon dispersion in these structures is imperative. Secondly, with regard to device applications, π -Si has a number of advantages over other material platforms. It may be possible to tune the position and width of the phononic and photonic band gaps by changing the porosities of the constituent layers. Furthermore, hypersonic phononic crystal-based applications such as thermal barriers, acoustic Bragg mirrors, and acoustic microcavities may be readily interfaced with existing silicon technology.

Chapter 1 References

- [1] A. Uhlir, Bell Syst. Tech. J. **35**, 333 (1956).
- [2] X.G. Zhang, J. Electrochem. Soc. **151**, C69 (2004).
- [3] A.G. Cullis, L.T. Canham, and P. D.J. Calcott, J. Appl. Phys. **82**, 909 (1997).
- [4] D. Neamen. *An Introduction to Semiconductor Devices*. (McGraw-Hill, New York, 2006).
- [5] H. Föll, M. Christophersen, J. Carstensen, and G. Hasse, Mat. Sci. Eng. R **39**, 93 (2002).
- [6] L. Pavesi, Riv. Nuovo Cimento **20**, 1 (1997).
- [7] S. Rönnebeck, J. Carstensen, S. Ottow, and H. Föll, Electrochem. Solid State Lett. **2**, 126 (1999).
- [8] V. Lehmann and S. Rönnebeck, J. Electrochem. Soc. **146**, 2968 (1999).
- [9] V. Lehmann. *Electrochemistry of Silicon*. (WILEY-VCH, Weinheim, 2002). p. 171-176.

- [10] L.T. Canham, Appl. Phys. Lett. **57**, 1046 (1990).
- [11] V. Lehmann. *Electrochemistry of Silicon*. (WILEY-VCH, Weinheim, 2002), p. 230-231.
- [12] L. Buckberry and S. Bayliss, Mater. World **7**, 213 (1999).
- [13] L. T. Canham. Porous silicon as a therapeutic biomaterial. In *1st Annual International IEEE-EMBS Special Topic Conference on Microtechnologies in Medicine and Biology*, (2000), p. 108.
- [14] L.T. Canham, C.L. Reeves, J.P. Newey, M.R. Houlton, T.I. Cox, J.M. Buriak, and M.P. Stewart, Adv. Mater. **11**, 1505 (1999).
- [15] A.H. Mayne, S.C. Bayliss, P. Barr, M. Tobin, and L.D. Buckberry, Phys. Status Solidi A **182**, 505 (2000).
- [16] D. Dimova-Malinovska, Nanostructured and Advanced Materials for Bio-Applications. In *Nanostructured and Advanced Materials for Applications in Sensor, Optoelectronic, and Photovoltaic Technology*, edited by A. Vaseashta, D. Dimova-Malinovska, and J.M. Marshall. (Springer, Netherlands, 2005).
- [17] L.T. Canham and A.J. Groszek, J. Appl. Phys. **63**, 2569 (1992).
- [18] K. Kordás, S. Beke A. E. Beke, A. Uusimäki, and S. Leppävuori, Opt. Mat. **25**, 257 (2004).

- [19] G. N. Aliev, B. Goller, D. Kovalev, and P. A. Snow. *Phys. Status Solidi C*, **6**, 1670 (2009).
- [20] J.M. Matinez-Duart and R.J. Martin-Palma. *Phys. Status Solidi B* **232**, 81 (2002).
- [21] M. T. Kelly and A. B. Bocarsly. *Coordin. Chem. Rev.* **171**, 251 (1998).
- [22] P.A. Snow, E.K. Squire, P. St. J. Russell, and L.T. Canham. *J. Appl. Phys.* **86**, 1781 (1999).
- [23] M.J. Sailor and J.R. Link. *Chem. Commun.* 1375 (2005).
- [24] J. Volk, T. Le Grand, I. Bársony, J. Gombkötő, and J.J. Ramsden. *J. Phys. D: Appl. Phys.* **38**, 1313 (2005).
- [25] S.E. Lewis, J.R. DeBoer, J.L. Gole, and P.J. Hesketh. *Sensor and Actuat. B-Chem.* **110**, 54 (2005).
- [26] E. Guillermain, V. Lysenko, R. Orobtschouk, T. Benyattou, S. Roux, A. Pillonet, and P. Perriat, *Appl. Phys. Lett.* **90**, 241116 (2007).
- [27] S. Chan, Y. Li, L.J. Rothberg, B.L. Miller, and P.M. Fauchet. *Mater. Sci. Eng. C* **15**, 277 (2001).
- [28] V.S.-Y. Lin, K. Motesharei, K.-P.S. Dancil, M.J. Sailor, and M.R. Ghadiri, *Science* **278**, 840 (1997).

- [29] M.P. Schwartz, F. Cunin, R.W. Cheung, and M.J. Sailor. *Phys. Status Solidi A* **202**, 1380 (2005).
- [30] H. Qiao, B. Guan, J.J. Gooding, and P.J. Reece. *Opt. Express* **18**, 15174 (2010).
- [31] L.T. Canham, C.L. Reeves, D.O. King, P.J. Branfield, J.G. Crabb, and M.C.L. Ward. *Adv. Mater.* **8**, 850 (1996).
- [32] J. Salonen, J. Paski, K. Vähä-Heikkilä, M. Björkqvist, and V.-P. Lehto, *Phys. Status Solidi A* **202**, 1629 (2005).
- [33] V. Lysenko, F. Bidault, S. Alekseev, V. Zaitsev, D. Barbier, C. Turpin, F. Geobaldo, P. Rivolo, and E. Garrone. *J. Phys. Chem. B* **109**, 19711 (2005).
- [34] F. Duerinckx, I Kuzma-Filipek, K. Van Nieuwenhuysen, G. Beaucarne, and J. Poortmans. *Prog. Photovolt: Res. Appl.* **16**, 399 (2008).
- [35] V. Lehmann. *Electrochemistry of Silicon*. (WILEY-VCH, Weinheim, 2002), p. 30-33.
- [36] V. Lehmann. *Electrochemistry of Silicon*. (WILEY-VCH, Weinheim, 2002), p. 93-94.
- [37] M.I.J. Beale, J.D. Benjamin, M.J. Uren, N.G. Chew, and A.G. Cullis, *Crystal Growth* **73**, 622 (1985).
- [38] S. Billat, M. Thönissen, R. Arens-Fischer, M.G. Berger, M. Kruger, and H. Lüth, *Thin Solid Films* **297**, 22 (1997).

- [39] V. Lehmann and U. Gosele, *Appl. Phys. Lett.* **58**, 856 (1991).
- [40] V. Lehmann. *Electrochemistry of Silicon*. (WILEY-VCH, Weinheim, 2002), p. 101-104.
- [41] G. Vincent, *Appl. Phys. Lett.* **64**, 2367 (1994).
- [42] M. G. Berger, C. Dieker, M. Thönissen, L. Vescan, H. Lüth, H. Münder, W. Theiß, M. Wernke, and P. Grosse, *J. Phys. D: Appl. Phys.* **27**, 1333 (1994).
- [43] J. Von Behren, L Tsybeskov, and P. M. Fauchet, *Mat. Res. Soc. Symp. Proc.* **358**, 333 (1995).
- [44] B. E. A. Saleh and M. C. Teich. *Fundamentals of Photonics*. (John Wiley and Sons, New Jersey, 2007), p. 243-288.
- [45] B. E. A. Saleh and M. C. Teich. *Fundamentals of Photonics*. (John Wiley and Sons, New Jersey, 2007), p. 311-313.
- [46] A Yariv and P. Yeh. *Photonics: Optical Electronics in Modern Communications*. (Oxford University Press, New York, 2007), p. 539-601.
- [47] R. S. Quimby. *Photonics and Lasers: An Introduction*. (John Wiley and Sons, New Jersey.
- [48] M. Krawczyk and H. Puzkarski, *Phys. Rev. B* **77**, 054437 (2008).
- [49] M.S. Kushwaha, *Recent Res. Devel. Appl. Phys.* **2**, 743 (1999).

- [50] A. Birner, R.B. Wehrspohn, U.M. Gosele, and K. Busch, *Adv. Mater.* **13**, 377 (2001).
- [51] N. Gutman, D. Lubarski, and A. Sa'ar, *Phys. Status Solidi C* **6**, 1634 (2009).
- [52] V. Torres-Costa, R. Gago, R. J. Matín-Palma, M Vinnichenko, R. Groötzschel, and J. M. Martínez-Duart, *Mater. Sci. Eng. C* **23**, 1043 (2003).
- [53] C. Mazzoleni and L. Pavesi, *Appl. Phys. Lett.* **67**, 2983 (1995).
- [54] Z. Wang, J. Zhang, S. Xu, L. Wang, Z. Cao, P. Zhan, and Z. Wang, *J. Phys. D: Appl. Phys.* **40**, 4482 (2007).
- [55] S. Zangoie, M. Schubert, C. Trimble, D. W. Thompson, and J. A. Woollam, *Appl. Opt.* **40**, 906 (2001).
- [56] L. Pavesi and P. Dubos, *Semicond. Sci. Technol.* **12**, 570 (1996).
- [57] S. Zangoie, R. Jansson, and H. Arwin, *J. Appl. Phys.* **86**, 850 (1999).
- [58] M. Ghulinyan, C. J. Oton, G. Bonetti, Z. Gaburro, and L. Pavesi, *J. Appl. Phys.* **93**, 9724 (2003).
- [59] N. Tokranova, B. Xu, and J. Castracane, *Mat. Res. Soc. Symp. Proc.* **797**, W1.3.1 (2004).
- [60] E. N. Economou and M. M. Sigalas, *Phys. Rev. B* **48**, 13434 (1993).

- [61] M.S. Kushwaha, P. Halevi, L. Dobrzynski, and B. Djafari-Rouhani, *Phys. Rev. Lett.* **71**, 2022 (1993).
- [62] T. Gorishnyy, M. Maldovan, C. Ullal, and E. Thomas, *Phys. World* **18**, 24 (2005).
- [63] C. Kittel. *Introduction to Solid State Physics*. (John Wiley and Sons, New Jersey, 2005), p. 73-85.
- [64] T. Gorishnyy, C. K. Ullal, M. Maldovan, G. Fytas, and E. L. Thomas, *Phys. Rev. Lett.* **94**, 115501 (2005).
- [65] P. M. Walker, A. J. Kent, M. Henini, B. A. Glavin, V. A. Kochelap, and T. L. Linnik, *Phys. Rev. B* **79**, 245313 (2007).
- [66] M. Maldovan and E. L. Thomas, *Appl. Phys. Lett.* **88**, 251907 (2006).
- [67] R. Martínez-Sala, J. Sancho, J. V. Sánchez, V. Gómez, J. Linares, and F. Mesguier, *Nature* **378**, 241 (1995).
- [68] L. Brillouin. *Wave Propagation in Periodic Structures*. (Dover, New York, 1953).
- [69] S.M. Rytov, *Soviet Phys. Acoustics* **2**, 68 (1956).
- [70] A. S. Barker, J. L. Merz, and A. C. Gossard, *Phys. Rev. B* **17**, 3181 (1978).

- [71] C. Colvard, R. Merlin, M. V. Klein, and A. C. Gossard, *Phys. Rev. Lett.* **45**, 298 (1980).
- [72] B. Jusserand, F. Alexandre, J. Dubard, and D. Paquet, *Phys. Rev. B* **33**, 2897 (1986).
- [73] D. Levi, S.-L. Zhang, M. V. Klein, J. Klem, and H. Morkoç, *Phys. Rev. B* **36**, 8032 (1987).
- [74] J. Sapriel, J. He, B. Djafari-Rouhani, R. Azoulay, and F. Mollot, *Phys. Rev. B* **37**, 4099 (1988).
- [75] J. He, J. Sapriel, and R. Azoulay, *Phys. Rev. B* **40**, 1121 (1989).
- [76] C. Colvard, T.A. Gant, M.V. Klein, R. Merlin, R. Fischer, H. Morkoc, and A.C. Gossard, *Phys. Rev. B* **31**, 2080 (1985).
- [77] H. Brugger, G. Abstreiter, H. Jorke, H. J. Herzog, and E. Kasper, *Phys. Rev. B* **33**, 5928 (1986).
- [78] D. J. Lockwood, M. W. C. Dharma wardana J.-M. Baribeau, and D. C. Houghton, *Phys. Rev. B* **35**, 2243 (1987).
- [79] M. W. C. Dharma-wardana, P. X. Zhang, and D. J. Lockwood, *Phys. Rev. B* **48**, 11960 (1993).
- [80] B. Jusserand, R. Ghasemi, E. Dynowska, M. Wiater, G. Karczewski, and T. Wojtowicz, *Appl. Phys. Lett.* **94**, 093102 (2009).

- [81] P. V. Santos, A. K. Sood, M. Cardona, K. Ploog, Y. Ohmori, and H. Okamoto, Phys. Rev. B **37**, 6381 (1988).
- [82] S. Kumar and H. J. Trodahl. J. Appl. Phys. **70**, 1 (1991).
- [83] P. V. Santos, M. Hundhausen, and L. Ley. Phys. Rev. B **33**, 1516 (1986).
- [84] P. V. Santos, L. Ley, J. Mebert, and O. Koblinger, Phys. Rev. B **36**, 4858 (1987).
- [85] V. P. Gnezdilov, D. J. Lockwood, and J. B. Webb, Phys. Rev. B **48**, 11228 (1993).
- [86] A. M. Urbas, E. L. Thomas, H. Kriegs, G. Fytas, R. S. Penciu, and L. N. Economou, Phys. Rev. Lett. **90**, 108302 (2003).
- [87] G. Tommaseo, R. S. Penciu, G. Fytas, E. N. Economou, T. Hashimoto, and N. Hadjichristidis, Macromol. **37**, 5006 (2004).
- [88] P. M. Walker, J. S. Sharp, A. V. Akimov, and A. J. Kent, Appl. Phys. Lett. **97**, 073106 (2010).
- [89] T. Gorishnyy, J.-H. Jang, C. Yang Koh, and E.L. Thomas, Appl. Phys. Lett. **91**, 121915 (2007).
- [90] W. Cheng, J. Wang, U. Jonas, G. Gytas, and N. Stefanou, Nature **5**, 830 (2006).

- [91] T. Still, W. Cheng, M. Retsch, R. Sainidou, J. Wang, U. Jonas, N. Stefanou, and G. Fytas, *Phys. Rev. Lett.* **100**, 194301 (2008).
- [92] A. S. Salasyuk, A. V. Scherbakov, D. M. Yakovlev, A. V. Akimov, A. A. Kaplyanskii, S. F. Kaplan, S. A. Grudinkin, A. V. Nashchekin, A. B. Pevtsov, V. G. Golubev, T. Berstermann, C. Brüggemann, M. Bombeck, and M. Bayer, *Nano Lett.* **10**, 1319 (2010).
- [93] W. Cheng, G. Fytas, A. V. Kiyanova, M. Y. Efremov, and P. F. Nealey, *Macromol. Rapid Commun.* **27**, 702 (2006).
- [94] N. Gomopoulos, D. Maschke, C. Y. Koh, E. L. Thomas, W. Tremel, H.-J. Butt, and G. Fytas, *NanoLett.* **10**, 980 (2010).
- [95] D. Schneider, F. Liaqat, E. H. El Boudouti, Y. El Hassouani, B. Djafari-Rouhani, W. Tremel, H.-J. Butt, and G. Fytas, *Nano Lett.* **12**, 3101 (2012).
- [96] J. R. Dutcher, S. Lee, B. Hillebrands, G. J. McLaughlin, B. G. Nickel, and G. I. Stegeman, *Phys. Rev. Lett.* **68**, 2464 (1992).
- [97] S. Mohammadi, A. A. Eftekhar, A. Khelif, H. Moubehir, R. Westafer, W. D. Hunt, and A. Adibi, *Electron. Lett.* **43**, 898 (2007).
- [98] S. Mohammadi, A. A. Eftekhar, A. Khelif, W. D. Hunt, and A. Adibi, *Appl. Phys. Lett.* **92**, 221905 (2008).

- [99] B. Djafari-Rouhani, L. Dobrzynski, O. Hardouin Duparc, R. E. Camley, and A. A. Maradudin. Phys. Rev. B **28**, 1711 (1983).
- [100] R. E. Camley, B. Djafari-Rouhani, L. Dobrzynski, and A. A. Maradudin. Phys. Rev. B **27**, 7318 (1983).
- [101] E. H. El Boudouti, B. Djafari-Rouhani, E. M. Khourdifi, and L. Dobrzynski. Phys. Rev. B **48**, 10987 (1993).
- [102] E. H. El Boudouti, B. Djafari-Rouhani, A. Akjouj, and L. Dobrzynski. Phys. Rev. B **54**, 14728 (1996).
- [103] M. Hammouchi, E. H. El Boudouti, A. Nougouei, B. Djafari-Rouhani, M. L. H. Lahlaoui, A. Akjouj, and L. Dobrzynski. Phys. Rev. B **59**, 1999 (1999).
- [104] E. H. El Boudouti, B. Djafari-Rouhani, A. Akjouj, and L. Dobrzynski. Surf. Sci. Rep. **64**, 471 (2009).
- [105] H. T. Grahn, H. J. Maris, J. Tauc, and B. Abeles. Phys. Rev. B **38**, 6066 (1988).
- [106] H. J. Trodahl, P. V. Santos, G. V. Williams, and A. Bittar. Phys. Rev. B **40**, 8577 (1989).
- [107] W. Chen, Y. Lu, H. J. Maris, and G. Xiao. Phys. Rev. B **50**, 14506 (1994).
- [108] B. Perrin, B. Bonello, J. C. Jeamet, and E. Romatet. Physica B **219 – 220**, 681 (1996).

- [109] B. Bonello, B. Perrin, E. Romatet, and J. C. Jeannet, *Ultrasonics* **35**, 223 (1997).
- [110] N.-W. Pu and J. Bokor, *Phys. Rev. Lett.* **91**, 076101 (2003).
- [111] N.-W. Pu, *Phys. Rev. B.* **72**, 115428 (2005).
- [112] A. Halabica, S. T. Pantelides, R. F. Haglund, Jr., R. H. Magruder, and A. Meldrum, III, *Phys. Rev. B* **80**, 165422 (2009).
- [113] D. Bellet, P. Lamagnère, A. Vincent, and Y. Bréchet, *J. Appl. Phys.* **80**, 3772 (1996).
- [114] R. J. M. Da Fonseca, J. M. Saurel, G. Despaux, A. Foucaran, E. Massone, T. Taliercio, and P. Lefebvre, *Superlattices Microstruct.* **16**, 21 (1994).
- [115] R. J. M. Da Fonseca, J. M. Saurel, A. Foucaran, E. Massone, T. Taliercio, and J. Camassel, *Thin Solid Films* **255**, 155 (1995).
- [116] G. T. Andrews, J. Zuk, H. Kiefte, M. J. Clouter, and E. Nossarzewska-Orlowska, *Appl. Phys. Lett.* **69**, 1217 (1996).
- [117] M. G. Beghi, C. E. Bottani, G. Ghislotti, G. Amato, and L. Boarino, *Solid Thin Films* **297**, 110 (1997).
- [118] D. J. Lockwood, M. H. Kuok, S. C. Ng, and R. L. Rang, *Phys. Rev. B* **60**, 8878 (1999).

- [119] G. T. Andrews and M. J. Clouter, *Semicond. Sci. Technol.* **16**, 679 (2001).
- [120] H. J. Fan, M. H. Kuok, S. C. Ng, R. Boukherroub, J.-M. Baribeau, J. W. Fraser, and D. J. Lockwood. *Phys. Rev. B* **65**. 165330 (2002).
- [121] H. J. Fan, M. H. Kuok, S. C. Ng, R. Boukherroub, and D. J. Lockwood, *Semicond. Sci. Technol.* **17**, 692 (2002).
- [122] G. T. Andrews, M. J. Clouter, and J. Zuk. *Semicond. Sci. Technol.* **19**, 1306 (2004).
- [123] G.T. Andrews. A.M. Polomska, E. Vazsonyi, and J. Volk, *Phys. Status Solidi A* **204**, 1372 (2007).
- [124] A. M. Polomska and G. T. Andrews, *Phys. Status Solidi C* **6**, 1665 (2009).
- [125] A. M. Polomska. *Elastic properties of porous silicon superlattices*. Ph.D. thesis, Memorial University of Newfoundland (2010).
- [126] A. M. Polomska-Harlick and G. T. Andrews, *J. Phys. D: Appl. Phys.* **45**, 075302 (2012).
- [127] A. Kiuchi. B. Gelloz. A. Kojima and N. Koshida, Possible Operation of Periodically Layered Nanocrystalline Porous Silicon as An Acoustic Band Crystal Device. In *Materials Research Society Symposium Proceedings Series, Vol. 832*, edited by L. Tsybeskov, D. J. Lockwood, C. Delerue and M. Ichikawa. (Warrendale, PA, 2005).

- [128] G. N. Aliev and P. A. Snow, Mater. Res. Soc. Symp. Proc. **1145**, MM13-04 (2009).
- [129] A. Reinhardt and P. A. Snow, Phys. Status Solidi A **204**, 1528 (2007).
- [130] A. Reinhardt, T. Pastureaud, S. Ballandras, and V. Laude. J. Appl. Phys. **94**, 6923 (2003).
- [131] G. N. Aliev, B. Goller, D. Kovalev, and P. A. Snow. Appl. Phys. Lett. **96**, 124101 (2010).
- [132] L. Thomas, G. N. Aliev, and P. A. Snow. Appl. Phys. Lett. **97**, 173503 (2010).
- [133] X.-L. Wu, F. Yan, F.-M. Pan, X. m. Bao, S.-S. Jiang, M.-S. Zhang, and D. Feng, Appl. Phys. Lett. **68**, 611 (1996).
- [134] J. He, B. Djafari-Rouhani, and J. Sapriel, Phys. Rev. B **37**, 4086 (1988).

Chapter 2

Theory

2.1 Phonon and Photon Propagation in a Superlattice

2.1.1 Overview

To understand phonon and photon propagation in a mesoporous silicon superlattice (SL), one needs to account for the commensurate periodicity in both the elastic and electromagnetic properties. Propagation in the bulk of the binary periodic SLs may be reasonably approximated by considering an infinite one-dimensional lattice with a square-wave modulation in both the elastic and optical parameters. Furthermore, since the probed SLs terminate at an air-solid interface, propagation in a semi-infinite one-dimensional lattice in contact with a gas will also be discussed. Figure 2.1 depicts both structures.

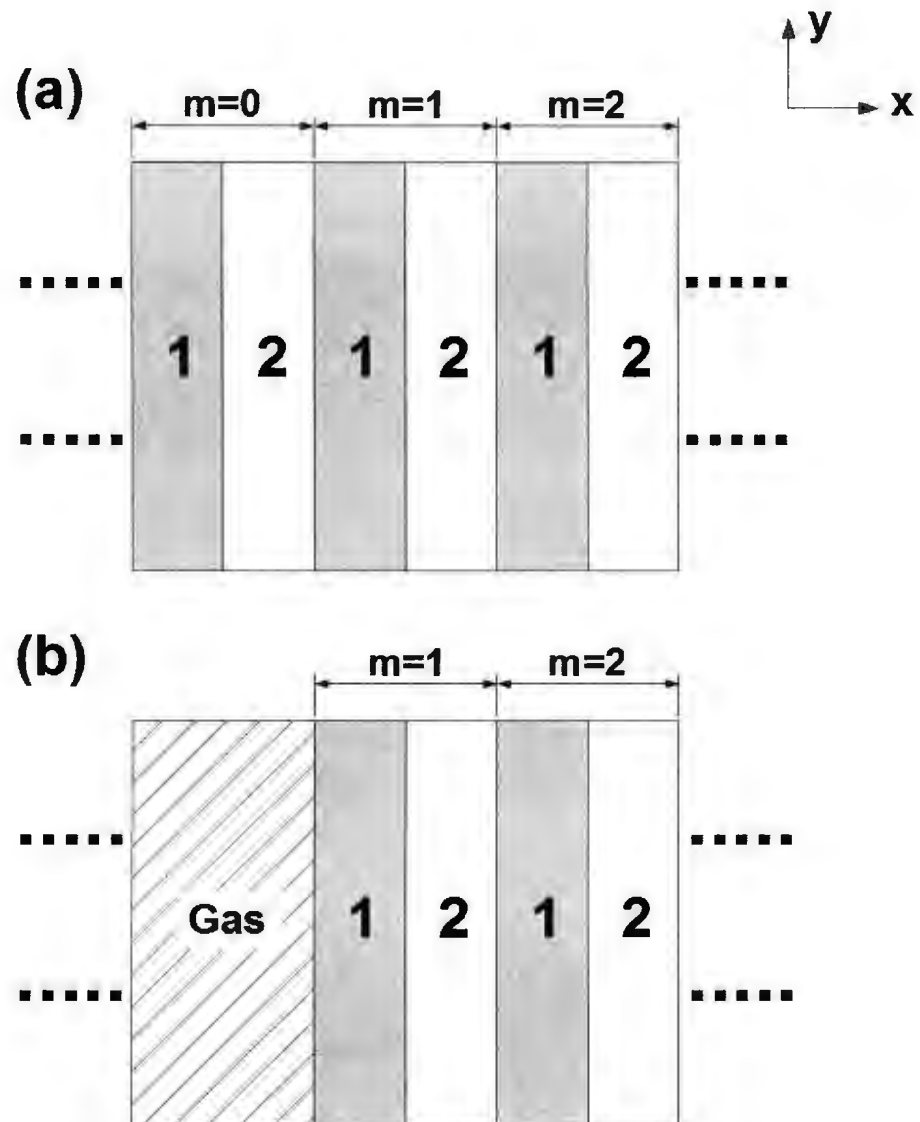


Figure 2.1: (a) Infinite and (b) semi-infinite two-component superlattices. The two constituent layers are assumed to have different elastic and optical properties. Integer m denotes the superlattice unit-cell.

2.1.2 Normal-Incidence Phonon Propagation in an Infinite Superlattice

Bulk acoustic phonon propagation along the modulation axis of an infinite SL is particularly interesting. The superlattice considered is marked by a square-wave modulation in the mass density ρ_j and the acoustic phonon velocity V_j (here, $j = 1, 2$; see Fig. 2.1(a)). Thus, the superlattice is composed of a two-layer unit-cell with layer thicknesses d_1 and d_2 . If the artificial modulation length, $D = d_1 + d_2$, is of the order of tens of nanometers, the acoustic phonons of interest will be in the long-wavelength regime [1]. Each individual layer may then be treated as an elastic continuum and, in turn, the displacement $u = u(x, t)$ corresponding to a given phonon (either transverse (T) or longitudinal (L)) obeys the wave equation:

$$\frac{\partial^2 u}{\partial t^2} = V_j^2 \frac{\partial^2 u}{\partial x^2}. \quad (2.1)$$

The time-harmonic plane-wave solutions to this wave equation in the $j = 1$ and $j = 2$ layers are given, respectively, by [2]

$$u_{m,1}(x_1, t) = U_{m,1}^+ e^{i(q_1 x_1 - \Omega t)} + U_{m,1}^- e^{i(-q_1 x_1 - \Omega t)} \quad (2.2a)$$

$$u_{m,2}(x_2, t) = U_{m,2}^+ e^{i(q_2 x_2 - \Omega t)} + U_{m,2}^- e^{i(-q_2 x_2 - \Omega t)}, \quad (2.2b)$$

where integer m denotes the superlattice unit-cell. $U_{m,j}^+$ and $U_{m,j}^-$ are the amplitudes of the forward- and backward-traveling plane waves in each layer, respectively, Ω is the phonon angular frequency, and $q_j = \Omega/V_j$ are the corresponding phonon wavevectors

in the individual layers. One should note that x_j is the local displacement within each layer and, thus, ranges from 0 to d_j . Boundary conditions require that $u_{m,j}(x_j, t)$ and $\rho V^2 \partial u_{m,j}(x_j, t) / \partial x_j$ be continuous at each interface (*i.e.*, the displacement and the normal stress component are continuous). Consequently, it follows from Eq. (2.2) that

$$U_{m,2}^+ + U_{m,2}^- = U_{m,1}^+ e^{iq_1 d_1} + U_{m,1}^- e^{-iq_1 d_1} \quad (2.3a)$$

$$iZ_2 (U_{m,2}^+ - U_{m,2}^-) = iZ_1 (U_{m,1}^+ e^{iq_1 d_1} - U_{m,1}^- e^{-iq_1 d_1}) \quad (2.3b)$$

and

$$U_{m+1,1}^+ + U_{m+1,1}^- = U_{m,2}^+ e^{iq_2 d_2} + U_{m,2}^- e^{-iq_2 d_2} \quad (2.4a)$$

$$iZ_1 (U_{m+1,1}^+ - U_{m+1,1}^-) = iZ_2 (U_{m,2}^+ e^{iq_2 d_2} - U_{m,2}^- e^{-iq_2 d_2}), \quad (2.4b)$$

where $Z_j = \rho_j V_j$ are the elastic impedances of the constituent layers. Re-expressing the above equations in matrix-form gives

$$\begin{pmatrix} 1 & 1 \\ 1 & -1 \end{pmatrix} \begin{pmatrix} U_{m,2}^+ \\ U_{m,2}^- \end{pmatrix} = \begin{pmatrix} e^{iq_1 d_1} & e^{-iq_1 d_1} \\ \left(\frac{Z_1}{Z_2}\right) e^{iq_1 d_1} & -\left(\frac{Z_1}{Z_2}\right) e^{-iq_1 d_1} \end{pmatrix} \begin{pmatrix} U_{m,1}^+ \\ U_{m,1}^- \end{pmatrix} \quad (2.5)$$

and

$$\begin{pmatrix} 1 & 1 \\ 1 & -1 \end{pmatrix} \begin{pmatrix} U_{m+1,1}^+ \\ U_{m+1,1}^- \end{pmatrix} = \begin{pmatrix} e^{iq_2 d_2} & e^{-iq_2 d_2} \\ \left(\frac{Z_2}{Z_1}\right) e^{iq_2 d_2} & -\left(\frac{Z_2}{Z_1}\right) e^{-iq_2 d_2} \end{pmatrix} \begin{pmatrix} U_{m,2}^+ \\ U_{m,2}^- \end{pmatrix}. \quad (2.6)$$

Since

$$\begin{pmatrix} 1 & 1 \\ 1 & -1 \end{pmatrix}^{-1} = \frac{1}{2} \begin{pmatrix} 1 & 1 \\ 1 & -1 \end{pmatrix}, \quad (2.7)$$

following from Eqs. (2.5) and (2.6), it is straightforward to show that

$$\begin{pmatrix} U_{m+1,1}^+ \\ U_{m+1,1}^- \end{pmatrix} = \mathbf{T} \begin{pmatrix} U_{m,1}^+ \\ U_{m,1}^- \end{pmatrix}. \quad (2.8)$$

Here, \mathbf{T} is a 2×2 transfer matrix which relates the plane wave amplitudes in the $j = 1$ layer of adjacent unit-cells. The elements of \mathbf{T} are given by [2]

$$T_{11} = T_{22}^* = \left(\cos(q_2 d_2) + \frac{i}{2} \left(\left(\frac{Z_2}{Z_1} \right) + \left(\frac{Z_1}{Z_2} \right) \right) \sin(q_2 d_2) \right) e^{iq_1 d_1} \quad (2.9)$$

and

$$T_{12} = T_{21}^* = \frac{i}{2} \left(\left(\frac{Z_1}{Z_2} \right) - \left(\frac{Z_2}{Z_1} \right) \right) \sin(q_2 d_2) e^{-iq_1 d_1}. \quad (2.10)$$

Due to the discrete translational symmetry along the SL modulation axis, the acoustic phonon is a Bloch wave and, therefore, it obeys the relation

$$\begin{pmatrix} U_{m+1,1}^+ \\ U_{m+1,1}^- \end{pmatrix} = e^{iQD} \begin{pmatrix} U_{m,1}^+ \\ U_{m,1}^- \end{pmatrix} \quad (2.11)$$

where Q is the phononic Bloch wavevector. Comparing Eqs. (2.8) and (2.11), one obtains

$$(\mathbf{T} - e^{iQD}\mathbf{I}) \begin{pmatrix} U_{m,1}^+ \\ U_{m,1}^- \end{pmatrix} = \begin{pmatrix} 0 \\ 0 \end{pmatrix} \quad (2.12)$$

and, consequently,

$$\det(\mathbf{T} - e^{iQD}\mathbf{I}) = 0. \quad (2.13)$$

where \mathbf{I} is the 2×2 identity matrix. Thus, e^{iQD} is the eigenvalue of \mathbf{T} . Combining Eqs. (2.9), (2.10), and (2.13), one obtains the well-known phononic Bloch wave

dispersion relation [2, 3]

$$\cos(QD) = \cos\left(\frac{\Omega d_1}{V_1}\right) \cos\left(\frac{\Omega d_2}{V_2}\right) - F \sin\left(\frac{\Omega d_1}{V_1}\right) \sin\left(\frac{\Omega d_2}{V_2}\right), \quad (2.14)$$

where $\Omega = V_j q_j$ and F is given by

$$F = \frac{1}{2} \left(\frac{Z_1}{Z_2} + \frac{Z_2}{Z_1} \right) = \left(\frac{1 + (Z_1/Z_2)^2}{2Z_1/Z_2} \right). \quad (2.15)$$

The resulting acoustic phonon dispersion curve consists of a series of bands. That is, the artificial periodicity of the system causes the phonon dispersion curve to undergo zone-folding into a mini-Brillouin zone of dimension $2\pi/D$. Figure (2.2) depicts a zone-folded phononic band structure in the repeated zone scheme.

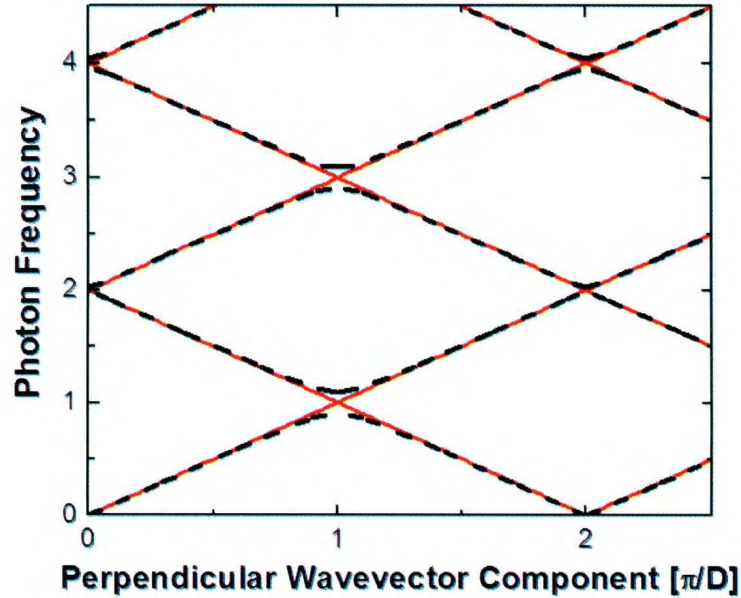


Figure 2.2: Schematic of the phononic band structure for propagation along the modulation axis of an infinite binary periodic superlattice. Black dashed curves: phonon dispersion relation given by Eq. (2.14); red lines: approximation of phonon dispersion relation given by Eq. (2.21).

The case when $Z_1/Z_2 \neq 1$ is of particular note. Parameter F is then greater than 1, which follows from Eq. (2.15) given that

$$1 + \left(\frac{Z_1}{Z_2}\right)^2 - 2\frac{Z_1}{Z_2} = \left(\frac{Z_1}{Z_2} - 1\right)^2 \geq 0 \quad (2.16)$$

and, consequently,

$$1 + \left(\frac{Z_1}{Z_2}\right)^2 \geq 2\frac{Z_1}{Z_2}. \quad (2.17)$$

Hence, with $Z_1/Z_2 \neq 1$, the absolute value of the righthand-side of Eq. (2.14) will be greater than 1 for certain value ranges of Ω (Ω is assumed to be real and positive), resulting in complex Q values. This occurs at $QD = b\pi$, where $\cos(QD) = \pm 1$ (here, b is an integer). The acoustic phonon dispersion then exhibits forbidden frequency bands for which the phonons are highly attenuated and, thus, do not propagate (see Fig. 2.2). These bands are known as one-dimensional hypersonic phononic band gaps. One should note that, for a given modulation length D , the width of these phononic band gaps tend to increase as the contrast between the elastic impedances increases (*i.e.*, as $|Z_1/Z_2 - 1|$ increases).

The center frequency of these phononic band gaps can be approximated by treating the system as a phononic Bragg reflector [4]. For waves undergoing partial specular reflection from consecutive unit-cells of the periodic structure, constructive interference occurs when the round-trip phase difference over a unit-cell equals a multiple of 2π :

$$2Q_h D = 2h\pi = 2 \left(\frac{\Omega_h d_1}{V_1} + \frac{\Omega_h d_2}{V_2} \right). \quad (2.18)$$

where h is an integer. The phononic Bragg angular frequencies Ω_h , which correspond to the center angular frequencies of the phononic band gaps, are then expressed as

$$\Omega_h = h\pi \left(\frac{V_1 V_2}{V_1 d_2 + V_2 d_1} \right). \quad (2.19)$$

The phononic Bragg wavevector $Q_h = h\pi/D$ corresponds to a standing wave with group velocity of zero. This is reflected in the phononic dispersion, where the slopes of the bands go to zero at $Q = h\pi/D$.

If the elastic impedance contrast is small such that the phononic band gap frequency widths are small compared to the available bands, Eq. (2.14) (which governs the phononic band structure) can be approximated by a much simpler algebraic form. Notice that when $Z_2 \approx Z_1$, $F \approx 1$. Therefore, following from Eq. 2.14, one can show that [5, 6]

$$\pm QD = \pm \left(q + \frac{2l\pi}{D} \right) \approx \left(\frac{d_1}{V_1} + \frac{d_2}{V_2} \right) \Omega, \quad (2.20)$$

where l is an integer, q is the extended-zone scheme (*i.e.*, $l = 0$) phonon wavevector, and folding of the phonon dispersion curves is accounted by the SL reciprocal lattice vector $2l\pi/D$. In turn, Ω is approximated by

$$\Omega \approx \pm V_{\text{eff}} Q = \pm V_{\text{eff}} \left(q + \frac{2l\pi}{D} \right), \quad (2.21)$$

where V_{eff} is an effective phonon velocity given by

$$V_{\text{eff}} = \frac{V_1 V_2}{(1 - \Gamma) V_1 + \Gamma V_2} \quad (2.22)$$

and the plus-minus sign accounts for the positive and negative dispersion of the folded phonon bands. Parameter $\Gamma = d_1/D$ is the fill-fraction of the $j = 1$ layer. One should

also note that Eq. (2.21) is a generalization of Eq. (2.19), with the expressions being equal when $Q = Q_h = h\pi/D$. It is then clear that the phonon band structure can be approximated by a series of linear dispersion curves, each with a slope of $\pm V_{\text{eff}}$, which pass through the center of phononic band gaps. Additionally, if $V_2 \geq V_1$, it can be seen that

$$V_{\text{eff}} - V_1 = \frac{(1 - \Gamma)}{V_2}(V_2 - V_1)V_{\text{eff}} \geq 0 \quad (2.23a)$$

$$V_{\text{eff}} - V_2 = \frac{(\Gamma)}{V_1}(V_1 - V_2)V_{\text{eff}} \leq 0 \quad (2.23b)$$

and, therefore,

$$V_1 \leq V_{\text{eff}} \leq V_2. \quad (2.24)$$

Finally, other than the assumption that the d_j values are large compared to the atomic spacing such that the constituent layers can be treated as continua, there are no characteristic length scales in the preceding theory. Substituting $d_1 = \Gamma D$ and $d_2 = (1 - \Gamma)D$ into Eqs. (2.14) and (2.21), one obtains expressions for QD versus ΩD . Thus, for a given set of constituent layer elastic parameters and layer fill-fraction Γ , the phononic band structure scales with D . As such, these results are scale-invariant.

2.1.3 Normal-Incidence Phonon Propagation in a Semi-Infinite Superlattice

As alluded to above, a complete treatment of normal-incidence phonon propagation in π -Si SLs will have to take into account phonons propagating in a semi-infinite

superlattice in contact with a gas (say air). In particular, the $j = 1$ layer of the $m = 1$ unit-cell is assumed to be in contact with the gas (see Figure 2.1(b)). Further, this interface is taken to be stress-free. In addition to bulk modes which obey Eq. (2.21), a surface-localized mode resulting from the broken symmetry at the superlattice-gas interface is also possible. This localized mode decays exponentially into the superlattice and, therefore, it is not a traveling wave. While Eqs. (2.1)-(2.10) still apply here, the Bloch condition (*i.e.*, Eq. (2.11)) is replaced by the expression [7 9]

$$\begin{pmatrix} U_{m+1,1}^+ \\ U_{m+1,1}^- \end{pmatrix} = e^{-\beta D} \begin{pmatrix} U_{m,1}^+ \\ U_{m,1}^- \end{pmatrix} \quad (2.25)$$

where $\beta > 0$ and is real. Thus, the constituent layer wave amplitudes decrease by a factor of $e^{-\beta D}$ with each consecutive unit-cell. Since the surface is stress-free, Eq. (2.2a) gives

$$iZ_1 (U_{1,1}^+ - U_{1,1}^-) = 0 \quad (2.26)$$

and, therefore,

$$U_{1,1}^- = U_{1,1}^+. \quad (2.27)$$

Eq. (2.25) then implies that, in general,

$$U_{m,1}^- = U_{m,1}^+. \quad (2.28)$$

Combining Eq. (2.28) and Eq. (2.8), one obtains

$$U_{2,1}^+ = (T_{11} + T_{12}) U_{1,1}^+ \quad (2.29a)$$

$$U_{2,1}^+ = (T_{21} + T_{22}) U_{1,1}^+. \quad (2.29b)$$

Comparing Eqs. (2.25) and (2.29), one finds that

$$e^{-\beta D} = T_{11} + T_{12} = T_{21} + T_{22}. \quad (2.30)$$

Further combining Eqs. (2.9), (2.10), and (2.30), it can be shown that

$$\left(\frac{Z_1}{Z_2}\right) \tan\left(\frac{\Omega_s d_1}{V_1}\right) + \tan\left(\frac{\Omega_s d_2}{V_2}\right) = 0 \quad (2.31)$$

and

$$e^{-\beta D} = \left| \frac{\cos(\Omega_s d_1/V_1)}{\cos(\Omega_s d_2/V_2)} \right| \quad (2.32)$$

where Ω_s is the angular frequency of the localized mode. Eq. (2.31) can be solved numerically to obtain a series of Ω_s values which lie within the bulk mode phononic band gaps governed by Eq. (2.14) (*i.e.*, Ω_s are associated with evanescent modes which decay into the bulk of the system). Furthermore, it can be shown that since $e^{-\beta D} < 1$, the presence of the localized mode hinges on the nature of the impedance ratio between the layers. That is, since Eq. (2.32) states that $|\cos(q_1 d_1)| = e^{-\beta D} |\cos(q_2 d_2)| < |\cos(q_2 d_2)|$, it follows from combining Eqs. (2.31) and (2.32) that

$$\left(\frac{Z_1}{Z_2}\right) = \sqrt{\frac{1 - \cos^2(q_2 d_2)}{1 - \cos^2(q_1 d_1)}} e^{-\beta D} < e^{-\beta D} < 1. \quad (2.33)$$

Hence, in order for the localized surface mode to exist, the $j = 1$ layer (which is adjacent to the gaseous half-space) must have a lower elastic impedance than that of the other constituent layer.

Additionally, one should note that, according to Eq. (2.31), the localized surface mode spectrum is independent of Q and, like Eqs. (2.14) and (2.21), it scales with

D when the constituent layer elastic parameters and Γ are fixed. Thus, a plot of $\Omega_s D$ versus QD consists of a series of flat bands lying within the bulk acoustic mode phononic band gaps.

2.1.4 Oblique-Incidence Photon Propagation in an Infinite Superlattice

For a photon propagating in an infinite superlattice (see Fig. 2.1(a)), the resulting theory is similar to that encountered for phonons. Furthermore, in the case of photons, it is fairly straightforward to extend the theory to account for propagation at oblique angles to the SL modulation direction. Similar to before, there is a square-wave modulation in both the permittivity and the permeability over a spatial period of $D = d_1 + d_2$. It is assumed that the structure's constituent layers are composed of linear media with constituent layer permittivity and permeability values of ϵ_j and μ_j , respectively. In the absence of free charge and current, Maxwell's equations for a linear medium are [10]

$$\vec{\nabla} \cdot \mathbf{B} = 0 \quad (2.34a)$$

$$\vec{\nabla} \times \mathbf{B} = \mu_j \epsilon_j \frac{\partial \mathbf{E}}{\partial t} \quad (2.34b)$$

$$\epsilon_j \vec{\nabla} \cdot \mathbf{E} = 0 \quad (2.34c)$$

$$\vec{\nabla} \times \mathbf{E} = -\frac{\partial \mathbf{B}}{\partial t}, \quad (2.34d)$$

where \mathbf{E} is the electric field and \mathbf{B} is the magnetic field. Using the vector identity $\vec{\nabla} \times (\vec{\nabla} \times \mathbf{C}) = \vec{\nabla} (\vec{\nabla} \cdot \mathbf{C}) - \vec{\nabla}^2 \mathbf{C}$, where \mathbf{C} is some arbitrary vector, together with Maxwell's equations, one obtains the electric and magnetic wave equations:

$$\vec{\nabla}^2 \mathbf{B} - \frac{1}{c_j^2} \frac{\partial^2 \mathbf{B}}{\partial t^2} = 0 \quad (2.35a)$$

$$\vec{\nabla}^2 \mathbf{E} - \frac{1}{c_j^2} \frac{\partial^2 \mathbf{E}}{\partial t^2} = 0 \quad (2.35b)$$

where $c_j = (\mu_j \epsilon_j)^{-\frac{1}{2}}$ is the speed of light in each layer. Since each layer is taken to be of infinite extent in the y - z plane (i.e., the y - z plane is parallel to the layer interfaces and the x -axis is along the superlattice modulation), the general expressions of the electromagnetic waves are [11, 12]

$$\mathbf{B}_j(x_j, y_j, t) = e^{i(K_{jy}y_j - \omega t)} \mathbf{B}_j(x_j) \quad (2.36a)$$

$$\mathbf{E}_j(x_j, y_j, t) = e^{i(K_{jy}y_j - \omega t)} \mathbf{E}_j(x_j) \quad (2.36b)$$

and, in turn, Eq. (2.35) can be rewritten as

$$-\left(\left(\frac{\omega}{c_j}\right)^2 - K_{jy}^2\right) \mathbf{B}_j(x_j) = \frac{\partial^2}{\partial x_j^2} \mathbf{B}_j(x_j) \quad (2.37a)$$

$$-\left(\left(\frac{\omega}{c_j}\right)^2 - K_{jy}^2\right) \mathbf{E}_j(x_j) = \frac{\partial^2}{\partial x_j^2} \mathbf{E}_j(x_j). \quad (2.37b)$$

Here, ω is the photon angular frequency, $K_{jy} = (\omega/c_j) \sin \Theta_j = (\omega/c) \sin \theta$ are the components of the internal photon wavevectors, \mathbf{K}_j , in the plane of the layer interfaces, Θ_j are the angles between the interface normal and \mathbf{K}_j , θ is the corresponding angle in vacuum deduced through Snell's Law, and c is the speed of light in vacuum. Boundary conditions between the interfaces require continuity of the components of

\mathbf{B} and $\epsilon_j \mathbf{E}$ parallel to the interface normal as well as the components of \mathbf{B}/μ_j and \mathbf{E} perpendicular to the interface normal [10]. Since the magnetic and electric fields are coupled through Maxwell's equations, only one of the waves (or a single component from each wave) needs to be considered in order to solve the problem. Thus, only two of the four boundary conditions will be utilized. In the discussion to follow, the incident electromagnetic wave will be assumed to be p-polarized and, therefore, $\mathbf{B} = B(x, y, t)\hat{z}$ (*i.e.*, the electric field is in the plane of incidence). According to Eqs. (2.34b) and (2.36), it follows that

$$E_{jy}(x_j) = -\frac{i}{\omega\epsilon_j\mu_j} \frac{\partial B_{jz}(x_j)}{\partial x} = -\frac{i}{\omega\epsilon_j\mu_j} \frac{\partial B_j(x_j)}{\partial x_j} \quad (2.38)$$

and, therefore, the general solutions to Eq. (2.37) are

$$B_{jz}(x_j) = A_{m,j}^+ e^{iK_{jx}x_j} + A_{m,j}^- e^{-iK_{jx}x_j} \quad (2.39a)$$

$$E_{jy}(x_j) = \frac{K_{jx}}{\omega\epsilon_j\mu_j} (A_{m,j}^+ e^{iK_{jx}x_j} - A_{m,j}^- e^{-iK_{jx}x_j}), \quad (2.39b)$$

where $A_{m,j}^+$ and $A_{m,j}^-$ are the amplitudes of the forward- and backward-traveling magnetic waves in the constituent layers of the superlattice and $K_{jx} = \sqrt{(\omega/c_j)^2 - K_{jy}^2}$ is the component of wavevector K_j perpendicular to the layer interfaces. Hence, continuity of the in-plane components of \mathbf{B}/μ_j and \mathbf{E} at each interface implies that [11]

$$\frac{1}{\mu_2} (A_{m,2}^+ + A_{m,2}^-) = \frac{1}{\mu_1} (A_{m,1}^+ e^{iK_{1x}d_1} + A_{m,1}^- e^{-iK_{1x}d_1}) \quad (2.40a)$$

$$\frac{K_{2x}}{\omega\epsilon_2\mu_2} (A_{m,2}^+ - A_{m,2}^-) = \frac{K_{1x}}{\omega\epsilon_1\mu_1} (A_{m,1}^+ e^{iK_{1x}d_1} - A_{m,1}^- e^{-iK_{1x}d_1}) \quad (2.40b)$$

and

$$\frac{1}{\mu_1} (A_{m+1,1}^+ + A_{m+1,1}^-) = \frac{1}{\mu_2} (A_{m,2}^+ e^{iK_{2x}d_2} + A_{m,2}^- e^{-iK_{2x}d_2}) \quad (2.41a)$$

$$\frac{K_{1x}}{\omega\epsilon_1\mu_1} (A_{m+1,1}^+ - A_{m+1,1}^-) = \frac{K_{2x}}{\omega\epsilon_2\mu_2} (A_{m,2}^+ e^{iK_{2x}d_2} - A_{m,2}^- e^{-iK_{2x}d_2}). \quad (2.41b)$$

In matrix-form, these above relations can be rewritten as

$$\begin{pmatrix} 1 & 1 \\ 1 & -1 \end{pmatrix} \begin{pmatrix} A_{m,2}^+ \\ A_{m,2}^- \end{pmatrix} = \begin{pmatrix} \left(\frac{\mu_2}{\mu_1}\right) e^{iK_{1x}d_1} & \left(\frac{\mu_2}{\mu_1}\right) e^{-iK_{1x}d_1} \\ \left(\frac{n_2^2 K_{1x}}{n_1^2 K_{2x}}\right) e^{iK_{1x}d_1} & -\left(\frac{n_2^2 K_{1x}}{n_1^2 K_{2x}}\right) e^{-iK_{1x}d_1} \end{pmatrix} \begin{pmatrix} A_{m,1}^+ \\ A_{m,1}^- \end{pmatrix} \quad (2.42)$$

and

$$\begin{pmatrix} 1 & 1 \\ 1 & -1 \end{pmatrix} \begin{pmatrix} A_{m+1,1}^+ \\ A_{m+1,1}^- \end{pmatrix} = \begin{pmatrix} \left(\frac{\mu_1}{\mu_2}\right) e^{iK_{2x}d_2} & \left(\frac{\mu_1}{\mu_2}\right) e^{-iK_{2x}d_2} \\ \left(\frac{n_2^2 K_{2x}}{n_1^2 K_{1x}}\right) e^{iK_{2x}d_2} & -\left(\frac{n_2^2 K_{2x}}{n_1^2 K_{1x}}\right) e^{-iK_{2x}d_2} \end{pmatrix} \begin{pmatrix} A_{m,2}^+ \\ A_{m,2}^- \end{pmatrix}. \quad (2.43)$$

where $n_j = \sqrt{\epsilon_j \mu_j} c$ are the refractive indices of the constituent layers. In a similar fashion to what was done in the discussion on phonons, one can show that

$$\begin{pmatrix} A_{m+1,1}^+ \\ A_{m+1,1}^- \end{pmatrix} = \tilde{\mathbf{T}} \begin{pmatrix} A_{m,1}^+ \\ A_{m,1}^- \end{pmatrix}, \quad (2.44)$$

where $\tilde{\mathbf{T}}$ is a 2×2 transfer matrix with elements given by

$$\tilde{T}_{11} = \tilde{T}_{22}^* = \left(\cos(K_{2x}d_2) + \frac{i}{2} \left(\left(\frac{\epsilon_1 K_{2x}}{\epsilon_2 K_{1x}} \right) + \left(\frac{\epsilon_2 K_{1x}}{\epsilon_1 K_{2x}} \right) \right) \sin(K_{2x}d_2) \right) e^{iK_{1x}d_1} \quad (2.45)$$

and

$$\tilde{T}_{12} = \tilde{T}_{21}^* = \frac{i}{2} \left(\left(\frac{\epsilon_1 K_{2x}}{\epsilon_2 K_{1x}} \right) - \left(\frac{\epsilon_2 K_{1x}}{\epsilon_1 K_{2x}} \right) \right) \sin(K_{2x}d_2) e^{-iK_{1x}d_1}. \quad (2.46)$$

The discrete translational invariance of the system implies that the photon must behave as a Bloch wave, and, consequently, the amplitudes of adjacent unit-cells are related as

$$\begin{pmatrix} A_{m+1,1}^+ \\ A_{m+1,1}^- \end{pmatrix} = e^{i\kappa D} \begin{pmatrix} A_{m,1}^+ \\ A_{m,1}^- \end{pmatrix} \quad (2.47)$$

where κ is the photonic Bloch wavevector. Comparing Eq. (2.47) with Eq. (2.44), one can see that

$$\left(\tilde{\mathbf{T}} - e^{i\kappa D} \mathbf{I} \right) \begin{pmatrix} A_{m,1}^+ \\ A_{m,1}^- \end{pmatrix} = \begin{pmatrix} 0 \\ 0 \end{pmatrix} \quad (2.48)$$

and, therefore,

$$\det \left(\tilde{\mathbf{T}} - e^{i\kappa D} \mathbf{I} \right) = 0. \quad (2.49)$$

Solving the above equation gives the photon dispersion relation [11–13]

$$\cos(\kappa D) = \cos(K_{1x}d_1) \cos(K_{2x}d_2) - P_p \sin(K_{1x}d_1) \sin(K_{2x}d_2). \quad (2.50)$$

Here, P_p is specific to the condition of p-polarization and is given by

$$P_p(\theta) = \frac{1}{2} \left(\frac{\epsilon_1 K_{2x}}{\epsilon_2 K_{1x}} + \frac{\epsilon_2 K_{1x}}{\epsilon_1 K_{2x}} \right) \quad (2.51)$$

Similarly, in the case that the electromagnetic wave is s-polarized (*i.e.*, the electric field is perpendicular to the plane of incidence), the dispersion relation has the same functional form with parameter P_p replaced by

$$P_s(\theta) = \frac{1}{2} \left(\frac{\mu_1 K_{2x}}{\mu_2 K_{1x}} + \frac{\mu_2 K_{1x}}{\mu_1 K_{2x}} \right). \quad (2.52)$$

$K_{1x}/K_{2x} = c_2/c_1$ and, not surprisingly,

$$P_s(0) = P_p(0) = P_{norm} = \frac{1}{2} \left(\sqrt{\frac{\epsilon_1 \mu_2}{\epsilon_2 \mu_1}} + \sqrt{\frac{\epsilon_2 \mu_1}{\epsilon_1 \mu_2}} \right) \quad (2.53)$$

If it is further assumed that the layers are nonmagnetic (*i.e.*, $\mu_2 = \mu_1 = \mu_0$, where μ_0 is the permeability of a vacuum), then $n_j = \sqrt{\epsilon_j \mu_0} c$ and one finds that

$$P_p(\theta) = \frac{1}{2} \left(\frac{n_1^2 K_{2x}}{n_2^2 K_{1x}} + \frac{n_2^2 K_{1x}}{n_1^2 K_{2x}} \right) \quad (2.54a)$$

$$P_s(\theta) = \frac{1}{2} \left(\frac{K_{2x}}{K_{1x}} + \frac{K_{1x}}{K_{2x}} \right) \quad (2.54b)$$

$$P_{norm} = \frac{1}{2} \left(\frac{n_1}{n_2} + \frac{n_2}{n_1} \right). \quad (2.54c)$$

For the remainder of the discussion, the SL is taken to be composed of non-magnetic materials.

For $n_2 \neq n_1$ and, therefore, $K_{2x} \neq K_{1x}$, one finds that $P_p \neq 1$ and $P_s \neq 1$. In turn, for certain ranges of values for ω , the absolute value of the righthand side of Eq. (2.50) will be greater than 1. Further, s-polarized light may be shown to behave the same way [12]. The resulting ranges of ω correspond to forbidden frequency bands, or photonic band gaps, where κ becomes complex. The gaps occur for $\text{Re}[\kappa D] = b\pi/2$.

In a similar fashion to what was done for phonons in the preceding discussion, the center-frequency of the photonic band gaps can be approximated by treating the system as a photonic Bragg reflector [14]. At normal incidence, constructive interference occurs when the round-trip phase difference over a unit-cell equals a multiple of 2π :

$$2\kappa_t D = 2t\pi = 2 \left(\frac{\omega_t d_1}{c_1} + \frac{\omega_t d_2}{c_2} \right), \quad (2.55)$$

where t is an integer. The resulting photonic Bragg angular frequencies ω_t are then expressed as

$$\omega_t = t\pi \left(\frac{c}{n_1 d_1 + n_2 d_2} \right). \quad (2.56)$$

The corresponding photon wavenumber is then

$$w_t = \frac{t}{2(n_1 d_1 + n_2 d_2)}. \quad (2.57)$$

The corresponding Bragg photonic wavevector $\kappa_t = t\pi/D$ is a standing wave with group velocity of zero. Consequently, these photons do not propagate in the SL and, in the case of reflectance measurements from a finite SL structure, are marked by a peak in the reflectance spectrum.

Continuing to consider normal-incidence, if the contrast in the optical properties (*i.e.*, refractive index) is small such that the frequency-width of the photonic band gaps are small compared to the available bands, the band structure can be approximated by a simple algebraic equation. That is, with $\theta = 0$ and $n_2 \approx n_1$, $P_p(0) = P_s(0) = P_{norm} \approx 1$ and it follows from Eq. 2.50 that [2]

$$\kappa D \approx \left(\frac{n_1 d_1 + n_2 d_2}{c} \right) \omega. \quad (2.58)$$

Written in the above form, κ is taken to be the extended-zone scheme photonic wavevector. It can be shown that

$$\omega \approx \frac{c\kappa}{n_{\text{eff}}}, \quad (2.59)$$

where n_{eff} is an effective refractive index given by

$$n_{\text{eff}} = \Gamma n_1 + (1 - \Gamma)n_2. \quad (2.60)$$

One should also note that Eq. (2.59) is a generalization of Eq. (2.56), and both expressions are equal when $\kappa = t\pi/D$. Hence, the extended-zone scheme photonic band structure can be approximated by a single linear dispersion curves with a slope of c/n_{eff} which passes through the center of the photonic band gaps. Figure 2.3 depicts the resulting photonic band structure. Further, if $n_2 \geq n_1$, one can show that

$$n_{\text{eff}} - n_1 = (1 - \Gamma)(n_2 - n_1) \geq 0 \quad (2.61a)$$

$$n_{\text{eff}} - n_2 = \Gamma(n_1 - n_2) \leq 0 \quad (2.61b)$$

and, consequently,

$$n_1 \leq n_{\text{eff}} \leq n_2. \quad (2.62)$$

Finally, substituting $d_1 = \Gamma D$ and $d_2 = (1 - \Gamma)D$, it is clear that Eqs. (2.50) and (2.58) give expressions of κD versus ωD . Therefore, as with the phononic band structure, for a given set of constituent layer optical parameters and layer fill-fraction Γ , the photonic band structure is scale-invariant.

2.2 Brillouin Light Scattering

2.2.1 Overview

In order to characterize the phononic band structure of π -Si SLs, inelastic Brillouin light scattering spectroscopy will be done. The resulting measurements provide a set of Ω versus q data for phonons directed along a given direction in the material and, in turn, the phononic band structure can be mapped.

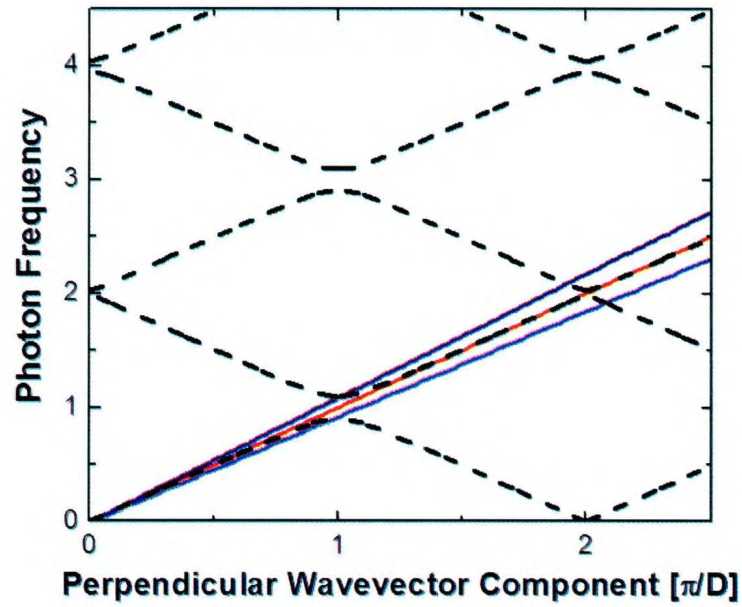


Figure 2.3: Schematic of the photonic band structure for propagation along the modulation axis of an infinite binary periodic superlattice. Black dashed curves: photon dispersion relation based on Eq. (2.50) with $\theta = 0$; red line: approximation of the zeroth-order photon band given by Eq. (2.59); blue lines: dispersion curves for the constituent layers.

Brillouin light scattering is used to probe acoustic phonons in a given material system. That is, when a photon impinges on a material, it may interact with a lattice vibration, or phonon, and subsequently scatter. This is accompanied by an exchange of energy and momentum between the photon and phonon. According to the laws of conservation of energy and momentum, for a homogeneous material this process is governed by [15]

$$\hbar\omega_s = \hbar\omega_i \pm \hbar\Omega \quad (2.63a)$$

$$\hbar\mathbf{K}_s = \hbar\mathbf{K}_i \pm \hbar\mathbf{q}, \quad (2.63b)$$

where ω_i and ω_s are the angular frequencies of the incident and scattered light, respectively, and \mathbf{K}_i and \mathbf{K}_s are the wavevectors of the incident and scattered light inside the material, respectively. The plus sign in the above expressions corresponds to the process of phonon annihilation, or anti-Stokes scattering, while the minus sign corresponds to the process of phonon creation, or Stokes scattering. Figure 2.4 illustrates a typical Brillouin scattering spectrum.

When considering inelastic light scattering from a SL, the periodicity of the lattice must be taken into account. Thus, Eq. (2.63) is rewritten as [2]

$$\hbar\omega_s = \hbar\omega_i \pm \hbar\Omega_l \quad (2.64a)$$

$$\hbar\mathbf{K}_s = \hbar\mathbf{K}_i \pm \hbar \left(\mathbf{q} + \frac{2\pi l}{D} \hat{x} \right) \quad (2.64b)$$

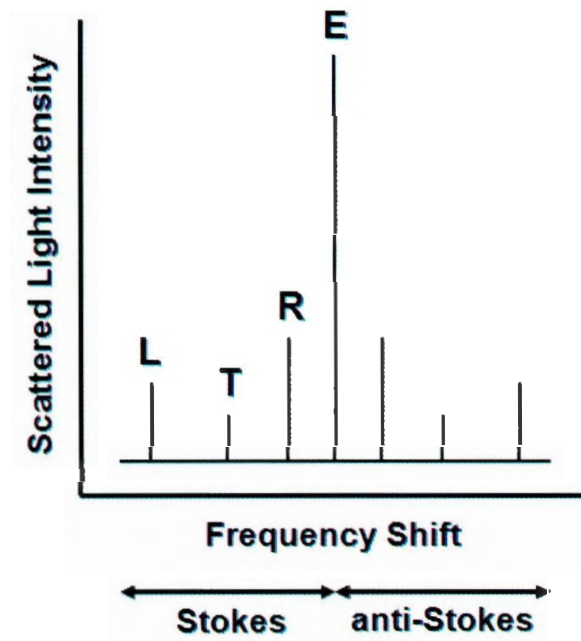


Figure 2.4: Schematic of a Brillouin spectrum. Double peak features due to Stokes and anti-Stokes scattering from various acoustic phonons, such as the Rayleigh surface mode (R), the bulk longitudinal mode (L), and the bulk transverse mode (T), are observed. These peak doublets are set symmetrically about the highly intense peak attributed to elastic scattering; the corresponding frequency shifts are equal to the frequencies of the probed phonons.

where $(2\pi/D)\cdot\hat{r}$ is the reciprocal lattice vector of the SL. Consequently, the resulting Brillouin spectrum will contain spectral features corresponding to folded branches of the zone-folded phononic band structure.

In Brillouin scattering, acoustic phonons are probed. It follows from Eq. (2.63b) that the wavelength and direction of the characterized phonon depends on the wavelength of the incident light as well as the scattering geometry. In fact, the phonons of interest typically have wavelengths of the order of 100 nm. Thus, these long-wavelength acoustic phonons behave as elastic waves which, for a homogeneous material, are gov-

erned by the dispersion relation [15]

$$\Omega = 2\pi\nu = Vq \quad (2.65)$$

where ν is the phonon frequency and V is the magnitude of the phonon velocity. Since V is of the order of 1 km/s (*i.e.*, much smaller than the speed of light c), $\Omega \ll \omega_i$. Hence, according to Eq. 2.63, $\omega_s \approx \omega_i$ and, consequently, $|K_s| \approx |K_i|$. Overall, this approximation applies when probing most material systems, including SLs.

2.2.2 180°-Backscattering and Pseudo-Reflection Brillouin Light Scattering Geometries

Figure 2.5 shows the scattering geometries used in the present study. For a 180°-backscattering geometry, where Θ_s , the angle between \mathbf{K}_s and the sample surface normal, is equal to Θ_i , the angle between \mathbf{K}_i and the sample surface normal, it follows from Eq. (2.63b) that the components of the probed phonon wavevector perpendicular and parallel to the surface of the material are given by

$$q_{BS\perp} = 2K_{i\perp} \quad (2.66a)$$

$$q_{BS\parallel} = 2K_{i\parallel}, \quad (2.66b)$$

where $K_{i\perp}$ and $K_{i\parallel}$ are the corresponding components of \mathbf{K}_i . Furthermore, the angle between \mathbf{q}_{BS} and the sample surface normal, α_{BS} , is expressed as

$$\alpha_{BS} = \tan^{-1} \left(\frac{q_{BS\parallel}}{q_{BS\perp}} \right) = \tan^{-1} \left(\frac{K_{i\parallel}}{K_{i\perp}} \right) \quad (2.67)$$

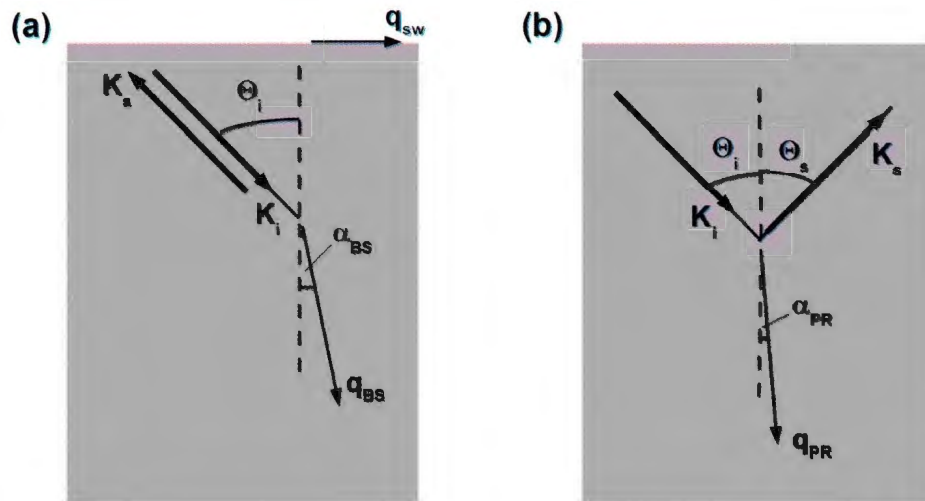


Figure 2.5: (a) 180°-backscattering and (b) pseudo-reflection Brillouin light scattering geometries. Here, \mathbf{q} correspond to the wavevectors of the probed phonon while \mathbf{K}_i (\mathbf{K}_s) is the wavevector of the incident (scattered) light inside the probed material. The angle between \mathbf{q} and the sample surface normal is denoted by α while the angle between Θ_i (Θ_s) denotes the angle between \mathbf{K}_i (\mathbf{K}_s) and the sample surface normal. Subscripts SW, BS and PR denote surface-propagating phonons, bulk phonons probed using a 180°-backscattering geometry, and bulk phonons probed using a pseudo-reflection geometry, respectively. For clarity, the incident and scattered photon wavevectors related to \mathbf{q}_{SW} are not shown.

and, thus, the direction of \mathbf{q}_{BS} is dictated by the direction of \mathbf{K}_i relative to the sample surface. Consequently, a 180°-backscattering geometry can be used to probe phonons along different directions in the material.

Additionally, a 180°-backscattering geometry is used to probe surface acoustic phonons within the sample surface plane. Since the amplitude of the surface-propagating phonon decays quickly away from the surface, the probed phonon wavevector is related to the in-plane component of the probing light [16]:

$$q_{SW} = 2K_{i||} = 2k_{i||}, \quad (2.68)$$

where $k_{i\parallel}$, the in-plane component of the incident photon wavevector outside the material, is equal to $K_{i\parallel}$ through Snell's Law. As one can see, the magnitude of the probed surface phonon wavevector can be changed by changing the direction of \mathbf{k}_i .

Figure 2.5(b) depicts a pseudo-reflection scattering geometry. In this case, $|\Theta_s - \Theta_i| \geq 0$ is small (*i.e.*, less than 10°). The components of the resulting probed phonon perpendicular and parallel to the sample surface plane are, in general, given by

$$q_{PR\perp} = K_{i\perp} + K_{s\perp} \quad (2.69a)$$

$$q_{PR\parallel} = K_{i\parallel} - K_{s\parallel} \quad (2.69b)$$

and the angle between \mathbf{q}_{PR} and the sample surface normal, α_{PR} , is expressed as

$$\alpha_{PR} = \tan^{-1} \left(\frac{q_{PR\parallel}}{q_{PR\perp}} \right) = \tan^{-1} \left(\frac{K_{i\parallel} - K_{s\parallel}}{K_{i\perp} + K_{s\perp}} \right). \quad (2.70)$$

With $\Theta_s \approx \Theta_i$, however, then $K_{i\parallel} \approx K_{s\parallel}$, so it follows from Eqs. (2.69) and (2.70) that

$$q_{PR} \approx q_{PR\perp} = K_{i\perp} + K_{s\perp} \quad (2.71)$$

and, further,

$$\alpha_{PR} \approx \tan^{-1}(0) = 0. \quad (2.72)$$

Hence, by tuning \mathbf{K}_i and \mathbf{K}_s while keeping $\Theta_s \approx \Theta_i$, pseudo-reflection geometry Brillouin light scattering can be used to characterize a range of q_{PR} values directed approximately along the sample surface normal. This is particularly useful for SLs as the corresponding phononic band structure could then be mapped.

The preceding discussion makes no assumption about the phononic and photonic dispersion relations and, thus, can be applied to homogeneous materials as well as SLs. Further details on the application of these scattering geometries will be provided in the following chapters.

Chapter 2 References

- [1] C. Kittel. *Introduction to Solid State Physics*. (John Wiley and Sons, New Jersey, 2005), p. 73-85.
- [2] J. He, B. Djafari-Rouhani, and J. Sapriel. *Phys. Rev. B* **37**, 4086 (1988).
- [3] S.M. Rytov. *Soviet Phys. Acoustics* **2**, 68 (1956).
- [4] G. N. Aliev and P. A. Snow, *Mater. Res. Soc. Symp. Proc.* **1145**, MM13-04 (2009).
- [5] S. Kumar and H. J. Trodahl, *J. Appl. Phys.* **70**, 1 (1991).
- [6] R. Hotz and R. Siems. *Solid State Commun.* **51**, 793 (1984).
- [7] B. Djafari-Rouhani, L. Dobrzynski, O. Hardouin Duparc, R. E. Camley, and A. A. Maradudin. *Phys. Rev. B* **28**, 1711 (1983).
- [8] R. E. Camley, B. Djafari-Rouhani, L. Dobrzynski, and A. A. Maradudin. *Phys. Rev. B* **27**, 7318 (1983).
- [9] H. T. Grahn, H. J. Maris, J. Tauc, and B. Abeles. *Phys. Rev. B* **38**, 6066 (1988).

- [10] J. Franklin. *Classical Electromagnetism*. (Pearson/Addison Wesley, New York, 2005).
- [11] P. Yeh, A. Yariv, and C. Hong, *J. Opt. Soc. Am.* **67**, 423 (1977).
- [12] A Yariv and P. Yeh. *Photonics: Optical Electronics in Modern Communications*. (Oxford University Press, New York, 2007), p. 539-601.
- [13] S.M. Rytov, *Soviet Phys. JETP* **2**, 466 (1956).
- [14] P.A. Snow, E.K. Squire, P. St. J. Russell, and L.T. Canham, *J. Appl. Phys.* **86**, 1781 (1999).
- [15] H. Z. Cummins and P. E. schoen. Light Scattering from Thermal Fluctuations. In *Laser Handbook, Vol 2*, edited by F. T. Arecchi and E. O. Schulz-Dubois. (North-Holland. New York, 1972), p. 1029-1075.
- [16] J. R. Sandercock. *Solid State Commun.* **26**. 547 (1978).

Chapter 3

Methods and Materials

3.1 Sample Preparation

The studied π -Si films were formed from p^+ -type [100]-oriented crystalline silicon with a resistivity in the range of 0.005-0.020 Ω cm. In particular, the electrochemical process used to make the films was such that the porous structure nucleated at the polished surface of a piece of bulk crystalline silicon. The ~ 4 cm² piece of parent crystalline silicon had been cleaved, using a diamond scribe, from ~ 500 μ m-thick p^+ -type crystalline silicon wafers with a diameter of ~ 10 cm.

There are a number of reasons for choosing to fabricate the π -Si films from p^+ -type crystalline silicon. First, mesoporous films made from p^+ -type crystalline silicon are well-characterized [1] and, in particular, studies have shown that periodically multilayered π -Si films made from this type of bulk silicon can behave as one-dimensional photonic crystals [2, 3]. Second, research suggests that these films are relatively robust in ambient conditions and, in contrast to samples made from p^- -type crystalline

silicon, do not oxide quickly [2]. Third, by taking additional measures throughout the fabrication process (as will be discussed in a proceeding paragraph), undesirable porosity gradients can be readily avoided for the case of films made from p^+ -type crystalline silicon [3]. This is critical since it is to be assumed that the films have a well-defined modulation in the porosity.

Supported π -Si films were fabricated by electrochemical anodization of a cleaved piece of p^+ -type crystalline silicon wafer in hydrofluoric acid-based electrolytes. Prior to anodization, a sample was dipped in hydrofluoric acid (HF) for 60 s to help remove native oxide on the surface. The sample was then placed in an electrolytic cell with either a 1:1:1 (water: 49% wt. HF: 98% wt. ethanol) electrolyte or a 1:1 (49% wt. HF: 98% wt. ethanol) electrolyte (note: all electrolyte composition ratios are by volume). Specifically, preliminary samples were made using the 1:1:1 (water: 49% wt. HF: 98% wt. ethanol) electrolyte; for later samples, the electrolyte composition was 1:1 (49% wt. HF: 98% wt. ethanol). This change in solution composition was spurred on by an observed lack of sample-to-sample reproducibility in the earlier films that was thought to stem from issues with the included deionized water.

Figure 3.1 shows the electrolytic cell that was used. The bottom of the inner cavity of the cell, where the anodization process occurred, was sealed using a small rubber o-ring. Copper (Cu) was used as the contact electrode, being placed in contact with the unpolished side of the p^+ -type silicon, and platinum (Pt) was used as the working electrode. The Cu and Pt electrodes were connected to the positive and the negative

terminals of a Keithley 2400 SourceMeter power supply, respectively. Figure 3.2 shows a schematic of the circuit. A user-defined current profile was applied across the sample, which was monitored by an ammeter. In order to minimize the effects of uncontrolled photochemical etching, the artificial lights in the laboratory were turned off during sample anodization. Furthermore, for many of the experiments, a teflon cover was placed over the top of the electrolytic cell during the anodization process. A small slot cut into the cover allowed it to be slipped over the Pt electrode without interfering with the electrode placement. In addition, to help prevent build-up of hydrogen gas which is produced during the anodization process [4], two small holes were drilled in the top of the cell cover. Moreover, the cover did not enclose the entire cell and, in fact, it typically rested on the alligator-clip used to connect the ammeter to the Cu electrode.

It is known that tuning the applied current density (or, in this case, current as the etch area is constant) while keeping all other etch parameters fixed results in a change in the film porosity with film thickness. Thus, single-layer π -Si films were fabricated by applying a constant current, while multilayered π -Si films with a binary periodicity in the porosity were made by alternating the current between two known values.

The fabrication of binary periodic multilayered π -Si films is only possible since π -Si formation approximates a self-limiting process [2] (see Section 1.1). Once a π -Si film is formed, additional etching of the sample proceeds at the pore tip and the pre-

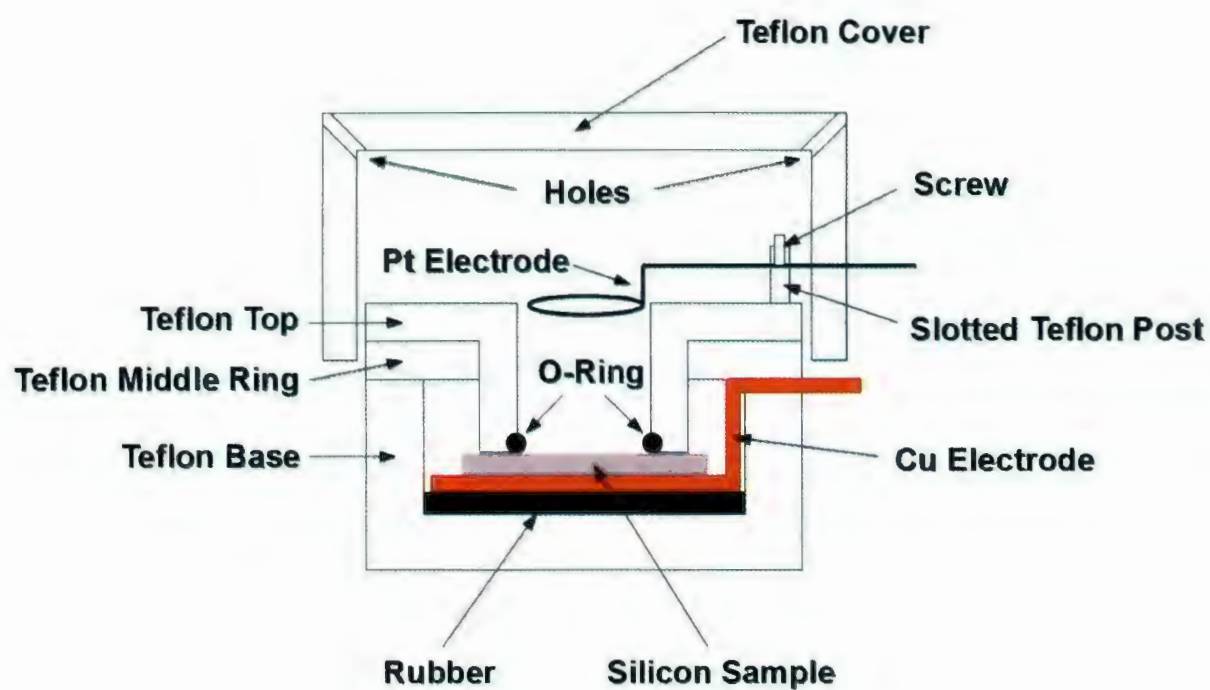


Figure 3.1: Cross-section of the electrolytic cell used for sample fabrication.

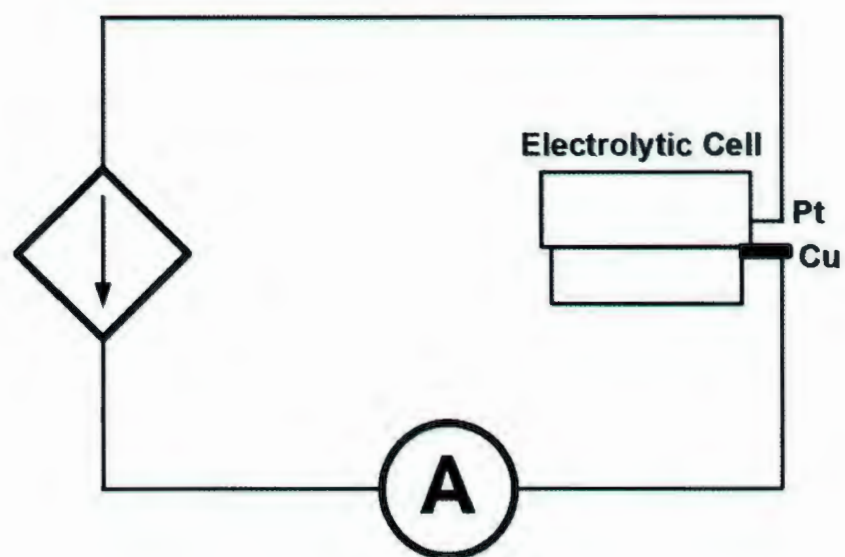


Figure 3.2: Circuit diagram for the fabrication setup.

viously formed nanostructure is not affected. This is an approximation, however, and π -Si films may exhibit a gradient in the porosity with depth due to (a) undesirable chemical etching of the upper portions of the film from prolonged exposure to the electrolyte and (b) changes in the electrochemical process stemming from depletion of the electrolyte at the pore tip. Fortunately, for samples fabricated from p^+ -type silicon, chemical etching of the pore walls is not usually significant and electrochemical-based gradients may be counteracted through the implementation of zero-current etch stops which allowed time for the electrolyte to replenish at the pore tip [3]. Consequently, when making the multilayered samples, 1 s etch stops were implemented between the alternations of the etch current. The resulting structures were then taken to be composed of constituent layers which had porosities equivalent to that of single-layer films made under the same etching conditions (*i.e.*, etching current).

The applied currents used to make the studied single-layer and multilayered films are given in Table 3.1. In the case of samples made using a 1:1 (49% wt. HF: 98% wt. ethanol) electrolyte, the applied currents were chosen since the corresponding single-layer films had been well-characterized in an earlier study conducted in this laboratory [5]. Thus, there was an existing body of knowledge regarding the physical parameters of the resulting films, such as film porosity as well as the elastic and optical properties. One should note that in this current study, no single-layer films were made using the 1:1:1 (water: 49% wt. HF: 98% wt. ethanol) electrolyte.

Table 3.1: Anodization current densities used to make single-layer and multilayered porous silicon films. The single-layer films were obtained by applying a constant current (either I_{high} or I_{low}), while the multilayered films were obtained by alternating between the two currents.

Solution	I_{high}	I_{low}
	(mA)	(mA)
1:1 (49% wt. HF: 98% wt. ethanol)	230	142
1:1:1 (water: 49% wt. HF: 98% wt. ethanol)	50	5

The applied currents were higher for samples made using the 1:1 (49% wt. HF: 98% wt. ethanol) solution since J_{crit} tends to increase as the HF concentration increases (*i.e.*, the pore formation regime occurs for a wider range of current densities as the HF concentration increases [6]). Additionally, the applied current density values, J , could be determined by dividing I by the π -Si film surface area, $(1.47 \pm 0.02) \text{ cm}^2$, which had been deduced from the diameter of the film: the film diameter was measured using a Vernier caliper, as described previously [5].

With the etching process completed, the resulting supported π -Si film (single-layer or multilayered) could be removed from the cell. Once removed, the supported films were rinsed with tap water, dried with paper towel, rinsed in pentane (whose low surface tension helped to reduce the possibility of structural cracking due to excess capillary forces), and dried in ambient air.

Alternatively, if one wished to detach the as-formed supported π -Si film from the crystalline silicon substrate, a secondary anodization process had to be done. Leaving

the formed supported π -Si film in the cell, the original electrolyte was replaced with a 1:7 (49% wt. HF: 98% wt. ethanol) solution. Decreasing the HF concentration decreases the critical current density, J_{crit} , required for electropolishing and, thus, reduces the undesirable effects of Joule heating [7]. By applying J_{crit} , the film-substrate interface is etched (recall the self-limiting nature of π -Si formation) and the film lifts off the substrate. In the present study, an applied current of ~ 30 mA was sufficient to detach the films. The electropolishing process usually took several minutes to finish, with the circuit current, as read on the ammeter, going to zero near completion (*i.e.*, the circuit shorted when the film lifted off the substrate).

The freestanding π -Si film was removed from the electrolytic cell by carefully disposing the electrolyte, rinsing the cell with water, and then using the silicon substrate as a base to carry the film out of the cell. The film was then transferred to a teflon sample holder. This was done by first placing the film (which was still resting on the silicon substrate) on the bottom part of the teflon holder, which was inside the overturned electrolytic cell cover (see Fig. 3.3(a)). In order to transfer the film from the substrate to the holder bottom, first, the cell cover was filled with pentane, resulting in the film floating off the substrate due to the positive buoyant force. Using tweezers, the silicon substrate was removed and, as the pentane drained through the gas-release holes in the electrolytic cell cover, the film was guided onto the center of the film holder bottom. Once the pentane had completely drained, both the sample holder base and film were retrieved. That is, using the tweezers to “hook” the screw

holes in the holder bottom, the holder bottom was lifted out of the cell cover. The top of the holder was attached using 3 thumb-screws which were set concentrically about the center of the sample holder. Furthermore, a small rubber o-ring served to hold the film in place (see Fig. 3.3(b)). To help reduce the possibility of the film cracking under excess capillary forces which may be present during the drying process, samples were held in a nitrogen-rich environment overnight. This was done by placing the sample holder in a container system situated over a dewar of boiling liquid nitrogen. Within the container system, the sample was ~ 20 cm above the opening of dewar and, therefore, the sample is not cooled to much below room temperature.

3.2 Determination of Film Thickness

Previous studies on similarly made π -Si samples suggest that film growth is approximately linear with time [5]. That is, the overall film thicknesses for single-layer and multilayered films are given by

$$H_{single} = r_y t_y \quad (3.1)$$

and

$$H_{multi} = \eta(r_{high}t_{high} + r_{low}t_{low}) = \eta D, \quad (3.2)$$

respectively, where r_y are the etch rates at the corresponding currents, t_y are the etch times, $y = high, low$ denotes the relative current value, η is the number of current cycles used to form a multilayered film, and D is, as stated before, the modulation

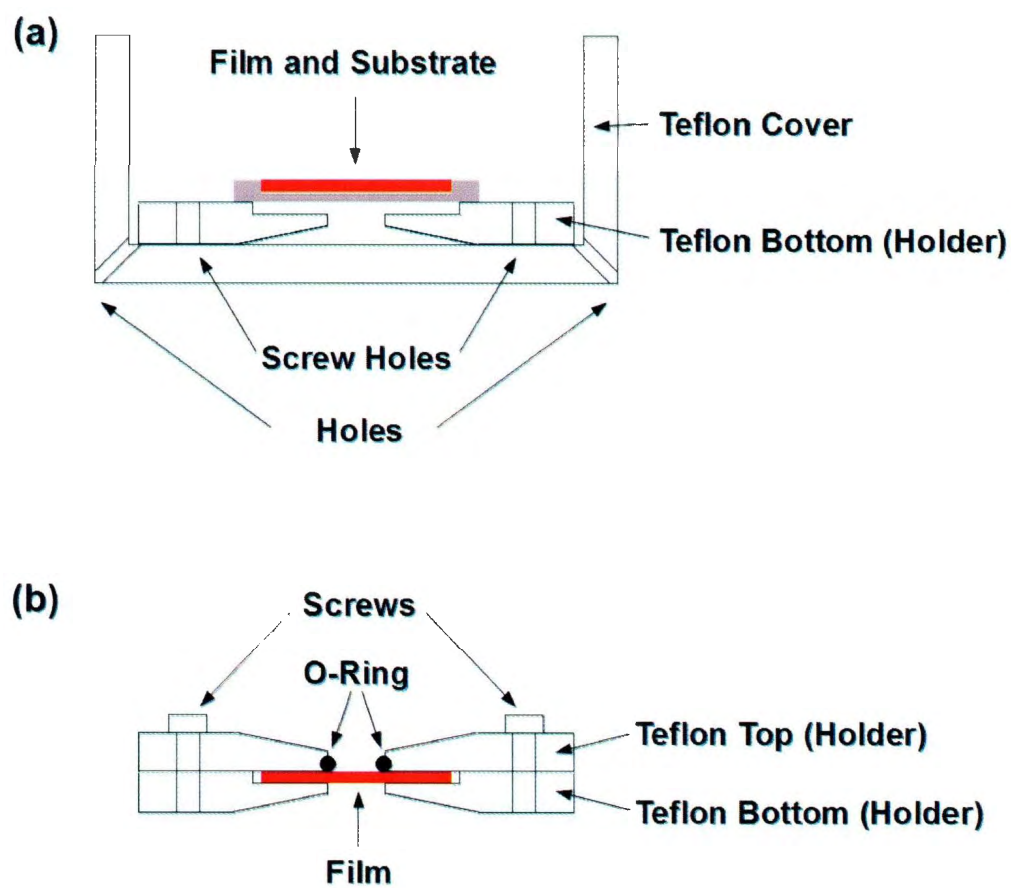


Figure 3.3: Cross-section of (a) the freestanding film retrieval setup and (b) the sample holder. The two pieces of the holder were held together by three screws.

wavelength in the resulting binary periodic multilayered film. Therefore, if the etch rates are known, both the overall film thicknesses and the SL modulation wavelength may be deduced from the fabrication etch times and the number of current cycles. For samples made using the 1:1 (49% wt. HF: 98% wt. ethanol) electrolyte, the relevant etch rates were determined in a previous study conducted in this laboratory [5]. Table 3.2 gives pertinent etch rates for these samples. Specifically, etch times were chosen such that the resulting films were $\sim 6 \mu\text{m}$ thick.

Another method for deducing the overall thickness of a supported or freestanding π -Si film is by using scanning electron microscopy (SEM) to image the sample cross-section. Prior to imaging, the samples were cleaved in order to expose a cross-sectional interface through the film. Care was taken to cleave approximately along the center line of the film. This helped to avoid a systematic uncertainty in the SEM-deduced film thickness: the film was thinner near the outer radius, owing to edge effects in the anodization process. In fact, these edge effects manifested as a change in sample colour near the outer edge of the film (see Fig. 3.4). The cleaved samples were mounted to a SEM-ready sample holder, typically using silver paste. To help with imaging contrast, a thin layer of gold was evaporated onto the samples.

Figures 3.5, 3.6 and 3.7 show cross-sectional SEM images collected from a freestanding single-layer π -Si film, a supported single-layer π -Si film, and a supported square-wave modulated multilayered π -Si film, respectively. For the supported films, the SEM images show cross-sections of the porous films as well as a portion of the

corresponding bulk crystalline silicon substrate: the image from the freestanding film shows the porous sample surrounded by vacuum. The brighter layers observed in the image of the multilayered film are assigned to the higher porosity constituent layers. As mentioned in Section 1.1, very bright regions near the outer surfaces of the films (see Figs. 1.1 and 3.5) are thought to be an artefact of electron charging effects which occur during the scanning electron imaging process and, thus, are not attributed to gradients in the film porosity. One should note that the three samples were fabricated according to the procedures outlined in Section 3.1.

For films made using the 1:1 (49% wt. HF: 98% wt. ethanol) electrolyte, values of H obtained using SEM imaging were within $\sim 15\%$ of those deduced using Eqs. (3.1) and (3.2) together with the etch rates given in Table 3.2. The main contribution to this difference is thought to be due to an unavoidable sample-to-sample variability in the etch procedure.

Table 3.2: Anodization etch rates and gravimetrically-deduced porosity values for samples made using a 1:1 (49% wt. HF: 98% wt. ethanol) electrolyte. Etch rates are from [5].

Current	r	ζ
(mA)	(nm/s)	
230	148 ± 1	0.58 ± 0.02
142	106 ± 5	0.50 ± 0.02

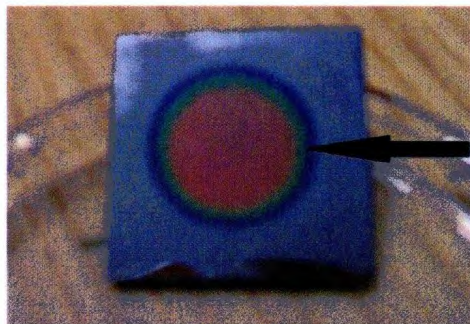


Figure 3.4: Top-down image of a supported π -Si multilayered film. The sample is a one-dimensional photonic crystal with a band gap in the red frequency range. The arrow points out the reduced film thickness along the outer edge of the film, denoted by a change in colour.

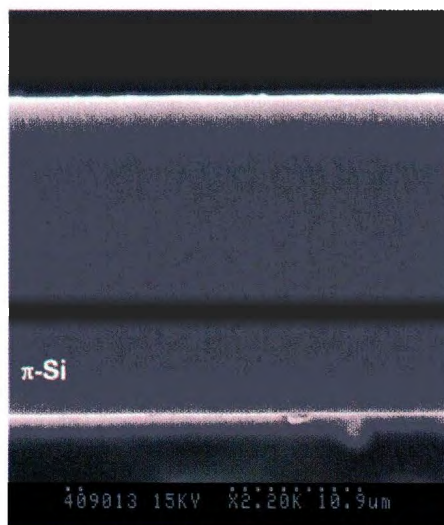


Figure 3.5: Cross-sectional scanning electron micrograph of a freestanding single-layer π -Si film. The sample (labeled P π Si4.9#1) was formed in a 1:1 (49% wt. HF: 98% wt. ethanol) electrolyte with an applied current of 230 mA. To minimize effects due to electrolyte depletion at the pore-tip over the long etch time (200 s), the current was pulsed. The resulting current profile consisted of 0.5 s etch intervals separated by 1 s etch-stops for 400 cycles. The measured film thickness was $\sim 28 \mu\text{m}$.

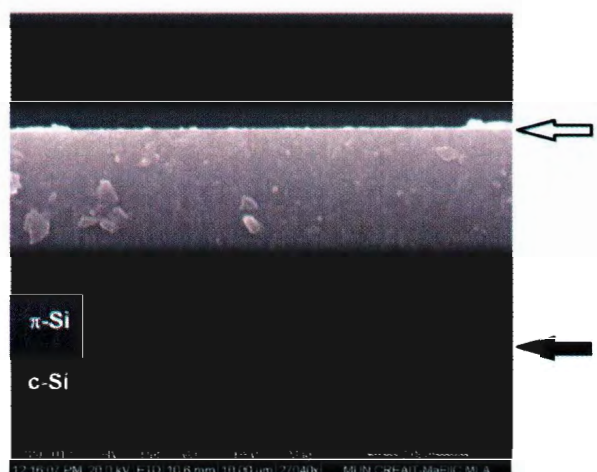


Figure 3.6: Cross-sectional scanning electron micrograph of a supported single-layer π -Si film. The sample (labeled P*Si*4.7#3) was formed in a 1:1 (49% wt. HF: 98% wt. ethanol) electrolyte with a constant applied current of 230 mA. The etch time was 34 s and the measured film thickness was $\sim 4.5 \mu\text{m}$. Empty (filled) arrow denotes the film-air (substrate-film) interface.

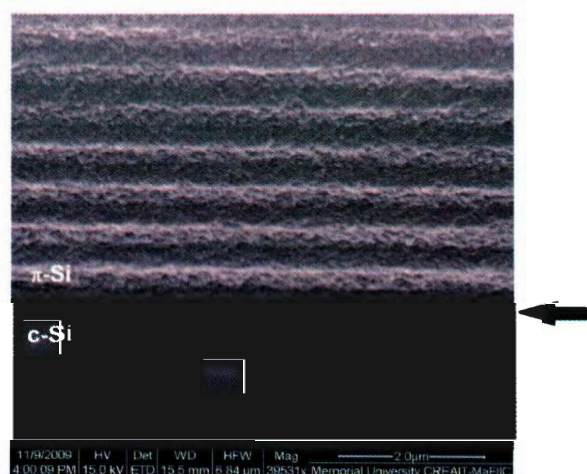


Figure 3.7: Cross-sectional scanning electron micrograph of a supported multilayered π -Si film. The sample (labeled P*Si*2.22#4) was formed in a 1:1 (49% wt. HF: 98% wt. ethanol) electrolyte with a periodic current profile. The etch times were $t_{high} = 1.67785 \text{ s}$ and $t_{low} = 2.25225 \text{ s}$. This resulted in constituent layers of approximately equal thickness and a SL modulation wavelength of $\sim 500 \text{ nm}$. Brighter regions correspond to the higher porosity layers formed at the high current value (*i.e.*, 230 mA). The filled arrow denotes the substrate-film interface.

For most of the studied SL films, the constituent layers were too thin (*i.e.*, $D/2 < 100$ nm) to be discernible in the collected SEM images. In spite of this, a value for D could be obtained by taking into account the SEM-deduced H_{multi} together with the known number of applied current cycles (it follows from Eq. (3.2) that $D = H_{multi}/\eta$).

3.3 Determination of the Porosity, Mass Density, and Refractive Index of a Single-Layer Film

The physical characteristics of a mesoporous silicon film, such as refractive index and mass density, are strongly dependent on the porosity value. The porosity of a single-layer π -Si film, ζ , is simply the fraction of voids in the porous structure. This is stated mathematically as

$$\zeta = \frac{V_{voids}}{V_{film}} = \frac{m_{voids}}{m_{silicon}}, \quad (3.3)$$

where $V_{voids} = (m_{voids})/\rho_{c-Si}$ is the volume of the voids, $V_{film} = (m_{silicon})/\rho_{c-Si}$ is the volume of the overall film, m_{voids} is the mass of silicon removed during the formation of the porous nanostructure, $m_{silicon}$ is the sum of m_{voids} and the silicon mass of the remaining nanostructure, and $\rho_{c-Si} = 2330$ kg/m³ is the density of crystalline silicon [8]. Thus, the porosity of a single-layer sample may be obtained by determining m_{voids} and $m_{silicon}$.

With this in mind, the mass of the test piece of silicon before anodization, $m_{pre-etch}$, and after anodization, $m_{post-etch}$, were obtained using an analytical balance. In turn,

one obtains $m_{voids} = m_{pre-etch} - m_{post-etch}$. In contrast, determining $m_{silicon}$ required that the film be destroyed. This was done through a selective etch in a 1% KOH solution [5]. Once in the solution, the film was etched away, as indicated by the evolution of gas bubbles on the film surface. This process took several minutes and, once bubbles stopped forming, the remaining substrate was removed from the solution. Using the same analytical balance, the mass of the KOH-etched sample, $m_{post-KOH}$, was obtained. One can then calculate $m_{silicon} = m_{pre-etch} - m_{post-KOH}$. Hence, the porosity may be determined gravimetrically through Eq. (3.3). Consequently, for each set of conditions, a series of films was made with the purpose of determining the porosity. Through statistical analysis of the gravimetric results, a single value for the layer porosity corresponding to each etch current was deduced. Table 3.2 shows the porosity values. As mentioned in section 3.1, only single-layer films made using a 1:1 (49% wt. HF: 98% wt. ethanol) electrolyte were studied.

With the porosity determined, both the mass density and refractive index of the single-layer film could be found. In particular, the mass density of the film is given by $\rho_{\pi-Si} = (1 - \zeta)\rho_{c-Si}$. The relationship between the refractive index and the porosity, on the other hand, is much more complex. For mesoporous silicon films made from p^+ -type crystalline silicon, as is the case here, studies have shown that the effective refractive index of the film, n_{eff} , can be obtained using the two-component Bruggemann effective medium model, expressed as [9]

$$1 - \zeta = \frac{(1 - n(w)^2)(N(w)^2 + 2n(w)^2)}{3n(w)^2(1 - N(w)^2)}. \quad (3.4)$$

where $N(w)$ is the refractive index of bulk crystalline silicon and w is the optical wavenumber. Thus, the dependence of $n(w)$ on light wavenumber may be determined using ζ and the corresponding values of $N(w)$ given in the literature [10].

3.4 Optical Reflectance Spectroscopy

3.4.1 Broad-Band Optical Reflectance Setup and Method

To help characterize the optical properties of the π -Si films, broad-band optical reflectance spectroscopy was done. The optical setup is shown in Fig. 3.8. An Ocean Optics LS-1 Tungsten Halogen lamp, optimized for output from 360 nm to 2500 nm, served as the source of incident light in these experiments. Source light was coupled into the outer six fibers of a seven-fiber, y-configuration Ocean optics QR600-7-SR-125F optical fiber system (FO), which had a transmission range of 200 nm to 1100 nm. The light traversed the fibers and was output from a fiber probe (PRO) which was held above the optical bench by a micrometer-adjustable bracket (MB). The output source light impinged on the sample (S) at near-normal incidence. The resulting reflected light coupled into the center fiber of the probe (the remaining fiber of the seven fiber bundle) and was sent to an Ocean Optics 2000USB VIS-NIR grating spectrometer, which was used to frequency-analyze the collected light. In particular, the spectrometer contained a 350 nm-1000 nm grating and the resolution was 1.5 nm. Furthermore, the spectrometer detector, a linear silicon CCD array, was sensitive

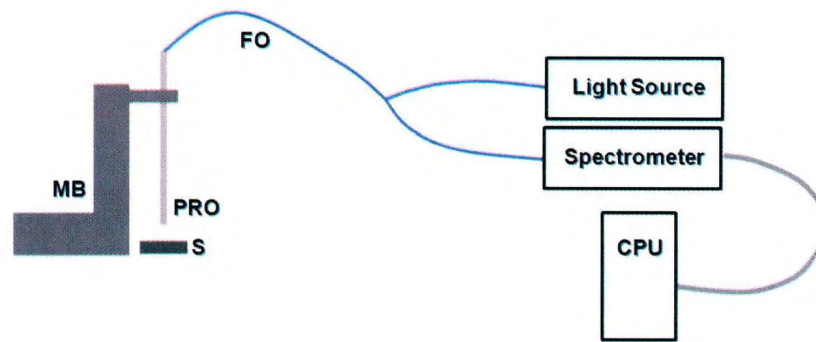


Figure 3.8: Broad-band optical reflectance spectroscopy setup. FO - y-configuration fiber optic bundle, PRO - optical reflectance probe, MB - micrometer-adjustment bracket, S - sample, CPU - computer.

from 200 nm to 1100 nm. Subsequently, the collected reflected light intensity versus optical wavelength was output to a computer, where it was displayed and stored.

In order to determine the absolute reflectance of the probed samples, the collected reflected light spectra were normalized against that of a known reference. This, in turn, removed any artefact stemming from the wavelength dependence of the tungsten halogen lamp output intensity as well as signal losses due to coupling and attenuation in the fiber. The chosen reference was a BB05-E02 broad-band dielectric mirror manufactured by Thor Labs. Figure 3.9 shows a typical absolute reflectance spectrum taken from a BB05-E02 mirror at near-normal incidence. As one can see, the reflectance is greater than 98% over wavenumbers ranging from $\sim 1.05 \mu\text{m}^{-1}$ to $\sim 2.50 \mu\text{m}^{-1}$ (*i.e.*, ~ 400 nm to ~ 950 nm). Note that from here on, the reflectance spectra will be plotted over wavenumber, which is proportional to frequency, allowing the data to be readily related to the calculated photon band structures.

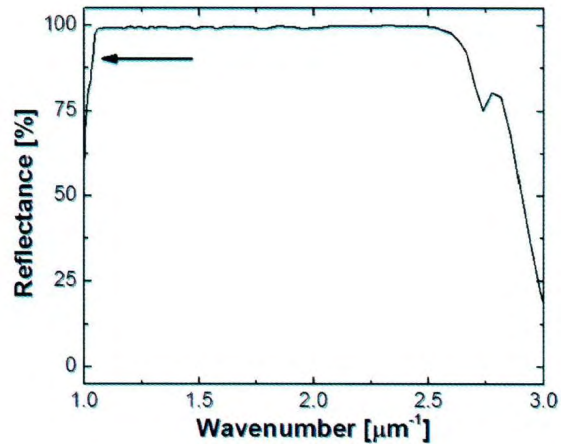


Figure 3.9: The absolute reflectance spectrum of a broad-band dielectric mirror. The mirror was manufactured by Thor Labs and the spectral data were collected at an angle of incidence of 8° . The arrow indicates a sharp decrease in reflectance in the near-infrared. Data were obtained from the manufacturer website [11].

The relative reflectance of a given sample may be calculated as

$$R_{rel} = \frac{I_{sample} - I_{background}}{I_{mirror} - I_{background}}. \quad (3.5)$$

where I_{sample} is the spectral response collected from the sample, I_{mirror} is the spectral response collected from the mirror, and $I_{background}$ is background response collected with the tungsten halogen source turned off. Given that the mirror is approximately 100% reflective over $\sim 1.05 \mu\text{m}^{-1}$ to $\sim 2.50 \mu\text{m}^{-1}$, R_{rel} is taken to be equal to the absolute reflectance of the sample, R_{abs} , over this wavenumber range.

When collecting spectra from the mirror and sample, the distance between the probe and probed material was adjusted to maximize the coupling response (recall that the probe was held in an adjustable bracket). That is, the spectral response was monitored in real-time on the computer display and the maximum intensity was

achieved at a sample-to-probe distance of about 5 mm. Further, in order to avoid sensor saturation when probing the mirror, the integration time was set to ~ 500 ms. For each set of measurements, all three spectra (sample, mirror, and background) were collected at the same integration time.

Figure 3.10 shows an example experimental optical reflectance spectrum collected from [100]-oriented gallium phosphide (GaP). The change in reflectance at $\sim 1.82 \mu\text{m}^{-1}$ is a manifestation of the expected electron band gap [12]. The peak at $\sim 1.1 \mu\text{m}^{-1}$, on the other hand, is an artefact of the decrease in reflectivity of the dielectric mirror in the near-infrared and therefore does not correspond to the true absolute reflectance of the GaP sample. That is, since there is a sharp decrease in the mirror reflectivity at $\sim 1.05 \mu\text{m}^{-1}$, the corresponding relative reflectance value obtained using Eq. (3.5) is much higher than the absolute reflectance of the sample.

3.4.2 Optical Reflectance from a Freestanding Multilayered π -Si Film

As the optical properties of a mesoporous silicon film are dependent on the porosity, analysis of the reflectance spectra can provide insight into the underlying nanostructure. With this in mind, reflectance measurements were collected from both surfaces of a freestanding multilayered π -Si film in order to obtain information about the consistency of the formation process. Figure 3.11 shows the collected spectra. As one can see, the spectral positions of the optical Bragg peaks and, thus, the photonic

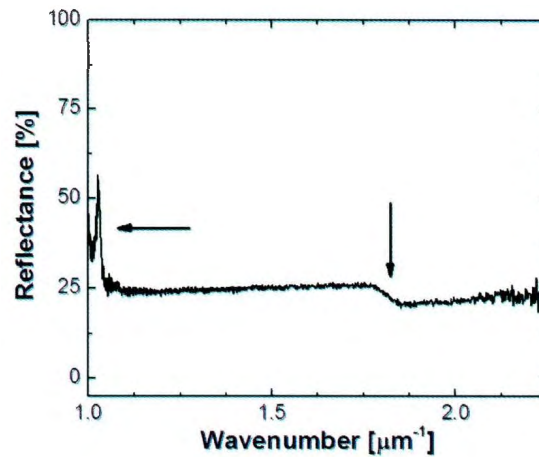


Figure 3.10: Optical reflectance spectrum of [100]-oriented GaP. The vertical arrow located at $\sim 1.82 \mu\text{m}^{-1}$ indicates a change in reflectance due to the electron band gap of GaP. The horizontal arrow indicates a sharp peak at $\sim 1.05 \mu\text{m}^{-1}$ which is a spectral artefact due to the decrease in the reference mirror reflectivity in the near-infrared.

band gaps were within $\sim 5\%$ of each other. It follows from Eqs. (2.57) and (2.60) that $n_{\text{eff}}D$ is approximately equal at both surfaces. One may then infer that the etch process was fairly consistent throughout the formation of the $\sim 50 \mu\text{m}$ -thick film. Hence, it is reasonable to assume that there is little effect due to porosity gradients with depth for a $\sim 6 \mu\text{m}$ -thick film (the typical thickness for samples investigated in the current study). Note: as there is uncertainty in which surface of the freestanding film was attached to the substrate, no other inferences are made based on the current data.

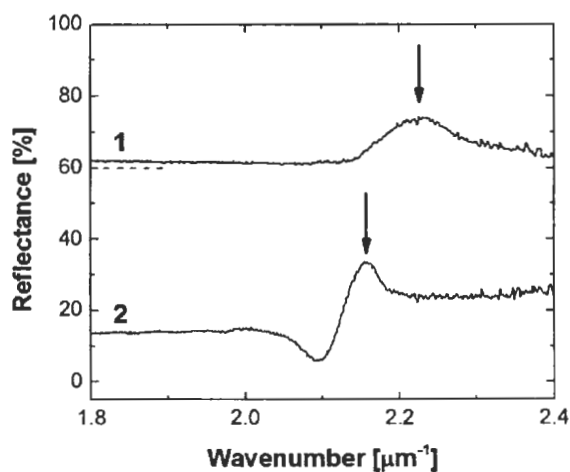


Figure 3.11: Optical reflectance spectra collected from the surfaces of a freestanding multilayered π -Si film. The arrows indicate the optical Bragg peak in each spectrum and the dashed horizontal line marks 0% reflectance for spectrum 1. The probed sample (labeled P*Si*4.9#2) was formed in a 1:1 (49% wt. HF: 98% wt. ethanol) electrolyte with a periodic current profile. The etch times were $t_{high} = 0.5$ s and $t_{low} = 0.5$ s and the current was alternated 400 times. This resulted in a SL modulation wavelength of ~ 125 nm and an overall film thickness of ~ 50 μm .

3.5 Brillouin Spectroscopy Setup

3.5.1 180°-Backscattering Geometry

The 180°-backscattering geometry Brillouin light scattering setup is shown in Fig. 3.12. A diode-pumped frequency-doubled Nd:YVO₄ solid-state laser (single-mode Coherent Verdi-2) emits a vertically polarized beam of light with a center wavelength of ~ 532 nm and a bandwidth of ~ 10 MHz. The 2 W beam was first passed through a variable neutral density filter (VNDF), which served to reduce the beam power, and then a half-wave plate (HWP), which rotated the beam polarization into the horizontal plane. The horizontally polarized light was incident on a beam splitter (BS), with the reflected portion of the light being used as a reference beam and the transmitted portion being used as the sample probe beam.

The reference beam was directed to a six-pass tandem Fabry-Perot interferometer by a front-surface mirror (M). Before entering the interferometer, the reference beam was passed through an aperture (A) and a variable neutral density filter (VNDF), which allowed for adjustment of the power. This beam was used to maintain alignment of the interferometer. Furthermore, used in conjunction with a shutter system inside the interferometer, it helped to prevent saturation of the photomultiplier tube when the interferometer was scanning over the portion of the scattered light spectrum (collected from the probed sample) that contained the very intense elastically scattered light.

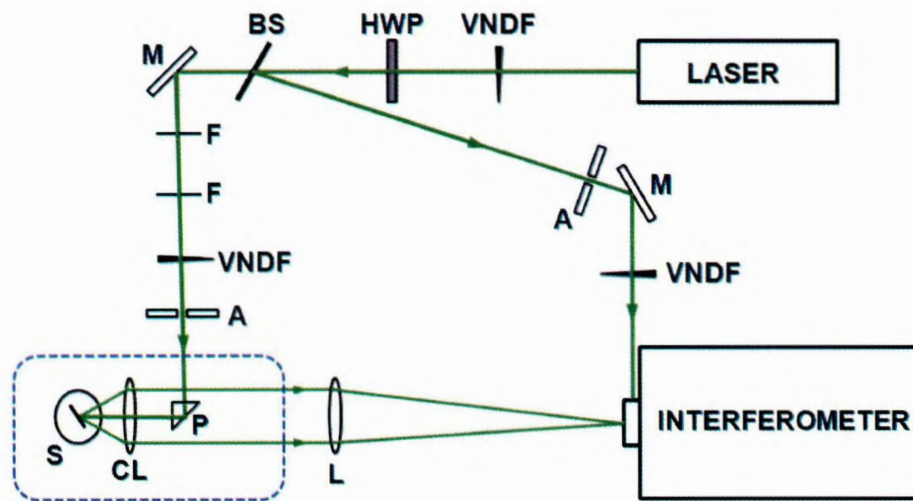


Figure 3.12: 180°-backscattering geometry Brillouin light scattering setup. HWP - half wave plate. BS - beam splitter. M - mirror. F - filter. VNDF - variable neutral density filter. A - aperture. L - lens. P - prism. CL - focusing/collecting lens. S - sample. The dashed box indicates the portion of the setup specific to this scattering geometry.

The path of the probe beam, which had been transmitted through the beam splitter, was deviated by 90° using a front surface mirror. It was passed through two filters (F) and a variable neutral density filter (VNDF), which served to reduce the beam power to within a range of ~ 50 mW to ~ 80 mW. The beam underwent internal reflection in a prism (P), directing it on a path parallel to the original beam. The probe beam was then focused by a 5 cm lens (CL) onto the sample (S), which was mounted on a rotation stage. Some of the scattered light was collected and collimated by the same lens, with the size of the collection cone being set by adjusting the $f/\#$ (CL was contained in a camera lens system which had an adjustable aperture). In particular, $1.8 \leq f/\# \leq 4.0$ for these experiments. With the axial ray of the scattered

light cone being anti-parallel to that of the incident light, the collected scattered light was 180° backscattered (*i.e.*, the scattering angle, defined as the angle between \mathbf{K}_s and \mathbf{K}_i , is 180°). This collimated scattered light passed through a second 40-cm lens (L) which focused the light onto the input pinhole of the tandem Fabry-Perot interferometer. Furthermore, fine-adjustments to the focus of the CL were achieved by tuning the position of the lens along the beam path while monitoring the focused beam spot on the interferometer pinhole (the beam was said to be focused when the spot size was at a minimum). The plane of the pinhole was viewed through a microscope (not shown). Moreover, for the 180° -backscattering geometry light scattering measurements, the pinhole size was set to $450 \mu\text{m}$.

Using this procedure, a range of incident angles could be accessed. By adjusting the rotation angle of the sample on the rotation stage, the incident angle between the probe beam and the sample surface normal, θ_i (which, in this geometry, is equal to the angle between the axial ray of the collected scattered light cone and the sample surface normal, θ_s), may be tuned. Specifically, θ_i was equal to the corresponding angle reading on the rotation stage minus that at normal incidence. The rotation stage angle at normal incidence was found by determining the orientation at which the incident beam underwent back-reflection through the collection lens (deduced using a piece of paper to monitor the reflected beam spot beyond the prism).

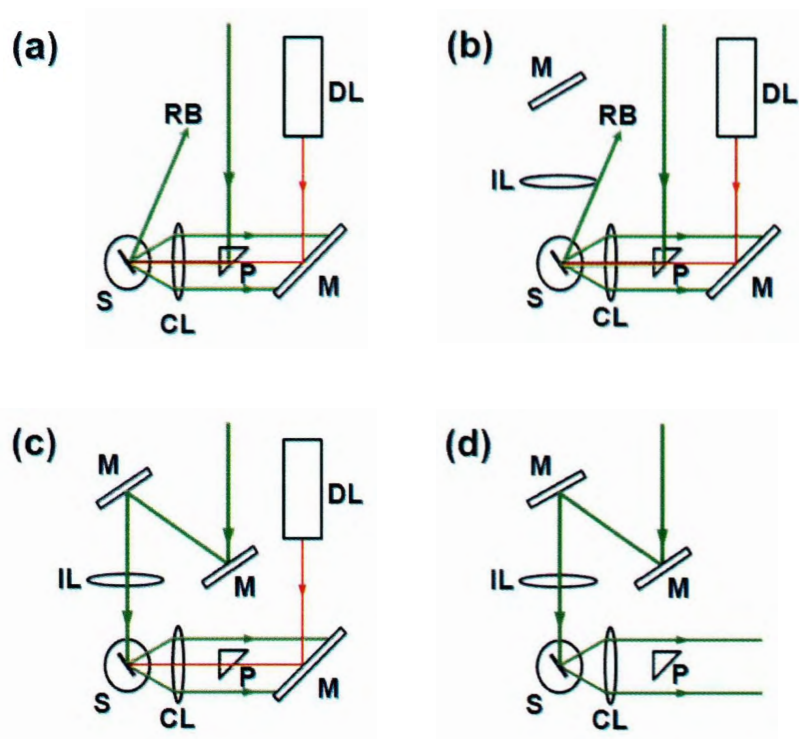


Figure 3.13: Procedure for setting up a pseudo-reflection Brillouin light scattering geometry. (a) The red diode laser, used to ensure that the focal points of the incident and collection lenses coincided, was put in place; (b) the incident lens was set such that the angle of the resulting specularly reflected light would be slightly offset from that of the scattered light collection cone axis; (c) the incident beam was focused on the sample; (d) the scattered light was sent to the interferometer. DL - red diode laser, M - mirror, IL - focusing lens for incident light, P - prism, CL - collecting lens, S - sample, RB - reflected light beam.

3.5.2 Pseudo-Reflection Scattering Geometry

With the exception of the focusing and collecting optics (indicated by the dashed box in Fig. 3.12), the experimental setup used to conduct pseudo-reflection geometry Brillouin light scattering measurements is the same as that used for the 180° -backscattering geometry measurements. Fig. 3.13 depicts the steps taken to set up the pseudo-reflection scattering geometry.

Initially, the setup follows the same procedure as described above, with the collection lens being used to focus the laser beam onto the sample and, thus, setting the sample scattering volume. Once this was done, a mirror (M) placed beyond the prism (P) directed the beam from a red diode laser (DL) onto the sample (see Fig. 3.13(a)). The orientation of the mirror and diode laser were adjusted such that the red and green beams were coincident on the sample and, in turn, the incident spot from DL was used to indicate the position of the sample scattering volume throughout the rest of the set up procedure. An additional mirror (M) and 7 cm lens (IL), mounted to a rotation arm centered on the post of the sample rotation stage, were then set into place such that the axis of the rotation arm was $\sim 5^\circ$ to $\sim 10^\circ$ beyond the axis of the reflected portion of the green laser beam (RB) (see Fig. 3.13(b)). A third mirror (M) was used to redirect the green probe beam onto the rotation-arm-mounted mirror (M). The orientation and position of the arm-mounted mirror and 7 cm lens were adjusted such that the redirected green probe beam impinged on the same position on the sample surface as the red beam. This step is shown in Fig. 3.13(c). Thus, as mentioned above, the red beam was used as a guide to ensure that lenses IL and CL were focused on approximately the same scattering volume of the sample. Fig. 3.13(d) shows the final step in the procedure. Here, both the mirror that had been placed beyond the prism as well as the red diode laser were removed. Consequently, the scattered light which was collected and collimated by the collection lens CL was then focused onto the pinhole of the interferometer using a 40 cm lens (L in Fig. 3.12).

Furthermore, by monitoring the scattered light spot on the pinhole, final adjustments were made to the position and orientation of the arm-mounted mirror and lens (IL) in order to ensure that the probe beam focused by IL was approximately coincident with the focal point of the collection lens CL (note: the diameter of the spot on the pinhole was at a minimum when the focal points of IL and CL were coincident). Due to the use of the 7 cm lens, the beam spot on the pinhole was larger than that encountered when using 180° -backscattering geometry and, therefore, the input pinhole size was set to either $700\ \mu\text{m}$ or $1000\ \mu\text{m}$, not $450\ \mu\text{m}$. Additionally, the $f/\#$ of CL was typically set between ~ 2.8 and ~ 4.0 for these experiments.

As with the 180° -backscattering geometry, angles θ_i and θ_s for the pseudo-reflection geometry could be tuned. In this case, however, the scattering angle changed with θ_i and θ_s . In particular, the value of θ_s was set when the focal point of the collection lens CL was initially positioned on the sample, prior to placing the red diode laser and corresponding mirror in the setup (before performing step (a) in the preceding setup procedure). This was done in the same way as described for the 180° -backscattering geometry. Furthermore, orienting the rotation-arm-mounted mirror and lens (IL) at an angle $\sim 5^\circ$ to $\sim 10^\circ$ beyond the axial ray of RB ensured that θ_i was $\sim 5^\circ$ to $\sim 10^\circ$ greater than θ_s . The exact value of θ_i was determined prior to completing step (c) of the pseudo-reflection geometry set up. That is, by rotating the sample and determining the rotation stage angle at which RB passed through the center of IL, the corresponding value of θ_i was deduced. Obviously, once θ_i was determined, the

sample was rotated back to its original position. Moreover, for the incident angles considered, the offset between θ_i and θ_s was large enough such that, for the angles typically considered in these experiments, the light reflected by the sample did not lie within the scattered light collection cone.

For a number of reasons, θ_s was typically within the limited range of $\sim 25^\circ$ to $\sim 65^\circ$ for these experiments. Firstly, due to the finite size of the optical elements (IL, CL, *etc.*), there was a lower limit on the angle at which the rotation arm could be oriented relative to the axial ray of the scattered light defined by CL. Secondly, at larger scattering angles, the $\sim 5^\circ$ to $\sim 10^\circ$ offset between θ_i and θ_s was insufficient to ensure that the reflected light did not fall within the scattered light collection cone. For measurements taken with θ_s greater than $\sim 70^\circ$, a ~ 30 GHz-shifted peak was observed on the anti-Stokes portion of the collected Brillouin spectra. This peak appeared to be independent of the probed sample material and, furthermore, it is not thought to be due to a Raman mode since the peak is positioned in the anti-Stokes portion of the spectrum. It is for these reasons that this spectral feature is taken to be a manifestation of a weak second beam mode that exists in the laser cavity. Fig. 3.14 shows a pair of example spectra.

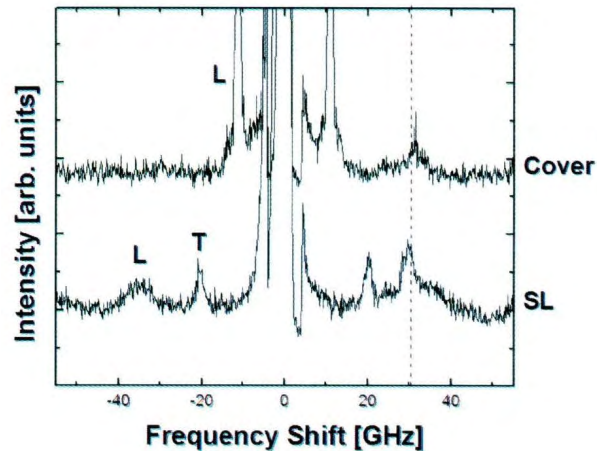


Figure 3.14: Pseudo-reflection geometry Brillouin light scattering spectra collected at a large angle of incidence. Spectra were taken from a supported multilayered π -Si sample (PSi2.20#8) and the cover of a clear plastic sample dish (possibly made of polystyrene). Both spectra were collected with $\theta_s = 70^\circ$ and $\theta_i = 75^\circ$. Labels T and L denote Brillouin peaks which were attributed to transverse and longitudinal bulk acoustic phonons. The vertical line indicates an additional peak which is thought to be due to a weak second mode in the cavity of the probing laser.

3.5.3 Tandem Fabry-Perot Interferometer

The six-pass tandem Fabry-Perot interferometer used in these experiments was manufactured by JRS Scientific Instruments. This system provides many advantages over a simple one-pass single Fabry-Perot interferometer.

A basic Fabry-Perot interferometer consists of an optical cavity made by two partially reflective parallel planar mirrors. Light entering the cavity undergoes multiple reflections and, due to interference effects, transmission through the etalon consists of a series of peaks, each corresponding to the frequency for which there is constructive interference. In particular, each transmission peak is due to a different order of interference. Assuming the light is normally incident on the cavity, constructive

interference occurs when the spacing between the mirrors, L , is [13]

$$L = \frac{b\lambda_b}{2} = \frac{bc}{2f_b}, \quad (3.6)$$

where b is an integer corresponding to the order of constructive interference, c is the speed of light in vacuum, λ_b is the wavelength of a given order, and f_b is the frequency of a given order. It was assumed that the cavity between the mirrors was a vacuum (or air); in general, the material properties of the etalon are accounted for in the speed of light within the material. The frequency of the transmitted light can be expressed as

$$f_b = \frac{bc}{2L} = bf_{FSR}, \quad (3.7)$$

where f_{FSR} is the difference between successive resonant frequencies of transmitted light, called the free-spectral-range (FSR). Thus, by scanning over the mirror spacing, the Fabry-Perot behaves as a tunable frequency filter [13, 14].

A schematic of a tandem Fabry-Perot interferometer is shown in Fig. 3.15. The setup is such that light entering the instrument passes through two separate Fabry-Perot optical cavities. The resulting output is equivalent to the superposition of the outputs from each individual Fabry-Perot interferometer. The spacings of the two optical cavities, L_1 and L_2 , are related by $L_2 = L_1 \cos \psi$ and, thus, have different values since $0 < \psi < \pi/2$. Due to the difference in spacing, the sequence of transmission frequencies is different for each cavity. With one mirror from each optical cavity mounted on the same movable base plate, the spacings of both cavities may be changed at the same time. Thus, by moving the base plate, the cavities are scanned

simultaneously and are fully synchronized. Further, the cavity spacings may be tuned such that a single transmission order of one cavity is frequency-matched with a different transmission order of the other. Due to the superposition of the outputs from both cavities, only the frequencies corresponding to the frequency-matched orders will be transmitted. Consequently, the advantages of the tandem Fabry-Perot interferometer are an increase in transmission contrast and the elimination of ambiguities due to the overlapping of transmission orders [14].

For the JRS Scientific Instruments TFP-1 six-pass tandem Fabry-Perot interferometer used in the current study, the internal optics were setup such that the collected scattered light made three passes through a synchronously-scanned tandem Fabry-Perot interferometer (*i.e.*, three passes through each individual Fabry-Perot interferometer) before being sent through an output pinhole to a photomultiplier tube. These multiple passes served to further increase the transmission intensity contrast of the system, which is crucial when trying to resolve weak spectral features in the collected scattered light spectrum [14]. Control electronics were used to simultaneously scan the mirror spacings as well as maintain the parallelism of the mirrors.

As mentioned in a previous paragraph, the scanned scattered light was passed through an output pinhole (700 μm for the 180° -backscattering geometry measurements; 1000 μm or 1300 μm for the pseudo-reflection geometry measurements) and impinged on a photomultiplier tube. As the tandem Fabry-Perot scanned over the scattered light frequencies, the deduced photon counts were sent to a computer where

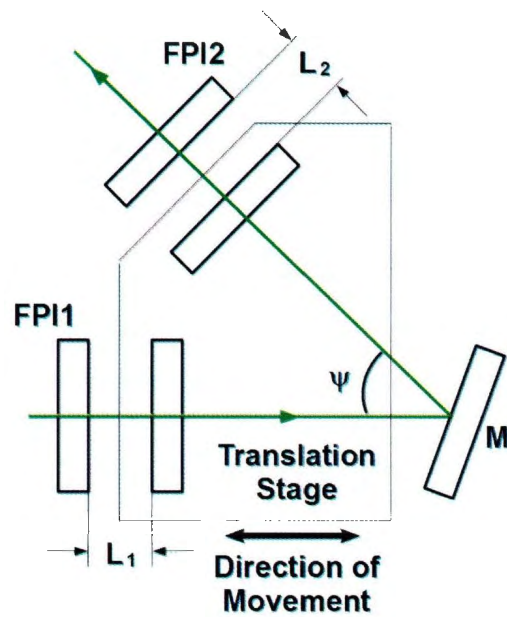


Figure 3.15: A tandem Fabry-Perot interferometer. The light passes through one Fabry-Perot optical cavity (FPI1), is reflected by a mirror (M), and then passes through a second Fabry-Perot optical cavity (FPI2). L_1 and L_2 are the cavity spacings of FPI1 and FPI2, respectively. Adapted from [14].

the data were displayed as an intensity versus frequency spectrum in the Ghost software package (University of Perugia).

3.5.4 Brillouin Scattering from a Liquid

In order to test the accuracy of the pseudo-reflection geometry Brillouin light scattering measurements, experiments were conducted on a number of known materials, including water. Fig. 3.16 depicts a schematic of the setup used to mount the water sample. A clear plastic sample dish (thought to be composed of polystyrene) had been partially filled with deionized water. The dish was closed and sealed at the edges using simple utility tape. As was the case for all samples, the water-filled container was then attached to the mounting post of the rotation stage in the optical setup using double-sided adhesive. Due to the relatively large weight of the sample, however, care had to be taken to ensure that the adhesive did not fail, causing the plastic container to fall from the mount during data collection. One should note that the utility tape was sufficient to prevent any noticeable amount water from leaking out of the covered dish (which was held at 90°).

With the water contained in the plastic sample dish, the resulting water-plastic interface was approximately planar and, hence, could be probed at a range of θ_i and θ_s values using the Brillouin setup. Focusing the probing light on the first water-plastic interface, the experiments proceeded in a fashion similar to that described above. In this case, however, care had to be taken when focusing on the sample as there were

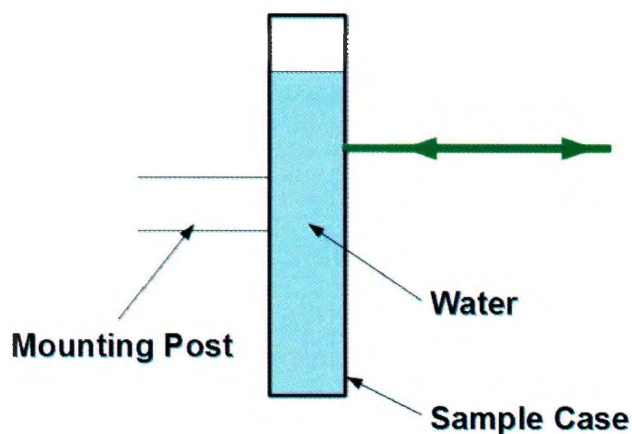


Figure 3.16: Sample mount used to probe water.

a number of material interfaces that could be accessed by the probing optics (*i.e.*, the air-plastic interface, the plastic-water interface, the water-plastic interface, and the plastic-air interface). In particular, two concentric beam spots were seen on the interferometer pinhole, corresponding to scattering from the first air-plastic interface and the plastic-water interface. Moving the focal point of the collection lens toward the sample, minimizing the size of the second focus spot, ensured that the probing light was focused at the water-plastic interface. Focusing the beam on the interface was crucial when setting up a pseudo-reflection geometry since the presence of the focused spot in the plane of the pinhole was a clear indication that the focal points of IL and CL were approximately coincident in the sample (see Fig. 3.13). In turn, the scattering volume contained a portion of water as well as a portion of the plastic case. Consequently, the collected Brillouin spectra contained peaks due to scattering from

acoustic waves in the water and the casing (see Appendix C). The data attributed to the case was not analyzed, however, since the exact composition of the plastic was unknown (it was assumed to be composed of polystyrene).

3.5.5 Analysis of Brillouin Spectra

Figure 3.17 shows a sample Brillouin spectrum collected from water. In general, the collected light spectra contained a series of peaks due to Stokes and anti-Stokes scattering from acoustic phonons set symmetrical about a very intense center peak set to a frequency shift of zero. As mentioned above, a shutter system was used in conjunction with a reference beam in order to prevent saturation of the photomultiplier tube when scanning over the spectral region corresponding to the elastically scattered light. In turn, the central peak is not due to elastically scattered light from the sample: it is due to the reference beam. While this center peak stems from input from the reference beam, throughout this work it is typically referred to as the elastically scattered light peak as the reference light is of equal frequency to that of the elastically scattered light. Consequently, the frequency shifts of the observed Brillouin peaks correspond to the frequency of the probed phonons.

In order to determine the exact frequency shift as well as the full-width-at-half-maximum of the observed peaks, the data were fit to mathematical functions using the Origin software package (Origin Labs). In particular, the Brillouin peaks were usually reasonably approximated by a Lorentzian function (see Fig. 3.18(a)). That

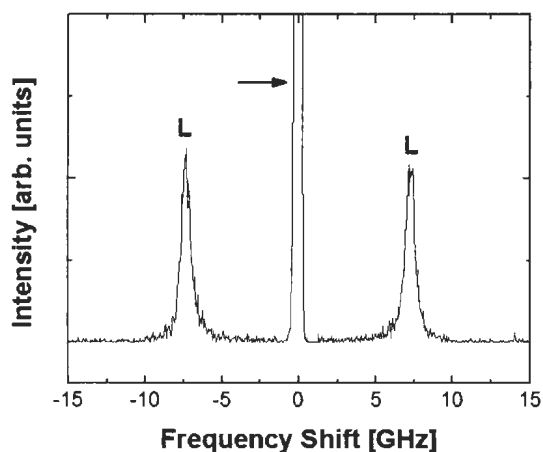


Figure 3.17: An example of a collected Brillouin light scattering spectrum. Specifically, the spectrum was collected from water using a 180° -backscattering geometry at $\theta_i = 7^\circ$. L denotes the Brillouin peak due to the bulk longitudinal acoustic wave, while the horizontal arrow indicates the peak due to reference beam.

is, provided the main contribution to the observed lineshapes is due to optical attenuation of the probing light or acoustic attenuation of the probed acoustic wave (not instrumental broadening or broadening due to the finite size of the collection optics [15]), the Brillouin peaks observed from either liquids or solids typically behave as Lorentzian functions [16–18]. For the elastically scattered light peak, on the other hand, the main contribution to the line shape was due to broadening caused by the interferometer and, in the case of the six-pass tandem Fabry-Perot interferometer, the observed peak could be approximated by a Lorentzian function raised to the power 6 [19] (see Fig. 3.18(b)). That is, instrumental broadening due to the interferometer optics was much greater than the linewidth of the reference beam (~ 10 MHz), so the collected center peak gives an indication of the resolution of the system.

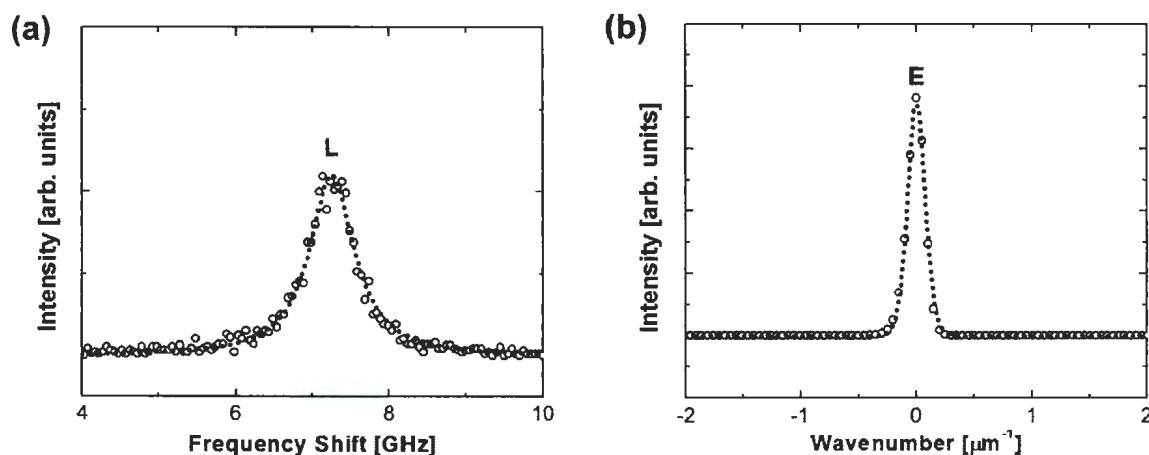


Figure 3.18: Examples of (a) a Brillouin peak and (b) a center peak due to the reference beam. The Brillouin peak (denoted by L), corresponding to the anti-Stokes component shown in Fig. 3.17, was fitted to a Lorentzian function. The corresponding center peak (denoted by E) was fitted to a Lorentzian raised to the power 6. Empty symbols: experimental data; dotted curves: mathematical fits.

One of two methods were used to deduce the frequency of a probed phonon:

(a) both the Stokes and anti-Stokes peaks were fitted and the resulting shifts were averaged or (b) the Stokes and anti-Stokes data were overlapped (taking into account any small frequency offset in the elastic scattering peak) and the resulting composite spectrum was fitted to a Lorentzian function. For most of the experiments conducted in the current work, the former method was used.

3.6 Determination of the Longitudinal and Transverse Bulk Acoustic Phonon Velocities of a Single-Layer Film

In order to determine the constituent layer sound velocities of the π -Si SLs, single-layer films of corresponding porosities were characterized. To facilitate this, near-normal incidence 180° -backscattering Brillouin measurements were taken from the films. With the refractive index deduced using the Bruggeman effective medium model together with the gravimetrically-obtained porosity value as outlined above, the longitudinal and transverse bulk acoustic phonon velocities could be determined from the frequency of the probed phonons. That is, combining Eqs. (2.65) and (2.66) with $|\mathbf{K}_{i\parallel}| = |\mathbf{K}_{s\parallel}| = (2\pi n/\lambda_o)\sin\Theta_i$ and $|\mathbf{K}_{i\perp}| = |\mathbf{K}_{s\perp}| = (2\pi n/\lambda_o)\cos\Theta_i$, the phonon velocities were given by

$$V = \frac{\nu\lambda_o}{2n(\lambda_o)}. \quad (3.8)$$

where ν is the bulk mode frequency (either transverse (T) or longitudinal (L)) deduced from the Brillouin spectrum. The resulting phonon velocities are for phonons directed approximately along the sample surface normal. Table 3.3 shows the phonon velocities for single-layer films made using a 1:1 (49% wt. HF: 98% wt. ethanol) electrolyte. The stated values are statistical averages of measurements taken from two series of films; each series corresponded to a given set of etch conditions. Furthermore, the series of samples characterized using Brillouin spectroscopy were a different set from those used to obtain the porosity (recall that the gravimetric method used to deduce ζ

Table 3.3: Bulk transverse phonon velocity, V_T , and bulk longitudinal phonon velocity, V_L , for single-layer π -Si films made using a 1:1 (49% wt. HF: 98% wt. ethanol) by volume electrolyte.

Current	V_T	V_L
(mA)	(km/s)	(km/s)
230	2.7 ± 0.4	4.6 ± 0.4
142	2.7 ± 0.2	4.8 ± 0.3

destroyed the π -Si film). One should note that an alternative method for determining both the refractive index and phonon velocities, using a pseudo-reflection Brillouin scattering geometry, will be outlined in a proceeding section.

3.7 Oblique Angle Reflectance Setup

To help gain insight into the optical properties of the SL samples along oblique angles to the modulation axis, oblique angle reflectance measurements were taken. The experimental setup used was similar to that described in [20]. Figure 3.19 shows a schematic of the setup. The ~ 532 nm laser beam was first passed through a filter (F) which reduced the beam power to < 10 mW. The beam was then directed through a polarizer (POL), oriented to transmit either horizontally or vertically polarized light (note: a small portion of the beam that passes through the half-wave plate is vertically polarized). A 15 cm lens (L) served to focus the light onto the sample (S). The sample was mounted on a rotation stage and, thus, the angle of incidence of the green beam

may be tuned by rotating S. Furthermore, the normal incidence reference angle was found by rotating the sample until the back-reflection of the beam was observed on the focusing lens. Using a power meter (PM) consisting of a silicon photodiode, the reflectance versus incidence angle for both p- and s- polarized light was investigated. That is, when illuminated with the laser beam, the photodiode produced a signal proportional to the power of the probed light and the angular-dependent reflectance, $R_{ob}(\theta)$, is given by

$$R_{ob}(\theta) = \frac{\varphi(\theta)}{\varphi_{in}}, \quad (3.9)$$

where $\varphi(\theta)$ is the power meter reading at reflection angle θ and φ_{in} is the power meter reading for the incident light, measured by placing the power meter in front of the focusing lens. One should note that the power meter did not rotate concentrically about the sample rotation stage and, in general, the distance between the silicon photodiode and the sample was not constant. This is not crucial, however, as the photodiode measured power, not intensity. Moreover, care was taken to ensure that the measured reflected beam spot did not “overflow” the silicon photodiode.

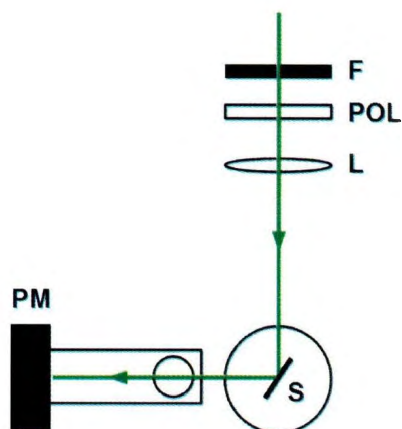


Figure 3.19: Experimental setup to measure oblique angle reflectance. F - filter, L - lens, POL - polarizer, S - sample. PM - power meter.

3.8 Comments on Each Study

3.8.1 Observation of Hypersonic Phononic Crystal Effects in Porous Silicon Superlattices

In this early study of π -Si SLs, the constituent layer parameters were not well established. To account for the sample-to-sample variation, the films were separated into two groups based on the time of fabrication (*i.e.*, samples made earlier in the study were in one; later samples in the other). In turn, slightly different constituent parameters were applied to each series of samples. In particular, the etch rates corresponding to etch currents I_{high} and I_{low} were ~ 120 nm/s and ~ 86 nm/s, respectively, for the first series and ~ 150 nm/s and ~ 100 nm/s, respectively, for the second series. With further experiments conducted on single-layer films after this

study concluded, however, the corresponding statistically-analyzed sample parameters were better understood [21] and, thus, throughout the later work, a single set of constituent parameters were applied to all SL films (see Tables 3.2 and 3.3). Additionally, the sample area used to calculate the etch current densities J_j from I_j was slightly different from that stated in the preceding discussion (*i.e.*, $1.47 \pm 0.02 \text{ cm}^2$).

3.8.2 Probing Near-Normally Propagating Bulk Acoustic Waves using Pseudo-Reflection Geometry Brillouin Spectroscopy

In this study, a methodology was developed to deduce the refractive index and sound velocities of a homogeneous material using Brillouin spectroscopy. The technique was validated through measurements on fused quartz, gallium phosphide, water, and porous silicon. Of particular note is that the obtained sample parameters were compared to literature values that had been obtained using a variety of experimental techniques (*e.g.*, the literature values for the sound velocities and refractive index of gallium phosphide were determined using ultrasonic measurements and spectroscopic ellipsometry, respectively). With this in mind, material-to-material variations in the difference between the current and literature values could be due, in part, to differences in the accuracy of the experimental measurements utilized to obtain the literature values.

For each of the collected spectra, analysis of the Brillouin peaks was done by overlapping the Stokes and anti-Stokes data and then fitting Lorentzian functions to

the resulting composite spectra. This is the only study in which this analysis method was used.

3.8.3 Brillouin Scattering from Porous Silicon-Based Optical Bragg Mirrors

This follow-up study on π -Si SLs reported results obtained through both 180°-backscattering geometry and pseudo-reflection geometry Brillouin scattering as well as broadband optical reflectance measurements. Furthermore, the Brillouin data reported in the earlier study were also included. In particular, all of the old data were re-analyzed, taking into account the more current values of the constituent parameters (see Table 3.2 and 3.3). Again, the sample area used to calculate J_j from I_j was slightly different from the final value stated here.

Many of the studied samples exhibited an optical Bragg peak in the visible spectral range. In particular, the peak reflectance ranged from $\sim 30\%$ to $\sim 75\%$ (see Appendix B). Previous studies have reported π -Si superlattices which had visible-range optical Bragg peaks with near 100% reflectance [6]. The relatively low reflectance of the current samples could be an artefact of interface roughness between the constituent layers [22]. By optimizing the etch process (through adjustment of etch parameters such as temperature and electrolyte composition) the interface roughness may be reduced.

Some of the observed optical Bragg peaks were not “sharp”, exhibiting a gradual change in reflectance over the peak feature or, in some cases, slight dips in reflectance near the center of the peak. Similar features have been reported in previous studies [6] and could be an artefact of interference effects resulting from the finite thickness of the films.

3.8.4 Oblique Acoustic Phonon Propagation in Porous Silicon Superlattices

This is the only study in this thesis conducted on SLs made from 1:1:1 (water: 49% wt. HF: 98% wt. ethanol) electrolyte. While corresponding single-layer films were not studied, estimates of the SL constituent layer parameters were deduced from etch rate versus current density and porosity versus current density data given in [2].

As part of the study, the pores of the SLs were filled with ethanol in order to determine its effect on the corresponding normal-incidence optical reflectance spectra. This was done by collecting reflectance spectra while the SLs were immersed in 98% wt. ethanol. Once the ethanol had evaporated, subsequently collected spectra were quantitatively the same as those collected before the SLs were immersed in ethanol, suggesting that the ethanol had no noticeable permanent effect on the samples.

Chapter 3 References

- [1] V. Lehmann. *Electrochemistry of Silicon*. (WILEY-VCH, Weinheim, 2002), p. 171-174.
- [2] L. Pavesi. Riv. Nuovo Cimento **20**, 1 (1997).
- [3] S. Billat, M. Thönissen, R. Arens-Fischer, M.G. Berger, M. Kruger, and H. Lüth. Thin Solid Films **297**, 22 (1997).
- [4] V. Lehmann. *Electrochemistry of Silicon*. (WILEY-VCH, Weinheim, 2002), p. 54-56.
- [5] A. M. Polomska. *Elastic properties of porous silicon superlattices*. Ph.D. thesis. Memorial University of Newfoundland (2010).
- [6] C. Vinegoni and M. Cazzanelli and L. Pavesi. Porous Silicon Microcavities. In *Silicon-Based Materials and Devices, Vol. 2*, edited by H.S. Nalwa (Academic Press, California, 2001), p.123-192.
- [7] J. Von Behren, L Tsybeskov, and P. M. Fauchet. Mat. Res. Soc. Symp. Proc. **358**, 333 (1995).

- [8] V. Lehmann. *Electrochemistry of Silicon*. (WILEY-VCH, Weinheim, 2002), p. 108.
- [9] C. Pickering, M. L. Beales, D. J. Robbins, D. J. Pearson, and R. Greef. *J. Phys. C* **17**, 6535 (1984).
- [10] J. Geist, Silicon (Si) Revisited (1.1-3.1 eV). In *Handbook of Optical Constants of Solids III*, edited by E. D. Palik. (Academic Press, San Diego, 1998), p. 519-531.
- [11] Thor Labs. Retrieved from the internet on 5 June, 2012. Webpage: http://www.thorlabs.com/NewGroupPage9.cfm?ObjectGroup_ID=139.
- [12] D. E. Aspnes and A. A. Studna, *Phys. Rev. B* **27**, 985 (1983).
- [13] A. Yariv and P. Yeh. *Photonics: Optical Electronics in Modern Communications*. (Oxford University Press, New York, 2007), p. 160-172.
- [14] J. R. Sandercock. *Tandem Fabry-Perot Interferometer TFP-1 Operator Manual*. JRS Scientific Instruments, (Switzerland, 2001).
- [15] W. F. Oliver, C. A. Herbst, S. M. Lindsay, and G. H. Wolf, *Rev. Sci. Instrum.* **63**, 1884 (1992).
- [16] J. R. Sandercock, *Phys. Rev. Lett.* **28**, 237 (1972).
- [17] J. R. Sandercock, *Phys. Rev. Lett.* **29**, 1735 (1972).
- [18] A. S. Pine, *Phys. Rev.* **185**, 1187 (1969).

- [19] C. Gigault and J. R. Dutcher, *Appl. Opt.* **37**, 3318 (1998).
- [20] J. Peckham and G. T. Andrews, *Thin Solid Films* **520**, 2526 (2012).
- [21] A. M. Polomska-Harlick and G. T. Andrews, *J. Phys. D: Appl. Phys.* **45**, 075302 (2012).
- [22] P.J. Reece, G. Lerondel, J. Mulder, W.H. Zheng, and M. Gal, *Phys. Status Solidi A* **197**, 321 (2003).

Chapter 4

Observation of Hypersonic Phononic Crystal

Effects in Porous Silicon Superlattices

Reproduced with permission from L.C. Parsons and G.T. Andrews, *Appl. Phys. Lett.* 95, 241909 (2009). Copyright 2009, American Institute of Physics.

4.1 Abstract

Brillouin light scattering experiments were carried out on porous silicon superlattices with modulation wavelengths in the range 37 nm to 167 nm. Phonon frequencies deduced from the Brillouin spectra show good agreement with those obtained from an elastic continuum model for a system with one-dimensional periodicity. Evidence for the existence of a hypersonic phononic band gap and zone-folded longitudinal acoustic phonons is reported.

4.2 Introduction

It is well known that the introduction of artificial spatial periodicity in the elastic properties of a materials system results in Brillouin zone-folding. Such folding is often accompanied by the appearance of band gaps in the phonon frequency spectrum and thus materials systems that exhibit this phenomenon are promising candidates for phononic crystals. Porous silicon (π -Si) is especially interesting in this regard since its elastic properties can be varied over nanometer length scales and because it can be readily integrated into existing silicon technologies.

In this letter, the results of Brillouin scattering experiments on π -Si superlattices (SLs) are reported. Good agreement is obtained between measured phonon frequencies and those calculated from a one-dimensional elastic continuum model. Clear evidence for the existence of an acoustic band gap and for zone-folding of longitudinal acoustic phonons is presented.

4.3 Experimental Details

Two sets of π -Si SLs and associated single layer films were synthesized by anodization of p^+ -type (100)-oriented crystalline silicon (5-20 $m\Omega\cdot\text{cm}$) in an electrolyte composed of 1 (49% HF) : 1 ($\text{C}_2\text{H}_5\text{OH}$). Each set was made using a different supply of HF with one solution yielding single layer films with gravimetrically-determined porosities of 0.59 ($J=149 \text{ mA/cm}^2$) and 0.52 ($J=101 \text{ mA/cm}^2$), while the other re-

sulted in films with porosities of 0.56 ($J=149 \text{ mA/cm}^2$) and 0.46 ($J=101 \text{ mA/cm}^2$). The difference in film porosity for the same applied current density is ascribed to slight differences in HF concentration in the two solutions. The single layer films were $\sim 5 \mu\text{m}$ thick. SLs with a binary periodic variation in porosity were formed by alternating the current density between the above values. Etching times were chosen so that the constituent layer thicknesses, d_1 and d_2 , were nearly equal (see Fig. 4.1(a)). SLs with modulation wavelengths of $D = d_1 + d_2$ from 37 nm to 167 nm were made for the Brillouin experiments. The porosities, refractive indices, and elastic properties of the SL constituent layers were taken to be the same as those of single layer films formed under identical conditions. It is noted that images like that of Fig. 4.1(a) were not obtained for SLs with $D < 500 \text{ nm}$. Indirect evidence of prescribed SL formation, however, was provided by measurements of overall SL film thickness ($\sim 5 \mu\text{m}$) which was within 10% of the value calculated using known etch parameters.

Brillouin scattering experiments were carried out in air at room temperature using a backscattering geometry (see Fig. 4.1 (b)). Incident light of wavelength $\lambda_i = 532 \text{ nm}$ at a power of $\sim 50 \text{ mW}$ was provided by a Nd:YVO₄ laser. The scattered light was collected with f/2.8 or f/4.0 optics, with the latter being used to prevent light specularly reflected from the sample from impinging on the active lens aperture when collecting spectra at very small incident angles. A tandem Fabry-Perot interferometer was used to frequency-analyze the scattered light.

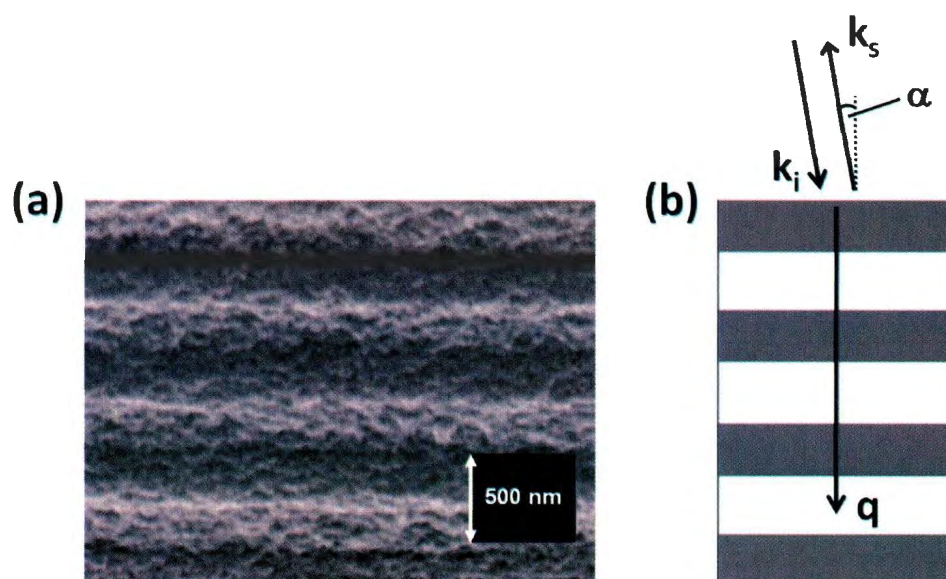


Figure 4.1: (a) Cross-sectional scanning electron micrograph of a $D = 500$ nm superlattice (SL). The bright (dark) regions correspond to layers with a porosity of 0.56 (0.46). (b) Scattering geometry. The wavevectors of the probed phonon and the incident (scattered) light are \mathbf{q} and \mathbf{k}_i (\mathbf{k}_s), respectively.

Brillouin spectra were collected from the single layer films in order to obtain the bulk acoustic mode velocities of the corresponding (*i.e.*, same porosity) SL constituent layers. These were required, together with the refractive indices of the single layer films, for the calculations described below. The bulk phonon velocities were determined from spectra collected at $5^\circ \leq \alpha \leq 10^\circ$. This corresponds to internal angles between 2° and 4° and hence these velocities were taken as those of phonons propagating in a direction perpendicular to the film surface. The refractive index of each single layer film was obtained using the gravimetrically-determined porosity and the two-component Bruggeman effective medium equation [1]. These values, along with film porosities, are given in Table 4.1. The lack of a clear trend in velocity with increasing porosity may be due to the influence of morphology, a second parameter upon which the acoustic velocities in π -Si are known to strongly depend [2].

SL spectra were collected at $5^\circ \leq \alpha \leq 8^\circ$, yielding, by Snell's law, an internal angle range of 2° to 4° . The probed phonon thus travelled in a direction that is very nearly perpendicular to the plane of the constituent layers. A series of Brillouin spectra collected under these conditions is shown in Fig. 4.2. For some of the SLs, spectra were also collected at higher α to check the dependence of peak frequency shift on incident angle. The shifts of all peaks observed at small α were found to be essentially independent of incident angle.

Table 4.1: Porosity, refractive index and bulk acoustic phonon velocities for single layer porous silicon films.

Set #	Porosity	Refractive Index	V_T (km/s)	V_L (km/s)
1	0.59 ± 0.02	2.1 ± 0.1	2.1 ± 0.1	4.3 ± 0.2
	0.52 ± 0.03	2.4 ± 0.1	2.8 ± 0.2	4.6 ± 0.2
2	0.56 ± 0.02	2.2 ± 0.1	2.3 ± 0.2	4.2 ± 0.2
	0.46 ± 0.02	2.6 ± 0.2	2.7 ± 0.3	4.4 ± 0.3

4.4 Theory

In a Brillouin scattering experiment conducted using a backscattering geometry, the magnitude of the probed phonon wavevector (either transverse or longitudinal) is

$$q = 2\kappa, \quad (4.1)$$

where κ , for a system with a square-wave spatial periodicity in refractive index, is the photonic Bloch wavevector given by [3]

$$\kappa = \frac{1}{D} \cos^{-1} \left[\cos(k_i n_1 d_1) \cos(k_i n_2 d_2) - \frac{1}{2} \left(\frac{n_1}{n_2} + \frac{n_2}{n_1} \right) \sin(k_i n_2 d_2) \sin(k_i n_1 d_1) \right]. \quad (4.2)$$

Here, n_1 and n_2 are the known constituent layer refractive indices and $k_i = 2\pi/\lambda_i$. For the 0.59/0.52 and the 0.56/0.46 SLs, Eq. 4.1 yields $q \approx 53 \mu\text{m}^{-1}$ and $q \approx 56 \mu\text{m}^{-1}$, respectively.

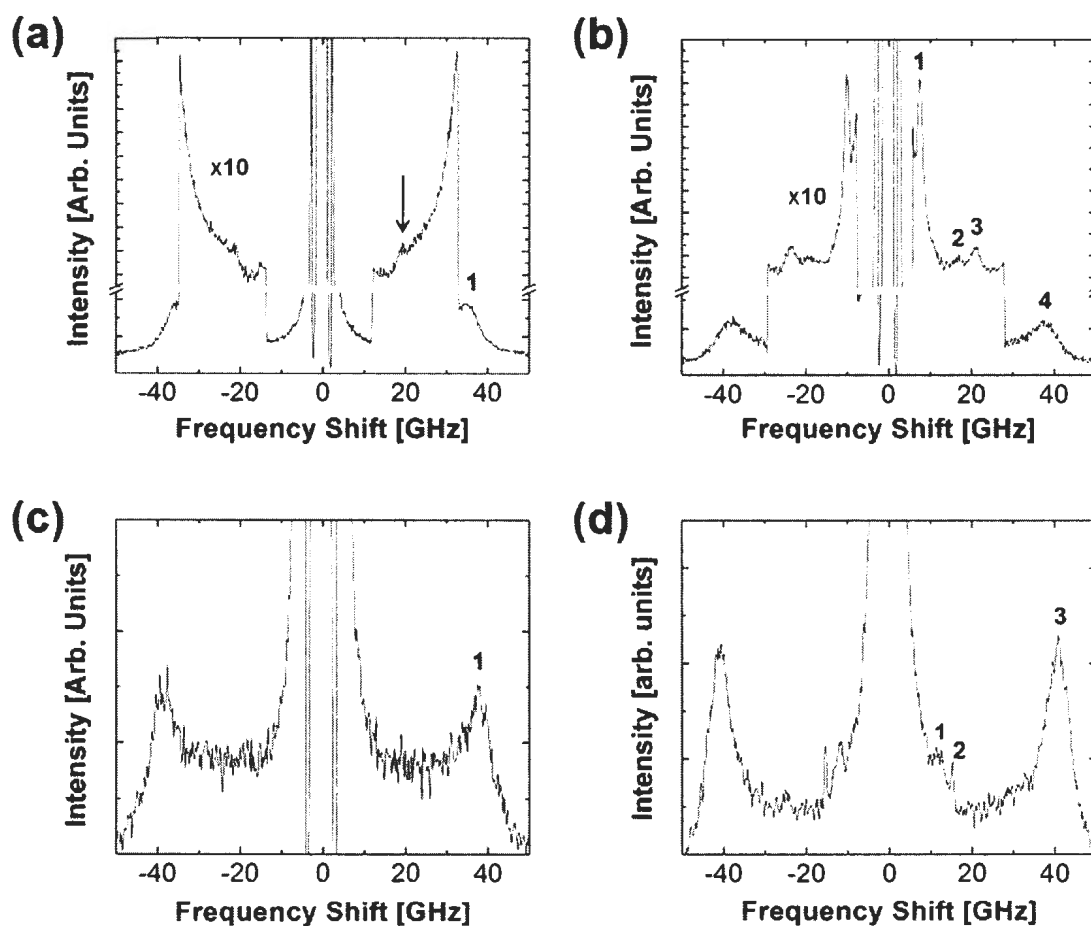


Figure 4.2: Spectra collected from (a) a $D = 61$ nm 0.59/0.52 superlattice, (b) a $D = 98$ nm 0.59/0.52 superlattice, (c) a $D = 123$ nm 0.59/0.52 superlattice, and (d) a $D = 167$ nm 0.56/0.46 superlattice (smoothed using 3-point averaging). The arrow indicates a weak feature that was difficult to fit to a Lorentzian and, hence, has a large uncertainty in frequency shift. This and similar features in other spectra appear in Fig. 4.3 and are indicated by large frequency-axis error bars.

Due to the square-wave periodicity in the elastic properties, the phonon should behave as a phononic Bloch wave and therefore undergo zone-folding into the mini-Brillouin zone corresponding to D . The phonon then obeys the selection rule for zone-folding given by [3]

$$Q = q + \frac{2l\pi}{D} \quad (4.3)$$

where l is an integer, Q is the phononic Bloch wavevector, expressed as

$$Q = \frac{1}{D} \cos^{-1} \left[\cos \left(\frac{\Omega d_1}{V_1} \right) \cos \left(\frac{\Omega d_2}{V_2} \right) - \frac{1}{2} F \sin \left(\frac{\Omega d_1}{V_1} \right) \sin \left(\frac{\Omega d_2}{V_2} \right) \right], \quad (4.4)$$

and F is a sample parameter given by

$$F = \left(\frac{\rho(1 - \zeta_1) V_1}{\rho(1 - \zeta_2) V_2} + \frac{\rho(1 - \zeta_2) V_2}{\rho(1 - \zeta_1) V_1} \right). \quad (4.5)$$

In the above equations, Ω denotes the phonon frequency, V_1 and V_2 are the constituent layer phonon velocities of the given mode (transverse or longitudinal), ζ_1 and ζ_2 are the constituent layer porosities, and $\rho = 2330 \text{ kg/m}^3$ is the density of bulk crystalline silicon.

4.5 Results and Discussion

With the optical and elastic parameters of the constituent layers known, the theoretically expected dependence of the phonon frequency on D (for a given constituent layer thickness ratio) was obtained. This was done for each set of SLs by numerically

determining the values of frequency that satisfy Eq. 4.3 for given values of D . The resulting curves are shown in Fig. 4.3 along with experimental data obtained directly from the Brillouin spectra. The agreement between the data and the curves corresponding to the folded longitudinal acoustic (FLA) modes indicates that zone-folding of the longitudinal phonon has occurred. Moreover, comparison of Fig. 4.3(a) and Fig. 4.3(b) suggests that small differences in the constituent layer parameters manifest as observable changes in the behaviour of the FLA modes. It is noted that the relative uncertainty in D was estimated as the $\sim 10\%$ difference between measured SL film thickness and that calculated using etch rates, etch times, and number of current alternations. The error in measured phonon frequency was taken to be the standard error in the Lorentzian fits of the Brillouin peaks or, in the case of weak features, simply estimated directly from the spectra. There is also $\sim 10\%$ uncertainty in the calculated frequencies due to uncertainties in the measured single layer film porosities, refractive indices and acoustic velocities which serve as input for the SL model calculations.

Observation of Brillouin zone-folding suggests that these π -Si SLs may behave as hypersonic phononic crystals. In fact, the $D = 167$ nm 0.56/0.46 SL, which was probed near the edge of the 3rd phononic Brillouin zone ($qD \approx 3\pi$), contains a spectral peak doublet that is the manifestation of a hypersonic phononic band gap in the longitudinal bulk phonon frequency spectrum (see Fig. 4.2(d)). The two peaks (1 and 2), which were assigned to two adjacent FLA branches (see Fig. 4.3 (b)),

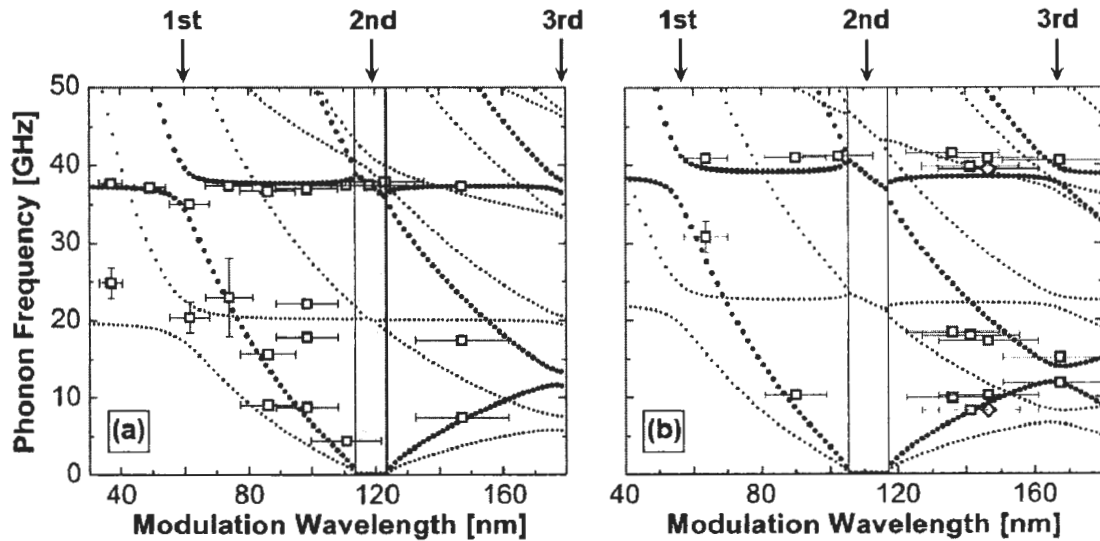


Figure 4.3: Phonon frequency versus modulation wavelength (D) for superlattices with constituent layer porosities of (a) 0.59 and 0.52 and (b) 0.56 and 0.46. Thick (thin) broken lines: calculated curves for the longitudinal (transverse) mode; shaded region: values of D for which the probing light is in a photonic band gap. Arrows mark the approximate values of D for which q coincides with the edges of the 1st, 2nd, and 3rd phononic Brillouin zones, respectively. Open symbols: experimental data; diamonds: duplicate $D = 147$ nm sample. The frequency scale on both plots is the same.

had frequency shifts of 11.8 GHz and 15.1 GHz, corresponding to a gap of width 3.3 GHz. This is in reasonable agreement with the calculated gap, which ranges over 11.8-13.9 GHz (2.1 GHz width). Also, a third peak (3) was observed and it corresponded to the edge of the second phononic band gap, which was expected at 37.5-39.5 GHz (2.0 GHz width). The absence of a peak doublet at these shifts may be due to phonon attenuation, an effect which is not accounted for in the current calculations. Attenuation may cause the expected gaps to shrink or even disappear altogether, resulting in a single spectral peak instead of the doublet predicted by the present model [4, 5].

From Fig. 4.3 it can also be seen that the data not attributed to the FLA modes agree only qualitatively with the calculations for the folded transverse acoustic (FTA) phonons. This may be because the corresponding spectral peaks are actually due to some unidentified mode rather than FTA phonons and thus the current theory might not apply. Transverse phonons, compared to longitudinal phonons, typically have a small scattering cross-section in backscattering geometry and hence it is possible that the FTA modes were not seen in the SL spectra.

In the region $2\pi \leq qD \leq 3\pi$ (between the 2nd and 3rd Brillouin zone edges) one can see that, with the exception of the $D = 167$ nm 0.56/0.46 SL, none of the data points show strong agreement with the second FLA curve. It is conceivable that this mode was too weak to be observed and the data at ~ 18 GHz, despite showing some agreement with the curve in question, may actually be due to some other mode.

Theoretically, the intensities of the zone-folded modes in a SL with perfectly planar layer interfaces vary dramatically from branch to branch and are expected to be dependent on qD (changing drastically near a zone edge) [3, 5]. The peak intensities are further affected by the presence of diffuse layer interfaces [6, 7] and optical-absorption [5], as may be the case with these π -Si SLs. These effects could lead to missing FLA orders which are only readily observed for certain values of qD .

Finally, according to Eq. 4.2, these SLs should be one-dimensional photonic crystals [8]. Preliminary results suggest that this is the case. In particular, SLs with values of D in or near the shaded region of Fig. 4.3 are green when viewed at normal incidence in ambient light, while those with D above or below this region appear red or violet, respectively. Work is ongoing to determine how the photonic nature of the SL affects the Brillouin spectrum.

4.6 Conclusions

In summary, Brillouin scattering experiments, coupled with calculations based on a one-dimensional elastic continuum model, have revealed the existence of zone-folded longitudinal acoustic phonons and a hypersonic phononic band gap in porous silicon superlattices.

This work was supported by NSERC and the Canada Foundation for Innovation. The authors would like to thank A. Polomska for helpful discussions.

Chapter 4 References

- [1] C. Pickering, M. L. Beales, D. J. Robbins, D. J. Pearson, and R. Greef, *J. Phys. C* **17**, 6535 (1984).
- [2] G.T. Andrews, A.M. Polomska, E. Vazsonyi, and J. Volk, *Phys. Status Solidi A* **204**, 1372 (2007).
- [3] J. He, B. Djafari-Rouhani, and J. Sapriel, *Phys. Rev. B* **37**, 4086 (1988).
- [4] G. N. Aliev, B. Goller, D. Kovalev, and P. A. Snow, *Phys. Status Solidi C*, **6**, 1670 (2009).
- [5] J. He, J. Sapriel, and R. Azoulay, *Phys. Rev. B* **40**, 1121 (1989).
- [6] C.E. Bottani and R. Caporali, *J. Phys. Condens. Matter* **9**, 5787 (1997).
- [7] C. Colvard, T.A. Gant, M.V. Klein, R. Merlin, R. Fischer, H. Morkoc, and A.C. Gossard, *Phys. Rev. B* **31**, 2080 (1985).
- [8] V. Agarwal and J. A. del Rio, *Appl. Phys. Lett.* **82**, 1512 (2003).

Chapter 5

Probing Near-Normally Propagating Bulk

Acoustic Waves using Pseudo-Reflection Geometry

Brillouin Spectroscopy

Reproduced from L. C. Parsons and G. T. Andrews, AIP Advances 2, 032157 (2012).

5.1 Abstract

Pseudo-reflection geometry Brillouin spectroscopy can be used to probe acoustic wave dispersion approximately along the surface normal of a material system while avoiding the difficulties associated with specularly reflected light encountered in an ideal reflection configuration. As an example of its application, we show analytically that it can be used to determine both the refractive index and bulk acoustic mode velocities of optically-isotropic non-metallic materials and confirm the utility of the

approach via a series of experiments on fused quartz, gallium phosphide, water, and porous silicon films.

5.2 Introduction

The bulk acoustic phonon band structure along the surface normal of thin films and periodic multilayered films can be quite complex, exhibiting multiple phonon bands resulting from the finite dimension of material in the former case [1] and the translational invariance in the latter [2, 3]. Furthermore, breaking the translational symmetry of a superlattice (either by introducing a buried defect within the structure or by terminating the superlattice at an interface with another material) may permit the existence of localized modes which lie within the forbidden frequency bands, or phononic band gaps, of the bulk phonon dispersion relation [3–5]. Additionally, more complicated multilayered systems have been shown to exhibit interesting acoustic phonon dispersion curves for propagation along the surface normal [6, 7].

Brillouin spectroscopy, an inelastic laser light scattering technique, has been used to study gigahertz-frequency acoustic phonons in a variety of films and multilayered structures. Traditionally, a near-normal incidence 180° -backscattering geometry is employed to probe phonons directed along the sample surface normal [1, 8–10]. Unfortunately, this geometry allows access to bulk phonons of only a single wavevector magnitude.

Recently, reflection geometry Brillouin scattering has been used to characterize the bulk acoustic phononic band structure of both thin polymer films [11, 12] and SiO₂-PMMA superlattices [13]. In particular, tuning the incident angle over a range of values allows a portion of the phonon dispersion curve along the sample surface normal to be mapped. There are, however, practical difficulties associated with implementing this technique, particularly when probing optically reflective samples. Specifically, specularly reflected light from the sample may swamp the desired scattered light signal. Moreover, dealing with this undesirable reflected light by blocking the corresponding portion of the collection aperture also results in loss of scattered light signal that may not be acceptable for samples with very small Brillouin scattering cross-sections.

In this paper, pseudo-reflection geometry Brillouin scattering, where the scattered light collection axis is slightly offset from the specularly-reflected light direction, will be presented. The primary advantage of this scattering geometry over an ideal reflection geometry is that it allows access to approximately the same range of probed acoustic wave (AW) wavevectors while avoiding the practical pitfalls that may arise when using an ideal reflection geometry. As an example, the relatively simple cases of scattering from homogeneous cubic and isotropic materials will be considered. By fitting the appropriate function to the resulting acoustic mode frequency versus angle data, both the refractive index and AW velocities for modes directed approximately along the normal are determined. Unlike previous Brillouin light scattering techniques

used to determine both the refractive index and AW velocities [14–21], the current method is not limited to probing transparent materials in a special configuration. In fact, a pseudo-reflection geometry can be used to characterize both transparent and absorbing optically-isotropic, non-metallic materials in bulk as well as supported and unsupported films. The accuracy of this technique was confirmed through measurements on fused quartz, GaP, water, and two non-transparent porous silicon films supported on silicon substrates.

5.3 Theory

5.3.1 Pseudo-Reflection Brillouin Scattering

In Brillouin scattering, conservation of momentum requires that the wavevector of the probed acoustic wave, \mathbf{q} , satisfy the relation

$$|\mathbf{q}| = |\mathbf{K}_s - \mathbf{K}_i|, \quad (5.1)$$

where \mathbf{K}_i and \mathbf{K}_s are the incident and scattered photon wavevectors inside the material, respectively [22]. In particular, $K_s \sim K_i = 2\pi n/\lambda_i$, where n is the refractive index of the probed optically-homogeneous material (outside the material, the refractive index is assumed to be 1) and λ_i is the wavelength of the incident light in vacuum.

Figure 5.1(a) illustrates a pseudo-reflection scattering geometry. In this case, the collected scattered light propagates at an angle which is offset slightly from that

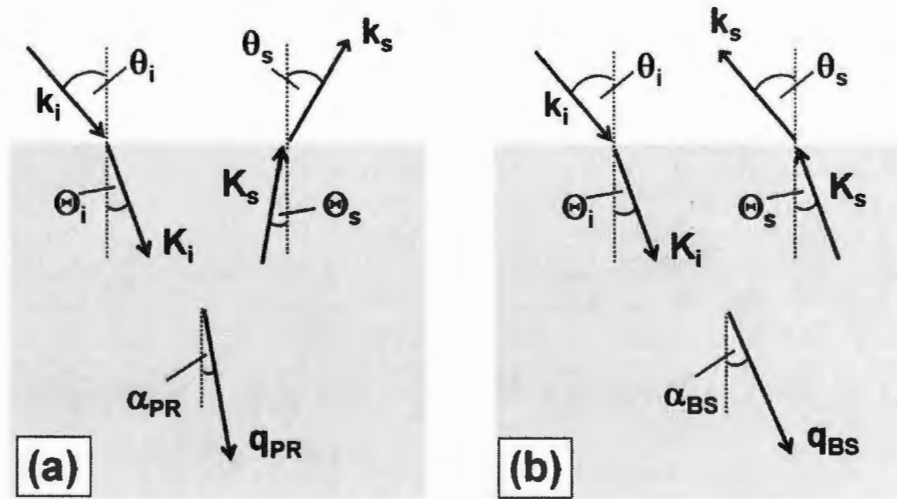


Figure 5.1: Brillouin scattering geometries: (a) pseudo-reflection and (b) 180°-backscattering. The wavevectors of the probed acoustic wave, external (internal) incident light, and external (internal) scattered light are \mathbf{q} , \mathbf{k}_i (\mathbf{K}_i), and \mathbf{k}_s (\mathbf{K}_s), respectively. The propagation directions of the acoustic wave, external (internal) incident light, and external (internal) scattered light are defined relative to the surface normal by angles α , θ_i (Θ_i), and θ_s (Θ_s), respectively. All angles are between 0 and $\pi/2$.

corresponding to the specularly reflected light (*i.e.*, $\theta_s - \theta_i \neq 0$, where θ_s and θ_i are, respectively, the angles that the scattered and incident light wavevectors make with the surface normal outside the sample). It follows from Eq. (5.1) that the components of the probed AW wavevector parallel and perpendicular to the sample surface are

$$q_{PR\parallel} = \frac{2\pi n}{\lambda_i} |\sin \Theta_i - \sin \Theta_s| = \frac{2\pi}{\lambda_i} |\sin \theta_i - \sin \theta_s| \quad (5.2a)$$

$$q_{PR\perp} = \frac{2\pi n}{\lambda_i} (\cos \Theta_i + \cos \Theta_s). \quad (5.2b)$$

Using the sum-to-product trigonometric identities for the sum of cosines and the difference in sines, Eq. (5.2) can be expressed as

$$q_{PR\parallel} = \frac{4\pi n}{\lambda_i} \cos \Theta_m \sin \Theta_d = \frac{4\pi}{\lambda_i} \cos \theta_m \sin \theta_d \quad (5.3a)$$

$$q_{PR\perp} = \frac{4\pi n}{\lambda_i} \cos \Theta_m \cos \Theta_d, \quad (5.3b)$$

where $\Theta_m = (\Theta_i + \Theta_s)/2$, $\Theta_d = |\Theta_i - \Theta_s|/2$, $\theta_m = (\theta_i + \theta_s)/2$, and $\theta_d = |\theta_i - \theta_s|/2$.

The magnitude of the acoustic wavevector is then

$$q_{PR} = \sqrt{(q_{PR\parallel})^2 + (q_{PR\perp})^2} = \frac{4\pi n}{\lambda_i} \cos \Theta_m. \quad (5.4)$$

Invoking Snell's Law, it can be seen that

$$n (\sin \Theta_i + \sin \Theta_s) = \sin \theta_i + \sin \theta_s \quad (5.5)$$

which, upon using the sum-to-product trigonometric identity for the sum of sines, can be rewritten as

$$\sin \Theta_m = \frac{1}{n} \left(\frac{\cos \theta_d}{\cos \Theta_d} \right) \sin \theta_m. \quad (5.6)$$

It then follows from Eqs. (5.4) and (5.6) that the magnitude of the AW wavevector is

$$q_{PR} = 2\sqrt{n^2 k_i^2 - k_{PR}^2}, \quad (5.7)$$

where $k_i = 2\pi/\lambda_i$ is the magnitude of the incident photon wavevector and k_{PR} is

$$k_{PR} = \frac{2\pi}{\lambda_i} \left(\frac{\cos \theta_d}{\cos \Theta_d} \right) \sin \theta_m. \quad (5.8)$$

The direction of AW propagation is defined by an angle α_{PR} relative to the sample surface normal given by

$$\alpha_{PR} = \tan^{-1} \left(\frac{q_{PR\parallel}}{q_{PR\perp}} \right) = \Theta_d. \quad (5.9)$$

Using Snell's Law to express Θ_d in terms of n , θ_m , and θ_d , the AW propagation direction can be rewritten as

$$\alpha_{PR} = \frac{1}{2} \left(\sin^{-1} \left(\frac{\sin \theta_i}{n} \right) - \sin^{-1} \left(\frac{\sin \theta_s}{n} \right) \right) > 0. \quad (5.10)$$

Without loss of generality, it was assumed that $\pi/2 \geq \theta_i \geq \theta_s \geq 0$. In order to determine how α_{PR} trends with θ_d , the partial derivative of α_{PR} with respect to θ_d is determined:

$$\frac{\partial \alpha_{PR}}{\partial \theta_d} = \frac{1}{2n} \left(\frac{\cos \theta_i}{\cos \Theta_i} + \frac{\cos \theta_s}{\cos \Theta_s} \right). \quad (5.11)$$

The right-hand side of the above expression is always positive for the range of angles considered and, therefore, α_{PR} increases with θ_d . Figure 5.2 shows the dependence of α_{PR} on θ_m and n for the cases of $\theta_d = 3^\circ$ and $\theta_d = 5^\circ$. As expected from Eq. (5.11), for any fixed values of θ_m and n , α_{PR} is larger for $\theta_d = 5^\circ$ than for $\theta_d = 3^\circ$. One should note that the range of physically possible θ_m values for $\theta_d = 5^\circ$ is smaller than that of $\theta_d = 3^\circ$ since both θ_i and θ_s lie between 0 and $\pi/2$. One can also see that for both values of θ_d , α_{PR} decreases as either n increases or $\theta_m \rightarrow (\pi/2 - \theta_d)$. Furthermore, $\alpha_{PR} = \theta_d$ at $n = 1$ for all values of θ_m . This is expected since in this case both the probed material and the external environment have the same refractive index and, thus, no refraction of the incident or scattered light occurs (*i.e.*, $\Theta_i = \theta_i$ and $\Theta_s = \theta_s$). Since $n \geq 1$ and $\theta_m \geq \Theta_m$, it follows from Eq. (5.3a) that

$$\Theta_d \leq \theta_d \quad (5.12)$$

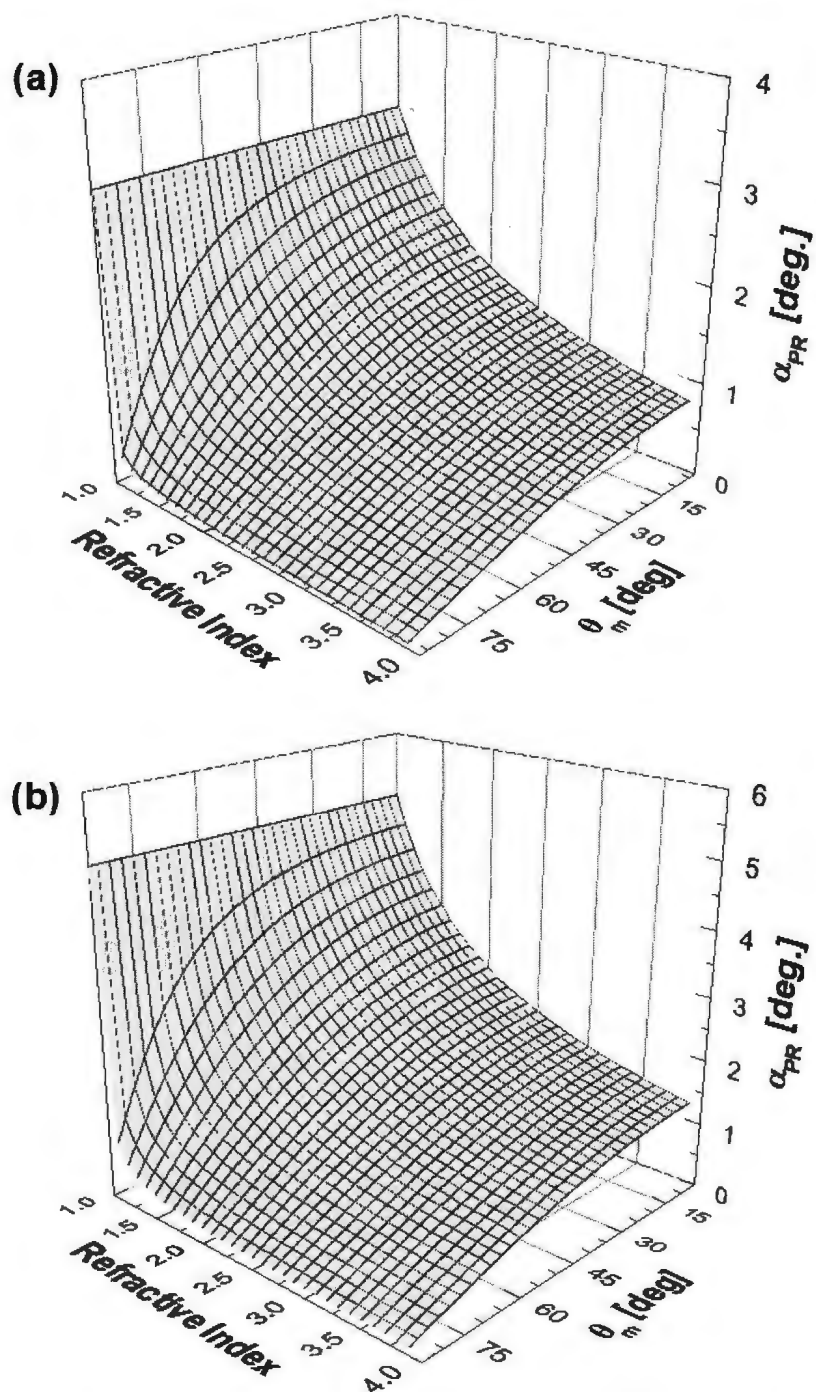


Figure 5.2: Dependence of α_{PR} on θ_m and refractive index for (a) $\theta_d = 3^\circ$ and (b) $\theta_d = 5^\circ$. Here, $\theta_d \leq \theta_m \leq (\pi/2 - \theta_d)$ ensures that both θ_i and θ_s lie between 0 and $\pi/2$.

with equality being realized when $n = 1$. Consequently, from Eq. (5.9) one can see that

$$\alpha_{PR} \leq \theta_d. \quad (5.13)$$

In the instance that θ_d is small, according to Eq. (5.12) $\cos \theta_d / \cos \Theta_d \approx 1$. Equations (5.7) and (5.13) then reveal that the resulting probed AW propagates approximately parallel/anti-parallel to the surface normal with a wavevector of magnitude

$$q_{PR} \approx 2\sqrt{n^2 k_i^2 - k_m^2}, \quad (5.14)$$

where $k_m = (2\pi/\lambda_i)\sin \theta_m$. One can see that ideal reflection geometry is realized for $\theta_d = 0$, where $k_{PR} = k_m$ [11].

Due to practical limitations such as the finite size of optical elements (*i.e.*, collection lens, mirrors), it may not be possible to access the full range of θ_m (*i.e.*, $\theta_d \leq \theta_m \leq (\pi/2 - \theta_d)$). In order to expand the range of probed AW wavevectors directed approximately along the surface normal, one can use a near-normal incidence 180°-backscattering geometry. In this case, the probed AW wavevector is $\approx q_{PR}$ at $\theta_m = 0$. For the backscattering geometry (see Fig. 5.1(b)), where $\theta_s = \theta_i$ (*i.e.*, $\Theta_s = \Theta_i$), it can be shown using Eq. (5.1) that the magnitude of the probed AW wavevector is

$$q_{BS} = \sqrt{(q_{BS\parallel})^2 + (q_{BS\perp})^2} = \frac{4\pi n}{\lambda_i}. \quad (5.15)$$

Furthermore, the AW propagates at an angle α_{BS} to the surface normal, given by

$$\alpha_{BS} = \tan^{-1} \left(\frac{q_{BS\parallel}}{q_{BS\perp}} \right) = \Theta_i. \quad (5.16)$$

This angle can be determined from θ_i using Snell's Law. Provided that θ_i is small, $\alpha_{BS} \approx \alpha_{PR} \approx 0$. Following from Eqs. 5.15 and 5.14, the corresponding \mathbf{q}_{BS} is equivalent to \mathbf{q}_{PR} for $\theta_m = 0$.

5.3.2 Scattering from an Elastically Homogeneous Material

For a homogeneous material, the angular frequency of an AW, Ω , is related to the wavevector magnitude, q , by

$$\Omega = 2\pi\nu = Vq. \quad (5.17)$$

where ν is the AW frequency and V is the magnitude of the AW velocity (transverse (T) or longitudinal (L)) [22]. Dispersion is assumed to be negligible and, thus, V for a given mode (T or L) is a constant. For probed AWs governed by Eq. (5.14), one then obtains

$$\nu \approx \frac{1}{\pi} V \sqrt{n^2 k_i^2 - k_m^2}. \quad (5.18)$$

Using the approximation $k_m \approx k_{PR}$ eliminates the θ_d - and n -dependence of the second term in the square-root and, thus, greatly simplifies the equation. Furthermore, the systematic error introduced by this approximation is relatively small (typically $< 1\%$), as will be shown below. It can be seen that an appropriate fit of Eq. (5.18) to experimentally-determined ν versus k_m data will yield the AW velocity along the surface normal as well as the refractive index.

This method is particularly useful for probing materials with cubic symmetry. With the refractive index and acoustic wave velocities determined along a well-defined

direction (*i.e.*, along the surface normal), in principle a portion of the AW slowness diagram could be mapped by using additional scattering geometries to access AWs propagating at oblique angles in the structure.

The preceding discussion assumed that the probed material was optically isotropic and, therefore, defined by a scalar dielectric tensor. The use of this technique, however, can be extended to lower symmetry systems provided the incident and scattered photon wavevectors can each be associated with a single dielectric constant for all angles accessed in the scattering plane. For instance, through special consideration of the polarization of the incident and scattered light as well as the orientation of the scattering plane relative to the crystal structure, this method has been used to obtain both the ordinary and extraordinary refractive indices of an uniaxial crystal [23].

5.3.3 Error Analysis

The systematic error resulting from the approximation $k_{PR} \approx k_m$ can be estimated by

$$\left| \frac{\Delta k_{PR_{sys}}}{k_{PR}} \right| = \left| \frac{k_{PR} - k_m}{k_{PR}} \right|. \quad (5.19)$$

Therefore, from the definitions of k_{PR} and k_m ,

$$\frac{\Delta k_{PR_{sys}}}{k_{PR}} = \left| 1 - \frac{\cos \Theta_d}{\cos \theta_d} \right| \approx \left| \frac{\Theta_d^2 - \theta_d^2}{2} \right|. \quad (5.20)$$

Since $\Theta_d \leq \theta_d$ and because it decreases as n increases, for fixed values of θ_m and θ_d , the systematic error is at a maximum when n is large. Consequently,

$$\left| \frac{k_{PR_{sys}}}{k_{PR}} \right|_{max} = \left| \frac{k_{PR_{sys}}}{k_{PR}} \right|_{n \rightarrow \infty} \approx \frac{\theta_d^2}{2} \quad (5.21)$$

and, therefore, the maximum percent systematic error due to the approximation is of the order of 1% for typical values of θ_d . Further, the minimum systematic error is 0, occurring when $n = 1$ (*i.e.*, $\Theta_d = \theta_d$).

The random experimental error in k_{PR} arises due to error in determining the external angles θ_i and θ_s and can be written as

$$\frac{\Delta k_{PR_{ran}}}{k_{PR}} = \frac{1}{k_{PR}} \left(\frac{\partial k_{PR}}{\partial \theta_d} \Delta \theta_d + \frac{\partial k_{PR}}{\partial \theta_m} \Delta \theta_m \right). \quad (5.22)$$

Note that $\Delta \theta_m = \Delta \theta_d = (\Delta \theta_i + \Delta \theta_s)$. Using Eqs. (5.9), (5.10), and (5.11) together with the appropriate trigonometric identities, it follows that

$$\frac{\Delta k_{PR_{ran}}}{k_{PR}} \approx \left(\frac{\cos \theta_i}{\sin \theta_m} + \frac{1}{n} \frac{\cos \theta_i}{\cos \Theta_i} \Theta_d \right) \Delta \theta_d \quad (5.23)$$

Since $\theta_d \geq \Theta_d$ is taken to be small, the small angle approximations for sine and cosine functions ($\sin \theta \sim \theta$ and $\cos \theta \sim 1$) were applied when deriving the above expression. As one can see, the random experimental error in k_{PR} depends on the refractive index of the probed material and, in general, cannot be quantified prior to analyzing the Brillouin light scattering data without obtaining the refractive index using an alternate method. In order to determine how this error trends with n , it is beneficial to analyze how Θ_d changes with n . From Eqs. (5.9) and (5.10), one can see

that

$$\frac{\partial \Theta_d}{\partial n} = -\frac{1}{2n^2} \left(\frac{\sin \theta_i}{\cos \Theta_i} - \frac{\sin \theta_s}{\cos \Theta_s} \right). \quad (5.24)$$

Since $\sin \theta_i \geq \sin \theta_s$ and $\cos \Theta_s \geq \cos \Theta_i$, the right-hand side of the above expression is negative and, hence, Θ_d decreases as n increases (as suggested in Fig. 5.2). Further, since Θ_i decreases from θ_i as n increases, $n \cos \Theta_i$ is at a minimum when $n = 1$. In turn, for fixed θ_m and θ_d , the random error given by Eq. (5.23) is at a maximum when $n = 1$ and may be written

$$\left| \frac{\Delta k_{PR_{ran}}}{k_{PR}} \right|_{max} = \left| \frac{\Delta k_{PR_{ran}}}{k_{PR}} \right|_{n=1} \approx \left(\frac{\cos \theta_i}{\sin \theta_m} + \theta_d \right) |\Delta \theta_d|. \quad (5.25)$$

As $n \rightarrow \infty$, the second term on the right-hand side of Eq. (5.23) goes to zero, and therefore for fixed values of θ_m and θ_d , the minimum random experimental error occurs when n is large:

$$\left| \frac{\Delta k_{PR_{ran}}}{k_{PR}} \right|_{min} = \left| \frac{\Delta k_{PR_{ran}}}{k_{PR}} \right|_{n \rightarrow \infty} \approx \frac{\cos \theta_i}{\sin \theta_m} |\Delta \theta_d|. \quad (5.26)$$

Since $|\Delta \theta_d| \sim \theta_d$, comparison between Eqs. (5.20) and (5.23) suggest that the random experimental error in k_{PR} is typically larger than the corresponding systematic error. In fact, the minimum random experimental error is typically only comparable to the maximum systematic error when $\theta_m \rightarrow (\pi/2 - \theta_d)$ (*i.e.*, at grazing angles). When probing a material with $n = 1.5$, for example, if $30^\circ \leq \theta_m \leq 70^\circ$ and $\theta_d = 5^\circ$, it follows from Eqs. (5.20) and (5.23) that the percent experimental error in k_{PR} ranges from $\sim 8.7\%$ to $\sim 1.5\%$ while the percent systematic error introduced by the simplifying approximation is $\sim 0.4\%$. Consequently, it is reasonable to approximate

k_{PR} with k_m . Note that here the uncertainty in $\Delta\theta_d$ was assumed to be 3° and that smaller values of $\Delta\theta_d$ would further reduce the random error.

Implicit in the above approximation of $k_{PR} \approx k_m$ is the assumption that the velocity of the probed AW corresponds to the value along the sample surface normal. Thus, there is a systematic error in V due to the fact that $\alpha_{PR} \neq 0$. In the case of elastically-isotropic materials, this error is zero. For cubic materials, however, this error must be considered and can be written as

$$\frac{\Delta V}{V} = \left| 1 - \frac{V(0)}{V(\alpha_{PR})} \right|. \quad (5.27)$$

where $V(0)$ corresponds to the AW velocity for propagation along the surface normal. It is difficult to quantify this error *a priori* without knowledge of the crystal orientation and the elastic properties of the probed material. By keeping θ_d small and, hence, minimizing α_{PR} , however, the error in V is typically quite small. As an example, propagation of AWs in the (001)-plane of a (100)-oriented cubic GaP sample, similar to those probed in the experiments discussed below, will be considered. There are three bulk acoustic modes present in a cubic crystal: the fast transverse (V_{FT}), the slow transverse (V_{ST}), and the longitudinal (V_L) modes. For propagation in the (001)-plane only V_{FT} is independent of angle and, in fact, $V_{FT} = V_{ST}(\alpha_{PR} = 0)$ (note: the surface normal coincides with the (100)-direction). Following from the results of Ref. [24], the dependence of the error in V_{ST} and V_L on α_{PR} given by Eq. (5.27) were calculated (see Fig. 5.3). While the percent errors in V_{ST} and V_L increase with angle, they are quite small and, in particular, they are both less than 1% for α_{PR} as large as

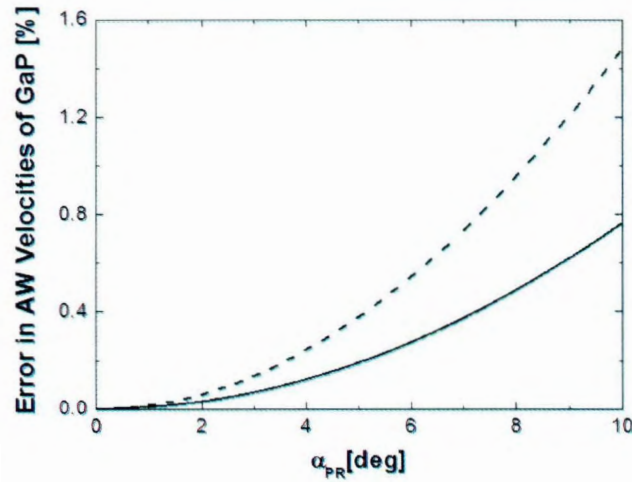


Figure 5.3: Dependence of error in the sound velocity on angle of propagation within the (001)-plane of GaP. The dashed (solid) curve corresponds to the calculated error in the velocity of the slow transverse (longitudinal) mode. Calculations were determined using equations (3.1), (3.2), and (3.3) in Ref. [24] together with the sample parameters therein. Since the velocity of the fast transverse mode is independent of propagation direction within this crystal plane, the expected error is zero.

7° . Further, since $V_{FT} = V_{ST}(0)$, the difference in V_{FT} and V_{ST} is less than 1% over this range of α_{PR} values. Thus, this technique is particularly useful for cubic crystals with relatively large refractive indices (*i.e.*, $n \sim 3$) since, as shown in Fig. 5.2, α_{PR} is very small (*i.e.*, $< 2^\circ$) for typical values of θ_d .

One should note that the systematic errors in k_{PR} and V stem from the fact that $\theta_d \neq 0$. If an ideal reflection geometry is used, $k_{PR} = k_m$ and, hence, Eq. (5.18) is exact.

5.4 Experimental Details

To validate the above method, Brillouin scattering experiments were carried out on fused quartz, (100)-oriented GaP, and deionized water. One should note that the refractive index and AW velocities of fused quartz are known, respectively, from previous studies conducted using minimum-deviation optical measurements [25] and 180°-backscattering Brillouin spectroscopy [26]. Further, the refractive index and AW velocities of GaP are known from spectroscopic ellipsometry [27] and ultrasonic measurements [28], respectively, while those of water have been previously obtained using Kramers-Kronig analysis of optical absorption/reflectance data [29] and ultrasonic measurements [30], respectively. Experiments were also done on two porous silicon films made from p^+ -type (100)-oriented crystalline silicon under conditions similar to those given in Ref. [10]. The films were $\sim 4.5 \mu\text{m}$ thick and had porosities of $(58 \pm 3)\%$ and $(50 \pm 4)\%$. It should be noted that these film porosities were obtained by statistical analysis of results taken from a series of samples made under the same conditions as those studied here (the gravimetric method used to obtain porosity resulted in the destruction of the films). Further, the effective refractive index of each film was deduced from the porosity by application of the two-component Bruggeman effective medium model [31]. Using the resulting refractive index values, the AW velocities were obtained in this laboratory through a previous 180°-backscattering Brillouin study conducted on a second series of samples made under the same conditions.

Brillouin scattering experiments were carried out in air at room temperature using both pseudo-reflection and 180°-backscattering geometries. Incident light of wavelength $\lambda_i = 532$ nm was provided by a Nd:YVO₄ laser. In the case of fused quartz and porous silicon, the incident beam power was reduced to ~ 50 mW while for GaP and water, the power was ~ 150 mW and ~ 25 mW, respectively. The deionized water sample was contained in a transparent plastic cell which had two thin, parallel planar sides. This cell was mounted to a rotation stage, allowing access to a range of incident angles. The solid samples were mounted to the same rotation stage, exposed to ambient air. Further, the GaP sample was oriented such that the plane of incidence was approximately parallel to the (001)-plane. For the pseudo-reflection geometry, incident light was focused on the sample using a lens of focal length 7.5 cm and scattered light was collected by a second 5 cm lens ($f/\# = 2.8$ or ~ 4.0). The angle of incidence, θ_i , ranged from 35° to 69°. To ensure that specularly reflected light did not enter the collection lens, θ_s was set 5° to 10° less than θ_i . The experimental uncertainties in θ_i and θ_s were estimated to be $\Delta\theta_i = 2^\circ$ and $\Delta\theta_s = 1^\circ$, respectively. For the backscattering geometry, the aforementioned 5 cm lens served to focus the incident light on the sample and also to collect scattered light. The backscattering spectra were collected at $\theta_i = \theta_s = 7^\circ$ ($\Delta\theta_s = \Delta\theta_i = 1^\circ$). Frequency analysis of the scattered light was done using a tandem Fabry-Perot interferometer.

Since $2.5^\circ \leq \theta_d \leq 5^\circ$ for the experiments reported here, the systematic error resulting from the simplifying approximation used in Eq. (5.14) is expected to be less

than 0.5% and is therefore neglected. With regard to the velocity values deduced for the cubic anisotropic (100)-oriented GaP sample, the systematic error is expected to be less than 1%, as shown in Fig. 5.3 (recall that $\alpha_{PR} \leq \theta_d$). Furthermore, while the porous silicon samples studied here have been shown to exhibit a slight cubic anisotropy in the elastic properties [32–34], the anisotropy factor is ≈ 1 (*i.e.*, less than that of GaP [24]). Hence, the systematic error in the AW velocities obtained for porous silicon is less than 1%.

Additionally, 180°-backscattering at $\theta_i = 7^\circ$ ($\alpha_{BS} \leq 7^\circ$) was taken to be equivalent to pseudo-reflection geometry at $\theta_m = 0$ since the probed AW propagates near the surface normal. While this additional assumption will not affect the results obtained from isotropic samples such as fused quartz and water, care must be taken when applying it to cubic GaP and porous silicon. Since n is expected to be greater than 2 for these samples, $\alpha_{BS} < 3^\circ$ and, as discussed above, the expected systematic error is very small. Hence, this assumption is reasonable.

5.5 Results and Discussion

Fig. 5.4 shows spectra collected from the fused quartz, (100)-oriented GaP, deionized water, and a 58% porous silicon film. Symmetrical peak doublets due to two different acoustic modes were observed in each solid sample, while only one set of peaks was observed from water.

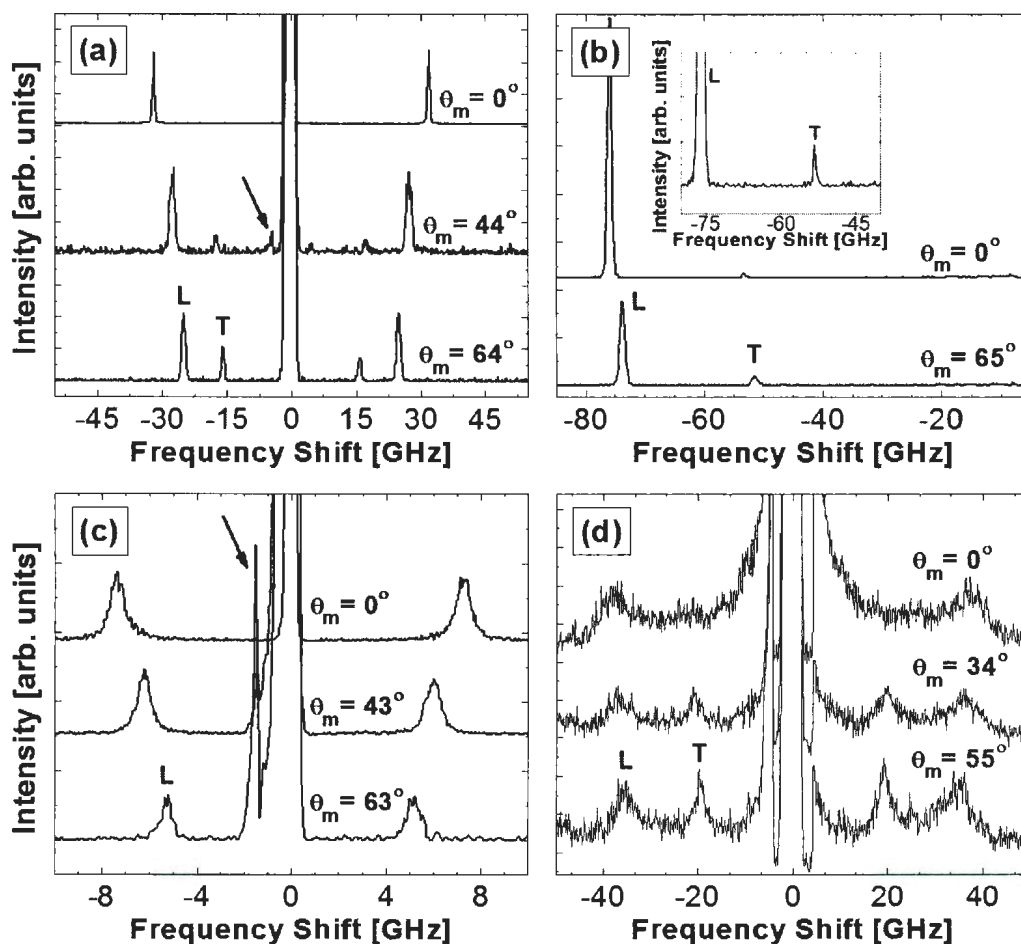


Figure 5.4: Brillouin spectra of (a) fused quartz, (b) (100)-oriented GaP, (c) deionized water, and (d) a 58% porous silicon film for different values of θ_m . Peaks due to transverse (T) and longitudinal (L) bulk acoustic modes were observed. The Rayleigh peak at ~ 0 GHz was shuttered to prevent photomultiplier saturation. The arrow indicates the base of this peak which is outside the shuttered region. In the case of water, the spectrum collected at $\theta_m = 63^\circ$ was smoothed using 3-point adjacent-averaging. For clarity, only the Stokes portions of the GaP spectra are shown. The inset is a close-up of the longitudinal and transverse mode peaks collected from GaP at $\theta_m = 0^\circ$. For all spectra shown, the collected scattered light was unpolarized.

In comparison to spectra collected from the solid samples at $\theta_m \neq 0$, the peak intensity ratios between the low and high frequency shifted peaks is drastically decreased in the corresponding $\theta_m = 0^\circ$ spectrum. In fact, the peak due to the lower frequency mode was not readily visible in the corresponding spectra collected from fused quartz and porous silicon. This behaviour is indicative of a transverse bulk mode since the scattering cross-section of this mode is expected to be negligible when both the incident and scattered light are directed at an angle near-normal to the sample surface [22]. In turn, the second spectral peak observed in these spectra was attributed to the longitudinal acoustic mode. Additionally, the fact that only one transverse mode peak is observed for (100)-oriented GaP and porous silicon suggests that the corresponding probed AWs are propagating approximately along a high-symmetry direction, which is expected since the surface normal coincides with the (100)-direction in each sample.

In the case of water, the single observed peak was ascribed to a longitudinal mode. This follows from the fact that fluids are only expected to support compressional waves.

To determine AW frequencies, Lorentzian functions were fitted to the spectral peaks. From Fig. 5.5, it can be seen that ν decreases with k_m as expected from Eq. (5.18). For each sample, a global least-squares fit was done on the corresponding longitudinal and transverse mode data. Further, these fits were weighted according to the experimental error in the AW frequency. For the solids, the refractive index value

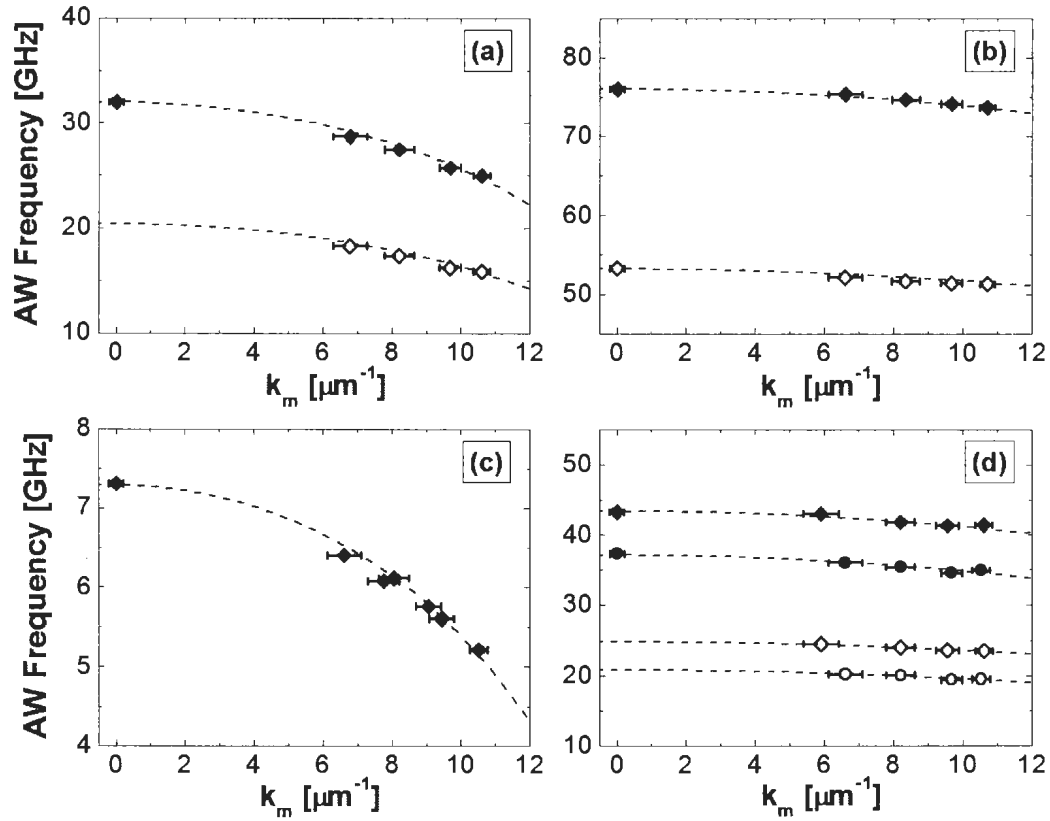


Figure 5.5: Acoustic wave frequency versus k_m for (a) fused quartz, (b) GaP, (c) water, and (d) 50% (diamonds) and 58% (circles) porous silicon. Filled (open) symbols: experimental longitudinal (transverse) mode data; dashed lines: best fits of Eq. (5.18). The shown fits include the data collected using the 180° -backscattering geometry. Fits with and without 180° -backscattering geometry data had adjusted R^2 values greater than 0.99. The vertical error bars are smaller than the symbols, while the horizontal error bars correspond to the experimental random error obtained from Eq. (5.23) using the refractive index values obtained using alternate methods.

Table 5.1: Refractive index and bulk acoustic velocities for fused quartz, GaP, water, and porous silicon (π -Si) determined using pseudo-reflection Brillouin spectroscopy. Values in parentheses correspond to fits done using both the pseudo-reflection and 180° -backscattering geometry data. Previously published values of these parameters are also given. Note: The n^{alt} values for porous silicon were deduced from gravimetrically-determined porosities using the two-component Bruggeman effective medium model. The corresponding V_T^{alt} (V_L^{alt}) value were obtained using n^{alt} with earlier 180° -backscattering Brillouin measurements done on similar samples.

Sample	n	n^{alt}	V_T	V_T^{alt}	V_L	V_L^{alt}
			(km/s)	(km/s)	(km/s)	(km/s)
Fused Quartz	1.52 ± 0.02	1.46[25]	3.45 ± 0.09	3.74[26]	5.4 ± 0.1	5.94[26]
	(1.42 ± 0.02)		(3.8 ± 0.1)		(6.00 ± 0.08)	
GaP	3.5 ± 0.1	3.49[27]	4.0 ± 0.1	4.13[28]	5.7 ± 0.2	5.83[28]
	(3.6 ± 0.1)		(3.9 ± 0.1)		(5.6 ± 0.1)	
Water	1.30 ± 0.02	1.34[29]	-	-	1.46 ± 0.03	1.49[30]
	(1.26 ± 0.01)				(1.54 ± 0.02)	
50% π -Si	2.6 ± 0.2	2.4 ± 0.2	2.5 ± 0.2	2.7 ± 0.3	4.4 ± 0.3	4.8 ± 0.5
	(2.7 ± 0.1)		(2.5 ± 0.1)		(4.3 ± 0.2)	
58% π -Si	2.7 ± 0.3	2.1 ± 0.1	2.0 ± 0.3	2.7 ± 0.4	3.6 ± 0.5	4.6 ± 0.4
	(2.5 ± 0.2)		(2.2 ± 0.2)		(4.0 ± 0.3)	

was shared between both the traverse and longitudinal mode data. The resulting values for the refractive index and the acoustic velocities are given in Table 5.1.

The obtained values of n , V_T , and V_L of fused quartz, GaP, and water showed reasonable agreement with the literature values (see Table 5.1). Further, the data collected using the 180° -backscattering geometry was not required to obtain accurate values of n and V and, thus, samples can be characterized using a pseudo-reflection geometry exclusively. Of these three samples, water showed the largest difference from previously published values. Since the error in the GaP values were less than those of water, this suggests that the elastic-anisotropy of GaP did not contribute significantly to the error in the measurements, as expected.

For the porous silicon samples, the percent difference between the current refractive index and AW velocity values and those obtained using alternate methods were larger than that of fused quartz, GaP, and water. These relatively large differences are thought to be due to sample-to-sample variation. More specifically, there may be slight porosity/pore morphology dissimilarities between samples made under similar conditions, leading to differences in the refractive index and AW velocities. Overall, comparison with the previously determined parameters suggest that the currently obtained values, particularly those taken from the calculations which included the backscattering data, were reasonable estimates of the refractive index and AW velocities of these porous silicon films. One should also note that, in the case of the calculations based on both the pseudo-reflection and 180° -backscattering data, both

Table 5.2: Ranges of k_m and corresponding q_{PR} probed in fused quartz, GaP, water and porous silicon films. The q_{PR} values were deduced from the refractive indices obtained through fits of Eq. 5.18 to the ν versus k_m data shown in Fig. 5.5.

Sample	Range of Probed k_m (μm^{-1})	Range of Probed q_{PR} (μm^{-1})
Fused Quartz	0 - 10.6	26.0 - 33.5
GaP	0 - 10.7	82.3 - 85.0
Water	0 - 10.5	21.0 - 29.8
50% π -Si	0 - 10.6	60.1 - 63.8
58% π -Si	0 - 10.5	55.2 - 59.0

the refractive index and AW velocities for the film of higher porosity (*i.e.*, 58%) are lower than the corresponding values for the lower porosity (*i.e.*, 50%) film. This is typical of porous silicon samples made from parent crystalline silicon wafers with similar dopant concentrations.

With the refractive index determined for each sample, the corresponding range of probed q_{PR} can be obtained from Eq. 5.14. That is, ν versus q_{PR} dispersion can be deduced using the ν versus k_m data together with the fitted n value. Figure 5.6 shows the dispersion curves for the longitudinal and transverse bulk acoustic waves in fused quartz over the range of q_{PR} probed. Table 5.2 gives the ranges of k_m and q_{PR} probed in fused quartz, GaP, water, and the porous silicon films.

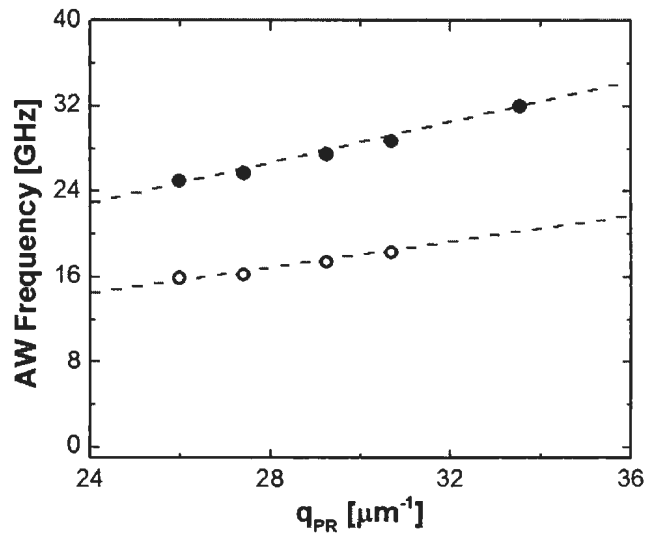


Figure 5.6: Acoustic wave frequency versus q_{PR} for fused quartz. Filled (open) symbols: experimental longitudinal (transverse) mode data; dashed lines: dispersion curves deduced from obtained V_L and V_T values. The refractive index used to compute the q_{PR} values was that obtained from the fit of Eq. 5.18 to the corresponding ν versus k_m data shown in Fig. 5.5(a). The vertical error bars are smaller than the symbols.

5.6 Conclusions

In conclusion, pseudo-reflection Brillouin light scattering was shown to be useful for investigating acoustic waves propagating approximately along the sample surface normal of various material systems. The only requirement for application of this method is that bulk acoustic mode peaks be discernible in the Brillouin spectrum and, consequently, it can be used to probe both transparent and non-transparent non-metallic materials. Moreover, this method does not require that the sample be thin or set in a special configuration and, therefore, can be applied to bulk samples as well as both supported and unsupported films. For the specific case of homogeneous isotropic and cubic materials, this technique can be used to obtain the refractive index and acoustic wave velocities along the sample surface normal. In principle, it could also be applied to lower symmetry systems provided due consideration is given to the incident and scattered light polarization and the orientation of the scattering plane.

Chapter 5 References

- [1] J. R. Sandercock, *Phys. Rev. Lett.* **29**, 1735 (1972).
- [2] J. Sapriel and B. Djafari-Rouhani, *Surf. Sci. Rep.* **10**, 189 (1989).
- [3] E. H. El Boudouti, B. Djafari-Rouhani, A. Akjouj, and L. Dobrzynski, *Surf. Sci. Rep.* **64**, 471 (2009).
- [4] R. E. Camley, B. Djafari-Rouhani, L. Dobrzynski, and A. A. Maradudin, *Phys. Rev. B* **27**, 7318 (1983).
- [5] B. Djafari-Rouhani, L. Dobrzynski, O. Hardouin Duparc, R. E. Camley, and A. A. Maradudin, *Phys. Rev. B* **28**, 1711 (1983).
- [6] M. W. C. Dharma-wardana, A. H. MacDonald, D. J. Lockwood, J.-M. Baribeau, and D. C. Houghton, *Phys. Rev. Lett.* **58**, 1761 (1987).
- [7] D. Moctezuma-Enriquez, Y. J. Rodriguez-Viveros, M. B. Manzanares-Martinez, P. Castro-Garay, E. Urrutia-Banuelos, and J. Manzanares-Martinez, *Appl. Phys. Lett.* **99**, 171901 (2011).
- [8] J. R. Sandercock, *Phys. Rev. Lett.* **28**, 237 (1972).

- [9] M. Grimsditch, W. Senn, G. Winterling, and M. H. Brodsky, *Solid State Commun.* **26**, 229 (1978).
- [10] L. C. Parsons and G. T. Andrews, *Appl. Phys. Lett.* **95**, 241909 (2009).
- [11] N. Gomopoulos, W. Cheng, M. Efremov, P. F. Nealey, and G. Fytas, *Macromolecules* **42**, 7164 (2009).
- [12] N. Gomopoulos, G. Saini, M. Efremov, P. F. Nealey, K. Nelson, and G. Fytas, *Macromolecules* **43**, 1551 (2010).
- [13] N. Gomopoulos, D. Maschke, C. Y. Koh, E. L. Thomas, W. Tremel, H.-J. Butt, and G. Fytas, *NanoLett.* **10**, 980 (2010).
- [14] E. S. Zouboulis, M. Grimsditch, A. K. Ramdas, and S. Rodriguez, *Phys. Rev. B* **57**, 2889 (1991).
- [15] J. K. Krüger, L. Peetz, and M. Pietralla, *Polymer* **19**, 1397 (1978).
- [16] J. K. Krüger, A. Marx, L. Peetz, R. Roberts, and H. -G. Unruh, *Colloid and Polymer Sci.* **264**, 403 (1986).
- [17] J. K. Krüger, Brillouin spectroscopy and its application to polymers. In *Optical Techniques to Characterize Polymer Systems*, edited by H. Bässler. (Elsevier, Amsterdam, 1989). p. 429-461.
- [18] J. K. Krüger, R. Jiménez, K. -P Bohn, J. Petersson, J. Albers, A. Klöpperpieper, E. Sauerland, and H. E. Müser, *Phys. Rev. B* **42**, 8537 (1990).

- [19] J. K. Krüger, J. Embs, J. Brierley, and R. Jiménez, *J. Phys. D: Appl. Phys.* **31**, 1913 (1998).
- [20] C. S. Zha, R. J. Hemley, H. K. Mao, T. S. Duffy, and C. Meade, *Phys. Rev. B* **50**, 13105 (1994).
- [21] H. Boukari and N. Lagakos, Determination of optical constants by Brillouin scattering. In *Handbook of Optical Constants of Solids III*, edited by E. D. Palik. (Academic Press, San Diego, 1998), p. 121-154.
- [22] H. Z. Cummins and P. E. schoen, Light Scattering from Thermal Fluctuations. In *Laser Handbook. Vol 2*, edited by F. T. Arecchi and E. O. Schulz-Dubois. (North-Holland, New York, 1972), p. 1029-1075.
- [23] O. Aktas and M. J. Clouter. personal communication, 3 March, 2012.
- [24] B. A. Auld. *Acoustic Fields and Waves in Solids*. (John Wiley and Sons, New Jersey, 1973).
- [25] W. S. Rodney and R. J. Spindler. *J. Opt. Soc. Am.* **44**, 677 (1954).
- [26] S. M. Shapiro, R. W. Gammon, and H. Z. Cummins, *Appl. Phys. Lett.* **9**, 157 (1966).
- [27] D. E. Aspnes and A. A. Studna, *Phys. Rev. B* **27**, 985 (1983).
- [28] S. Adachi, editor. *Handbook on Physical Properties of Semiconductors, Volume 2*. Kluwer Academic, New York, 2004.

- [29] M. R. Querry, D. M. Wieliczka and D. J. Segelstein, Water (H_2O). In *Handbook of Optical Constants of Solids II*, edited by E. D. Palik. (Academic Press, San Diego, 1991), p. 1059-1077.
- [30] W. Marczak, J. Acoust. Soc. Am. **102**, 2776 (1997).
- [31] C. Pickering, M. L. Beales, D. J. Robbins, D. J. Pearson, and R. Greef, J. Phys. C **17**, 6535 (1984).
- [32] G. T. Andrews, J. Zuk, H. Kieft, M. J. Clouter, and E. Nossarzewska-Orlowska, Appl. Phys. Lett. **69**, 1217 (1996).
- [33] A. M. Polomska. *Elastic properties of porous silicon superlattices*. Ph.D. thesis, Memorial University of Newfoundland (2010).
- [34] A. M. Polomska-Harlick and G. T. Andrews, J. Phys. D: Appl. Phys. **45**, 075302 (2012).

Chapter 6

Brillouin Scattering from Porous Silicon-Based Optical Bragg Mirrors

Reproduced with permission from L.C. Parsons and G.T. Andrews. *J. Appl. Phys.* 111, 123521 (2012). Copyright 2012, American Institute of Physics.

6.1 Abstract

Brillouin light scattering experiments were done on porous silicon-based optical Bragg mirrors with modulation wavelengths of ~ 100 nm. By using a combination of pseudo-reflection and backscattering geometries, phonon dispersion curves along the superlattice modulation axis were mapped. Excellent agreement is obtained with the bulk acoustic mode band structure calculated using a one-dimensional elastic continuum model. In addition to zone-folding of the bulk longitudinal mode dispersion curve, the samples are marked by a surface-localized acoustic mode at the

superlattice-air interface. The frequency of this mode lies near the upper edge of a phononic band gap centered at ~ 16 GHz. These results, along with optical reflectance data showing visible-range photonic band gaps, reveal that these samples are one-dimensional hypersonic phononic-photonic crystals.

6.2 Introduction

It is well-known that superlattices (SLs) with a one-dimensional periodic modulation in the elastic properties exhibit complex acoustic phonon dispersion curves [1, 2]. Analogous to the electronic band structure, the phonon dispersion curve folds into multiple branches within the mini-Brillouin zone corresponding to the artificial periodicity. This may be accompanied by the formation of forbidden frequency bands, or phononic band gaps, for which acoustic phonons cannot propagate in the bulk of the structure. The broken translational symmetry introduced by the SL-external environment interface in a real periodic structure, however, may permit the existence of evanescent modes within these gaps [3, 4]. Previous studies using picosecond ultrasonic measurements [5–11] and Raman light scattering [12, 13] have shown evidence of these surface-localized modes in various material systems.

Due to the porosity-dependent elastic properties, mesoporous silicon (π -Si) SLs are characterized by a one-dimensional periodicity in the elastic impedance and, in turn, are good candidates for one-dimensional phononic crystals [14–16]. This is important from an applications perspective because of the possibilities it presents for seamless

integration of phononic crystal-based devices such as acoustic superlenses [17], acoustic wave resonators [18], and the so-called saser [19], into existing silicon technologies. Furthermore, due to the biocompatibility and bioactivity [20, 21] of porous silicon, these devices could be interfaced with biological systems. Porous silicon SLs can also serve as model systems for the study of novel photon-phonon interactions such as optical cooling [22]. This is because the spatial variation in the elasticity is accompanied by a commensurate periodicity in the refractive index and, thus, these films also behave as optical Bragg mirrors characterized by band gaps in the photon spectrum [23–25]. In fact, recent ultrasonic transmission and optical reflectance measurements have shown evidence of both phononic band gaps and infra-red range photonic band gaps for structures with a square-wave modulation in the porosity with depth [16]. Further ultrasonic measurements on π -Si rugate filters with a sinusoidal variation in the porosity also showed evidence of hypersonic phononic band gaps in these structures [26]. Broad-band hypersonic mirrors consisting of stacks of π -Si-based one-dimensional phononic crystals of different modulation wavelengths have also been theoretically predicted [27].

Hypersonic phononic crystal effects were also observed in Brillouin light scattering experiments on π -Si SLs with modulation wavelengths, D , ranging from ~ 40 nm to ~ 170 nm [28]. Near-normal incidence 180° -backscattering measurements were used to access a single phonon wavevector in each sample, (directed approximately along the modulation axis), and, in turn, a set of acoustic phonon frequency versus D data

were obtained. Comparison between experiment and theoretical calculations based on a one-dimensional continuum model suggested that the bulk longitudinal acoustic phonon had folded into multiple branches. The polarization of the probed phonons, however, could not be readily deduced experimentally, resulting in ambiguities with some of the mode assignments upon comparison with theory. Moreover, an additional peak of unknown origin was observed in some spectra.

In this paper, the results of a comprehensive Brillouin light scattering study conducted on π -Si optical Bragg mirrors with $D \sim 100$ nm will be presented. Using both pseudo-reflection and backscattering geometries, a portion of the phononic band structure directed along the periodicity was mapped for each SL. A polarization analysis of the observed modes was also carried out. The results reveal that, in addition to zone-folding of the longitudinal bulk acoustic phonon, there exists a surface-localized mode lying near the upper edge of a hypersonic band gap in the bulk longitudinal band structure. The frequency of this mode is an order of magnitude lower than that observed in Raman scattering experiments [12, 13]. Further, the associated phononic band gap is centered at a frequency of ~ 16 GHz, an order of magnitude larger than the mid-gap frequencies observed in ultrasonic studies on π -Si SLs [16, 26]. Complementary optical reflectance measurements also confirm that these SLs are one-dimensional photonic crystals.

6.3 Theory

6.3.1 Acoustic Phonon Propagation along the Modulation Axis of an Infinite Superlattice

Acoustic phonon propagation along the modulation axis of an infinite superlattice will first be considered (see Fig. 6.1(a)). The superlattice has a square-wave variation in elastic impedance $Z_j = \rho_j V_j$, where ρ_j are the mass densities of the constituent layers, V_j are the corresponding acoustic phonon sound velocities (either transverse (T) or longitudinal (L)), and $j = 1, 2$ labels the constituent layers. The modulation wavelength $D = d_1 + d_2$, where d_j are the constituent layer thicknesses, is of the order of tens-of-nanometers and, assuming $d_2 \sim d_1$, the thickness of each constituent layer is much larger than the atomic spacing. In turn, for long-wavelength phonons, each layer can be treated as a continuum [29, 30]. Interface boundary conditions require that the displacement $u = u(x)$ and the normal component of the stress $\rho_j V_j^2 \partial u / \partial x$ be continuous. Furthermore, the discrete translational invariance of the system implies that the phonon behave as a Bloch wave. Taking this into account, one can find that the dispersion relation for the phononic Bloch wave is [31]

$$QD = \cos^{-1} \left[\cos \left(\frac{\Omega d_1}{V_1} \right) \cos \left(\frac{\Omega d_2}{V_2} \right) - F \sin \left(\frac{\Omega d_1}{V_1} \right) \sin \left(\frac{\Omega d_2}{V_2} \right) \right], \quad (6.1)$$

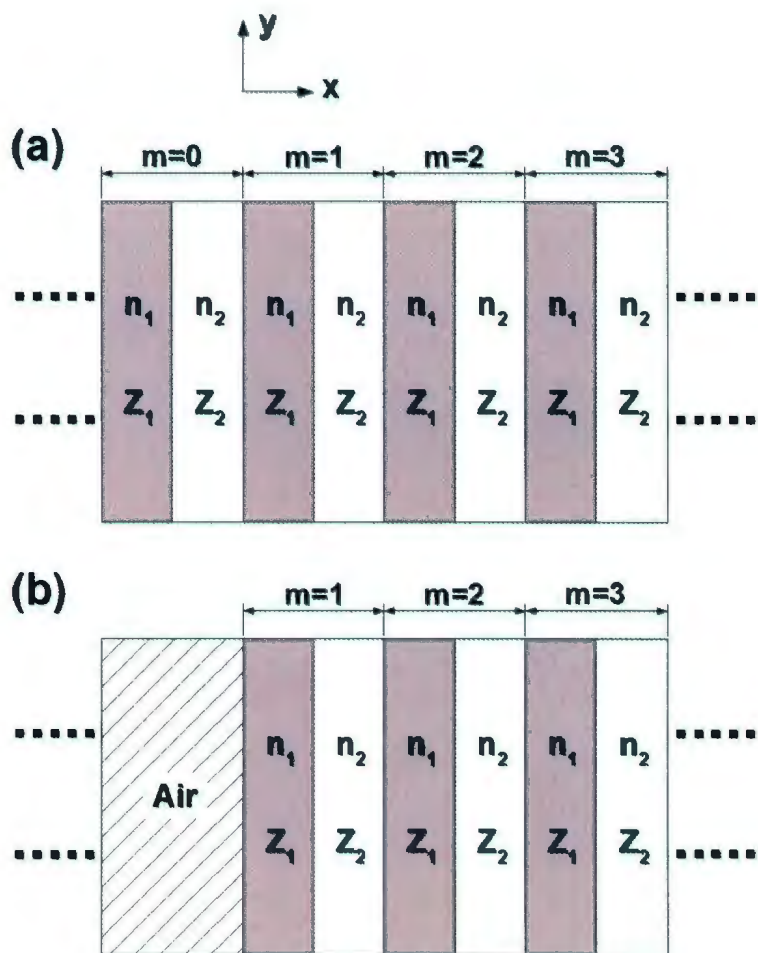


Figure 6.1: (a) Infinite and (b) semi-infinite superlattices containing a two-layer unit cell. The integer m denotes the unit cell.

where Q is the phonon Bloch wavevector, $\Omega = 2\pi\nu = V_j q_j$ is the phonon angular frequency, ν is the phonon frequency, q_j are the phonon wavevectors associated with the constituent layers, and F is given by

$$F = \frac{1}{2} \left(\frac{Z_1}{Z_2} + \frac{Z_2}{Z_1} \right). \quad (6.2)$$

With reference to the above, an effective medium model [32] that treats individual layers as elastic continua has been successfully used to predict the elastic properties of SLs with ≤ 10 nm-thick constituent layers [33, 34] and polymeric Langmuir-Blodgett films in which different portions of the molecules comprising the film are treated as separate SL constituents [35]. There has also been, however, at least one instance where this model was unable to accurately predict the elastic properties of SLs with very small modulation wavelengths [36].

6.3.2 Acoustic Phonon Propagation along the Modulation Axis of a Semi-Infinite Superlattice

In addition to the bulk modes discussed above, the phonon spectrum for propagation along the surface normal of a semi-infinite binary periodic structure in contact with a gaseous half-space (say air) may contain surface-localized modes. Figure 6.1(b) illustrates the semi-infinite structure. In particular, the physical parameters of the semi-infinite structure will be the same as those used for the above infinite superlattice. Further, the gas-solid interface is assumed to be stress-free. The surface-localized

modes, which stem from the broken translational symmetry introduced by the gas-solid interface, decay with depth and the associated eigenvalue is given by $|e^{-\beta D}|$, where β is positive and real. Taking into account the zero stress at the gas-solid interface and assuming that constituent layer 1 is in contact with the gas, one can show that [3, 4]

$$|e^{-\beta D}| = \left| \frac{\cos(\Omega_s d_1/V_1)}{\cos(\Omega_s d_2/V_2)} \right| < 1 \quad (6.3)$$

It can also be shown that [3, 4] the angular frequencies $\Omega_s = 2\pi\nu_s$ of the localized surface modes are governed by

$$\left(\frac{Z_1}{Z_2}\right) \tan\left(\frac{\Omega_s d_1}{V_1}\right) + \tan\left(\frac{\Omega_s d_2}{V_2}\right) = 0. \quad (6.4)$$

Thus, the ν_s values are independent of phonon wavevector. Since $|e^{-\beta D}| < 1$, Eqs. (6.3) and (6.4) are both satisfied only when $Z_1 < Z_2$ (*i.e.*, when the layer adjacent to the gas has the lower elastic impedance) [5]. One should also note that $|e^{-\beta D}|$ is associated with a complex phonon wavevector and, hence, these modes are evanescent waves with frequencies ν_s within the band gaps of the bulk modes corresponding to Eq. (6.1).

6.3.3 Photon Propagation at Oblique Angles to the Modulation Axis of an Infinite Superlattice

Similar to phonon propagation along the modulation axis of a superlattice, photons propagating at oblique angles to the modulation direction of an infinite SL with

a periodicity in the refractive index exhibit complex dispersion curves. In particular, the unit-cell of the periodic structure is comprised of two optically homogeneous layers with refractive indices n_1 and n_2 (see Fig. 6.1(a)). Further, the photons are taken to be polarized within the plane of incidence (*i.e.*, p-polarized). Due to the translational invariance of the optical properties, the component of the photon wavevector along the modulation axis of the superlattice, κ , is governed by [37]

$$\kappa D = \kappa(\theta)D = \cos^{-1} \left[\cos(K_{1x}d_1) \cos(K_{2x}d_2) - P_p \sin(K_{1x}d_1) \sin(K_{2x}d_2) \right], \quad (6.5)$$

where $K_{jx} = (2\pi/\lambda) \sqrt{n_j^2 - \sin^2\theta}$ are the photon wavevector components perpendicular to the layer interfaces in each constituent layer. λ is the corresponding photon wavelength in vacuum, and θ corresponds to the angle of incidence if the photon propagated in vacuum (deduced using Snell's Law). Here, P_p is a parameter specific to the case of p-polarized light:

$$P_p = P_p(\theta) = \left(\frac{n_1^2 K_{2x}}{n_2^2 K_{1x}} + \frac{n_2^2 K_{1x}}{n_1^2 K_{2x}} \right). \quad (6.6)$$

One should note that the photon wavevector given by Eq. (6.5) is taken to be in the extended-zone scheme throughout the following discussion.

In the case that $n_2 \sim n_1$, for propagation along the modulation axis, it follows from Eq. (6.5) that the photon wavenumbers corresponding to the center of the photonic band gaps, w_t , can be approximated as [38]

$$w_t = \frac{t}{2(n_1 d_1 + n_2 d_2)} = \frac{t}{2n_{\text{eff}} D} \quad (6.7)$$

where t is a positive integer corresponding to the order of the photonic gap and $n_{\text{eff}} = (n_1 d_1 + n_2 d_2)/D$.

6.3.4 Brillouin Scattering from a Semi-Infinite Superlattice

Brillouin light scattering can be used to map the acoustic phonon band structure along the modulation axis of a semi-infinite superlattice. In particular, both near-normal incidence backscattering and pseudo-reflection scattering geometries will be considered. One should also note that when probing a phonon of wavevector \mathbf{q} , conservation of momentum dictates that

$$|\mathbf{q}| = |\mathbf{K}_s - \mathbf{K}_i|, \quad (6.8)$$

where \mathbf{K}_i and \mathbf{K}_s are the incident and scattered photon wavevectors inside the material, respectively [39]. Further, the components of the photon wavevectors along the superlattice normal are governed by Eq. (6.5) with $\lambda = \lambda_i$, where λ_i is the wavelength of the probing laser light. In this case, \mathbf{q} corresponds to a phonon wavevector in an extended-zone scheme. Folding of the phonon band structure is accounted for by a vector $(2lp/D)\hat{x}$ in the above expression, where l is an integer corresponding to the folding-order of the phonon branches.

When using a backscattering geometry (see Fig. 6.2(a)), where $\theta_s = \theta_i$, the angle between the direction of phonon propagation and the surface normal, α_{BS} , can be

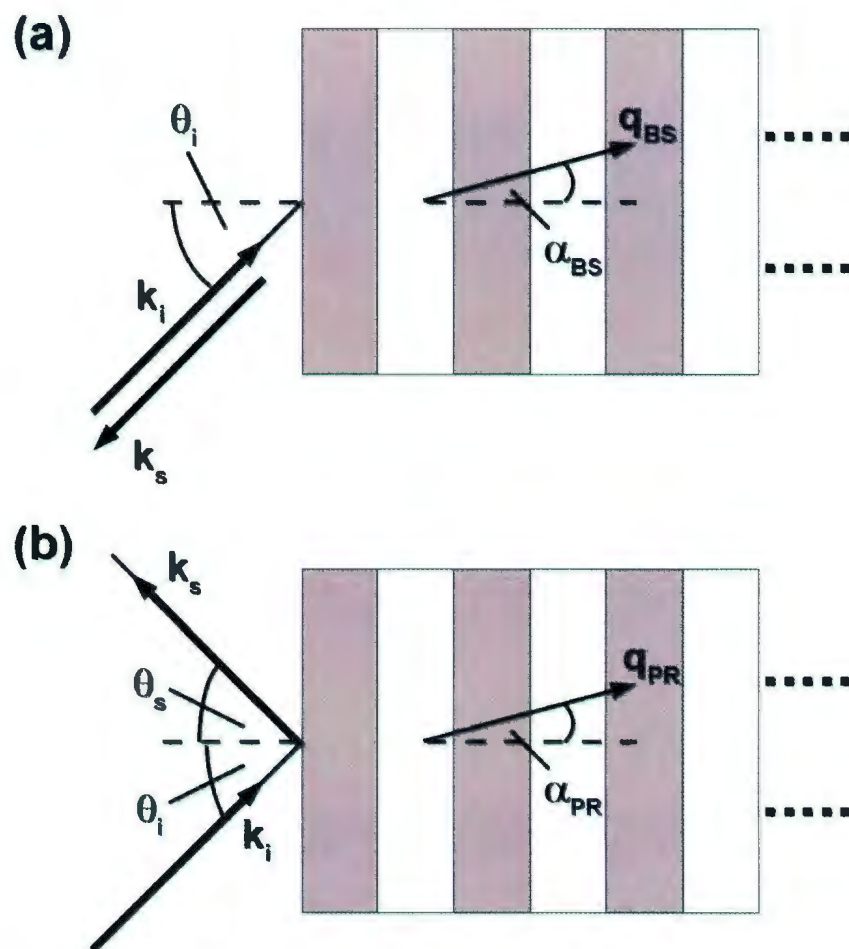


Figure 6.2: (a) 180°-backscattering and (b) pseudo-reflection geometries. The incident (scattered) photon wavevector and probed phonon wavevector are denoted by \mathbf{k}_i (\mathbf{k}_s) and \mathbf{q} , respectively. The angles \mathbf{k}_i , \mathbf{k}_s , and \mathbf{q} make with surface normal are θ_i , θ_s , and α , respectively. In the case of 180°-backscattering, $\theta_s = \theta_i$.

related to θ_i via Snell's law and is expressed as

$$\alpha_{BS} = \tan^{-1} \left(\frac{q_{BS\parallel}}{q_{BS\perp}} \right) \leq \sin^{-1} \left(\frac{1}{n_1} \sin \theta_i \right) \leq \theta_i, \quad (6.9)$$

where $q_{BS\parallel}$ and $q_{BS\perp}$ are the components of the phonon wavevector \mathbf{q}_{BS} parallel and perpendicular to the sample surface plane, respectively. Without loss of generality, it was assumed that $n_1 < n_2$ and, thus, $\theta_i > \sin^{-1}(\sin(\theta_i)/n_1) > \sin^{-1}(\sin(\theta_i)/n_2)$. If n_1 is sufficiently large and θ_i is small, $\alpha_{BS} \approx 0^\circ$. In turn, for a near-normal incidence backscattering geometry, the resulting probed phonon propagates approximately parallel/antiparallel to the superlattice modulation axis with a wavevector of magnitude

$$q_{BS} = q_{BS\perp} \sqrt{1 + \tan^2 \alpha_{BS}} \approx q_{BS\perp}. \quad (6.10)$$

Thus, taking into account Eq. (6.8), it follows that

$$q_{BS} \approx 2\kappa(\theta_i). \quad (6.11)$$

For a pseudo-reflection scattering geometry (see Fig. 6.2(b)), where $\theta_s \sim \theta_i$, the resulting probed phonon propagates at an angle α_{PR} given by [40]

$$\alpha_{PR} \leq \left| \frac{\theta_i - \theta_s}{2} \right|. \quad (6.12)$$

This probed phonon propagates nearly along the superlattice modulation axis with wavevector \mathbf{q}_{PR} of magnitude

$$q_{PR} = q_{PR\perp} \sqrt{1 + \tan^2 \alpha_{PR}} \approx q_{PR\perp}. \quad (6.13)$$

Again, following from Eq. (6.8), one can see that

$$q_{PR} \approx \kappa(\theta_i) + \kappa(\theta_s). \quad (6.14)$$

Due to the periodicity of the elastic properties, phonons probed using the above geometries behave as phononic Bloch waves. Since the probed phonons are directed along the interface normal of the SL, folding of the phonon band structure may be accounted for by the simple selection rules

$$Q = q_{BS} + \frac{2l\pi}{D}, \quad (6.15a)$$

$$Q = q_{PR} + \frac{2l\pi}{D}. \quad (6.15b)$$

6.4 Experimental Details

Porous silicon SLs and associated single layer films were made by anodization of p^+ -type (100)-oriented crystalline silicon (5-20 $m\Omega\cdot\text{cm}$) in an electrolyte composed of 1 (49% HF) : 1 ($\text{C}_2\text{H}_5\text{OH}$). Single layer films were fabricated with thicknesses of $\sim 5 \mu\text{m}$. Cross-sectional scanning electron microscopy imaging showed that the characteristic pore diameter was $\sim 10 \text{ nm}$, comparable to previous results obtained for films made under similar conditions from p^+ -type crystalline silicon substrates [41]. Etching current densities of 149 mA/cm^2 and 101 mA/cm^2 were used resulting in samples with gravimetrically-determined porosities of 0.58 ± 0.02 and 0.50 ± 0.02 , respectively. The porosity values were deduced by statistical analysis of results taken from two series of samples, one for each current density, combined with results obtained from similar samples studied previously in this laboratory [42]. In contrast to an earlier Brillouin scattering study [28], each porosity value was associated with a given current density and the observed sample-to-sample variation was taken into ac-

count in the experimental uncertainty. The refractive indices of the single-layer films were obtained using the porosities together with the two-component Bruggeman effective medium model [43]. Using these effective refractive indices, the acoustic wave velocities for the constituent layers were determined through statistical analysis of near-normal incidence 180° -backscattering Brillouin data ($V = \nu\lambda_i/2n$, where ν is the phonon frequency deduced from the Brillouin peak frequency shift) obtained for two sets of single-layer films, one for each current density. It should also be noted that for π -Si films, the effective mass density is $\rho = \rho_{bulk}(1 - \zeta)$, where $\rho_{bulk} = 2330 \text{ kg/m}^3$ is the density of crystalline silicon and ζ is the film porosity.

Superlattices with a square-wave modulation in the porosity were formed by alternating the current density between the above values. These SLs, as well as those in the previous study [28], were fabricated such that the 58% constituent layer was the first formed and, hence, located at the SL-air interface. In order to ascertain the effect of constituent layer configuration on the SL acoustic phonon spectrum, experiments were also done on a number of π -Si SLs fabricated with the lower porosity (*i.e.*, 50%) layer adjacent to air. To minimize electrochemically-induced gradients in porosity with depth, 1 s etch-stops were included between each etching step to allow the electrolyte to replenish at the pore tip. Etching times were chosen so that the constituent layer thicknesses, d_1 and d_2 , were approximately equal and SLs were made with modulation wavelengths D ranging from 38 nm to 172 nm. Thus, $D/2$ was typically much larger than the characteristic pore diameter. The modulation wave-

length for each superlattice was determined by taking into account the etch times together with etch rates deduced from the associated single-layer films [44] or, more precisely, through cross-sectional scanning electron microscopy imaging. Individual constituent layers could not be discerned in the micrographs but D could be obtained by dividing the total film thickness by the number of current density cycles. The number of modulations was such that each SL film was $\sim 5 \mu\text{m}$ thick. The porosities, refractive indices, effective mass density, and bulk acoustic phonon velocities of the SL constituent layers were taken to be the same as those of single layer films formed under identical etching conditions.

Brillouin scattering experiments were carried out in air at room temperature using both a backscattering geometry and a pseudo-reflection geometry. Incident light of wavelength $\lambda_i = 532 \text{ nm}$ reduced to a power ranging from $\sim 50 \text{ mW}$ to $\sim 80 \text{ mW}$ was provided by a Nd:YVO₄ laser. For the backscattering geometry, a 5 cm lens ($1.8 \leq f/\# \leq 4.0$) served to focus the incident light on the sample and was also used to collect scattered light. The backscattering spectra were collected at $6^\circ \leq \theta_i = \theta_s \leq 8^\circ$. For the pseudo-reflection geometry, incident light was focused on the sample using a lens with a focal length of either 10.0 cm or 7.5 cm and scattered light was collected by the aforementioned 5 cm lens. In this case, θ_i ranged from 30° to 68° . To ensure that specularly reflected light did not enter the collection lens, θ_s was set 5° to 11° less than θ_i . Frequency analysis of the scattered light was done using a tandem Fabry-Perot interferometer. Most spectra were collected using a free spectral

range of 60 GHz, but lower values were used when higher resolution was required (*e.g.*, to resolve spectral peaks close to the central elastic peak). It should be noted that the intensities of some of the observed Brillouin peaks were quite small and, in fact, a collection time of several days was needed in order to discern particularly weak features in each spectrum. In addition, it was observed for a number of the single-layer films and SLs that spectra collected from a given sample at vastly different times (months in some cases) were practically indistinguishable. Moreover, studies conducted on single layer films as well as porous silicon-based microcavities report no significant oxidation-induced aging effects on the optical properties for samples made from p^+ -type substrates [43, 45]. Hence, the current Brillouin scattering results suggest that the influence of aging on the elastic properties of the films is negligible.

In conjunction with the Brillouin light scattering experiments, normal-incidence optical reflectance measurements were done. Incident light was provided by a tungsten halogen broadband white light source. Spectral data were collected and analyzed using an Ocean Optics fiber optical grating spectrometer configured for response over a spectral range of ~ 400 nm to ~ 1100 nm. The reference used for these experiments was a broadband dielectric mirror manufactured by Thor Labs which exhibits reflectance of $\simeq 99\%$ from ~ 400 nm to ~ 900 nm. Thus, over this spectral range the resulting relative reflectance values were approximately equal to the absolute reflectance of the corresponding π -Si films.

6.5 Results and Discussion

6.5.1 Optical Reflectance

Figure 6.3(a) shows typical optical reflectance spectra collected from π -Si superlattices. The observed reflectance peaks corresponded to the $t = 1$ one-dimensional photonic band gap, which was in the visible spectral range, while the side lobes were due to interference over the whole film. Spectral peaks due to the $t = 1$ photonic band gap were not observed in samples with $D < 99$ nm as the expected peak position was outside the sensitivity range of the optical reflectance setup. For each sample, the center of the optical Bragg peak was assigned to w_1 . Since $\zeta_2 \sim \zeta_1$, $n_2(w) \sim n_1(w)$ and, thus, the theoretical dependence of w_1 on D was determined from the continuum model given by Eq. (6.7), as has been successfully done for mesoporous silicon SLs in the past [23, 24, 38]. In particular, the wavenumber-dependent refractive indices $n_j(w)$ of the constituent layers were obtained using the two-component Bruggeman effective medium model [43]:

$$1 - \zeta_j = \frac{(1 - n_j(w)^2)(N(w)^2 + 2n_j(w)^2)}{3n_j(w)^2(1 - N(w)^2)}, \quad (6.16)$$

where $N(w)$ is the wavenumber-dependent refractive index of bulk crystalline silicon [46]. Thus, in order to calculate w_1 versus D , the corresponding $n_j(w_1)$ values were used as inputs in Eq. (6.7). The resulting theoretical curve, which takes into account optical dispersion, is in good agreement with the experimental data (see Fig. 6.3(b)). One should note that for samples in which the Bragg peak was ob-

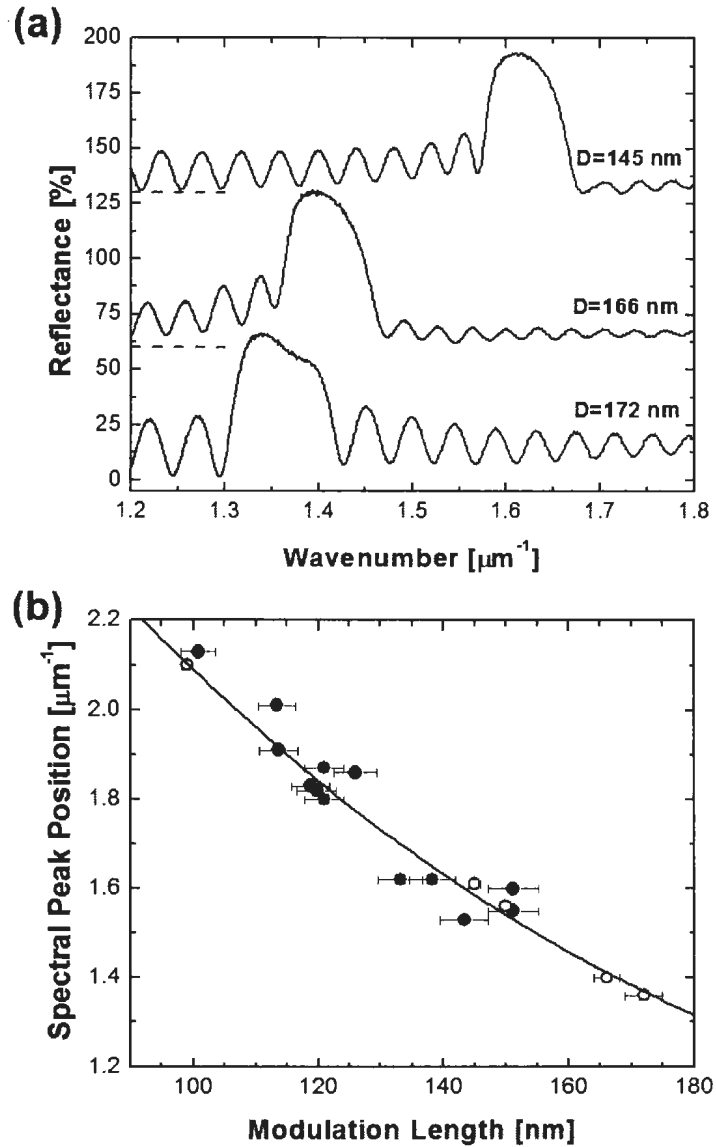


Figure 6.3: (a) Optical reflectance spectra collected from $D = 145$ nm, $D = 166$ nm, and $D = 172$ nm porous silicon superlattices. Horizontal dashed lines mark the 0% reflectance level for the $D = 145$ nm and the $D = 166$ nm spectra. (b) Dependence of the $t = 1$ photonic band gap center w_1 on superlattice modulation length D . Symbols: experimental data; curve: theoretical calculations based on Eq. (6.7) together with Eq. (6.16). Filled and empty symbols correspond to samples for which D was calculated using the constituent layer etch rates together with the etch times and cross-sectional scanning electron microscopy-deduced overall film thickness, respectively. Error in spectral position is smaller than the symbols.

served, the individual layer thickness was ~ 5 times the characteristic pore diameter of ~ 10 nm and the wavelength of the refracted light corresponding to $1/(w_1 n_{\text{eff}}(w_1))$ (> 180 nm) was more than an order of magnitude larger than the pore size. Hence, it is not surprising that these SLs can be treated as optical continua.

As a final note, the reflectance at the optical Bragg peak wavelength was typically between $\sim 50\%$ and $\sim 70\%$ for each sample. That is, samples were not perfect reflectors over this spectral region. This type of response has been observed in previous studies and is thought to be due to losses stemming from absorption and layer-to-layer interface roughness [47-49]. Following from the fact that roughness at the film-substrate interface of single layer films made from p^+ -type silicon is less than 10 nm [49], it is assumed that layer-to-layer interface roughness in the current SL films is ~ 10 nm (*i.e.*, comparable to the pore diameter).

6.5.2 Brillouin Light Scattering

Brillouin scattering experiments were done on superlattices with D values of 88 nm, 99 nm, 145 nm, 166 nm, and 172 nm using both 180° -backscattering and pseudo-reflection geometries. The wavelength of the probed acoustic phonons was determined from Eqs. (6.11) and (6.14) to be approximately 120 nm (about an order of magnitude larger than the characteristic pore diameter). For each sample, three peaks were observed with frequency shifts dependent on the angle of incidence and, hence, the magnitude of the phonon wavevector component directed along the mod-

ulation axis (see Fig. 6.4(a)). In order to determine the polarization of these three modes, it was noted that for p-polarized incident light, the light scattered from longitudinal and transverse bulk modes is p- and s-polarized, respectively, when using a pseudo-reflection geometry [39]. Thus by placing an appropriately-oriented polarizer in the scattered light, the character of these modes could be determined. Such a polarization analysis revealed that two of the peaks could be attributed to scattering from bulk longitudinal modes (labeled L_0 and L_{-1}) while the third was attributed to scattering from a transverse bulk mode (labeled T_0) (see Fig. 6.4(b)). Further, when the probing light is at near-normal incidence, where the scattering cross-section for transverse modes should be negligible [39], the peak assigned to the transverse mode was not discernible in the collected spectra. Finally, the peak associated with the L_{-1} mode for the $D = 166$ nm and the $D = 172$ nm samples was very weak and, in fact, could not be readily fit to a Lorentzian function in most cases (see Fig. 6.5).

In the case of the $D = 145$ nm, $D = 166$ nm, and $D = 172$ nm samples, a fourth peak was observed. This peak had a lineshape which was similar to the unassigned peak reported previously for samples of comparable modulation wavelength [28] (see Fig. 6.6(a)). Aside from spectra collected from the $D = 166$ nm and $D = 172$ nm sample, this weak spectral feature (labeled S) was only discernible in the 180° -backscattering spectra collected at near-normal incidence. Figure 6.6(b) shows a series of spectra collected from the $D = 172$ nm sample and, as one can see, the frequency shift of the peak is independent of the incident angle of the probing

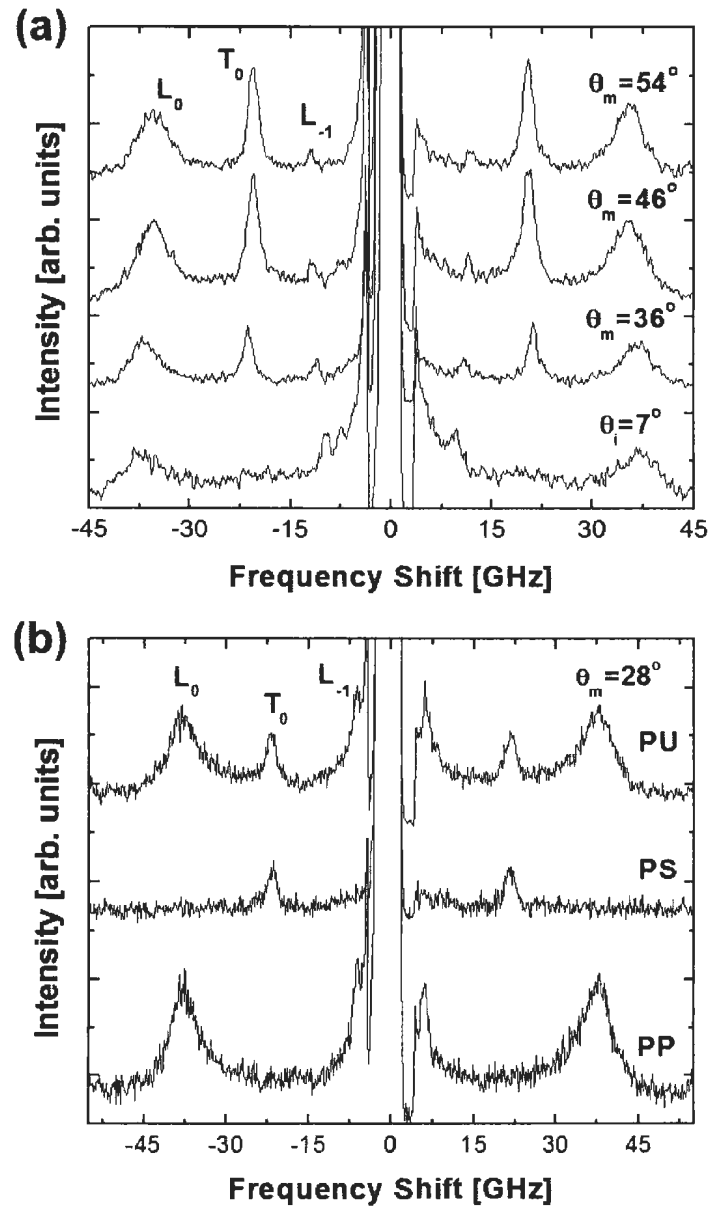


Figure 6.4: (a) Brillouin spectra collected from a $D = 99$ nm porous silicon superlattice at different angles of incidence. Angle θ_i corresponds to the incident angle used in a 180° -backscattering geometry, while $\theta_m = |\theta_i + \theta_s|/2$ corresponds to the average angle used in a pseudo-reflection geometry. Spectra were smoothed using 3-point adjacent averaging. L_0 (L_{-1}): peak ascribed to the $l = 0$ ($l = -1$) folded bulk longitudinal mode; T_0 : peak ascribed to the $l = 0$ bulk transverse mode. (b) Polarized Brillouin spectra collected from a $D = 145$ nm porous silicon superlattice at $\theta_m = 28^\circ$. PU: p-polarized (unpolarized) incident (scattered) light; PS: p-polarized (s-polarized) incident (scattered) light; PP: p-polarized (p-polarized) incident (scattered) light. Note: a fourth spectrum collected at a free spectral range of 30 GHz was used to determine the frequency shift of the L_{-1} mode.

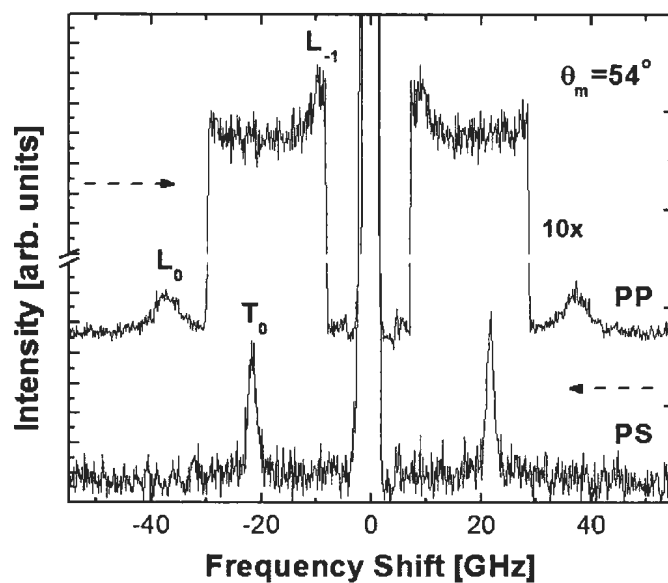


Figure 6.5: Polarized Brillouin spectra collected from a $D = 166$ nm porous silicon superlattice at $\theta_m = 54^\circ$. PP: p-polarized (p-polarized) incident (scattered) light; PS: p-polarized (s-polarized) incident (scattered) light. The PP spectrum was segmented such that the collection time for this region was ten times that of the rest of the spectrum. The horizontal dashed arrows indicate the relevant scattered light intensity scale for each spectrum.

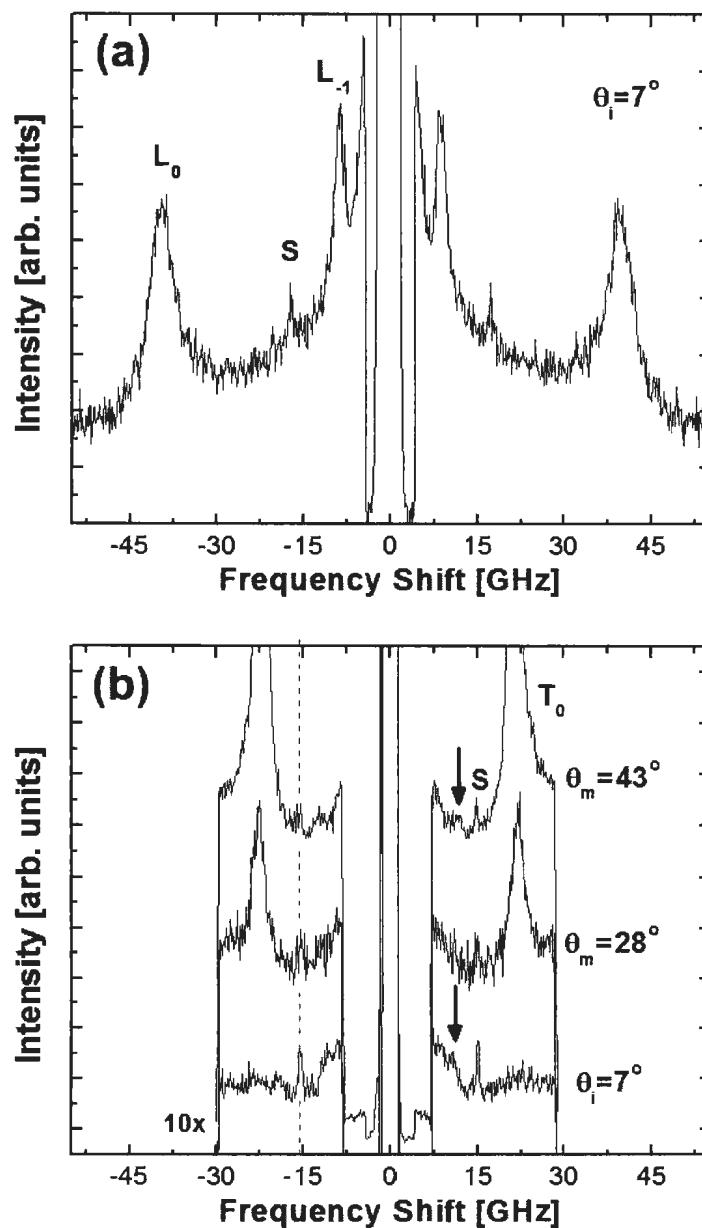


Figure 6.6: (a) Near-normal incidence 180° -backscattering geometry Brillouin spectrum collected from a $D = 151$ nm sample. The data deduced from this spectrum were reported previously [28]. (b) Brillouin spectra collected from a $D = 172$ nm sample. The dashed line is a guide for the eye, marking the position of the S mode. The spectra were segmented such that the collection time for the frequency region shown was ten times that of the rest of the spectrum. Arrows mark weak features that may be due to the $l = -1$ folded longitudinal mode branch.

light, suggesting that the frequency of the corresponding phonon mode is independent of wavevector. Since the intensity of this peak and, therefore, the scattering cross-section does not appear to increase appreciably as the incident angle of the probing light increases, it suggests that this mode has a longitudinal, not transverse, polarization. In addition, the linewidth of the S peak is comparable to the instrumental linewidth (*i.e.*, full-width at half-maximum of < 1 GHz), typical of a surface mode. Furthermore, since the peak is narrower than the lower frequency L_{-1} peak assigned to a longitudinal bulk mode, it is unlikely that the S peak is due to a bulk phonon as this would be counter to usual mechanisms for Brillouin peak broadening for bulk modes, such as opacity broadening [50], broadening due to Akheiser damping [51] or Rayleigh scattering [52], where the linewidth increases with the phonon frequency. Finally, this mode was only observed in samples for which the lower impedance (*i.e.*, high porosity) constituent layer was adjacent to ambient air (see Fig. 6.7). It is for these reasons that the S peak is attributed to a localized-surface mode lying within a phononic band gap in the bulk longitudinal acoustic mode dispersion curve. It should be noted that in the case of the $D = 166$ nm sample, this peak had been previously assigned to the $l = -2$ folded longitudinal bulk mode [28].

6.5.3 Comparison to Theory

Figure 6.8 shows data collected from the $D = 88$ nm, the $D = 99$ nm, the $D = 145$ nm, the $D = 166$ nm, and the $D = 172$ nm samples together with re-

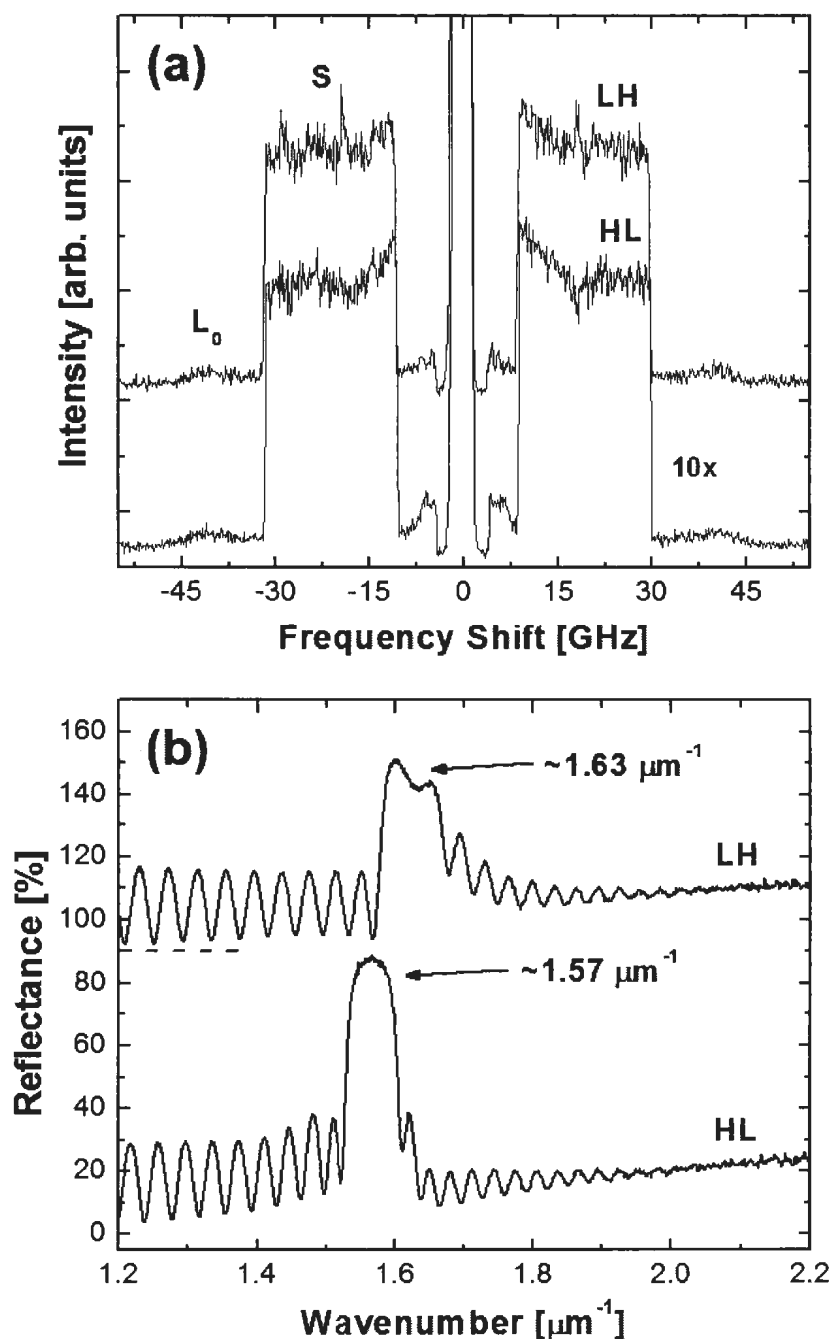


Figure 6.7: (a) Near-normal incidence 180° -backscattering geometry Brillouin spectrum collected from two $D \sim 150$ nm superlattices, one with the lower elastic impedance (*i.e.*, higher porosity) layer adjacent to air (denoted by LH) and the other vice-versa (denoted by HL). The collection time for the HL spectrum was 2.5 times longer than that of the LH spectrum. (b) Optical reflectance spectra collected from the $D \sim 150$ nm superlattices mentioned in (a). The horizontal dashed line marks the 0% reflectance level for the spectrum collected from the LH sample. Since there is only $\sim 4\%$ percent difference in the position of the $t = 1$ photonic band gap, both samples have approximately the same periodicity.

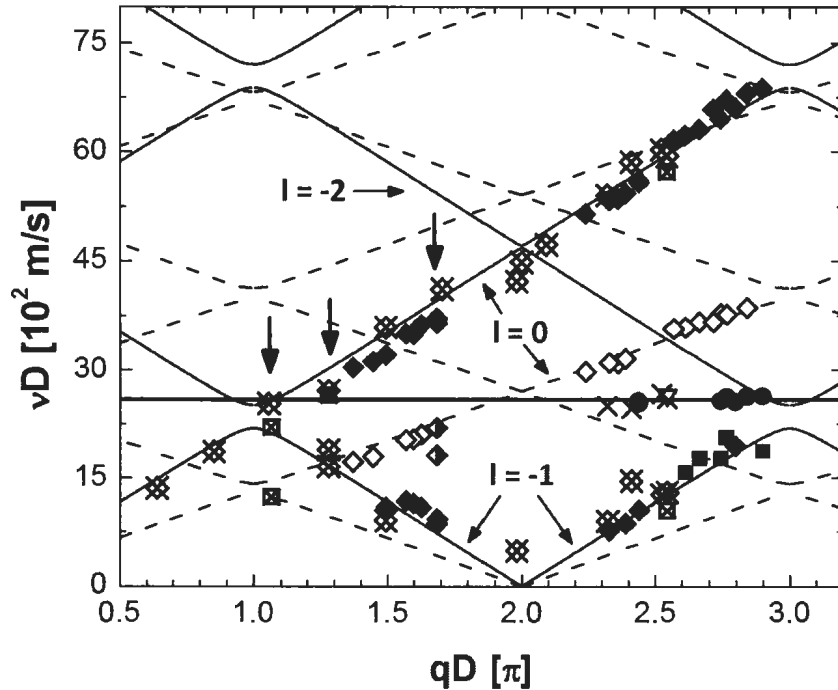


Figure 6.8: Dependence of νD on qD for the porous silicon superlattices. Solid (dashed) curves: theoretical longitudinal (transverse) mode band structure obtained from Eq. (6.1); \blacklozenge (\blacklozenge): bulk longitudinal (transverse) mode data deduced using both backscattering and pseudo-reflection geometries; \blacksquare : weak features observed in spectra collected from the $D = 166$ nm and $D = 172$ nm samples (denoted by arrows in Fig. 6.6); \bullet : surface-localized mode data deduced using both backscattering and pseudo-reflection geometries. Note that the preceding data corresponds to the combined results obtained from the $D = 88$ nm, $D = 99$ nm, $D = 145$ nm, $D = 166$ nm, $D = 172$ nm superlattices. \otimes : previously reported data [28] deduced using a backscattering geometry (each qD value corresponds to a different sample); \boxtimes : previously reported data collected from duplicate samples; \blacklozenge : previously reported data from $D = 99$ nm sample using backscattering geometry; \times : unassigned peak from previous study which is now attributed to localized-surface mode; ∇ : unassigned peak from previously studied duplicate sample which is now attributed to localized-surface mode; thick horizontal line: horizontal linear fit of all surface-localized mode data. Folding order l is indicated. Thick vertical arrows show samples for which weak spectral features in backscattering spectra were assigned to bulk transverse modes. Previously reported backscattering spectrum from $D = 99$ nm contained a peak at $\nu D \sim 18$ m/s of unassigned origin (see Fig. 2(b) in Ref. [28]). The linewidth of this mode is comparable to the bulk transverse mode and, thus, not thought to be due a surface-localized mode. The experimental uncertainties in νD and qD are approximately equal to and twice the size of the symbols, respectively. Furthermore, there is a $\sim 15\%$ error in the calculated band structure stemming from experimental uncertainties in the constituent layer porosities and phonon velocities from which it was calculated.

Table 6.1: Porosity, refractive index and bulk acoustic phonon velocities for single-layer porous silicon films. The refractive index values were deduced using Eq. (6.16) together with the bulk crystalline silicon refractive index value at $\lambda_i = 532$ nm (*i.e.*, $w_i \sim 1.88 \mu\text{m}^{-1}$) [46]. The phonon velocities were obtained from phonons propagating approximately parallel to the sample surface normal.

Porosity	Refractive Index	V_T	V_L
		(km/s)	(km/s)
0.58 ± 0.02	2.1 ± 0.1	2.7 ± 0.4	4.6 ± 0.4
0.50 ± 0.02	2.4 ± 0.1	2.7 ± 0.2	4.8 ± 0.3

sults from the previously studied films [28]. With regard to the previously reported results, which were obtained using only a 180° -backscattering geometry, all of the spectra were scrutinized again and, in particular, any past peak assignments which were deemed questionable were not included. Since the fill-ratio d_1/D (*i.e.*, ~ 0.5) and the constituent layer parameters (see Table 6.1) were taken to be the same for each sample, according to Eqs. (6.1) and (6.4), νD versus qD is invariant of D . The experimental qD values were obtained using Eqs. (6.11) and (6.14) together with D and the known constituent layer refractive indices. It is worth noting that since $n_1 = 2.1$ for the probed structures, $\alpha_{BS} < 4^\circ$ and $\alpha_{PR} < 5.5^\circ$ in these experiments (recall Eqs. (6.9) and (6.12)) and, therefore, Eqs. (6.11) and (6.14) were applicable. Using the values for the constituent layer porosities (recall: $\rho_j = \rho_{bulk}(1 - \zeta_j)$) and phonon velocities as inputs in Eq. 6.1, the theoretically expected bulk longitudinal and bulk transverse phononic band structures could be compared to the experimental

data. Excellent agreement was obtained between the bulk mode data and the corresponding theoretical curves. In particular, the agreement suggests that both the $l = 0$ and $l = -1$ branches of the folded bulk longitudinal mode band structure were observed, while only the $l = 0$ transverse mode branch was observed. Evidence of zone-folding was only observed for SLs with constituent layer thicknesses that were more than ~ 4 times the characteristic pore size. Of related interest are the results of Brillouin studies on mesoporous silicon SLs with constituent layer thicknesses comparable to the pore diameter in which only partial agreement was obtained between experimentally-determined SL elastic constants and those predicted by an effective medium model [44].

The intensity ratio between the L_{-1} and L_0 peaks appeared to change drastically with D (see Figs. 6.4, 6.5, and 6.6). Since the range of probed phonon wavevector magnitudes is approximately the same for each sample, this suggests that the relative scattering cross-section for the $l = -1$ folded longitudinal mode is strongly dependent on qD and, in fact, becomes negligible at the edge of the third mini-Brillouin zone. Considering the photoelastic properties of these structures, this result is in qualitative agreement with Raman scattering studies on folded bulk longitudinal phonons in SLs [53–55]. Further, studies have shown that diffuse interfaces in the SL, such as is the case here, can have a strong effect on the relative intensities and typically result in a decrease in the scattering cross-sections of the folded modes [56, 57]. Moreover, it is not surprising that no peaks were observed for the $l = -2$ longitudinal

branch. Again, taking into account the photoelastic properties, the corresponding scattering cross-sections for even order modes are expected to be negligible when $Z_2d_2 \sim Z_1d_1$ [53, 54, 56], as is the case in this study.

The νD values corresponding to the surface-localized mode appeared to be independent of QD (see Fig. 6.8), as expected from Eq. (6.4). Comparison between data and theory suggest that the localized mode is near the high frequency edge of a hypersonic phononic band gap centered at a νD value of ~ 2350 m/s. Fitting the localized mode data to a horizontal line gave a value of $\nu_s D = 2590 \pm 20$ m/s, which is in reasonable agreement with the value of $\nu_s D = 2300 \pm 200$ m/s determined from Eq. (6.4). It should be noted that the random error in the theoretical value is due to the uncertainty in the sample parameters, including the modulation length, the constituent layer fill-ratio (taken to be 0.51), the porosities, and the phonon velocities. Further, phonon damping was neglected in the theory, which means that there is a systematic error in the theoretical value of $\nu_s D$.

6.6 Conclusions

Brillouin light scattering experiments carried out on porous silicon superlattices with modulation wavelengths in the range ~ 40 nm to ~ 170 nm reveal a complex phononic band structure for propagation along the superlattice modulation axis. Two zone-folded bulk longitudinal acoustic phonon modes together with a mode of longitudinal character localized at the superlattice-air interface are observed. The frequency

of this surface-localized mode is independent of wavevector and lies near the upper edge of a hypersonic band gap in the bulk longitudinal dispersion curve centered at ~ 16 GHz. These results, along with complementary optical reflectance data showing stop bands at optical wavelengths, reveal that these superlattices are one-dimensional hypersonic phononic-photonics crystals.

Chapter 6 References

- [1] E. H. El Boudouti, B. Djafari-Rouhani, A. Akjouj, and L. Dobrzynski, Surf. Sci. Rep. **64**, 471 (2009).
- [2] J. Sapriel and B. Djafari-Rouhani, Surf. Sci. Rep. **10**, 189 (1989).
- [3] R. E. Camley, B. Djafari-Rouhani, L. Dobrzynski, and A. A. Maradudin, Phys. Rev. B **27**, 7318 (1983).
- [4] B. Djafari-Rouhani, L. Dobrzynski, O. Hardouin Duparc, R. E. Camley, and A. A. Maradudin, Phys. Rev. B **28**, 1711 (1983).
- [5] H. T. Grahn, H. J. Maris, J. Tauc, and B. Abeles, Phys. Rev. B **38**, 6066 (1988).
- [6] W. Chen, Y. Lu, H. J. Maris, and G. Xiao, Phys. Rev. B **50**, 14506 (1994).
- [7] A. Halabica, S. T. Pantelides, R. F. Haglund, Jr., R. H. Magruder, and A. Meldrum, III, Phys. Rev. B **80**, 165422 (2009).
- [8] N.-W. Pu and J. Bokor, Phys. Rev. Lett. **91**, 076101 (2003).
- [9] N.-W. Pu, Phys. Rev. B. **72**, 115428 (2005).

- [10] B. Bonello, B. Perrin, E. Romatet, and J. C. Jeannet, *Ultrasonics* **35**, 223 (1997).
- [11] B. Perrin, B. Bonello, J. C. Jeannet, and E. Romatet, *Physica B* **219 – 220**, 681 (1996).
- [12] H. J. Trodahl, P. V. Santos, G. V. Williams, and A. Bittar, *Phys. Rev. B* **40**, 8577 (1989).
- [13] V. Lemos, O. Pilla, M. Montagna, and C. F. de Souza, *Superlattice Microstruc.* **17**, 51 (1995).
- [14] A. Kiuchi, B. Gelloz, A. Kojima and N. Koshida, Possible Operation of Periodically Layered Nanocrystalline Porous Silicon as An Acoustic Band Crystal Device. In *Materials Research Society Symposium Proceedings Series, Vol. 832*, edited by L. Tsybeskov, D. J. Lockwood, C. Delerue and M. Ichikawa. (Warrendale, PA, 2005).
- [15] A. Reinhardt and P. A. Snow, *Phys. Status Solidi A* **204**, 1528 (2007).
- [16] G. N. Aliev, B. Goller, D. Kovalev, and P. A. Snow, *Appl. Phys. Lett.* **96**, 124101 (2010).
- [17] S. Yang, J. H. Page, Z. Liu, M. L. Cowan, C. T. Chan, and P. Sheng, *Phys. Rev. Lett.* **93**, 024301 (2004).
- [18] G. N. Aliev, B. Goller, P. A. Snow, H. Heinrich, B. Yuan, and R. Aigner. Porous silicon bulk-acoustic-wave resonator with integrated transducer. presented at

the International Conference on Porous Semiconductors Science and Technology, 2012.

- [19] A. J. Kent, R. N. Kini, N. M. Stanton, M. Henini, B. A. Glavin, V. A. Kochelap, and T. L. Linnik, *Phys. Rev. Lett.* **96**, 215504 (2006).
- [20] L. T. Canham, *Adv. Mater.* **7**, 1033 (1995).
- [21] L. T. Canham, Porous silicon as a therapeutic biomaterial. In *1st Annual International IEEE-EMBS Special Topic Conference on Microtechnologies in Medicine and Biology*, (2000), p. 108.
- [22] M. Maldovan and E. L. Thomas, *Appl. Phys. Lett.* **88**, 251907 (2006).
- [23] G. Vincent, *Appl. Phys. Lett.* **64**, 2367 (1994).
- [24] C. Mazzoleni and L. Pavesi, *Appl. Phys. Lett.* **67**, 2983 (1995).
- [25] V. Agarwal and J. A. del Rio, *Appl. Phys. Lett.* **82**, 1512 (2003).
- [26] L. Thomas, G. N. Aliev, and P. A. Snow, *Appl. Phys. Lett.* **97**, 173503 (2010).
- [27] D. Moctezuma-Enriquez, Y. J. Rodriguez-Viveros, M. B. Manzanares-Martinez, P. Castro-Garay, E. Urrutia-Banuelos, and J. Manzanares-Martinez, *Appl. Phys. Lett.* **99**, 171901 (2011).
- [28] L. C. Parsons and G. T. Andrews, *Appl. Phys. Lett.* **95**, 241909 (2009).
- [29] R. Ramprasad and N. Shi, *Appl. Phys. Lett.* **87**, 111101 (2005).

- [30] A.-L. Chen and Y.-S. Wang, *Physica E Low-dimensional Systems and Nanostructures* **44**, 317 (2011).
- [31] S.M. Rytov, *Soviet Phys. Acoustics* **2**, 68 (1956).
- [32] M. Grimsditch and F. Nizzoli, *Phys. Rev. B* **33**, 5891 (1986).
- [33] M. Grimsditch, R. Bhadra, I. K. Schuller, F. Chambers, and G. Devane, *Phys. Rev. B* **42**, 2923 (1990).
- [34] G. Carlotti, D. Fioretto, L. Palmieri, G. Socino, A. Verdini, and C. Rigo, *J. Phys. Condens. Matter* **8**, 2265 (1996).
- [35] S. Lee, J. R. Dutcher, G. I. Stegeman, G. Duda, G. Wegner, and W. Knoll, *Phys. Rev. Lett.* **70**, 2427 (1993).
- [36] J. Dutcher, S. Lee, J. Kim, G. I. Stegeman, and C. M. Falco, *Phys. Rev. Lett.* **65**, 1231 (1990).
- [37] P. Yeh, A. Yariv, and C. Hong, *J. Opt. Soc. Am.* **67**, 423 (1977).
- [38] P.A. Snow, E.K. Squire, P. St. J. Russell, and L.T. Canham, *J. Appl. Phys.* **86**, 1781 (1999).
- [39] H. Z. Cummins and P. E. schoen, *Light Scattering from Thermal Fluctuations*. In *Laser Handbook. Vol 2*, edited by F. T. Arecchi and E. O. Schulz-Dubois. (North-Holland, New York, 1972), p. 1029-1075.

- [40] L. C. Parsons and G. T. Andrews, AIP Advances **2**, 032157 (2012).
- [41] R. Herino, G. Bomchil, K. Barla, C. Bertrand, and J. L. Ginoux, J. Electrochem. Soc. **134**, 1994 (1987).
- [42] A. M. Polomska. *Elastic properties of porous silicon superlattices*. Ph.D. thesis, Memorial University of Newfoundland (2010).
- [43] C. Pickering, M. L. Beales, D. J. Robbins, D. J. Pearson, and R. Greef, J. Phys. C **17**, 6535 (1984).
- [44] A. M. Polomska-Harlick and G. T. Andrews. J. Phys. D: Appl. Phys. **45**, 075302 (2012).
- [45] L. Pavesi, Riv. Nuovo Cimento **20**, 1 (1997).
- [46] J. Geist, Silicon (Si) Revisited (1.1-3.1 eV). In *Handbook of Optical Constants of Solids III*, edited by E. D. Palik. (Academic Press, San Diego, 1998), p. 519-531.
- [47] G. L  rondel, R. Romestain, F. Mad  ore, and F. Muller. Thin Solid Films **276**, 80 (1996).
- [48] S. Setzu, G. L  rondel, and R. Romestain. J. Appl. Phys. **84**, 3129 (1998).
- [49] G. L  rondel, R. Romestain, and S. Barret. J. Appl. Phys., **81**, 6171 (1997).
- [50] J. R. Sandercock, Phys. Rev. Lett. **28**, 237 (1972).

- [51] G. N. Aliev, B. Goller, D. Kovalev, and P. A. Snow, *Phys. Status Solidi C*, **6**, 1670 (2009).
- [52] D. B. Hondongwa, B. C. Daly, T. B. Norris, B. Yan, J. Yang, and S. Guha, *Phys. Rev. B* **83**, 121303 (2011).
- [53] J. He, B. Djafari-Rouhani, and J. Sapriel, *Phys. Rev. B* **37**, 4086 (1988).
- [54] J. Sapriel, J. He, B. Djafari-Rouhani, R. Azoulay, and F. Mollot, *Phys. Rev. B* **37**, 4099 (1988).
- [55] J. He, J. Sapriel, and R. Azoulay, *Phys. Rev. B* **40**, 1121 (1989).
- [56] C. Colvard, T.A. Gant, M.V. Klein, R. Merlin, R. Fischer, H. Morkoc, and A.C. Gossard, *Phys. Rev. B* **31**, 2080 (1985).
- [57] C.E. Bottani and R. Caporali, *J. Phys. Condens. Matter* **9**, 5787 (1997).

Chapter 7

Off-Axis Phonon Propagation in Porous Silicon

Superlattices

7.1 Abstract

Brillouin light scattering experiments and optical reflectance measurements were performed on two binary periodic porous silicon superlattices which had constituent layer porosity ratios close to unity. The phononic and photonic band structures of the superlattices were effectively modeled as a series of intersecting linear dispersion curves. Zone-folding was observed for the longitudinal bulk acoustic phonon, with Brillouin spectra containing peaks associated with two branches of the corresponding band structure. Analysis of the Brillouin peaks suggested that the longitudinal bulk modes underwent viscous attenuation, with attenuation coefficients orders of magnitude larger than that of bulk crystalline silicon. Additionally, using an oblique angle 180° -backscattering geometry, the frequency of the probed zone-folded longitu-

dinal phonon was shown to be dependent on the propagation direction as well as the folding order of the mode branch. There was no conclusive evidence of coupling between the transverse and the folded longitudinal modes. Furthermore, two additional Brillouin peaks were observed which were attributed to the Rayleigh surface mode and a pseudo-surface mode. Both surface modes were dispersive, with the velocity increasing as the wavevector decreased.

7.2 Introduction

It is well known that mesoporous silicon films with a spatial modulation in the porosity and, hence, a modulation in the elastic impedance exhibit rich acoustic phonon band structures [1–6]. The resulting bulk acoustic dispersion curves contain multiple zone-folded branches which may be accompanied by the appearance of forbidden phonon frequency bands, or in analogy to photonic crystals, phononic band gaps. Recent studies conducted using ultrasonic measurements along the modulation direction of films with square-wave [4] and sinusoidal [5] variations in the porosity have reported the existence of one-dimensional phononic band gaps in the bulk longitudinal acoustic phonon band structure that have mid-gap frequencies of the order of 1 GHz. As well, Brillouin light scattering studies on binary periodic porous silicon (π -Si) superlattices (SLs) showed a complex bulk longitudinal acoustic band structure [3, 6], with a second longitudinal mode branch observed for phonons directed along the superlattice modulation axis. Furthermore, these light scatter-

ing experiments gave evidence of an additional Brillouin peak which was attributed to a surface-localized mode with a frequency within a one-dimensional hypersonic phononic band gap of the bulk longitudinal band structure centered at ~ 16 GHz.

In contrast to the recent surge of studies that have focused on phonon propagation along the modulation axis of periodically-layered π -Si structures, little work has been carried out to study oblique phonon propagation in these samples. The acoustic phonon dispersion along off-axis directions can be particularly complex, with the possibility of additional intra-zone forbidden phonon bands, or hybridization gaps, due to coupling between phonon modes of different polarization [7]. While oblique incidence 180° -backscattering geometry Brillouin light scattering experiments have been conducted on porous silicon superlattices [8–10], no phononic crystal effects were reported. In particular, investigations were carried out on the applicability of effective medium elasticity models for the treatment of π -Si structures with modulation lengths much smaller than the probed phonon wavelength [8, 9], while other work has focused on surface-propagating modes with only a qualitative discussion of the observed bulk modes [10].

In this paper, results collected for Brillouin light scattering from both near-normally propagating and obliquely propagating phonons in π -Si optical Bragg mirrors will be reported. In particular, comparison between the bulk mode data and theoretical calculations based on a one-dimensional continuum model suggest that the frequency shift of the Brillouin component corresponding to the observed folded

longitudinal bulk mode is strongly dependent on the propagation direction. Furthermore, analysis of the spectral peaks attributed to the folded longitudinal modes suggest that the dominant mechanism for phonon damping is viscous attenuation [11]. Moreover, the quantitative agreement between the data and the calculations suggested that coupling between the transverse and folded longitudinal modes is negligible and, specifically, there was no evidence of corresponding hybridization gaps. Finally, the experimental observations suggested that the π -Si SLs supported a Rayleigh surface phonon and some kind of pseudo-surface mode, both of which were dispersive with wavevector-dependent velocities.

7.3 Experimental Details

Porous silicon SLs were made by anodization of p^+ -type [100]-oriented crystalline silicon (5-20 $m\Omega\cdot\text{cm}$) in an electrolyte composed of 1 (49% HF) : 1 ($\text{C}_2\text{H}_5\text{OH}$) : 1 (H_2O) by volume using a procedure similar to that described elsewhere [6]. The resulting electrolyte solution had an HF concentration of $\sim 16.3\%$. Since the etching process is strongly dependent on HF concentration, interpolating from the porosity versus current density and etch rate versus current density data given in Ref. [12] for π -Si films made from similarly doped wafers, the porosity and layer thickness for a given film could be estimated from the applied current density value and the etch time. A pair of multilayered films with binary periodicity in the porosity were fabricated by applying a current density profile consisting of alternating current densities of \sim

34 mA/cm² and ~ 3.4 mA/cm² separated by 1 s etch-stops. The resulting constituent layers had estimated porosities of $\zeta_1 \sim 54$ % and $\zeta_2 \sim 45$ %, respectively, and were formed at estimated etch rates of ~ 28 nm/s and ~ 11 nm/s, respectively [12]. Critical to the creation of these SLs is the fact that π -Si formation is a self-limiting process and, furthermore, each constituent porous layer grows linearly with time. Moreover, for both SLs, the etch times were chosen such that the constituent layer thicknesses, d_1 and d_2 , were approximately equal. Cross-sectional scanning electron microscope images were collected for each SL and the modulation wavelengths $D = d_1 + d_2$ were determined from the overall film thickness (total film thickness is equal to $(D \times \text{number of cycles})$). Table 7.1 gives the etch times as well as the modulation wavelengths determined from the estimated etch rates, D^{EM} , and the cross-sectional scanning electron micrographs, D^{SEM} . In particular, D^{EM} was determined using the estimated etch rates together with the defined etch times. As one can see, D^{SEM} is comparable to D^{EM} and, in fact, the values for sample 1 agree within uncertainty. This suggests that, for the currently studied films, the sample parameters interpolated from the results given in Ref. [12] provide reasonable estimates of the constituent layer porosities and etch rates.

It is known that mesoporous silicon films are marked by a porosity-dependent mass density (*i.e.*, $\rho = \rho_{c-Si}(1 - \zeta_j)$, where $\rho_{c-Si} = 2330$ kg/m³ is the mass density of crystalline silicon and $j = 1, 2$ is the constituent layer index). Furthermore, both the sound velocities [8, 13–15] and the refractive index [12, 16] decrease with increasing

Table 7.1: π -Si superlattice etch times, t_1 and t_2 , the modulation wavelength value as determined using the estimated etch rates with the given etch times, D^{EM} , and the modulation wavelength value as determined from cross-sectional scanning electron microscope images, D^{SEM} .

Sample	t_1	t_2	D^{EM}	D^{SEM}
	s	s	nm	nm
1	1.568	4.703	93 ± 9	87 ± 2
2	2.059	6.176	120 ± 10	102 ± 3

porosity. In turn, the binary periodic SLs have a square-wave periodicity in both the elastic and electromagnetic properties. In particular, the sound velocities behave according to $V_j = V_{c-Si}(1 - \zeta_j)^\phi$, where V_{c-Si} is the corresponding sound velocity in crystalline silicon (either transverse (T) or longitudinal (L)) and ϕ is an empirical fit parameter, specific to the transverse and longitudinal modes, which is typically of the order of 1 [17]. Furthermore, the π -Si refractive indices may be deduced from ζ_j using the two-component Bruggeman effective medium model [16]. Taking into account the estimated constituent layer porosities, it follows from these previous works that there is at most a $\sim 20\%$ difference in the constituent layer mass densities, sound velocities [8, 13–15], and refractive indices [16]. In fact, the bulk longitudinal acoustic mode velocity is expected to be between ~ 4 km/s and ~ 5 km/s for each layer, while the corresponding bulk transverse acoustic mode velocities are expected to be between ~ 2 km/s and ~ 3 km/s [17]. As well, one should keep in mind that the refractive indices are wavenumber-dependent and, more specifically, the stated

estimate in the refractive index variation was determined assuming electromagnetic excitations in the visible spectral range.

Brillouin scattering experiments were carried out under ambient conditions using both a pseudo-reflection geometry and a 180°-backscattering geometry. The experimental methodology has been described previously [6]. In particular, a Nd:YVO₄ solid-state laser with beam wavelength of 532 nm (wavenumber $w_{\lambda_0} = 1.88 \mu\text{m}^{-1}$) was used to probe the samples. The resulting scattered light was collected using a 5 cm lens with $f/\# = 2.8$ or ~ 4.0 . For the pseudo-reflection geometry, the angle of incidence, θ_i , ranged from 35° to 67° while the angle between the axial ray of the scattered light and the sample surface normal, θ_s , was set 6° to 10° less than θ_i . The backscattering measurements were done for θ_i ranging from 7° to 80°. Note that $\theta_s = \theta_i$ in the 180°-backscattering geometry. Moreover, as was done in a previous study [18], spectra collected at near-normal incidence 180°-backscattering were taken to approximate spectra at ideal normal incidence. By extension, the near-normal incidence 180°-backscattering spectra then approximate pseudo-reflection geometry Brillouin spectra collected at $\theta_m \equiv (\theta_s + \theta_i)/2 = 0$ (*i.e.*, when both θ_i and θ_s are equal to zero).

In conjunction with the Brillouin light scattering measurements, additional experiments were done to characterize the optical properties of the SLs. Firstly, in order to confirm that the samples were one-dimensional visible range photonic crystals, normal-incidence broad-band reflectance measurements were done. These reflectance

readings were done using an optical setup outlined previously [6]. Secondly, in order to better understand how the probing 532 nm laser light propagates in the SLs, the angular dependence of sample reflectance at $\lambda = 532$ nm was measured using a simple optical setup which has been described elsewhere [19]. In particular, the reflectance of both p- and s-polarized light was investigated.

7.4 Theory

7.4.1 Phonon Propagation in an Infinite Superlattice

For π -Si SLs with a square-wave spatial modulation in the porosity of the order of 100 nm, acoustic phonons propagating along the layer-interface normal may be treated using a one-dimensional elastic continuum model and, thus, are governed by the dispersion relation [1, 2, 6]

$$\cos(QD) = \cos\left(\frac{\Omega d_1}{V_1}\right) \cos\left(\frac{\Omega d_2}{V_2}\right) - F \sin\left(\frac{\Omega d_1}{V_1}\right) \sin\left(\frac{\Omega d_2}{V_2}\right), \quad (7.1)$$

where Q is the phonon Bloch wavevector, $\Omega = 2\pi\nu$ is the phonon angular frequency, ν is the phonon frequency. V_j are the constituent layer phonon velocities (either longitudinal (L) or transverse (T)), F is

$$F = \frac{1}{2} \left(\frac{Z_1}{Z_2} + \frac{Z_2}{Z_1} \right), \quad (7.2)$$

and $Z_j = \rho_j V_j$ are the constituent layer elastic impedances. Without loss of generality, it may be assumed that $V_2 > V_1$ and $\rho_2 > \rho_1$. It follows from Eq. 7.1 that the acoustic

phonon dispersion curves are folded into mini-Brillouin zones of dimension $2\pi/D$ in reciprocal space. In the case that $Z_2 \approx Z_1$ or, more specifically, $V_2 \approx V_1$ and $\rho_2 \approx \rho_1$, then $F \approx 1$ and, consequently, the phonon dispersion relation can be approximated as [20, 21]

$$\Omega \approx V_{\text{eff}}Q = \pm V_{\text{eff}}|q| \pm 2l\pi \frac{V_{\text{eff}}}{D} \quad (7.3)$$

with effective velocity V_{eff} given by

$$V_{\text{eff}} = \left(\frac{V_1 V_2}{V_1 d_2 + V_2 d_1} \right) D \quad (7.4)$$

and Q defined as

$$Q = q + \frac{2l\pi}{D}. \quad (7.5)$$

In particular, q is the extended-zone-scheme (*i.e.*, zeroth-order) phonon wavevector and integer l is the phonon mode folding-order. The phonon band structure, in turn, can be treated as a series of intersecting linear dispersion curves with slopes of $\pm V_{\text{eff}}$ (see Fig. 7.1). Moreover, it can be shown that $V_2 \geq V_{\text{eff}} \geq V_1$ and, thus, the $l = 0$ band of the SL lies between that of the constituent layers. Furthermore, with $V_2 \approx V_1$, then $V_{\text{eff}} \approx V_2 \approx V_1$ and, consequently, away from the edges of a Brillouin, where the effect of phononic band gaps is most significant, the dependence of Ω on q exhibits behaviour similar to that of an elastically homogeneous material with elastic wave velocity V_{eff} .

For off-axis propagation, the phonon dispersion relation is, in general, much more complex than for the normal-incidence case [7]. In particular, the model must account

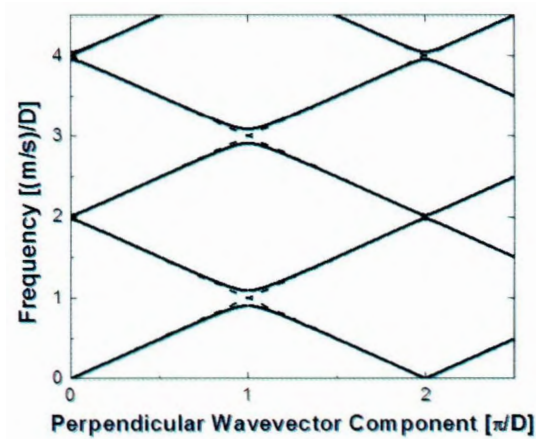


Figure 7.1: Schematic of the bulk acoustic phononic band structure along the modulation axis of a binary-periodic superlattice. The ratio in the acoustic velocities and mass density was 0.85 and 0.87, respectively. Calculations based on a one-dimensional elastic continuum model (solid curves) were reasonably approximated by a series of intersecting linear dispersion curves (dashed curves) which had slopes of $\pm V_{\text{eff}}$.

for the difference in refraction angle in each constituent layer and, in turn, the angle-dependent path in each layer. Continuing with the assumption that $V_2 \approx V_1$ and $\rho_2 \approx \rho_1$, however, the angle of refraction is approximately the same in both layers. Consequently, the SL band structure can be related to effective velocity $V_{\text{eff}} \approx V_2 \approx V_1$, which is approximately independent of propagation angle. That is, assuming the directional anisotropy of V_1 and V_2 is negligible and that $V_2 \approx V_1$, then V_{eff} is independent of propagation direction [22]. The off-axis phonon dispersion relation may then be approximated by

$$\Omega \approx V_{\text{eff}} \sqrt{Q_{\perp}^2 + q_{\parallel}^2}, \quad (7.6)$$

where Bloch wavevector Q_{\perp} (in contrast to Q stated above) depends on the components of the constituent layer phonon wavevectors directed perpendicular to the layer

interfaces and q_{\parallel} is the in-plane component of the phonon wavevector. Consequently, the SL exhibits an effective acoustic phonon phase velocity of V_{eff} with zone-folding accounted for in Q_{\perp} .

One should note that mode conversion and, therefore, coupling between the longitudinal and the horizontal transverse phonons was neglected in the preceding discussion. As has been shown in previous works [7, 23], the effects of this coupling will be most pronounced in regions where the longitudinal and horizontal transverse bands overlap, resulting in intra-zone band gaps. Furthermore, the widths of the intra-zone gaps tend to increase as $q_{\parallel}/(Q_{\perp}^2 + q_{\parallel}^2)^{\frac{1}{2}}$ increases. Hence, for spectral regions where the longitudinal and horizontal transverse phonon bands overlap, there will be a systematic error in the calculated folded dispersion curves obtained using Eq. (7.6). If, however, the width of a given intra-zone gap is small, this error in the band curvature is also small. As will be shown, the systematic error in the curvature of the bands is typically small for the samples studied here and, thus, oblique acoustic phonon propagation in π -Si can be reasonably treated with the simplified theory outlined above.

7.4.2 Oblique Angle Photon Propagation in an Infinite Superlattice

For visible-range photons in a π -Si SL with a binary periodicity in the porosity, propagation along the modulation axis of the SL is governed by [6, 24]

$$\cos(\kappa D) = \cos(K_1 d_1) \cos(K_2 d_2) - P \sin(K_1 d_1) \sin(K_2 d_2) \quad (7.7)$$

where κ is the photonic Bloch wavevector, $K_j = (2\pi n_j/\lambda)$ are the photon wavevectors in each constituent layer, n_j are the constituent layer refractive indices obtained using the two-component Bruggeman effective medium model [16], and λ is the corresponding photon wavelength in vacuum. The parameter P is expressed as

$$P = \frac{1}{2} \left(\frac{n_1}{n_2} + \frac{n_2}{n_1} \right). \quad (7.8)$$

Without loss of generality, it may be assumed that $n_2 > n_1$. In the case that $n_2 \approx n_1$, $P \approx 1$, Eq. (7.7) may be approximated by [25]

$$\kappa = \frac{2\pi}{\lambda} n_{\text{eff}} = \frac{\omega}{c} n_{\text{eff}}, \quad (7.9)$$

where ω is the photon angular frequency and n_{eff} is an effective refractive index of the overall SL:

$$n_{\text{eff}} = \frac{n_1 d_1 + n_2 d_2}{D}. \quad (7.10)$$

Hence, with κ taken to be in the extended-zone scheme, the photon dispersion curve is treated as a linear dispersion curve of slope c/n_{eff} . Further, it can be shown that

$$n_2 \geq n_{\text{eff}} \geq n_1$$

For oblique propagation, the photon dispersion takes the form [26, 27]

$$\cos(\kappa D) = \cos(K_{1x}d_1) \cos(K_{2x}d_2) - P_a \sin(K_{1x}d_1) \sin(K_{2x}d_2), \quad (7.11)$$

where $K_{jx} = (2\pi/\lambda)\sqrt{n_j^2 - \sin^2(\theta)}$ are the components of the constituent layer photon wavevectors perpendicular to the plane of the layer interface (the x-axis is set along the SL modulation axis), θ is the angle of propagation in vacuum and a denotes the polarization of the light. Parameter P_a is dependent on both the angle of incidence and the polarization of the propagating light (either p- or s-polarized), and takes the form

$$P_p(\theta) = \frac{1}{2} \left(\frac{n_1^2 K_{2x}}{n_2^2 K_{1x}} + \frac{n_2^2 K_{1x}}{n_1^2 K_{2x}} \right). \quad (7.12)$$

for p-polarized light. For s-polarized light, on the other hand, the parameter is expressed as

$$P_s(\theta) = \frac{1}{2} \left(\frac{K_{1x}}{K_{2x}} + \frac{K_{2x}}{K_{1x}} \right). \quad (7.13)$$

In the case that $n_2 \approx n_1$ (*i.e.*, $K_{2x} \approx K_{1x}$), however, $P_p(\theta) \approx P_s(\theta) \approx 1$. Further, with $n_2 \approx n_1 \approx n_{\text{eff}}$, the refraction angle within each constituent layer is approximately the same and, in a similar fashion as was discussed for V_{eff} , the value of the effective refractive index is essentially independent of the propagation direction. To put it another way, since $n_1 \leq n_{\text{eff}} \leq n_2$ for all angles of propagation, n_{eff} is approximately constant if $n_2 \approx n_1$. In particular, n_{eff} is a constant given by Eq. (7.10). In turn, for zeroth-order band, the optical behaviour of the SL can be approximated as an optically homogenous material with refractive index $n_{\text{eff}} \approx n_2 \approx n_1$. Similar assumptions

were made in previous Brillouin light scattering studies on phononic crystal materials in which the constituent materials exhibited a slight optical mismatch [22, 28, 29].

7.4.3 Brillouin Scattering from a Superlattice

In the case of Brillouin light scattering, a photon inelastically scatters from an acoustic phonon propagating in the probed material. Conservation of momentum dictates that

$$|\mathbf{q}| = |\mathbf{K}_s - \mathbf{K}_i|, \quad (7.14)$$

where \mathbf{q} is the probed phonon wavevector, while \mathbf{K}_i and \mathbf{K}_s are the incident and scattered photon wavevectors inside the material, respectively [30], and $K_s \approx K_i$. For scattering from a SL, the preceding conservation of momentum equation corresponds to the extended-zone scheme wavevectors (*i.e.*, $l = 0$ phonon band). That is, in order to take into account the translational invariance of the elastic properties along the SL modulation axis, the vector $(2l\pi/D)\hat{x}$, where \hat{x} is a unit vector directed along the modulation axis, must be added to the right-hand side of the above expression [25].

In the following discussion, Brillouin scattering from SLs will be outlined. In particular, it will be assumed that $V_2 \approx V_1$, $\rho_2 \approx \rho_1$ and $n_2 \approx n_1$ such that the phonon and photon band structures of the SL behaves according to the preceding effective band structure model. Furthermore, since the elastic and optical properties of the SLs exhibit a commensurate modulation, the corresponding mini-Brillouin zones

are the same size. Following from Eq. (7.14), however, the probed phonon wavevector is typically in a higher order mini-Brillouin zone than that of the probing photon.

When using a pseudo-reflection scattering geometry (see Fig. 7.2(a)), where $\theta_s \sim \theta_i$ (θ_i and θ_s are the angles that the incident photon wavevector and the scattering photon wavevector make with the surface normal, respectively), the angle between the phonon wavevector, \mathbf{q}_{PR} , and the surface normal, α_{PR} , is small. Thus, the phonon propagates nearly along the SL modulation axis with wavevector of magnitude

$$q_{PR} \approx q_{PR\perp}. \quad (7.15)$$

In such a case, it follows from Eq. (7.14) that [18]

$$q_{PR} = \frac{2\pi}{\lambda_o} n_{\text{eff}} (\cos(\theta_i) + \cos(\theta_s)) \approx 2\sqrt{\left(\frac{2\pi}{\lambda_o} n_{\text{eff}}\right)^2 - k_m^2}. \quad (7.16)$$

where $k_m = (2\pi/\lambda_o)\sin(\theta_m)$. λ_o is the wavelength of the probing laser, and $\theta_m = |\theta_i + \theta_s|/2$. Since the probed phonon propagates along the interface normal, Eq. (7.16) may be combined with Eq. (7.3) to obtain an expression for the probed phonon frequency which takes into account zone-folding of the phonon wavevector:

$$\nu_{PR} \approx \pm \frac{1}{\pi} V_{\text{eff}} \sqrt{\left(\frac{2\pi}{\lambda_o} n_{\text{eff}}\right)^2 - k_m^2} \pm l \left(\frac{V_{\text{eff}}}{D}\right). \quad (7.17)$$

Hence, values for V_{eff} , n_{eff} , and D can be obtained through an appropriate fit of experimentally-determined ν_{PR} versus k_m data. One should note that the plus-minus sign on the first term of the above expression takes into account both positive and negative dispersion of the zone-folded acoustic phonon bands, respectively. Specifi-

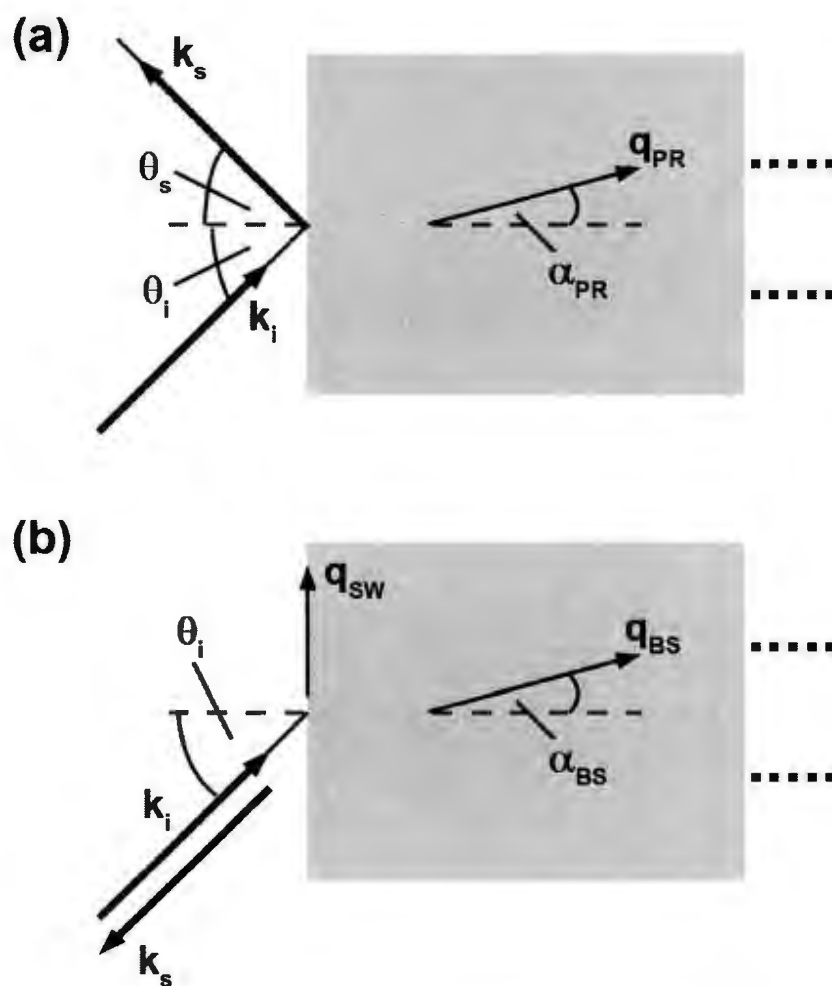


Figure 7.2: (a) pseudo-reflection and (b) 180°-backscattering geometries. The external incident (scattered) photon wavevector and probed phonon wavevector are, respectively, \mathbf{k}_i (\mathbf{k}_s) and \mathbf{q} . Bulk modes accessed by the pseudo-reflection geometry as well as surface-propagating and bulk modes accessed by the 180°-backscattering geometry are denoted by subscripts PR , BS , and SW , respectively. The angles \mathbf{k}_i , \mathbf{k}_s , and the bulk mode \mathbf{q} make with the surface normal are θ_i , θ_s , and α , respectively. For 180°-backscattering, $\theta_s = \theta_i$.

cally, for the l -th folding order mode, the first term is positive if q_{PR} , as defined by Eq. (7.16), is greater than $2l\pi/D$. Otherwise, the first term is negative.

When using a backscattering geometry, where $\theta_s = \theta_i$, the probing light may interact with either bulk phonons of wavevector \mathbf{q}_{BS} or surface phonons of wavevector \mathbf{q}_{SW} . In the case of bulk phonons, it follows from Eq. (7.14) that the components of q_{BS} perpendicular and parallel to the layer are given by

$$q_{BS\perp} = \frac{4\pi}{\lambda_o} \sqrt{n_{\text{eff}}^2 - \sin^2 \theta_i} \quad (7.18a)$$

$$q_{BS\parallel} = \frac{4\pi}{\lambda_o} \sin \theta_i. \quad (7.18b)$$

In order to take into account zone-folding of the bulk phonons, Eq. (7.18a) is combined with Eq. (7.5) while taking into consideration the fact that the phononic Bloch wavevector will depend on the perpendicular components of the constituent layer wavevectors. Consequently one finds that

$$Q_{BS} = q_{BS\perp} + \frac{2l\pi}{D} \quad (7.19)$$

and, following from Eq. (7.6), the probed phonon frequency is given by

$$\nu \approx \frac{1}{\pi} V_{\text{eff}} \sqrt{\left(q_{BS\perp} + \frac{2l\pi}{D} \right)^2 + (q_{BS\parallel})^2}. \quad (7.20)$$

It follows from Eqs. (7.18) and (7.20) that for the 180° -backscattering geometry, the frequency of the probed $l = 0$ bulk modes are approximately independent of θ_i (recall that Eqs. (7.18) and (7.20) are approximations). For all other folded phonon branches, however, $2\pi l/2 \neq 0$ and, thus, the frequencies of the corresponding observed phonon modes, in general, depend on θ_i .

In the case of surface-propagating modes probed using a 180° -backscattering geometry, only the in-plane components of the wavevectors are conserved (the amplitude of the surface phonon decays quickly away from the surface [31]). In turn, Eq. (7.14) gives

$$q_{SW} = \frac{4\pi}{\lambda_o} \sin \theta_i. \quad (7.21)$$

One should notice that there is no folding of the surface-propagating phonons as the wavevector is perpendicular to the SL modulation axis. Consequently, the frequency of the probed surface phonon is given by

$$\nu_{SW} = \frac{V_{SW} q_{SW}}{2\pi} = \frac{2V_{SW}}{\lambda_o} \sin \theta_i, \quad (7.22)$$

where V_{SW} is the surface phonon phase velocity. One can see from the above expression that if V_{SW} is constant, the surface phonon frequency increases linearly with $\sin \theta_i$ (or q_{SW}).

7.4.4 Brillouin Linewidth

Neglecting contributions to the spectral lineshape due to the instrumentation and the collection optics, it has been shown that Brillouin peaks can typically be approximated as Lorentz functions with a full-width-at-half-maximum of

$$\Delta\nu = \frac{C}{\pi} \chi V_g, \quad (7.23)$$

where V_g is the probed phonon group velocity, χ is an attenuation coefficient, and C is a constant which depends on the physical mechanism of attenuation ($C = 2$ if the

peak broadening is due to attenuation of the laser light, while $C = 1$ in the case of typical phonon attenuation) [32, 33]. If the main contribution to the peak broadening is due to attenuation of the probing laser light (termed opacity broadening), then χ is equal to the optical attenuation coefficient at λ_o [33]. On the other hand, if the main contribution to the linewidth is due to attenuation of the probed phonon, χ is the attenuation coefficient of the phonon mode [2, 32].

The attenuation coefficient corresponding to a given physical mechanism is typically dependent on the photon or phonon frequency. In fact, if the phonon (or photon) attenuation is dominated by a single physical mechanism, then $\chi \propto \nu^\gamma$, where γ is a real number which depends on the physical cause of the attenuation [2, 11, 32, 33]. For example, $\gamma = 0$ for opacity broadening [33] (the optical attenuation coefficient is practically constant over the photon frequency range considered), $\gamma = 2$ for viscous (Akheiser) broadening of the phonons [2, 11], and $\gamma = 4$ for Rayleigh scattering of the phonons [34].

For Brillouin spectra collected from SLs exhibiting the band structure as described above, $\chi = \chi_{eff}$, defined as

$$\chi_{eff} = \frac{\chi_1 d_1 + \chi_2 d_2}{D}, \quad (7.24)$$

where χ_j are the coefficients in each constituent layer. Furthermore, if the phonon or photon attenuation in each constituent layer is dominated by the same single physical mechanism (which is plausible for π -Si layers of comparable porosity), then it follows

that

$$\chi_{eff} \propto \nu^\gamma. \quad (7.25)$$

Moreover, since the SL phonon band structure is treated as a series of intersecting linear dispersion curves with slope $\pm V_{eff}$, then $V_g = |V_{eff}|$. Consequently, following from Eqs. (7.23) and (7.25), γ may be related to the Brillouin peak line shapes associated with two zone-folded modes of the same polarization as

$$\gamma = \frac{\ln(\Delta\nu_l/\Delta\nu_{l+\tau})}{\ln(\nu_l/\nu_{l+\tau})}. \quad (7.26)$$

where the subscripts denote the folding order and, in particular, the integer τ is the difference in the mode orders. Implicit in the above expression is the assumption that the broadening of the spectral peak corresponding to each zone-folded mode is attributed to the same physical mechanism. As well, the folded phonon bands are assumed to be approximately linear.

7.5 Results and Discussion

7.5.1 Optical Reflectance

To aid in the characterization of the photonic band structure of the π -Si films and, thus, understand how the probing laser light used in the Brillouin scattering experiments interacted with the SLs, normal-incidence broadband reflectance spectra were collected from each sample. Collected spectra contained peaks corresponding to

one-dimensional photonic band gaps in the visible spectral range, exhibiting the expected behaviour of increasing mid-gap wavenumber with decreasing D (see Fig. 7.3). In fact, the spectral position of the photonic band gap can be approximated by [6] $w_t = t/(2n_{\text{eff}}D)$, where t is the gap order. When the pores are filled with air, the observed Bragg peak in each SL is centered at wavenumber $w_{\text{gap}} \sim 2.25 \mu\text{m}^{-1}$, or a wavelength of $\sim 450 \text{ nm}$ (see Table 7.2). Since $D \sim 100 \text{ nm}$ and $n_{\text{eff}}(w_{\text{gap}}) \sim 2.5$ (an estimate of the effective refractive may be deduced from the estimated constituent layer porosities using the two-component Bruggeman effective medium model [16]), it follows that the photonic band gap is first-order (*i.e.*, $t = 1$). Additionally, filling the pores with ethanol led to a $\sim 0.06 \mu\text{m}^{-1}$ decrease in the peak position, indicative of an optical Bragg peak (*i.e.*, the introduction of the ethanol resulted in a corresponding increase in the effective refractive index, which resulted in a decrease in the mid-gap wavenumber).

The full-width-at-half-maximum of the reflectance peaks are $\sim 10\%$ of w_{gap} , suggesting that the corresponding photonic band gap is relatively narrow. This corroborates the fact that the contrast in the constituent refractive indices is small. Hence, the visible-range electromagnetic properties of the SLs may be reasonably treated using the effective photon band structure model outlined above. Note that the effect of photon attenuation, which would result in narrowing of the expected photonic band gaps, is taken to be negligible (studies have shown that visible-range optical

attenuation in π -Si films made from p^+ -type silicon is about an order of magnitude lower than that of bulk crystalline silicon [19, 35]).

Of particular interest is the behaviour of photons with a vacuum wavelength of 532 nm (*i.e.*, the laser line used in the Brillouin scattering experiments). The corresponding wavenumber, $w_{\lambda_o} = 1.88 \mu\text{m}^{-1}$, is below w_{gap} in both SLs and, thus, the resulting zeroth-order photon wavevector is within the first photonic mini-Brillouin zone. In fact, in the visible frequency range, the refractive index of π -Si increases with wavenumber [12] and, thus, $q(w_{\lambda_o})/q(w_{gap}) \approx (n_{\text{eff}}(w_{\lambda_o})w_{\lambda_o})/(n_{\text{eff}}(w_{gap})w_{gap}) < w_{\lambda_o}/w_{gap}$. In turn, the ratio in wavenumbers provides an estimate of the upper limit for the ratio between the corresponding photon wavevectors. Table 7.2 gives the wavenumber ratios and, hence, it is suggested that the wavevector of the probing laser light inside the SL is less than 0.86 that of the reciprocal lattice vector of the SL. Since the photonic band gap width is relatively small (approximately $w_{gap}/10$), it is reasonable to assume that the refracted wavevector of photons with vacuum wavenumbers of w_{λ_o} is far enough away from the edge of the first photonic mini-Brillouin zone such that, at this photon wavenumber, the SLs behave like optically homogeneous materials for the zeroth-order photon branch.

To further characterize the behaviour of the probing laser beam within the SLs, oblique angle reflectance measurements were taken. Figure 7.4 shows the incident angle-dependence of optical reflectance for both p- and s-polarized 532 nm ($w_{\lambda_o} = 1.88 \mu\text{m}^{-1}$) light. For each sample, the p- and s-polarization reflectance data were

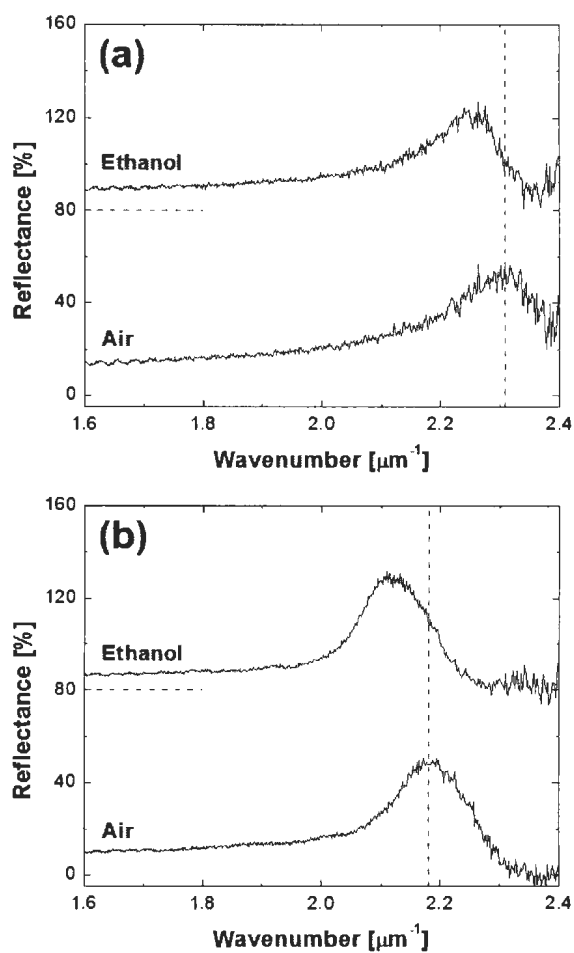


Figure 7.3: Optical reflectance spectra collected from (a) sample 1 and (b) sample 2. In each case, spectra were collected with the pores filled with air and ethanol. Horizontal dashed lines mark the 0% reflectance level for the spectra collected when the samples were filled with ethanol, while the vertical dashed line is a guide for the eye.

Table 7.2: Spectral positions of the first-order photonic band gaps, w_{gap} , the wavenumber ratio w_{λ_o}/w_{gap} , and the superlattice effective refractive index deduced using from the oblique reflectance measurements, $n_{\text{eff}}^{ob}(w_{\lambda_o})$.

Sample	w_{gap} (μm^{-1})	w_{λ_o}/w_{gap}	$n_{\text{eff}}^{ob}(w_{\lambda_o})$
1	2.18 ± 0.01	0.86	2.35 ± 0.01
2	2.31 ± 0.01	0.81	2.23 ± 0.02

fitted to the corresponding Fresnel equations for optical reflectance from a homogeneous dielectric material [36] using a least-squares fitting procedure. For each SL, the refractive index value fit parameter, n_{eff}^{ob} , was shared between the p- and s-polarization fits. As one can see, the data trended very well with the corresponding Fresnel equations, suggesting that the SLs do in fact behave like optically-homogeneous materials at w_{λ_o} . Table 7.2 gives the resulting n_{eff}^{ob} values. It is clear that sample 2 has a slightly lower n_{eff} value than that of sample 1, implying that there is a small difference in the constituent layer porosities for each SL. This is not surprising as sample-to-sample variation in porosity is common using the prescribed fabrication method [3, 6, 18].

7.5.2 Pseudo-Reflection Geometry Brillouin Scattering

Figure 7.5 shows typical Brillouin scattering spectra collected using a pseudo-reflection geometry as well as a near-normal incidence 180° -backscattering geometry. Three spectral peaks were observed, attributed to three bulk modes. The peak asso-

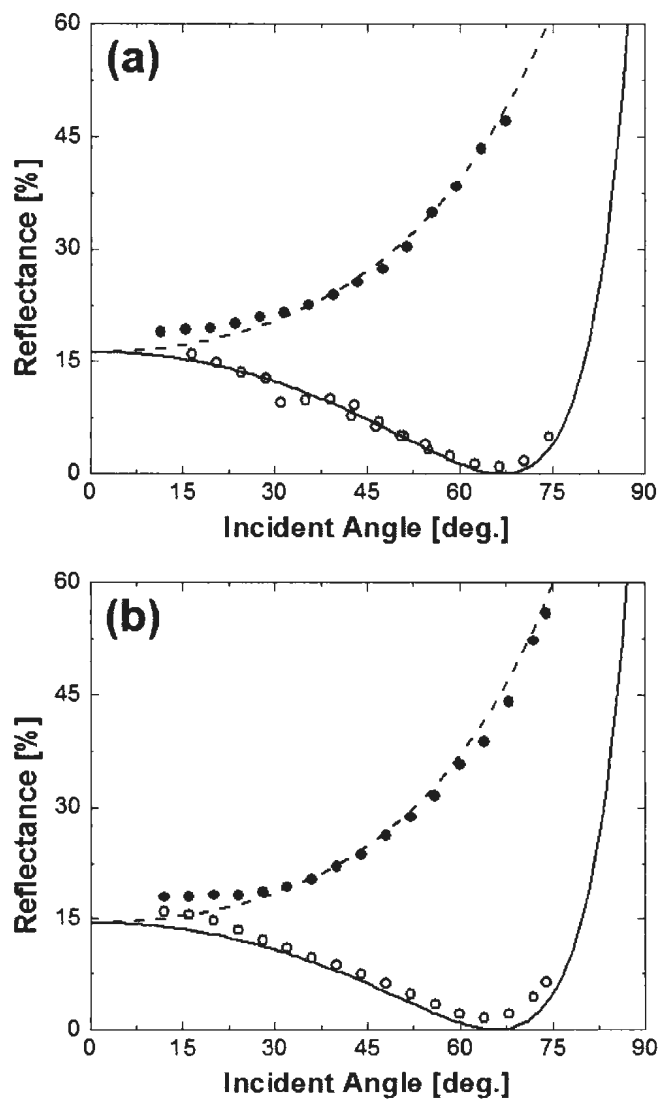


Figure 7.4: Optical reflectance versus incident angle for (a) sample 1 and (b) sample 2 with $\lambda_o = 532$ nm. Filled symbols: reflectance data for s-polarized light; empty symbols: reflectance data for p-polarized light. Fits of the Fresnel equation for reflectance from an optically-homogeneous material were done for each data set (solid and dashed curves).

ciated with one mode (labeled T_0) was not discernible in the $\theta_m = 0$ spectrum (*i.e.*, the spectrum collected using a near-normal incidence 180° backscattering geometry). Further, polarization analysis of the scattered light (achieved by placing a polarizer of either horizontal or vertical orientation in the path of the collected scattered light) showed that the light scattered by the T_0 mode was depolarized while the light scattered by the other two modes (labeled L_0 and L_{-1}) was not (see Fig. 7.6). It should be noted that when using a pseudo-reflection geometry, light scattered by transverse and longitudinal bulk modes is expected to be depolarized and polarized, respectively, and, further, the scattering cross-sections of transverse modes are expected to become negligible for probing light at near-normal incidence [30]. It is for these reasons that the T_0 peak was assigned to a bulk acoustic transverse mode while the L_0 and L_{-1} peaks were assigned to bulk acoustic longitudinal modes.

It is worth noting that since $K(w_{\lambda_o}) = \kappa(w_{\lambda_o}) < 0.86(\pi/D)$, it follows from Eq. (7.16) that $q_{PR} < 1.72(\pi/D)$. Thus, the bulk phonons accessed through Brillouin scattering have wavevectors located near the center of the second phononic mini-Brillouin zone. The three probed phonons are, thus, expected to behave according to Eq. (7.17) and, consequently, exhibit approximately linear dispersion. Since $n_{\text{eff}}^{\text{ob}} \sim 2.3$ and, taking into account the constituent layer sound velocity estimates deduced from the layer porosity values, the effective bulk mode sound velocities are $V_{T,\text{eff}} \sim 2.5$ km/s and $V_{L,\text{eff}} \sim 4.5$ km/s, it follows from Eq. (7.16) that for $\theta_m = 0$, $\nu_{T,l=0} \sim 22$ GHz and $\nu_{L,l=0} \sim 39$ GHz. Consequently, this suggests that the T_0 and L_0 peaks are due to the

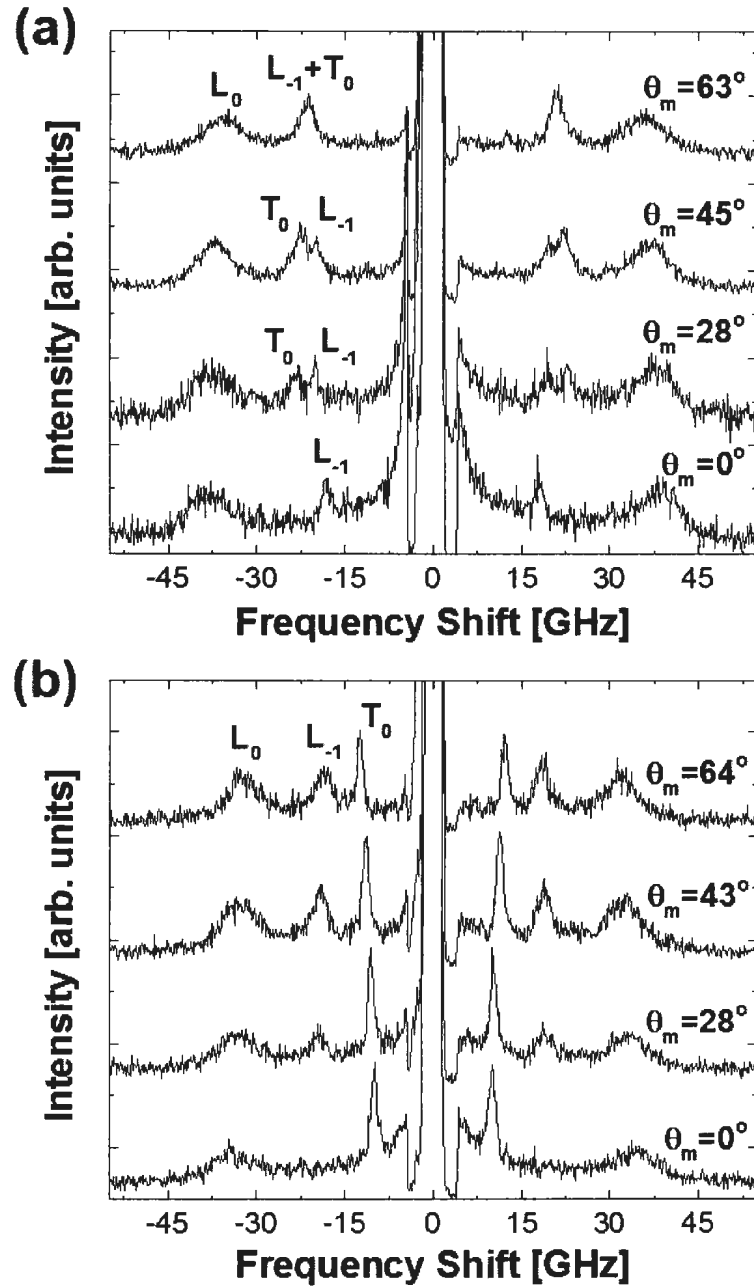


Figure 7.5: Brillouin spectra collected from (a) sample 1 and (b) sample 2 at different angles of incidence. Angle θ_i corresponds to the incident angle used in a 180° -backscattering geometry, while θ_m corresponds to the average angle used in a pseudo-reflection geometry. L_0 (L_{-1}): peak attributed to the $l = 0$ ($l = -1$) folded bulk longitudinal mode; T_0 : peak attributed to the $l = 0$ bulk transverse mode.

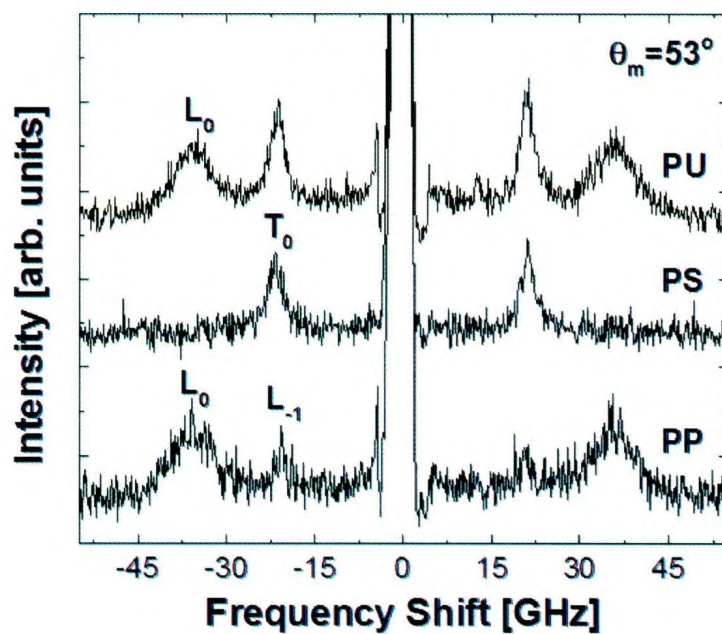


Figure 7.6: Polarized Brillouin spectra collected from the sample 1 at $\theta_m = 53^\circ$. PU: p-polarized (unpolarized) incident (scattered) light; PS: p-polarized (s-polarized) incident (scattered) light; PP: p-polarized (p-polarized) incident (scattered) light.

$l = 0$ transverse bulk acoustic mode and the $l = 0$ longitudinal bulk acoustic mode, respectively. This is corroborated by the fact that, for both peaks, the frequency decreases with increasing θ_m (*i.e.*, decreasing q_{PR}) which, according to Eq. (7.17), is the trend expected for the $l = 0$ bands. The frequency shift of the L_{-1} peak, on the other hand, increased with increasing θ_m (*i.e.*, decreasing q_{PR}). Taking into account the fact that q_{PR} is in the second mini-Brillouin zone and comparing the observed wavevector-dependence of the phonon frequency with that expected from Eq. (7.17), the L_{-1} peak is attributed to the $l = -1$ folded bulk longitudinal acoustic phonon. Consequently, as in the previous Brillouin scattering studies on acoustic phonon propagation in π -Si SLs [3, 6], zone-folding of the longitudinal bulk acoustic phonon dispersion curve was observed, while no zone-folding was observed for the transverse bulk acoustic phonon.

Equation (7.17) was fitted to the k_m^2 -dependent phonon frequency data corresponding to the three modes in each SL (see Fig. 7.7). In particular, the form of Eq. (7.17) specific to a given mode (*i.e.*, given l value) was fit to the applicable data through a least-squares fitting procedure. Further, the three sets of mode data for each SL were analyzed simultaneously with n_{eff} and $V_{L,\text{eff}}$ shared between the different mode fits. While the function could be fitted to the data without placing constraints on the fit parameters, in order to have consistency with the previously obtained $n_{\text{eff}}^{\text{ob}}$ and D^{SEM} , these particular parameters had to be fixed. Fixing both n_{eff} and D resulted in very poor fits (*i.e.*, adjusted coefficient of determination $R^2 < 0.70$), how-

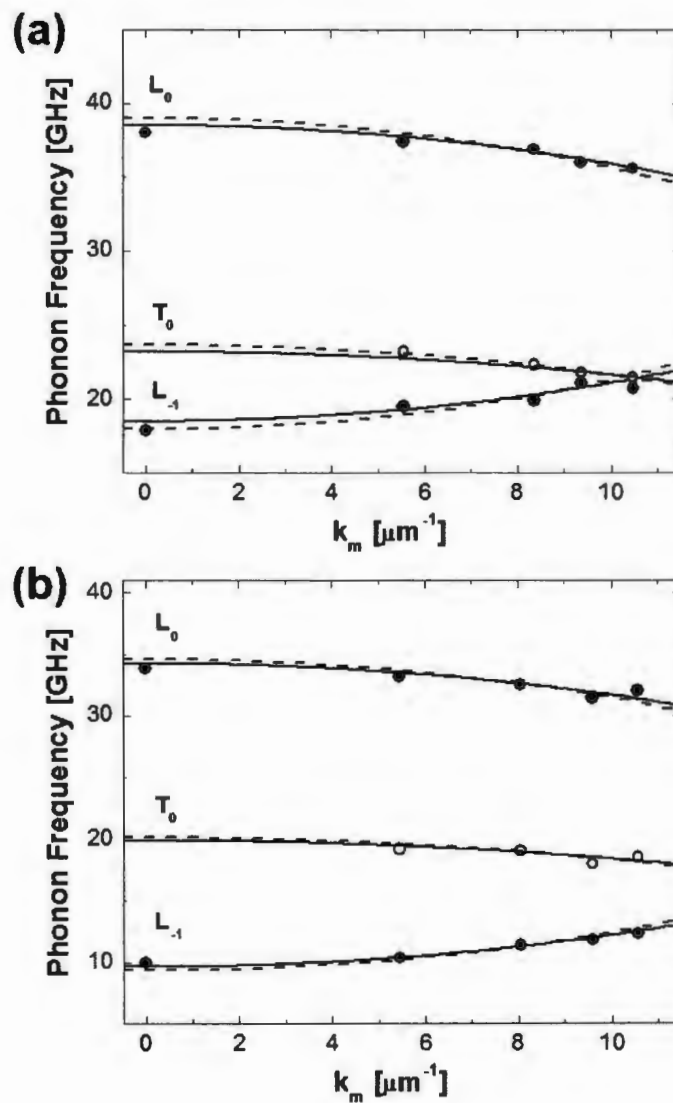


Figure 7.7: Dependence of bulk longitudinal (filled symbols) and transverse (empty symbols) mode frequency on k_m^2 for (a) sample 1 and (b) sample 2. The solid (dashed) curves correspond to the fits of Eq. (7.17) with fixed n_{eff} (D). The three different bands are labeled. Note: error bars corresponding to the uncertainty in the phonon frequency is comparable to the symbols.

Table 7.3: Porous silicon SL effective refractive index n_{eff} , effective bulk acoustic longitudinal mode velocity $V_{\text{L,eff}}$, effective bulk acoustic transverse mode velocity $V_{\text{T,eff}}$, and modulation wavelength D . The fit parameters in parentheses are those obtained for D fixed to the D^{SEM} value given in Table 7.1, while the other fits parameters were obtained with n_{eff} fixed to the $n_{\text{eff}}^{\text{ob}}$ value given in Table 7.2.

Sample	n_{eff}	$V_{\text{L,eff}}$ (km/s)	$V_{\text{T,eff}}$ (km/s)	D (nm)
1	2.35 (2.09 ± 0.01)	4.36 ± 0.02 (4.96 ± 0.02)	2.62 ± 0.03 (3.01 ± 0.04)	76.4 ± 0.2 (87)
2	2.23 (2.05 ± 0.01)	4.08 ± 0.04 (4.48 ± 0.06)	2.37 ± 0.06 (2.6 ± 0.1)	93.1 ± 0.21 (102)

ever, and it was found that only one of the two parameters in question could be constrained at a time while still achieving $R^2 \sim 1$. Table 7.3 shows the results of the fits deduced for each SL. Comparing the two fits obtained for each SL, there was $\sim 10\%$ variation in the effective refractive index, effective longitudinal and transverse sound velocities, and the modulation wavelength. Further, for both samples, the fixed- n_{eff} fit gave a slightly better result, with a larger R^2 value. Overall, these results suggest that $4 \text{ km/s} < V_{\text{L,eff}} < 5 \text{ km/s}$ and $2 \text{ km/s} < V_{\text{T,eff}} < 3.1 \text{ km/s}$, as expected from the consideration of the dependence of acoustic phonon sound velocity on porosity. Additionally, the effective sound velocities for sample 2 are, in general, slightly less than that of sample 1 which, together with the trend observed in n_{eff} , further suggests a slight sample-to-sample variation in the porosity of the SL films.

7.5.3 Bulk Longitudinal Mode Linewidths

The linewidths of both folded bulk longitudinal modes were studied in order to gain insight into the mechanism behind the peak broadening. In particular, the near-normal incidence 180° backscattering spectrum of each SL was analyzed. The reasons for choosing these particular spectra are three-fold. Firstly, there is no contribution to the bulk mode linewidth stemming from the aperture broadening that results from the finite size of the collection optics (aperture broadening depends on sine of the scattering angle) [37]. Secondly, as implied by Eqs. (7.18), (7.19), and (7.20), both longitudinal modes would be propagating approximately along the same direction (*i.e.*, near-normal to the layer interfaces). Thirdly, coupling between the transverse and longitudinal mode bands was expected to be negligible as phonon propagation is approximately normal to the layer interfaces [7] and thus effects due to changes in the band curvature (*i.e.*, phonon group velocity) due to the presence of intra-zone gaps can be neglected. The latter two points are particularly important when comparing the linewidths of both longitudinal modes, as mode coupling and a change in the propagation direction may not affect both bands in the same way.

Figure 7.8 show the near-normal incidence 180° -backscattering geometry spectrum collected from sample 1. Prior to analyzing the spectral linewidths of the Brillouin peaks, the shoulder of the central elastic peak had to be taken into account. To facilitate removal of this spectral contribution, both the Stokes and anti-stokes portion of the spectrum were fitted with a zero-frequency-shifted Lorentian raised to an arbi-

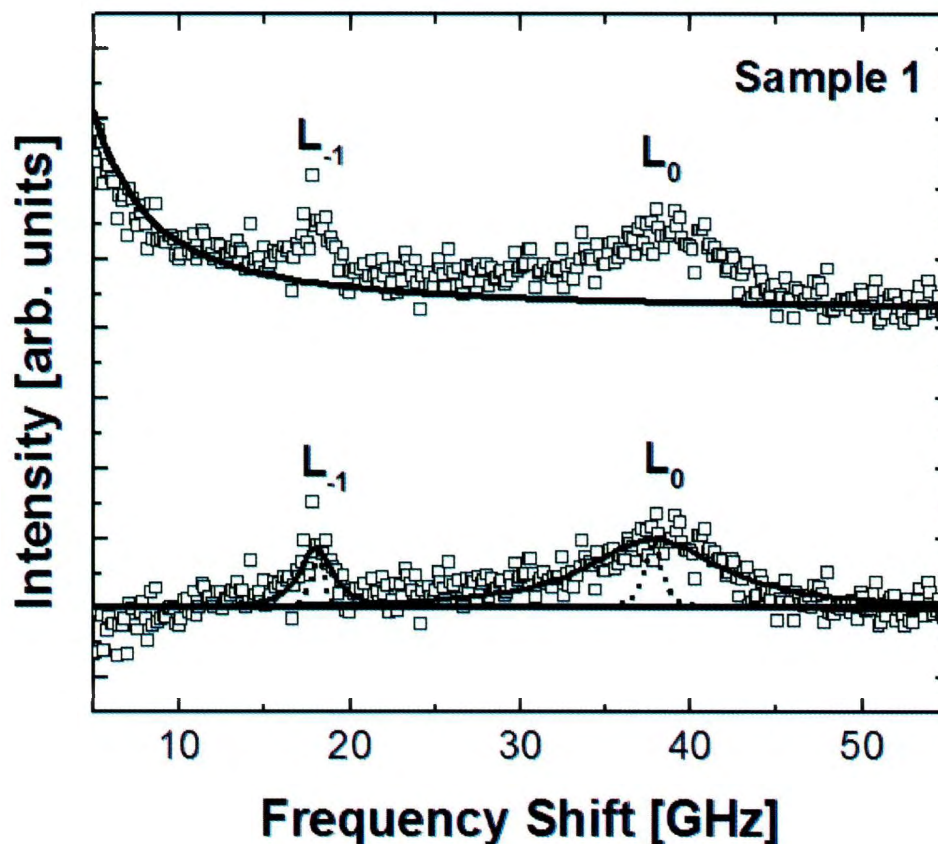


Figure 7.8: (a) Anti-Stokes portion of the near-normal incidence 180° -backscattering spectrum collected from sample 1. The contribution from the low-frequency shoulder was fitted with a zero-frequency-shifted Lorentzian raised to a power. Empty symbols: experimental data; thick curve: resulting fit to the low-frequency shoulder. (b) The corresponding near-normal incidence 180° -backscattering spectrum with the shoulder contribution removed. Empty symbols: experimental data; thick solid peak Lorentz functions: peaks resulting from the de-convolution of the fitted spectral peaks with the instrumental response function; thick dotted Lorentz functions: peaks corresponding to the opacity-broadening feature obtained when assuming optical attenuation equal to that of crystalline silicon [38].

trary power: the peak baseline was fixed to ensure that the resulting function agreed with the data corresponding to frequency shifts beyond the Stokes and anti-Stokes L_0 peaks. Once the fit to the center line shoulder was obtained, this contribution was removed through simple subtraction. The resulting Brillouin peaks were fitted with Lorentzians and the contribution of the instrumental response (taken to be a Lorentzian raised to the sixth power as spectral analysis was done with a six-pass tandem Fabry-Perot interferometer [39]) was removed through a discrete de-convolution. Removing the instrument response, however, had little effect on the original Lorentz functions.

One should note that the linewidth of the L_0 peak was comparable to that of the bulk longitudinal mode in single-layer π -Si films [8], suggesting that effects due to scattering at the constituent layer interfaces were negligible. Furthermore, since the optical attenuation of π -Si is relatively small over the visible-range (*i.e.*, about an order of magnitude smaller than that of crystalline silicon [35]), opacity broadening is not considered a major contributor to the linewidths. In fact, even if the optical attenuation was equivalent to that of bulk silicon, the resulting calculated line-shape would not account for the broad features observed in the Brillouin spectra (see Fig. 7.8). Moreover, since the probed phonon wavelength (~ 120 nm) is about an order of magnitude larger than the characteristic size of the pore walls in the structure (~ 10 nm) [6], any potential contribution to the line-shape due to scattering within the nanostructure would probably be from Rayleigh scattering.

With this in mind, the linewidths of both the L_0 and L_{-1} spectral peaks were compared in order to gain further insight into the physics underlying the Brillouin peak broadening. That is, assuming that the same (single) physical mechanism causes the broadening of both peaks and that $|V_g|$ was the same for the $l = 0$ and $l = -1$ bands, then it follows from Eq. (7.26) that $\gamma \sim 2$ for both SLs (the exact values of γ , as well as the spectral data from which they were deduced, are given in Table 7.4). Hence, the linewidths appear to be due to near-ideal viscous (Akheiser) attenuation of the probed phonons. In view of this simple analysis, however, one should note that while there may in fact be more than one physical process contributing to the observed Brillouin line-shapes, the current analysis seems to be sufficient to eliminate both opacity broadening and phonon Rayleigh scattering as possibilities.

Using Eq. (7.23) together with $C = 1$, the resulting bulk longitudinal acoustic mode attenuation coefficients were calculated (see Table 7.4). Taking into account the frequency-dependence of the attenuation coefficient, these values are in line with results obtained via ultrasonic measurements (*i.e.*, phonon frequency of about 1 GHz) on single-layer mesoporous silicon made from p^+ -type silicon [40]. Furthermore, these attenuation coefficients are about 2 orders of magnitude larger than that expected for bulk crystalline silicon at comparable frequencies (*i.e.*, $\sim 0.001 \mu\text{m}^{-1}$ to $\sim 0.01 \mu\text{m}^{-1}$ [41, 42]). This increase in phonon attenuation is thought to be a manifestation of the porous nature of the SLs. Additionally, considering that the amplitude of the mode displacement is proportional to $e^{-\lambda_{eff}x}$ [11], the amplitude of the

Table 7.4: The peak positions, ν_0 and ν_{-1} , the fitted linewidths, $\Delta\nu_0$ and $\Delta\nu_{-1}$, the attenuation exponent value, γ , the associated folded bulk longitudinal mode attenuation coefficients, χ_0 and χ_{-1} , and the corresponding propagation distances of the phonons, h_0 and h_{-1} , for the probed SLs. $V_g = V_{L,\text{eff}}$ given in Table 7.3 for the fits with n_{eff} fixed to $n_{\text{eff}}^{\text{ob}}$ since the corresponding pseudo-reflection data fit had a higher R^2 value.

Sample	ν_0	$\Delta\nu_0$	ν_{-1}	$\Delta\nu_{-1}$	γ	χ_0	χ_{-1}	h_0	h_{-1}
	(GHz)	(GHz)	(GHz)	(GHz)		(μm^{-1})	(μm^{-1})	(μm)	(μm)
1	37.9 ± 0.2	9 ± 1	18.1 ± 0.1	2.1 ± 0.4	2.0 ± 0.5	6.5 ± 0.7	1.5 ± 0.3	0.15 ± 0.02	0.7 ± 0.1
2	33.7 ± 0.2	9 ± 1	10.0 ± 0.1	1.2 ± 0.1	1.7 ± 0.2	6.9 ± 0.8	0.92 ± 0.09	0.15 ± 0.02	1.1 ± 0.1

L_0 and L_{-1} modes decrease to e^{-1} at distances of $h_0 \sim 0.15 \mu\text{m}$ and $h_{-1} \sim 1 \mu\text{m}$, respectively. Since $h_0 \sim D$, it is not surprising that no zone-folded modes were observed at frequencies greater than that of the $l = 0$ branch.

7.5.4 Oblique 180° -Backscattering Geometry Brillouin Scattering

Figure 7.9 shows typical oblique-angle 180° -backscattering geometry Brillouin spectra collected from the SLs. Up to five peaks were observed in these spectra. Unlike with the pseudo-reflection geometry experiments, the relationship between the polarization of the scattered light and the polarization of the scattering phonon modes is not trivial when using an oblique backscattering geometry and, consequently, the character of the modes associated with each peak could not be deduced in a similar fashion to what was done above. Following from the peak assignments made during the analysis of the pseudo-reflection geometry measurements, the three broad, relatively high frequency-shift, low intensity peaks were thought to be due to the $l = 0$ and $l = -1$ longitudinal bulk acoustic phonons and the $l = 0$ transverse bulk acoustic phonon (denoted by L_0 , L_{-1} , and T_0 , respectively). The relatively high intensity and narrow line-shape of the remaining two peaks (denoted by R and PS) suggest that these are associated with surface-propagating phonons. The presence of two surface modes in the π -Si SLs was not surprising as studies on single-layer π -Si films in this laboratory showed evidence of a Rayleigh phonon as well as other

q_{\parallel} -dependent modes which was assigned to pseudo-surface or guided phonons located at the air-film interface of the relatively thick (*i.e.*, $\sim 5 \mu\text{m}$) films [17]. That is, the exact nature of the supposed pseudo-surface mode is not known, but in the case of the previously studied single-layer films, the samples were thought to be too thick to suggest that the PS peak was due to a film-substrate interface-propagating mode or a film guided mode.

Analysis of the three peaks attributed to bulk acoustic phonons (see Fig. 7.10) revealed that the frequency shifts of two of the peaks were relatively independent of θ_i (centered at ~ 35 GHz and ~ 20 GHz). Taking into account the bulk mode assignments in the pseudo-reflection experiments together with the fact that the frequency of the probed $l = 0$ modes are expected to be θ_i -independent when using a 180° -backscattering geometry (as outlined by Eq. (7.20)), these peaks are attributed to the L_0 and T_0 bulk acoustic phonons. The mode assignment for the T_0 peak is corroborated by the fact that this spectral feature was not discernible in oblique angle 180° -backscattering geometry Brillouin spectra collected at incident angles less than $\theta_i \approx 30^\circ$ (*i.e.*, when approaching near-normal incidence), which, as mentioned above, is indicative of scattering from a transverse phonon [30]. Additionally, the frequency shift of the third peak was found to be dependent on incident angle. Further, comparison of the spectra suggest that this peak overlaps the T_0 peak and, in the case of the sample 1, surpasses the frequency shift of the T_0 peak over the accessed values of θ_i . Considering the mode assignments deduced from the pseudo-reflection geometry

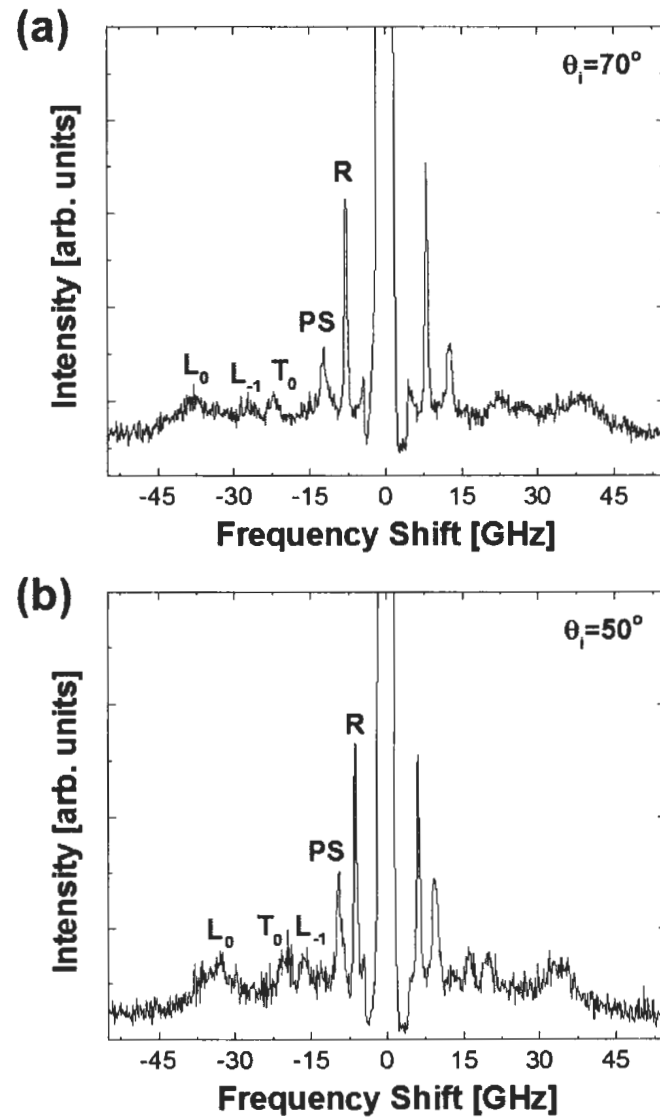


Figure 7.9: Oblique 180° -backscattering Brillouin spectra collected from (a) sample 1 and (b) sample 2 with $\theta_i = 70^\circ$ and 50° , respectively. R: peak attributed to the Rayleigh surface mode; PS: peak attributed to a pseudo-surface mode.

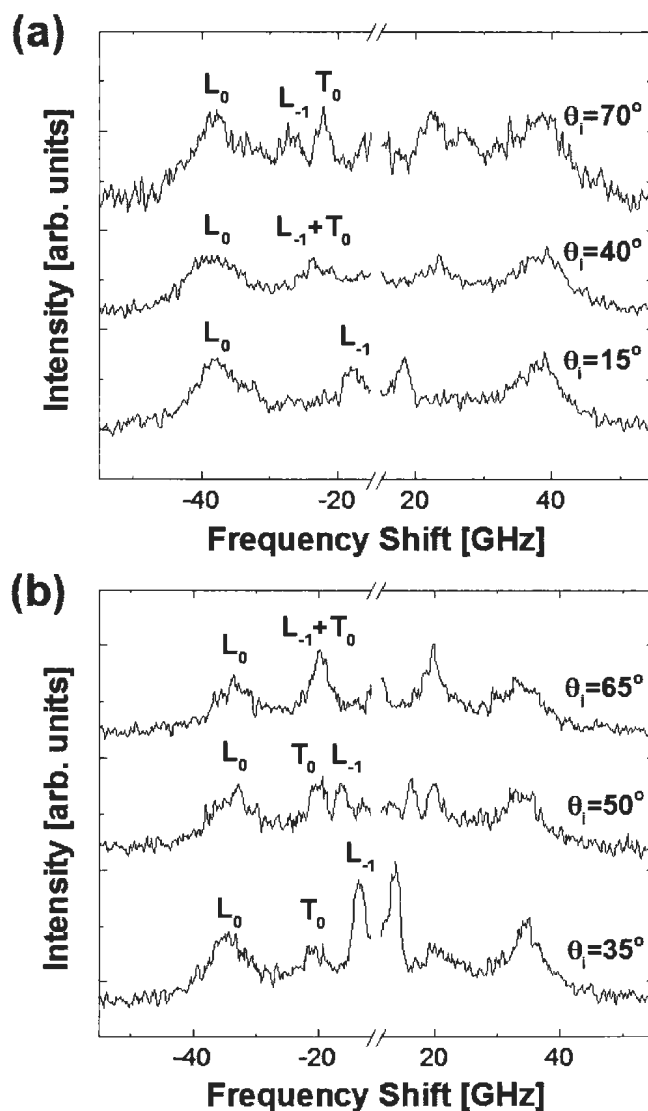


Figure 7.10: Oblique 180° -backscattering Brillouin spectra focusing on spectral features from bulk modes in (a) sample 1 and (b) sample 2. Spectra are smoothed using three-point adjacent averaging. $L_{-1}+T_0$: spectral feature which appears to correspond to overlapped L_{-1} and T_0 peaks.

measurements, the θ_i -dependence of the peak frequency shift (*i.e.*, phonon frequency), and the expected dependence of ν_{BS} on θ_i for $l \neq 0$ (following from Eq. (7.20)), this third peak was assigned to the L_{-1} mode.

Figure 7.11 shows a comparison between the experimental bulk phonon frequency versus q_{\parallel}^2 data with calculations based on Eq. (7.20). In particular, the calculations were based on the effective refractive index, the effective sound velocities, and the modulation wavelengths deduced in pseudo-reflection geometry experiments. As one can see, the data agrees very well with the calculated curves. The agreement suggests that for the phonon wavevectors probed in both the pseudo-reflection geometry and the oblique 180° -backscatter geometry Brillouin scattering experiments, the phonon and photon band structures of the SLs were reasonably treated as a series of linear dispersion curves. Further, it implies that it was fair to neglect the effects of phonon mode conversion and, in particular, coupling between the $l = -1$ bulk longitudinal acoustic phonon and the $l = 0$ bulk transverse acoustic phonon. Overall, there is no strong evidence that there is an intra-zone gap in these SLs.

Figure 7.12 shows spectra containing Brillouin peaks attributed to the Rayleigh surface mode (R) and a pseudo-surface mode (PS). The frequency shifts of both the R and PS peaks increase with θ_i , thereby implying that the corresponding phonon frequencies increase with increasing q_{\parallel} . Plotting surface mode velocity versus $q_{\parallel}D$, however, one can see that the velocities of the modes increase with decreasing $q_{\parallel}D$ (see Fig. 7.13). Thus, the observed surface modes are dispersive. Since no evidence

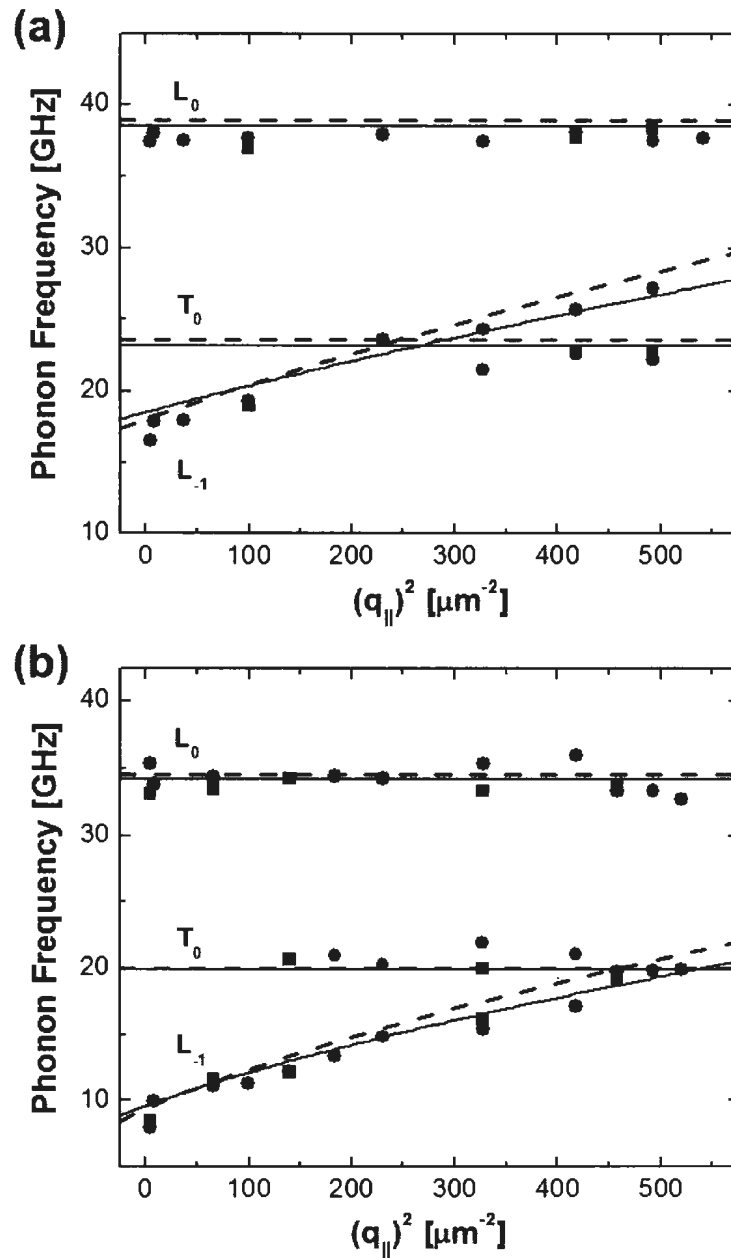


Figure 7.11: Dependence of bulk mode frequency on q_{\parallel}^2 for (a) sample 1 and (b) sample 2. Filled squares: duplicate data collected from sample 2; solid (dashed) curves: calculations using Eq. (7.20) together with the fit parameters obtained with n_{eff} fixed to $n_{\text{eff}}^{\text{ob}}$ (D fixed to D^{SEM}) given in Table (7.3). The three different bands are labeled. Note: error bars corresponding to the uncertainty in the phonon frequency is comparable to the size of the symbols.

of such surface mode dispersion was reported in previous studies on single-layer π -Si films [17, 43, 44], it is conceivable that this dispersive effect is an artefact of the layered structure of the current films. Specifically, it is possible that as q_{\parallel} decreases and, thus, the surface mode wavelength (~ 300 nm) increases, material at a greater depth in the structure begins to influence the surface phonon behaviour. In turn, the influence of the second constituent layer, which has the lower porosity (*i.e.*, larger sound velocities), increases as q_{\parallel} decreases and, hence, the velocity of the corresponding surface phonon increases [45]. In this case, it is expected that at some phonon wavelength much greater than D , the phonon velocity will no longer change with decreasing wavelength; this trend was not observed in the current results, which may be due to the limited range of q values accessed in the Brillouin experiments. Overall, further experiments should be done to gain a more complete understanding of the dispersive nature of these phonon modes.

As one can see, the range of Rayleigh phonon velocities, $2.1 \text{ km/s} < V_R < 2.5 \text{ km/s}$ is of the order of $V_{T,\text{eff}}$, which is expected [17]. Furthermore, $3.0 \text{ km/s} < V_{PS} < 4.2 \text{ km/s}$, which is in the range of $V_{T,\text{eff}}$ and $V_{L,\text{eff}}$, typical of a pseudo-surface mode [46]. While the obtained results suggest that the PS peak is due to scattering from a pseudo-surface mode, the exact nature of the phonon could not be deduced.

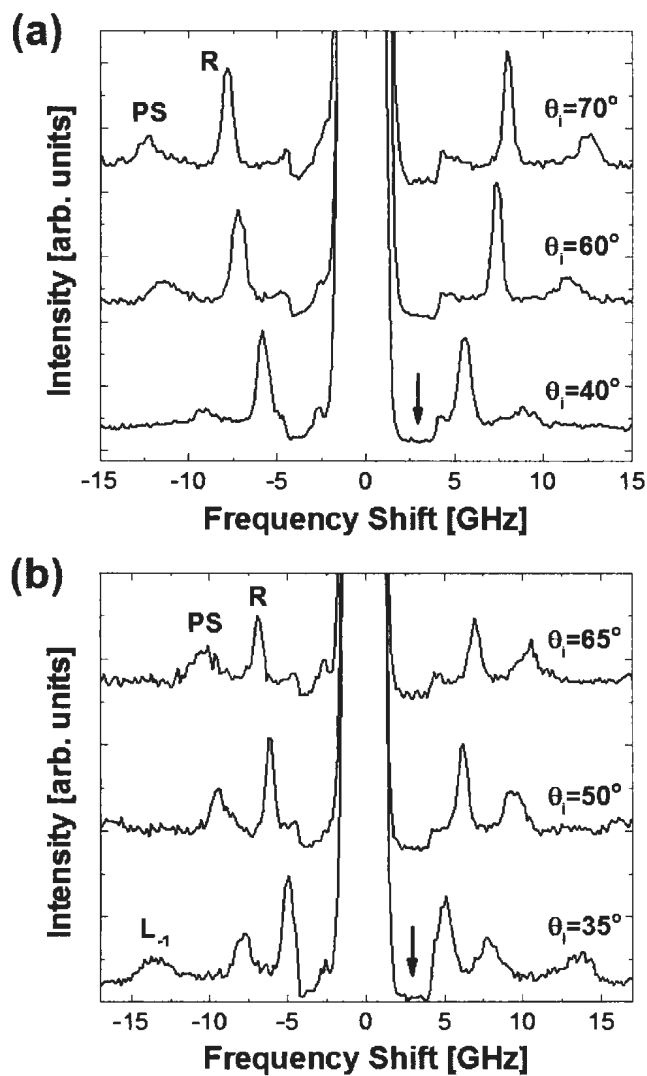


Figure 7.12: Oblique 180° -backscattering Brillouin spectra focusing on the θ_i -dependence of spectral features attributed to surface-propagating modes in (a) sample 1 and (b) sample 2. The peak at ~ 0 GHz corresponding to elastically scattered light was shuttered to prevent photomultiplier saturation. The arrow indicates a portion of the spectra that is within this shuttered region.

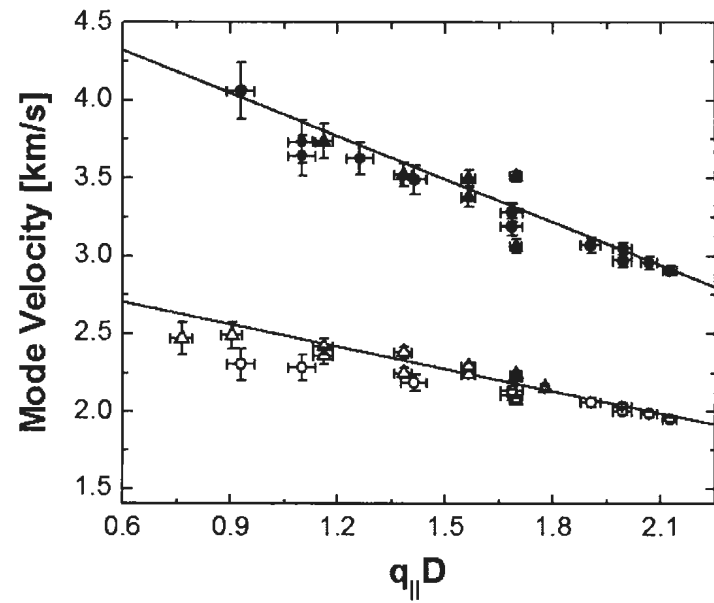


Figure 7.13: Surface mode velocity versus $q_{||}D$ for the Rayleigh (empty) and a pseudo-surface (filled) in sample 1 (triangles) and sample 2 (circles). The values of D obtained from the fits of the pseudo-reflection geometry with $n_{\text{eff}} = n_{\text{eff}}^{\text{ob}}$ were used since the corresponding pseudo-reflection data fit had given a higher R^2 value. The solid lines serve as a guide for the eye.

7.6 Conclusions

Both Brillouin light scattering experiments and optical reflectance measurements were performed on two binary periodic π -Si SLs. In particular, two longitudinal bulk acoustic phonons and a single transverse bulk acoustic phonon were observed and the SLs exhibited an optical Bragg peak corresponding to a one-dimensional photonic band gap in the visible range. Results showed that, provided the porosity ratio between the constituent layers was close to one, the complex phononic-photonic crystal behaviour of these films could be effectively modeled by simply treating the band structures as a series of intersecting linear dispersion curves. Combining results obtained through pseudo-reflection geometry Brillouin spectroscopy and optical reflectance measurements, values for the effective sound velocities, the effective refractive index, and the SL modulation wavelength were obtained. Furthermore, bulk acoustic phonons propagating at oblique angles to the SL were also probed through oblique 180° -backscattering geometry Brillouin scattering. Comparing the obtained data to calculations based on the above theory, it was confirmed that, unlike the zeroth-order longitudinal and transverse phonons, the Brillouin shift of the observed zone-folded longitudinal acoustic phonon depends on the propagation direction. Interestingly, no intra-zone gaps due to coupling between the folded longitudinal bulk acoustic phonon band and the transverse bulk acoustic phonon band were observed.

Moreover, analysis of the Brillouin peaks corresponding to both of the observed zone-folded bulk longitudinal phonons suggested that the main contribution to the

linewidth stems from viscous attenuation of the phonons. The resulting phonon attenuation coefficients were found to be several orders of magnitude larger than that of bulk crystalline silicon. This suggests that the porosity has a strong effect on bulk phonon attenuation.

In addition to the bulk acoustic phonons, the Rayleigh surface mode as well as a pseudo-surface mode were observed. Both modes were dispersive, with the velocity increasing as the wavevector decreased. It is suggested that this dispersion is due to the fact that as the wavevector decreases, there is an increased influence of the second, lower-porosity layer of the SL unit-cell.

Chapter 7 References

- [1] A. Kiuchi, B. Gelloz, A. Kojima and N. Koshida, Possible Operation of Periodically Layered Nanocrystalline Porous Silicon as An Acoustic Band Crystal Device. In *Materials Research Society Symposium Proceedings Series, Vol. 832*, edited by L. Tsybeskov, D. J. Lockwood, C. Delerue and M. Ichikawa. (Warrendale, PA, 2005).
- [2] G. N. Aliev and P. A. Snow, *Mater. Res. Soc. Symp. Proc.* **1145**, MM13-04 (2009).
- [3] L. C. Parsons and G. T. Andrews, *Appl. Phys. Lett.* **95**, 241909 (2009).
- [4] G. N. Aliev, B. Goller, D. Kovalev, and P. A. Snow, *Appl. Phys. Lett.* **96**, 124101 (2010).
- [5] L. Thomas, G. N. Aliev, and P. A. Snow, *Appl. Phys. Lett.* **97**, 173503 (2010).
- [6] L. C. Parsons and G. T. Andrews, *J. Appl. Phys.* **111**, 123521 (2012).
- [7] S. Tamura, D.C. Hurley, and J.P. Wolfe, *Phys. Rev. B* **38**, 1427 (1988).

- [8] A. M. Polomska-Harlick and G. T. Andrews, *J. Phys. D: Appl. Phys.* **45**, 075302 (2012).
- [9] A. M. Polomska and G. T. Andrews, *Phys. Status Solidi C* **6**, 1665 (2009).
- [10] G.T. Andrews, A.M. Polomska, E. Vazsonyi, and J. Volk, *Phys. Status Solidi A* **204**, 1372 (2007).
- [11] B. A. Auld. *Acoustic Fields and Waves in Solids*. (John Wiley and Sons, New Jersey, 1973).
- [12] L. Pavesi, *Riv. Nuovo Cimento* **20**, 1 (1997).
- [13] R. J. M. Da Fonseca, J. M. Saurel, G. Despaux, A. Foucaran, E. Massone, T. Taliercio, and P. Lefebvre, *Superlattices Microstruct.* **16**, 21 (1994).
- [14] R. J. M. Da Fonseca, J. M. Saurel, A. Foucaran, E. Massone, T. Taliercio, and J. Camassel, *Thin Solid Films* **255**, 155 (1995).
- [15] G. N. Aliev, B. Goller, D. Kovalev, and P. A. Snow, *Phys. Status Solidi C*, **6**, 1670 (2009).
- [16] C. Pickering, M. L. Beales, D. J. Robbins, D. J. Pearson, and R. Greef, *J. Phys. C* **17**, 6535 (1984).
- [17] A. M. Polomska. *Elastic properties of porous silicon superlattices*. Ph.D. thesis, Memorial University of Newfoundland (2010).

- [18] L. C. Parsons and G. T. Andrews, *AIP Advances* **2**, 032157 (2012).
- [19] J. Peckham and G. T. Andrews, *Thin Solid Films* **520**, 2526 (2012).
- [20] S. Kumar and H. J. Trodahl, *J. Appl. Phys.* **70**, 1 (1991).
- [21] R. Hotz and R. Siems, *Solid State Commun.* **51**, 793 (1984).
- [22] D. Schneider, F. Liaqat, E. H. El Boudouti, Y. El Hassouani, B. Djafari-Rouhani, W. Tremel, H.-J. Butt, and G. Fytas, *Nano Lett.* **12**, 3101 (2012).
- [23] P. V. Santos, J. Mebert, O. Koblinger, and L. Ley, *Phys. Rev. B* **36**, 1306 (1987).
- [24] P.A. Snow, E.K. Squire, P. St. J. Russell, and L.T. Canham, *J. Appl. Phys.* **86**, 1781 (1999).
- [25] J. He, B. Djafari-Rouhani, and J. Sapiael, *Phys. Rev. B* **37**, 4086 (1988).
- [26] A Yariv and P. Yeh. *Photonics: Optical Electronics in Modern Communications*. (Oxford University Press, New York, 2007), p. 539-601.
- [27] P. Yeh, A. Yariv, and C. Hong, *J. Opt. Soc. Am.* **67**, 423 (1977).
- [28] N. Gomopoulos, D. Maschke, C. Y. Koh, E. L. Thomas, W. Tremel, H.-J. Butt, and G. Fytas, *NanoLett.* **10**, 980 (2010).
- [29] W. Cheng, J. Wang, U. Jonas, G. Gytas, and N. Stefanou, *Nature* **5**, 830 (2006).

- [30] H. Z. Cummins and P. E. schoen, Light Scattering from Thermal Fluctuations. In *Laser Handbook, Vol 2*, edited by F. T. Arecchi and E. O. Schulz-Dubois. (North-Holland, New York, 1972), p. 1029-1075.
- [31] J. R. Sandercock, Solid State Commun. **26**, 547 (1978).
- [32] A. S. Pine. Phys. Rev. **185**, 1187 (1969).
- [33] J. R. Sandercock, Phys. Rev. Lett. **28**, 237 (1972).
- [34] M. Randeria and J. P. Sethna, Phys. Rev. B **38**, 12607 (1988).
- [35] J. Von Behren, L Tsybeskov, and P. M. Fauchet, Mat. Res. Soc. Symp. Proc. **358**, 333 (1995).
- [36] F. L. Pedrotti and L. S. Pedrotti, editors. *Introduction to Optics*. Prentice Hall. New Jersey, 1993.
- [37] W. F. Oliver C. A. Herbst, S. M. Lindsay, and G. H. Wolf, Rev. Sci. Instrum. **63**, 1884 (1992).
- [38] J. Geist. Silicon (Si) Revisited (1.1-3.1 eV). In *Handbook of Optical Constants of Solids III*, edited by E. D. Palik. (Academic Press, San Diego, 1998), p. 519-531.
- [39] C. Gigault and J. R. Dutcher. Appl. Opt. **37**, 3318 (1998).
- [40] L. Thomas. *Porous Silicon Multilayers For Gigahertz Bulk Acoustic Wave Devices*. Ph.D. thesis, University of Bath (2011).

- [41] B. C. Daly, K. Kang, Y. Yang, and D. G. Cahill, *Phys. Rev. B* **80**, 174112 (2009).
- [42] D. B. Hondongwa, B. C. Daly, T. B. Norris, B. Yan, J. Yang, and S. Guha, *Phys. Rev. B* **83**, 121303 (2011).
- [43] H. J. Fan, M. H. Kuok, S. C. Ng, R. Boukherroub, J.-M. Baribeau, J. W. Fraser, and D. J. Lockwood, *Phys. Rev. B* **65**, 165330 (2002).
- [44] G. T. Andrews, J. Zuk, H. Kieft, M. J. Clouter, and E. Nossarzewska-Orlowska, *Appl. Phys. Lett.* **69**, 1217 (1996).
- [45] H. Yasuda and A. Yoshihara, *J. Phys. Condes. Matter* **10**, 9623 (1998).
- [46] G. Carlotti, D. Fioretto, L. Giovamini, F. Nizzoli, G. Socino, and L. Verdini, *J. Phys. Condes. Matter* **4**, 257 (1992).

Chapter 8

Summary

8.1 Current Results

The main focus of this work was to study the potential of porous silicon superlattices as one-dimensional hypersonic phononic crystals using inelastic Brillouin light scattering. In particular, superlattices with a binary spatial periodicity in the porosity of the order of ~ 100 nm were studied. Due to the porosity-dependence of both the elastic impedance and refractive index, these samples are one-dimensional phononic-photonics crystals.

The first studies within this project saw the use of near-normal incidence 180° -backscattering geometry Brillouin light scattering to probe superlattices with modulation lengths ranging from ~ 40 nm to ~ 170 nm, an approximately 1:1 constituent layer thickness ratio, and constituent layer porosities of $\sim 55\%$ and $\sim 45\%$. For a given set of samples, the constituent layer parameters were taken to be the same. In turn, the phonon frequency versus wavevector data collected for each superlattice of a series

of samples could be combined and, thus, a set of phonon frequency versus modulation wavelength data were obtained. In particular, spectral features corresponding to as many as four modes were observed in spectra collected from the samples. These data were compared to calculations based on a one-dimensional elastic/electromagnetic continuum model, with the known constituent layer elastic and optical properties used as model inputs. Agreement between experiment and theory suggested that two of the modes were due to zone-folded bulk longitudinal acoustic phonons, while one was attributed to a bulk transverse acoustic mode. One peak, which was observed in a number of samples, did not appear to agree with the theory and, in turn, it was unassigned.

One issue in the preceding work was that only one phonon wavevector directed along the superlattice modulation axis was accessed per sample and, thus, physically relevant trends in the resulting phonon frequency versus modulation wavelength data may have been obscured by sample-to-sample variation in the constituent layer porosity and etch rates. Furthermore, the polarization of the probed phonons could not be determined experimentally, thus leading to ambiguities in the mode assignments. With this in mind, a methodology for a so-called pseudo-reflection geometry Brillouin light scattering technique was developed: this allowed a small portion of the bulk acoustic phonon band structure corresponding to phonons directed approximately along the normal of a sample surface to be mapped. This technique is advantageous over an ideal reflection geometry as it allowed one to avoid many of the practical

pitfalls associated with an ideal reflection geometry, such as the possibility of the reflected light swamping the scattered light spectrum, while still accessing approximately the same phonon wavevectors. Further analysis of the polarization of the scattering allowed for experimental determination of the polarization of the observed modes. This technique was shown to be useful for determining both the refractive index and the bulk acoustic mode velocities along the surface normal for both isotropic and cubic materials. Results obtained from measurements on fused quartz, gallium phosphide, water, and two supported mesoporous silicon films confirmed the validity of the method.

A more comprehensive study was done in order to better understand both the acoustic phonon and photon band structures of mesoporous silicon superlattices with modulation wavelengths of the order of 100 nm and constituent parameters similar to those mentioned above. In particular, both pseudo-reflection geometry and near-normal incidence 180° -backscattering geometry Brillouin scattering as well as normal-incidence broadband visible-range optical reflectance measurements were done in order to characterize the phonon and photon band structures along the modulation axis of the superlattices. The optical reflectance spectra showed evidence of a one-dimensional photonic band gap in the visible-range whose behaviour was well-described by a one-dimensional optical continuum model. Results from the pseudo-reflection geometry Brillouin scattering experiments confirmed that there was zone-folding of the longitudinal bulk acoustic phonon band structure, with two longitudi-

nal modes observed in the spectra. A peak due to a single transverse bulk phonon was observed and, thus, there was no evidence of folding for the transverse mode band structure. Good agreement was obtained between the phonon frequency versus wavevector data and the one-dimensional elastic continuum model and, using the pseudo-reflection geometry, a portion of the acoustic phonon band structure was mapped for each of the probed samples. Of particular interest was a fourth peak which had been unassigned in the first study. This relatively narrow peak, which pseudo-reflection geometry results showed had a phonon wavevector-independent frequency, was attributed to an evanescent mode localized at the superlattice-air interface with a frequency within a longitudinal bulk acoustic mode band gap centered at ~ 16 GHz. Hence, it was confirmed that these porous silicon superlattices behaved as one-dimensional hypersonic phononic-photonics crystals.

Extending the above work, Brillouin scattering spectroscopy and optical reflectance measurements were done on two $D \sim 100$ nm π -Si SLs with the intention of characterizing acoustic phonon propagation at oblique angles to the modulation axis. Using a simplified theory, both the bulk phonon and photon band structures were treated as a series of intersecting linear dispersion curves. Again, two longitudinal bulk modes were observed while data corresponding to a single transverse bulk mode were obtained. Using an oblique angle 180° -backscattering geometry, the effect of propagation direction on the phonon frequency was probed. Unlike the zeroth-order folded longitudinal and transverse bulk phonons, the frequency of the other observed

folded longitudinal phonon was found to be strongly dependent on the direction of propagation. This was accurately modeled using the simplified band structure theory. Additionally, analysis of the peaks corresponding to the two longitudinal bulk modes suggested that the dominant contributor to the linewidth was viscous attenuation of the phonon. These results suggest that the longitudinal acoustic wave attenuation in porous silicon is several orders of magnitude larger than that of crystalline silicon at the same frequencies. This increase in attenuation is thought to be an artefact of the nanoporous nature of the films. Finally, the Rayleigh surface mode and a pseudo-surface mode was observed for each superlattice, with each mode velocity increasing as the phonon wavevector decreased. This dependence of mode velocity on wavevector is thought to stem from the influence of the second, lower-porosity constituent layer in the superlattice unit-cell, which increases as the phonon wavelength increases.

8.2 Future Work

While the preceding work provides some insight into the potential of porous silicon-based hypersonic phononic crystals, there is still much to learn about these structures. Future work would be of significance due to the fundamental science involved as well as the possibilities for device applications. From the perspective of fundamental science, there are a number of avenues that could be explored. These include utilizing porous silicon films as a platform to study novel physical interactions between phonons and photons and, if the pores were filled with a magnetic material, interactions between

phonons and magnons. Additionally, work could be done to gain further details about surface and bulk acoustic phonon propagation in binary periodic multilayered porous silicon films as well as more complicated layered structures. Each of these research concepts could probably serve as the basis for a graduate thesis project. Furthermore, Brillouin light scattering spectroscopy would be ideal for such studies as this technique can be used to probe acoustic phononic, magnonic and, under certain circumstances, photonic properties of a given material system. From an engineering standpoint, these structures are attractive due to the ease with which they can be fabricated, the low cost of fabrication, the myriad of existing porous silicon-based device applications, as well as the ability to readily integrate porous silicon devices into bulk crystalline silicon-based technologies. With this in mind, however, further experiments must be carried out in order to optimize the porous silicon hypersonic phononic crystal fabrication process and, in particular, reduce variability in the resulting sample parameters. Further, steps should be taken to reduce the constituent layer interface roughness and, in turn, improve the quality of the resulting hypersonic phononic crystals. This work is crucial if these samples are to be considered viable for device applications.

Acoustic phonon propagation in more complex multilayered mesoporous silicon films should be studied. For example, a stratified system consisting of stacked binary-periodic structures that exhibits broadband hypersonic phononic band gaps has been proposed [1]. Furthermore, porous silicon gigahertz-range acoustic micro-

cavities should be considered. While work has already been done on porous silicon acoustic microcavities in the high-frequency ultrasonic regime, there is an opportunity to extend this in the gigahertz-range. Additionally, since such structures would also behave as one-dimensional optical microcavities, it would serve as a platform in which to study novel phonon-photon effects, such as optical-cooling [2], as both excitations would be localized at the same defect.

If the pores were filled with a magnetic material, it is conceivable that the resulting film would behave as a phononic-magnonic crystal [3, 4]. While it may be difficult to fill the pores of a mesoporous film with a magnetic material, an alternative would be to use a hexagonally-patterned macroporous silicon sample [5]. In this case, there would be a two-dimensional periodicity in both the elastic and magnetic properties and one would expect zone-folding to occur for the surface phonons and dipolar spin-waves.

Returning to mesoporous silicon films, further experiments must be done to better understand the mechanism behind the acoustic attenuation. Measurements collected over a wider range of frequencies (ultrasonic to hypersonic) would provide a more complete sense of the underlying physics.

Analogous to how the optical properties of mesoporous silicon superlattices have been utilized in optical gas sensors [6], these films may be a good platform for sound-based sensors where sensing is a consequence of changes in the acoustic properties of the structure. The effect of varying environmental conditions, such as changes in ambient temperature and pressure, on the phononic band structure must then

be studied. Related to this type of work, one could also study the effect of fluid infiltration on the phonon band structure.

Potential applications such as porous silicon drug delivery systems [7] may necessitate that the film be freestanding. Thus, Brillouin light scattering studies should be done to characterize acoustic mode propagation in freestanding porous silicon superlattices. This would be a continuation of preliminary work carried out by the author on freestanding single-layer mesoporous silicon films [8]. Results obtained in early experiments, however, found that the incident Brillouin laser burned the sample, even at very low power. Consequently, the silicon substrate is crucial for heat-sinking the porous silicon film. Thus, work must be done to find a reliable way to dissipate the excess heat during Brillouin scattering experiments on freestanding films.

Since the current work studied binary-periodic superlattices with $\sim 1:1$ thickness ratio and constituent porosities of $\sim 55\%$ and $\sim 45\%$, one obvious step to evolve the study of porous silicon-based hypersonic phononic crystals is to characterize the effect of the consistent layer thickness ratio and the constituent layer porosity contrast on the acoustic phonon band structure. In a preliminary study done by the author [9], 180° -backscattering geometry Brillouin scattering was done on three series of superlattices, with the samples in each series corresponding to a given D value but different constituent layer fill-ratio. The expected change in the probed phonon frequency versus constituent layer fill-ratio was comparable to the uncertainty due to sample-to-sample variation, however, and the utility of this work was, therefore,

limited. With the introduction of the pseudo-reflection scattering geometry, it may be worthwhile to revisit this study. That is, pseudo-reflection geometry allows a set of frequency versus wavevector data to be collected for a given sample and, in turn, sample-to-sample variation is less likely to obscure the underlying physics as trends in the phonon dispersion can be deduced on a sample-by-sample basis.

Studies could be done to characterize the effect of constituent layer interface roughness on the Brillouin spectrum of the porous silicon films. Previous work has shown that the relative intensities of Brillouin peaks corresponding to zone-folded bulk acoustic phonons in superlattices are strongly dependent on the quality of the layer interfaces [10]. In order to complete the proposed study, the sample fabrication procedures must be re-evaluated in order to reduce interface roughness in the obtained superlattices. Etching at subzero temperatures may help to facilitate the fabrication of higher quality samples [11]. In addition, the photoelastic constants of the constituent layers must be known in order to properly model the Brillouin peak intensities. This would require a study of corresponding single-layer porous silicon films.

Chapter 8 References

- [1] D. Moctezuma-Enriquez, Y. J. Rodriguez-Viveros, M. B. Manzanares-Martinez, P. Castro-Garay, E. Urrutia-Banuelos, and J. Manzanares-Martinez, *Appl. Phys. Lett.* **99**, 171901 (2011).
- [2] M. Maldovan and E. L. Thomas, *Appl. Phys. Lett.* **88**, 251907 (2006).
- [3] M. Krawczyk and H. Puzkarski, *Phys. Rev. B* **77**, 054437 (2008).
- [4] V. L. Zhang, F. S. Ma, H. H. Pan, C. S. Lin, H. S. Lim, S. C. Ng, M. H. Kuok, S. Jain, and A. O. Adeyeye, *Appl. Phys. Lett.* **100**, 163118 (2012).
- [5] A. Birner, R.B. Wehrspohn, U.M. Gosele, and K. Busch. *Adv. Mater.* **13**, 377 (2001).
- [6] P.A. Snow, E.K. Squire, P. St. J. Russell, and L.T. Canham, *J. Appl. Phys.* **86**, 1781 (1999).
- [7] E. J. Anglin, L. Cheng, W. R. Freeman, and M. J. Sailor, *Adv. Drug Deliv. Rev.* **60**, 1266 (2008).

- [8] L. C. Parsons. *Brillouin Light Scattering from Freestanding Porous Silicon Films*. B.Sc. (Honours) thesis. (Memorial University, 2006).
- [9] L. C. Parsons and G. T. Andrews. Zone-folded longitudinal acoustic phonons in porous silicon superlattices. presented at the 7th International Conference on Porous Semiconductors Science and Technology. 2010.
- [10] C.E. Bottani and R. Caporali, J. Phys. Condens. Matter **9**, 5787 (1997).
- [11] P.J. Reece, G. Lerondel, J. Mulder, W.H. Zheng, and M. Gal, Phys. Status Solidi A **197**, 321 (2003).

Appendix A

Raw Data from Experiments on Single-Layer

Porous Silicon Films

In order to deduce the constituent layer parameters of the binary periodic π -Si SLs made with a 1:1 (49% wt. HF: 98% wt. ethanol) electrolyte, corresponding single layer films were made with etch currents of $I_{high} = 230$ mA and $I_{low} = 142$ mA. For each set of etch parameters, two series of samples were made: near-normal incidence 180° -backscattering geometry Brillouin spectroscopy was done on one series of films, while the gravimetrically-deduced porosity was obtained from the other (recall that the gravimetric method for determining the porosity destroyed the films). The bulk acoustic phonon frequencies, ν_T and ν_L , as well as the porosity values were averaged, with the experimental uncertainty taken to be 2 standard deviations of the mean (see Tables A.1, A.2, A.3, A.4, A.5). One should note that the Brillouin spectroscopy-deduced phonon frequencies collected from samples PSi2.11#9 and PSi2.13#10 were

obtained in a previous study done in this laboratory [1]; both spectra were collected at $\theta_i \leq 10^\circ$.

Figures A.1 to A.9 show the near-normal incidence 180° -backscattering geometry Brillouin spectra as well as near-normal incidence broadband optical reflectance spectra collected from the studied single-layer π -Si films. The spectra collection dates as well as the θ_i value and FSR corresponding to the Brillouin scattering measurements are provided. The reflectance spectra contained interference fringes stemming from optical interference over the $\sim 5 \mu\text{m}$ thick films. As well, some reflectance spectra contained a peak at a wavenumber of $\sim 1 \text{ mm}^{-1}$: as mentioned in Chapter 3, this peak is thought to be an artefact of the sharp decrease in the reflectance of the reference broadband mirror and, thus, not a true peak in absolute reflectance spectrum of the π -Si films.

The statistically-determined porosity values obtained from the data in Tables A.3 and A.4, ζ_{current} , were combined with those stated in a previous study on similarly made films [1], ζ_{polomska} . The resulting porosity values, ζ , were used together with the two-component Bruggeman effective medium model to deduce the refractive index at the laser wavenumber, $n(w_{\lambda_o})$. The average Brillouin scattering-deduced bulk acoustic phonon frequencies, $\nu_{T,ave}$ and $\nu_{L,ave}$, (determined from the data given in Tables A.1 and A.2) were used together with $n(w_{\lambda_o})$ in order to obtain the corresponding phonon velocities, V_T and V_L using Eq. (3.8).

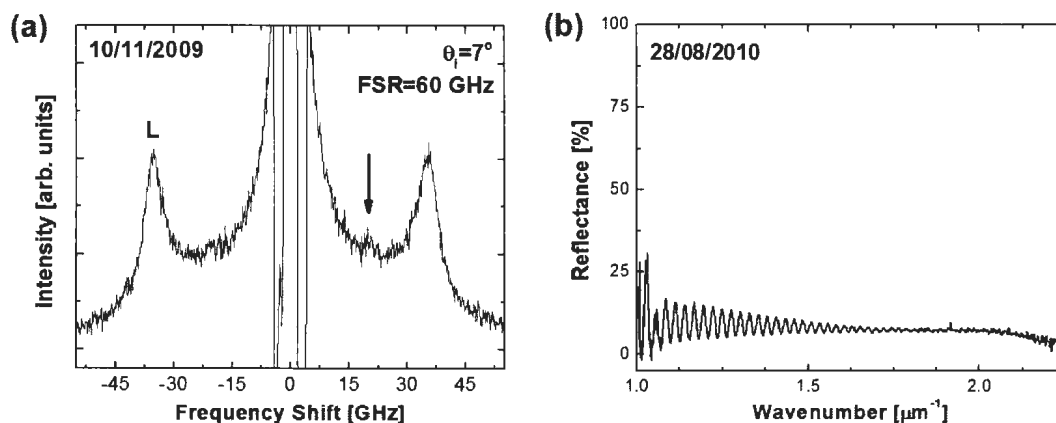


Figure A.1: (a) Near-normal incidence 180-backscattering geometry Brillouin spectrum and (b) near-normal incidence broadband optical reflectance spectrum collected from sample PSi2.20#3, a higher-porosity single-layer π -Si film. Brillouin peak L was attributed to the longitudinal bulk acoustic mode. The arrow indicates a spectral feature thought to be due to scattering from the transverse bulk acoustic mode.

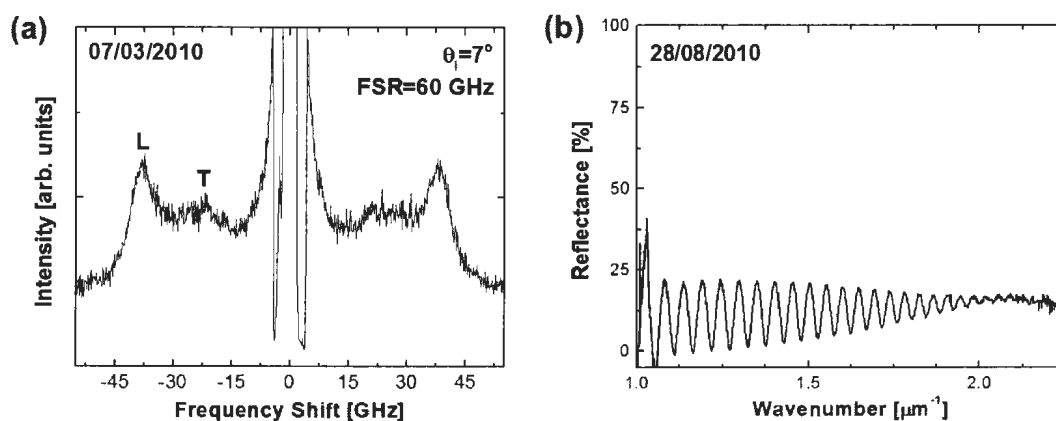


Figure A.2: (a) Near-normal incidence 180-backscattering geometry Brillouin spectrum and (b) near-normal incidence broadband optical reflectance spectrum collected from sample PSi4.3#8, a higher-porosity single-layer π -Si film. Brillouin peaks L and T were attributed to the longitudinal bulk acoustic mode and the transverse bulk acoustic mode, respectively.

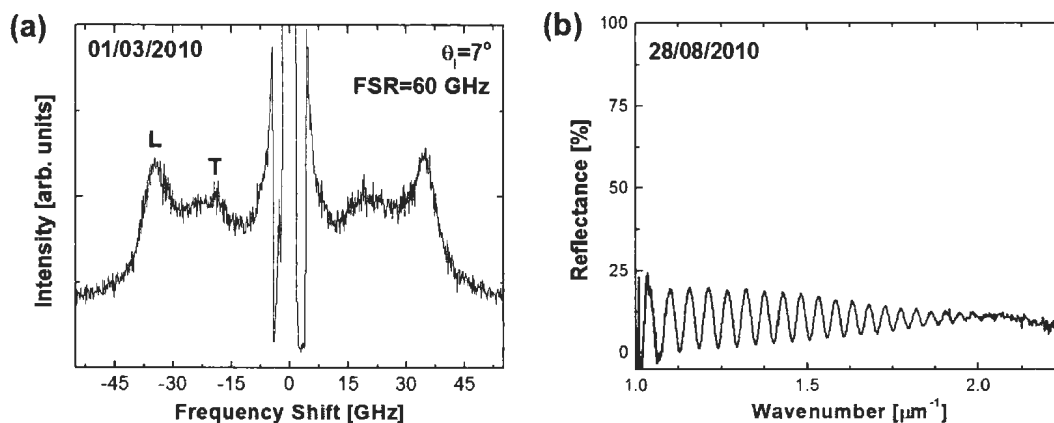


Figure A.3: (a) Near-normal incidence 180-backscattering geometry Brillouin spectrum and (b) near-normal incidence broadband optical reflectance spectrum collected from sample PSi4.6#1, a higher-porosity single-layer π -Si film. Brillouin peaks L and T were attributed to the longitudinal bulk acoustic mode and the transverse bulk acoustic mode, respectively.

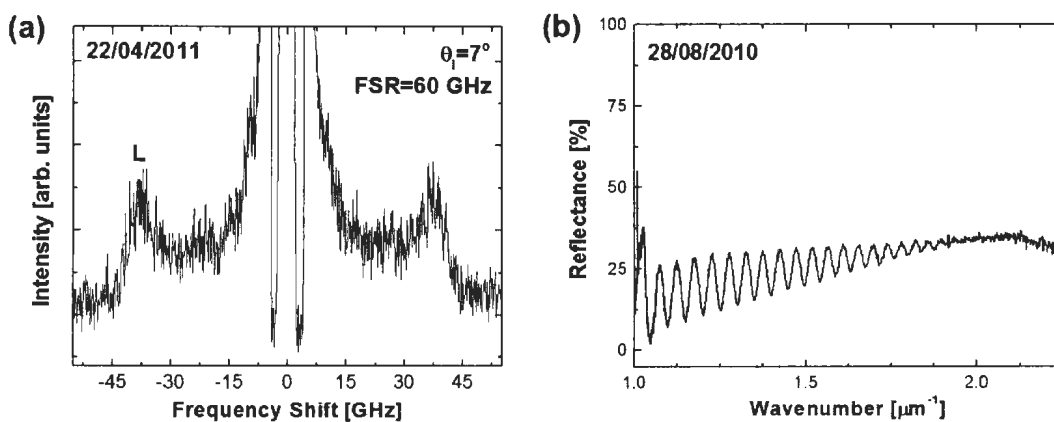


Figure A.4: (a) Near-normal incidence 180-backscattering geometry Brillouin spectrum and (b) near-normal incidence broadband optical reflectance spectrum collected from sample PSi4.7#3, a higher-porosity single-layer π -Si film. Brillouin peak L was attributed to the longitudinal bulk acoustic mode.

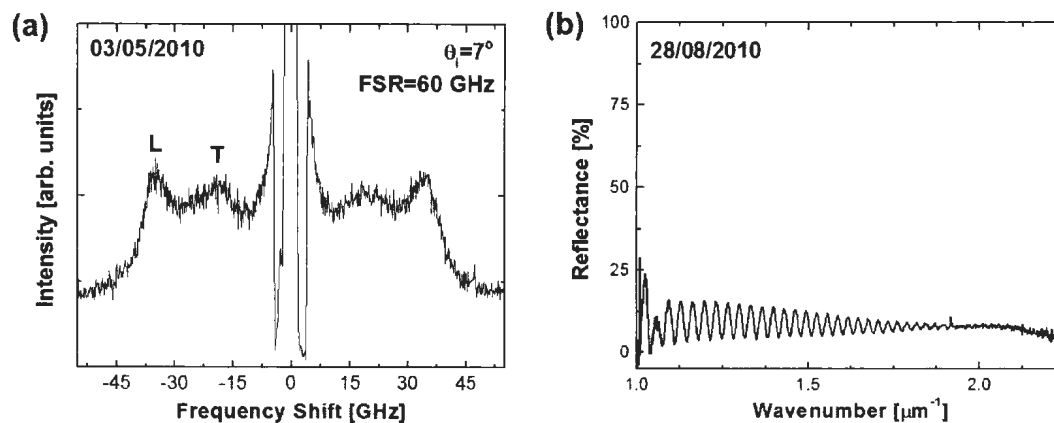


Figure A.5: (a) Near-normal incidence 180-backscattering geometry Brillouin spectrum and (b) near-normal incidence broadband optical reflectance spectrum collected from sample PSi4.8#8, a higher-porosity single-layer π -Si film. Brillouin peaks L and T were attributed to the longitudinal bulk acoustic mode and the transverse bulk acoustic mode, respectively.

Table A.1: Fabrication date as well as the frequencies of the BLS-probed transverse mode, ν_T , and the BLS-probed longitudinal mode, ν_L , for single-layer π -Si films made using an etch current of $I_{high} = 230$ mA.

Sample	Fabrication Date	ν_T	ν_L
	(GHz)	(GHz)	
PSi2.20#3	14/08/2009	20.5	34.96
PSi4.3#8	22/01/2010	22.80	38.14
PSi4.6#1	29/01/2010	20.25	34.74
PSi4.7#3	19/02/2010	-	37.19
PSi4.8#8	27/03/2010	18.79	34.83
PSi2.11#9	-	17.0	34.1

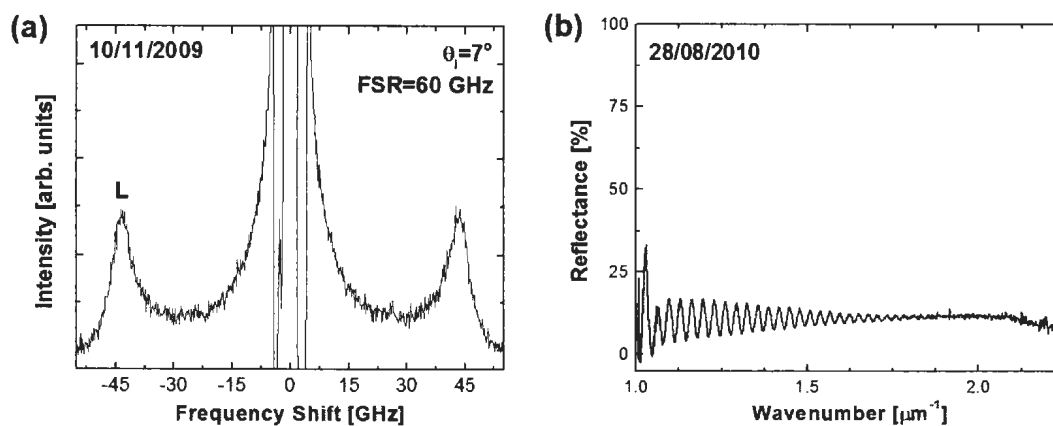


Figure A.6: (a) Near-normal incidence 180-backscattering geometry Brillouin spectrum and (b) near-normal incidence broadband optical reflectance spectrum collected from sample PSi2.20#4, a lower-porosity single-layer π -Si film. Brillouin peak L was attributed to the longitudinal bulk acoustic mode.

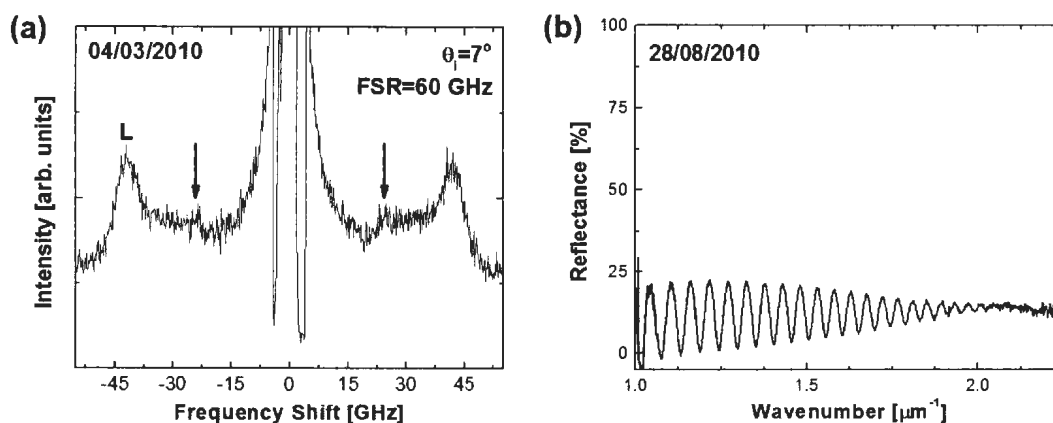


Figure A.7: (a) Near-normal incidence 180-backscattering geometry Brillouin spectrum and (b) near-normal incidence broadband optical reflectance spectrum collected from sample PSi4.4#1, a lower-porosity single-layer π -Si film. Brillouin peak L was attributed to the longitudinal bulk acoustic mode. The arrow indicates a spectral feature thought to be due to scattering from the transverse bulk acoustic mode.

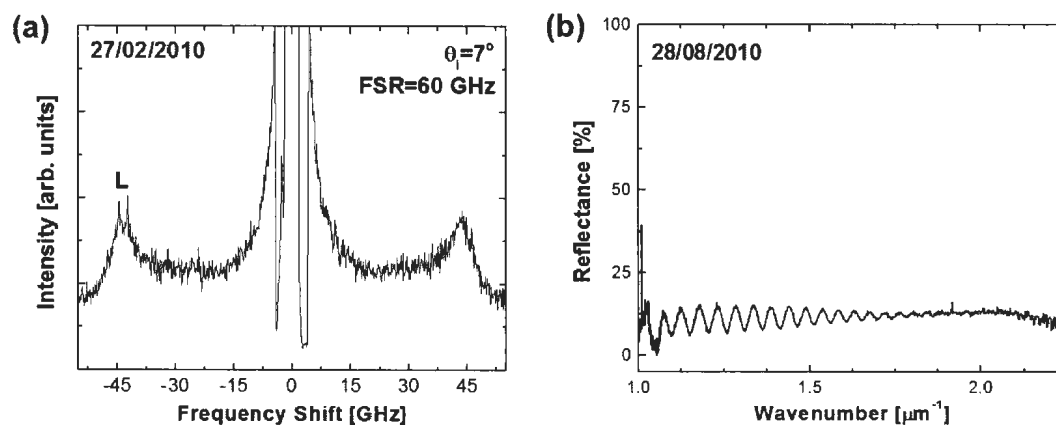


Figure A.8: (a) Near-normal incidence 180-backscattering geometry Brillouin spectrum and (b) near-normal incidence broadband optical reflectance spectrum collected from sample PSi4.6#2, a lower-porosity single-layer π -Si film. Brillouin peak L was attributed to the longitudinal bulk acoustic mode.

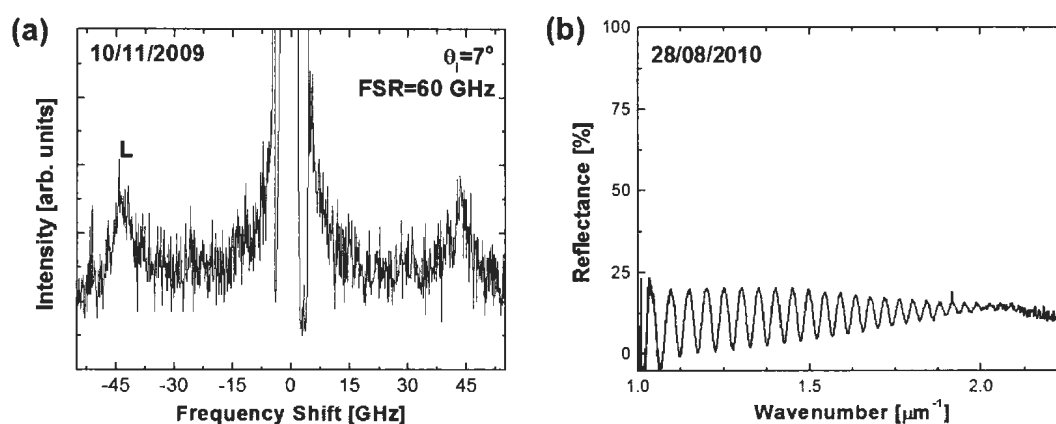


Figure A.9: (a) Near-normal incidence 180-backscattering geometry Brillouin spectrum and (b) near-normal incidence broadband optical reflectance spectrum collected from sample PSi4.7#2, a lower-porosity single-layer π -Si film. Brillouin peak L was attributed to the longitudinal bulk acoustic mode.

Table A.2: Fabrication date as well as the frequencies of the BLS-probed transverse mode, ν_T , and the BLS-probed longitudinal mode, ν_L , for single-layer π -Si films made using an etch current of $I_{low} = 142$ mA.

Sample	Fabrication Date	ν_T	ν_L
	(GHz)	(GHz)	
PSi2.20#4	14/08/2009	-	43.20
PSi4.4#1	22/01/2010	24.25	41.96
PSi4.6#2	29/01/2010	-	43.31
PSi4.7#2	19/02/2010	-	43.40
PSi2.13#10	-	25.0	41.8

Table A.3: Fabrication date as well as the gravimetrically-deduced porosity value for single-layer π -Si films made using an etch current of $I_{high} = 230$ mA.

Sample	Fabrication Date	ζ
PSi2.23#4	22/01/2010	0.5463
PSi4.5#2	29/01/2010	0.5859
PSi4.7#1	19/02/2010	0.5497
PSi4.8#1	27/04/2010	0.5945
PSi4.8#2	27/04/2010	0.6143
PSi2.20#1	10/08/2009	0.5441
PSi2.20#2	10/08/2009	0.5687

Table A.4: Fabrication date as well as the gravimetrically-deduced porosity value for single-layer π -Si films made using an etch current of $I_{high} = 142$ mA. The porosity value obtained from sample PSi4.5#3 was omitted from subsequent statistical analysis; it was suspiciously large, being greater than the porosity of the I_{high} sample made during the same set of experiments (sample PSi4.5#2; see Table A.3).

Sample	Fabrication Date	ζ
PSi2.23#6	22/01/2010	0.4760
PSi4.5#3	29/01/2010	0.6062(omitted)
PSi4.7#4	19/02/2010	0.5020
PSi2.20#5	10/08/2009	0.4457
PSi2.20#1	10/08/2009	0.4811

Table A.5: Average porosity values obtained through statistical analysis of the data in Tables A.3 and A.4, $\zeta_{current}$; corresponding porosity values obtained in a previous study conducted in this laboratory [2], $\zeta_{polomska}$; the average of $\zeta_{current}$ and $\zeta_{polomska}$, ζ_{ave} ; the film refractive index at the Brillouin laser line (obtained using the two-component Bruggeman effective medium model together with ζ_{ave}), $n(w_{\lambda_o})$; the average probed transverse and longitudinal phonon frequencies, $\nu_{T,ave}$ and $\nu_{L,ave}$; and the transverse and longitudinal phonon velocities (obtained using Eq. (3.8) together with $n(w_{\lambda_o})$, $\nu_{T,ave}$, and $\nu_{L,ave}$), V_T and V_L , for single-layer π -Si samples made with etch currents $I_{high} = 230$ mA and $I_{high} = 142$ mA.

Current (mA)	$\zeta_{current}$	$\zeta_{polomska}$	ζ_{ave}	$n(w_{\lambda_o})$	$\nu_{T,ave}$ (GHz)	V_T (km/s)	$\nu_{L,ave}$ (GHz)	V_L (km/s)
230	0.57 ± 0.02	0.59 ± 0.02	0.58 ± 0.02	2.1 ± 0.1	21 ± 2	2.7 ± 0.4	36 ± 1	4.6 ± 0.4
142	0.48 ± 0.02	0.53 ± 0.03	0.50 ± 0.02	2.4 ± 0.1	24.6 ± 0.8	2.7 ± 0.2	43.0 ± 0.7	4.8 ± 0.3

Appendix A References

- [1] A. M. Polomska. *Elastic properties of porous silicon superlattices*. Ph.D. thesis, Memorial University of Newfoundland (2010).
- [2] A. M. Polomska-Harlick and G. T. Andrews, *J. Phys. D: Appl. Phys.* **45**, 075302 (2012).

Appendix B

Raw Data for Chapters 4 and 6

Both optical reflectance measurements and Brillouin scattering experiments were done on a series of binary periodic porous silicon films made using a 1:1 (49% wt. HF: 98% wt. ethanol) electrolyte. Unless stated otherwise, all SLs were fabricated such that the higher-porosity layer of the SL unit cell was adjacent to air. The Brillouin spectra within Figs. B.1 to B.18 as well as Figs. B.30, B.33, B.35, and B.39 contain near-normal incidence 180° -backscattering geometry Brillouin scattering data that were originally discussed in Chapter 4. In a follow-up study (see Chapter 6), all of the these data were re-analyzed and, in many cases, additional near-normal incidence 180° geometry Brillouin measurements were done. In addition to the near-normal incidence backscattering geometry Brillouin scattering experiments, pseudo-reflection geometry Brillouin spectroscopy was done on samples PSi2.12#5, PSi2.14A#1, PSi2.20#8, PSi2.20#10, and PSi4.9#9 (see Figs. B.31, B.34, B.36, B.37, B.40, B.41, and B.44 as well as the corresponding tables).

In order to help confirm the photonic crystal behaviour of the π -Si SLs, broadband optical reflectance measurements were done on an additional set of samples (see Figs. B.20 to B.24 and Table B.18). Moreover, to help ascertain how the Brillouin spectrum was affected by the relative ordering of the constituent layer porosity in the SL unit cell, additional experiments were done on SLs with the lower-porosity constituent layer adjacent to air. The obtained results were compared to those of samples for which the higher-porosity layer was adjacent to air (see Figs. B.25 to B.29 and the corresponding tables).

Cross-sectional scanning electron microscopy was done on some of the samples. Figures B.16, B.19, B.32, B.38, B.42, and D.1 show examples of scanning electron micrographs that were collected. For each sample in which scanning electron microscopy was done, multiple images were obtained. In an effort to emphasize the film-substrate interface, the digitized scanning electron micrographs were processed. In particular, adjustments were made to the image contrast and brightness. One should note that white, irregular features in the SEM images correspond to dirt and debris on the samples.

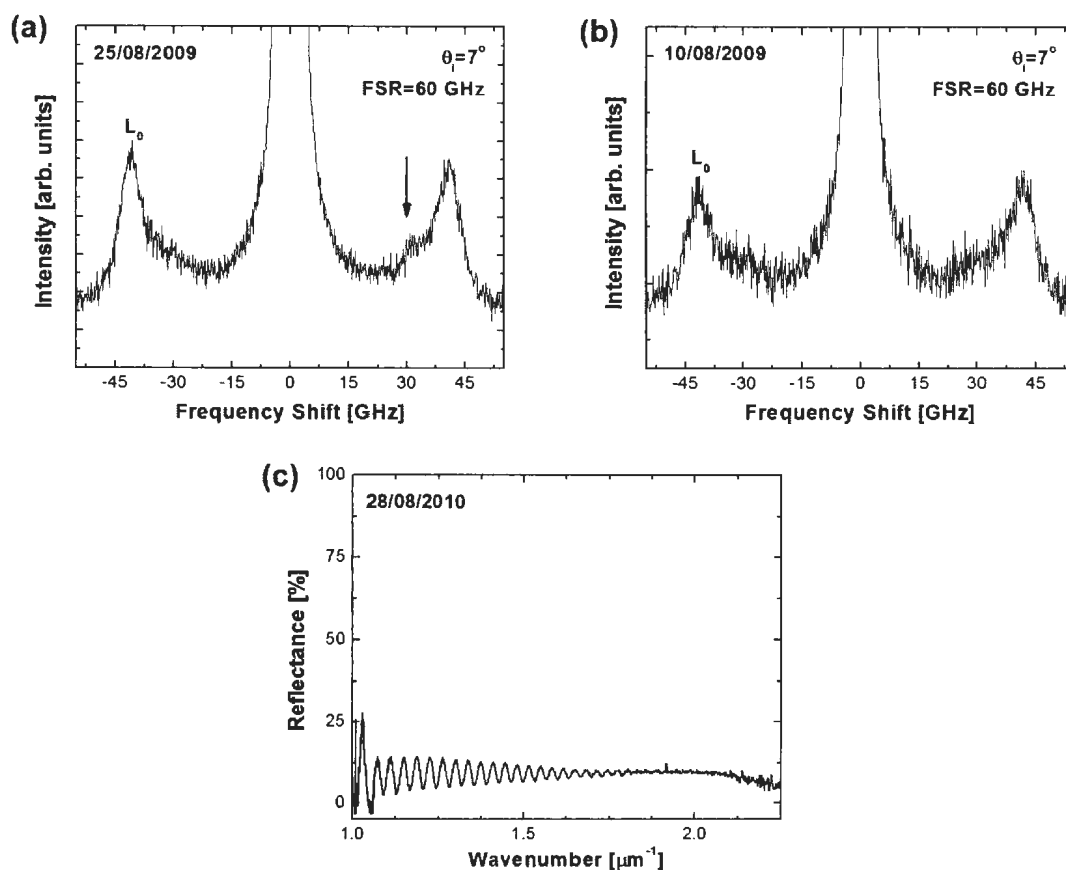


Figure B.1: (a)-(b) Near-normal incidence 180° -backscattering geometry Brillouin spectra and (c) near-normal incidence broadband optical reflectance spectrum collected from sample PSi2.6#1, a binary periodic multilayered π -Si film. Brillouin peak L_0 was attributed to the zeroth-order folded longitudinal bulk acoustic mode. The arrow indicates an additional spectral feature that may be due to another bulk acoustic mode (included in the data for Chapter 4; removed upon subsequent analysis).

Table B.1: The θ_i value, the Brillouin spectrum collection date, and the observed phonon modes and corresponding frequencies obtained for sample P*Si*2.6#1, a binary periodic multilayered π -Si film fabricated on 31/07/2009. The anodization times per cycle were $t_1 = 0.21432$ s and $t_2 = 0.28990$ s, the number of etch cycles was $\eta = 82$, and the SL modulation wavelength deduced using the etch times and etch rates was $D = (62 \pm 2)$ nm.

θ_i (deg.)	Collection Date	ν_{L_0} (GHz)
7	25/08/2009	40.59 ± 0.06
7	10/08/2009	41.2 ± 0.1

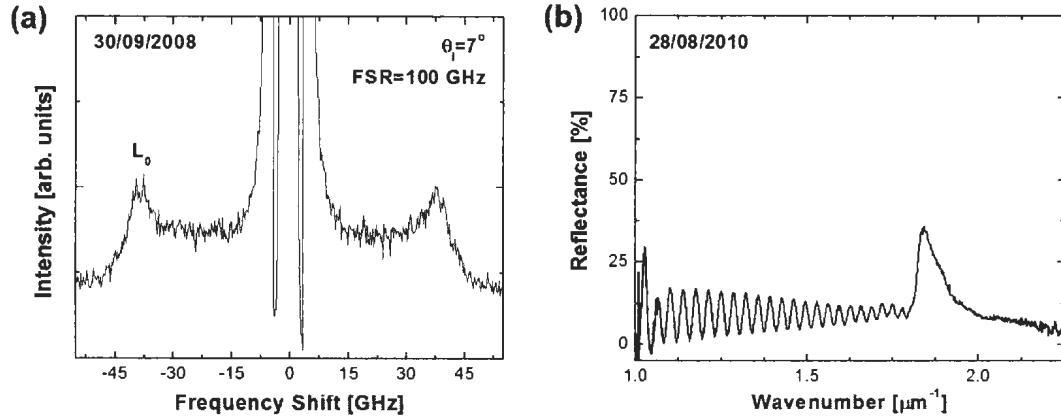


Figure B.2: (a) Near-normal incidence 180° -backscattering geometry Brillouin spectrum and (b) near-normal incidence broadband optical reflectance spectrum collected from sample PSi2.12#9, a binary periodic multilayered π -Si film. Brillouin peak L_0 was attributed to the zeroth-order folded longitudinal bulk acoustic mode.

Table B.2: The θ_i value, the Brillouin spectrum collection date, and the observed phonon modes and corresponding frequencies obtained for sample PSi2.12#9, a binary periodic multilayered π -Si film fabricated on 29/09/2008. The anodization times per cycle were $t_1 = 0.43478$ s and $t_2 = 0.58139$ s, the number of etch cycles was $\eta = 50$, and the SL modulation wavelength deduced using the etch times and etch rates was $D = (126 \pm 3)$ nm.

θ_i	Collection Date	ν_{L_0}
(deg.)		(GHz)
7	30/09/2008	37.5 ± 0.1

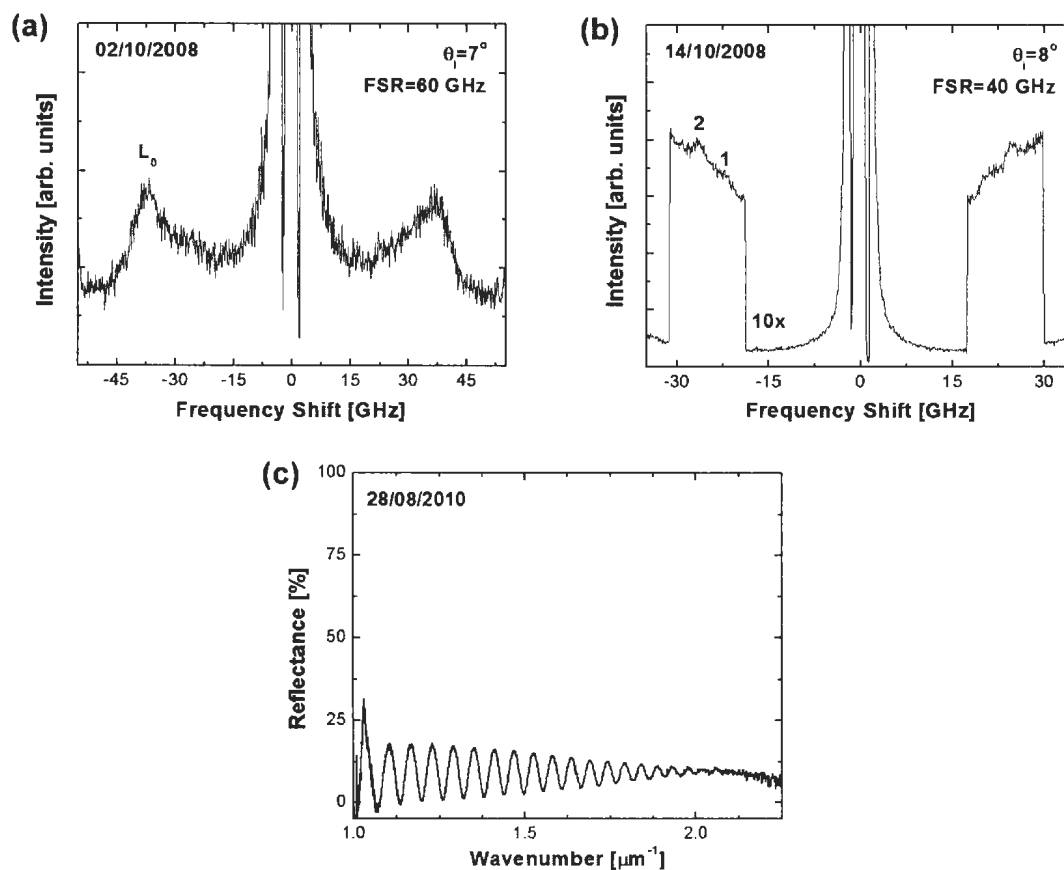


Figure B.3: (a)-(b) Near-normal incidence 180° -backscattering geometry Brillouin spectra and (c) near-normal incidence broadband optical reflectance spectrum collected from sample PSi2.11#11, a binary periodic multilayered π -Si film. Brillouin peak L_0 was attributed to the zeroth-order folded longitudinal bulk acoustic mode, while peaks 1 and 2 were thought to be due to the $l = -1$ folded longitudinal bulk acoustic phonon and the $l = 0$ folded transverse bulk acoustic phonon, respectively. This peak doublet feature was reported as a single broad peak in the earlier study (see Chapter 4).

Table B.3: The θ_i value, the Brillouin spectrum collection date, and the observed phonon modes and corresponding frequencies obtained for sample P*Si*2.11#11, a binary periodic multilayered π -Si film fabricated on 29/09/2008. The anodization times per cycle were $t_1 = 0.26087$ s and $t_2 = 0.34884$ s, the number of etch cycles was $\eta = 50$, and the SL modulation wavelength deduced using the etch times and etch rates was $D = (76 \pm 2)$ nm.

θ_i (deg.)	Collection Date	ν_{L_0} (GHz)	ν_1 (GHz)	ν_2 (GHz)
7	02/10/2008	35.9 ± 0.2	-	-
8	14/10/2008	-	22 ± 1	25 ± 1

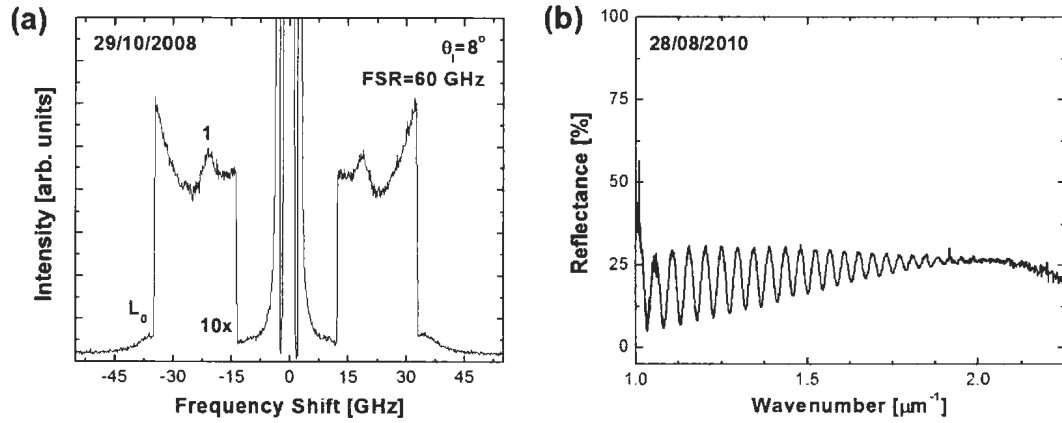


Figure B.4: (a) Near-normal incidence 180° -backscattering geometry Brillouin spectrum and (b) near-normal incidence broadband optical reflectance spectrum collected from sample P*Si*2.12#11, a binary periodic multilayered π -Si film. Brillouin peak L_0 was attributed to the zeroth-order folded longitudinal bulk acoustic mode, while peak 1 was thought to be due to the $l = 0$ folded transverse bulk acoustic phonon.

Table B.4: The θ_i value, the Brillouin spectrum collection date, and the observed phonon modes and corresponding frequencies obtained for sample P*Si*2.12#11, a binary periodic multilayered π -Si film fabricated on 22/10/2008. The anodization times per cycle were $t_1 = 0.21739$ s and $t_2 = 0.29069$ s, while the SL modulation wavelength deduced using the etch times and etch rates was $D = (63 \pm 2)$ nm.

θ_i	Collection Date	ν_{L_0}	ν_1
(deg.)		(GHz)	(GHz)
8	29/10/2008	35 ± 2	19.6 ± 0.1

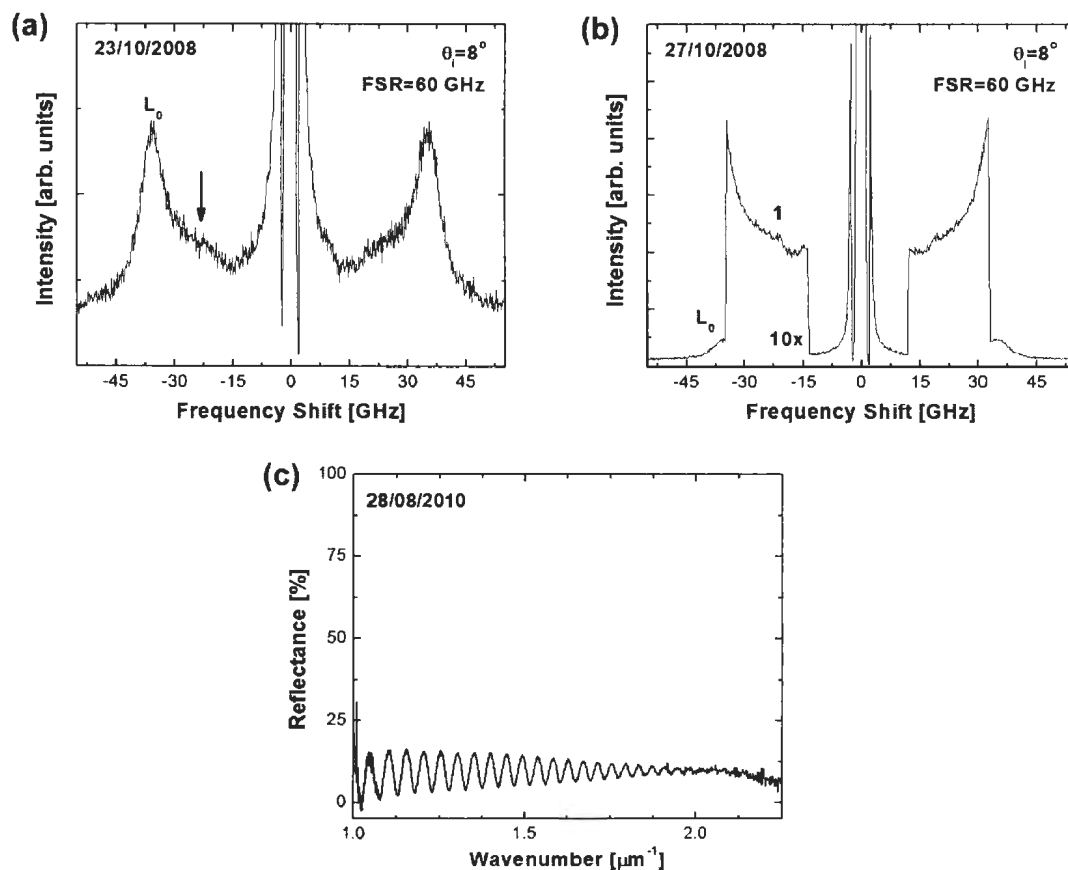


Figure B.5: (a)-(b) Near-normal incidence 180° -backscattering geometry Brillouin spectra and (c) near-normal incidence broadband optical reflectance spectrum collected from sample PSi2.12#12, a binary periodic multilayered π -Si film. Brillouin peak L_0 was attributed to the zeroth-order folded longitudinal bulk acoustic mode, while peak 1 was thought to be due to the $l = 0$ folded transverse bulk acoustic phonon. The arrow indicates a spectral feature that is attributed to the $l = 0$ folded transverse bulk acoustic phonon.

Table B.5: The θ_i value, the Brillouin spectrum collection date, and the observed phonon modes and corresponding frequencies obtained for sample PSi2.12#12, a binary periodic multilayered π -Si film fabricated on 22/10/2008. The anodization times per cycle were $t_1 = 0.21739$ s and $t_2 = 0.29069$ s, while the SL modulation wavelength deduced using the etch times and etch rates was $D = (63 \pm 2)$ nm.

θ_i	Collection Date	ν_{L_0}	ν_1
(deg.)		(GHz)	(GHz)
8	23/10/2008	34.81 ± 0.06	-
8	27/10/2008	-	20 ± 1

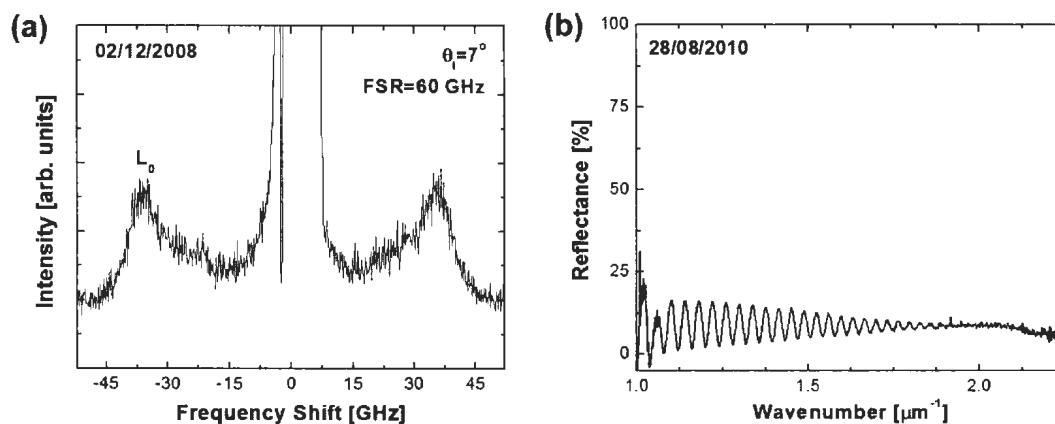


Figure B.6: (a) Near-normal incidence 180° -backscattering geometry Brillouin spectrum and (b) near-normal incidence broadband optical reflectance spectrum collected from sample P*Si*2.12#13, a binary periodic multilayered π -Si film. Brillouin peak L_0 was attributed to the zeroth-order folded longitudinal bulk acoustic mode.

Table B.6: The θ_i value, the Brillouin spectrum collection date, and the observed phonon modes and corresponding frequencies obtained for sample P*Si*2.12#13, a binary periodic multilayered π -Si film fabricated on 22/10/2008. The anodization times per cycle were $t_1 = 0.26087$ s and $t_2 = 0.34884$ s, while the SL modulation wavelength deduced using the etch times and etch rates was $D = (76 \pm 2)$ nm.

θ_i	Collection Date	ν_{L_0}
(deg.)		(GHz)
7	02/12/2008	35.1 ± 0.1

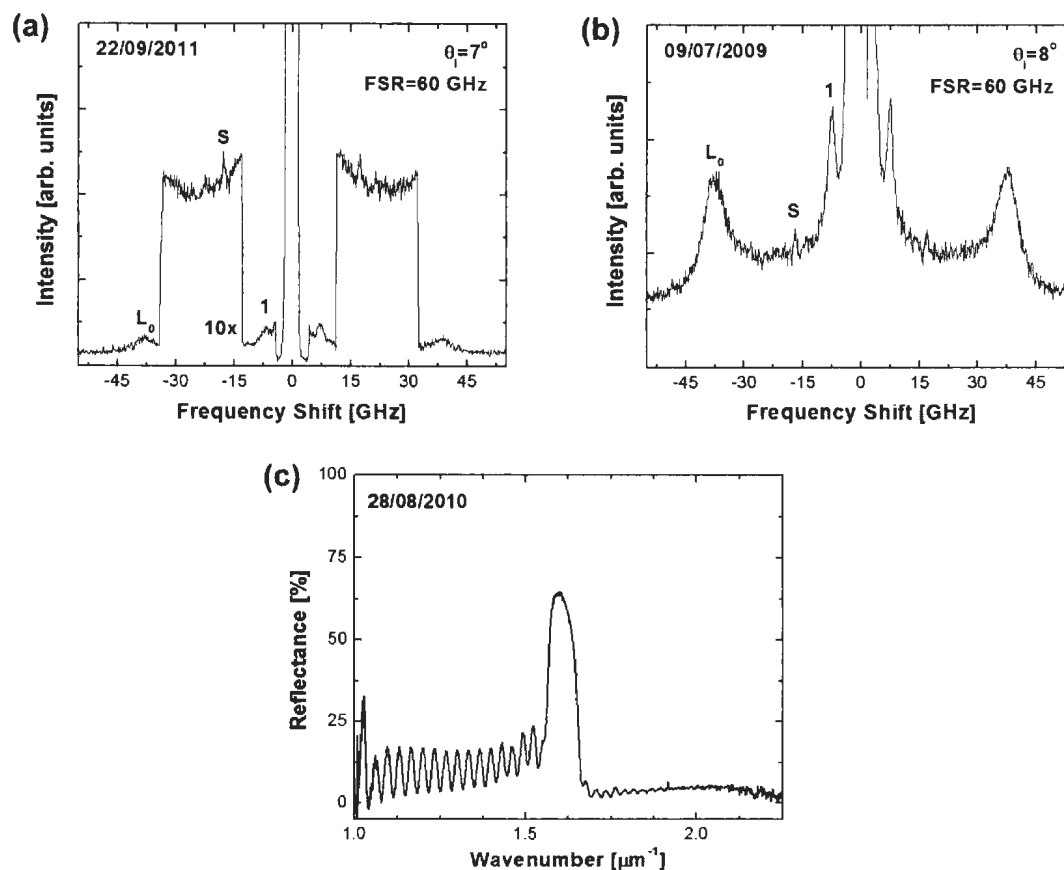


Figure B.7: (a)-(b) Near-normal incidence 180° -backscattering geometry Brillouin spectra and (c) near-normal incidence broadband optical reflectance spectrum collected from sample PSi2.13#11, a binary periodic multilayered π -Si film. Brillouin peaks L_0 and S were attributed to the zeroth-order folded longitudinal bulk acoustic mode and a surface-localized mode, respectively, while peak 1 was thought to be due to the $l = -1$ folded longitudinal bulk acoustic phonon.

Table B.7: The θ_i value, the Brillouin spectrum collection date, and the observed phonon modes and corresponding frequencies obtained for sample PSi2.13#11, a binary periodic multilayered π -Si film fabricated on 16/12/2008. The anodization times per cycle were $t_1 = 0.52174$ s and $t_2 = 0.69767$ s, the SL modulation wavelength deduced using the etch times and etch rates was $D = (151 \pm 4)$ nm, and the spectral position of the observed first-order optical Bragg peak was $w_1 = (1.60 \pm 0.01) \mu\text{m}^{-1}$.

θ_i	Collection Date	ν_{L_0}	ν_S	ν_1
(deg.)		(GHz)	(GHz)	(GHz)
7	22/09/2011	37.9 ± 0.1	17.54 ± 0.07	6.92 ± 0.07
8	09/07/2009	37.54 ± 0.05	16.97 ± 0.07	7.44 ± 0.03

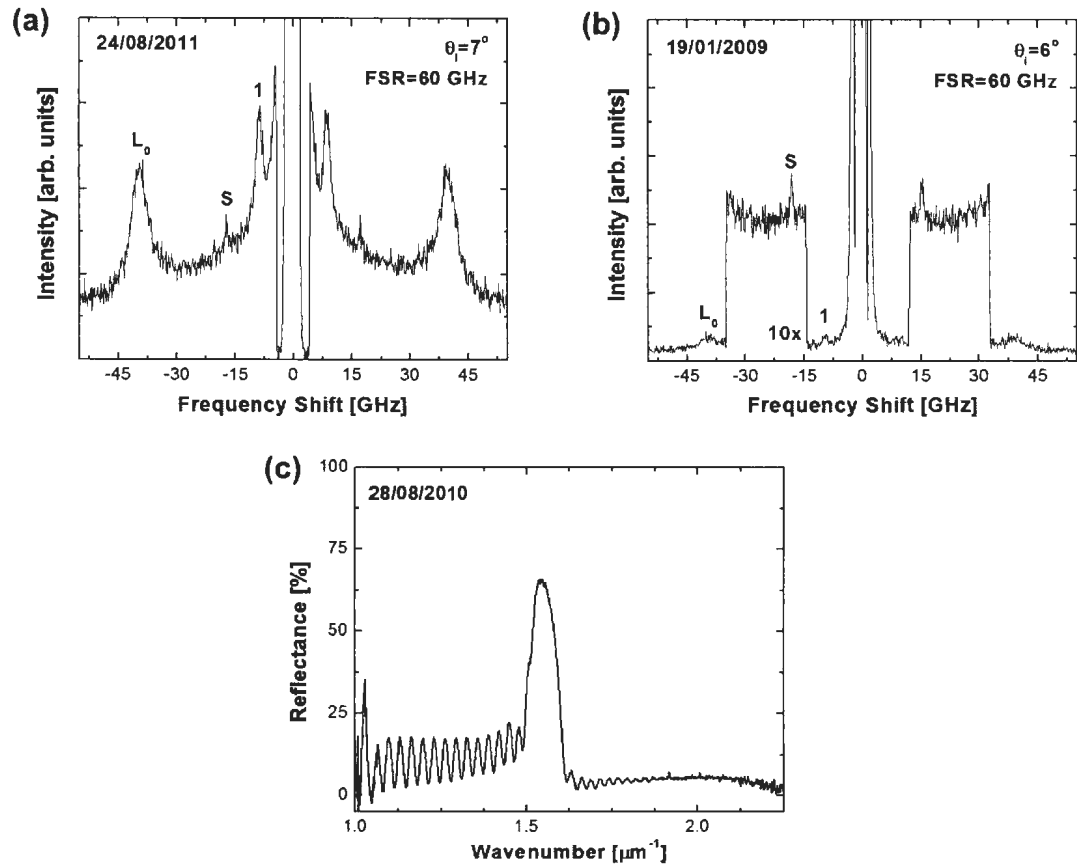


Figure B.8: (a)-(b) Near-normal incidence 180° -backscattering geometry Brillouin spectra and (c) near-normal incidence broadband optical reflectance spectrum collected from sample PSi2.13#12, a binary periodic multilayered π -Si film. Brillouin peaks L_0 and S were attributed to the zeroth-order folded longitudinal bulk acoustic mode and a surface-localized mode, respectively, while peak 1 was thought to be due to the $l = -1$ folded longitudinal bulk acoustic phonon.

Table B.8: The θ_i value, the Brillouin spectrum collection date, and the observed phonon modes and corresponding frequencies obtained for sample PSi2.13#12, a binary periodic multilayered π -Si film fabricated on 16/12/2008. The anodization times per cycle were $t_1 = 0.52174$ s and $t_2 = 0.69767$ s, the SL modulation wavelength deduced using the etch times and etch rates was $D = (151 \pm 4)$ nm, and the spectral position of the observed first-order optical Bragg peak was $w_1 = (1.55 \pm 0.01) \mu\text{m}^{-1}$.

θ_i	Collection Date	ν_{L_0}	ν_S	ν_1
(deg.)		(GHz)	(GHz)	(GHz)
7	24/08/2011	39.33 ± 0.06	17.22 ± 0.07	8.62 ± 0.04
6	19/01/2009	38.9 ± 0.2	16.81 ± 0.06	9.5 ± 0.3

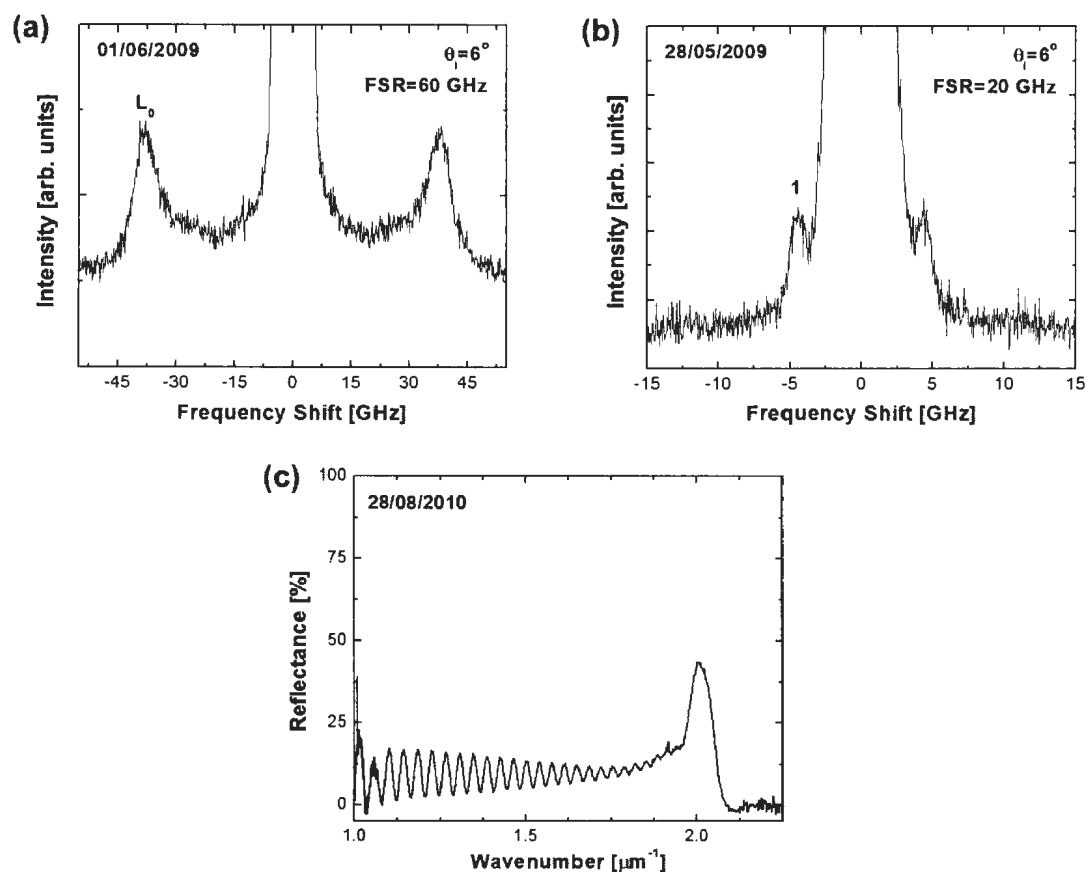


Figure B.9: (a)-(b) Near-normal incidence 180° -backscattering geometry Brillouin spectra and (c) near-normal incidence broadband optical reflectance spectrum collected from sample PSi2.14A#1, a binary periodic multilayered π -Si film. Brillouin peak L_0 was attributed to the zeroth-order folded longitudinal bulk acoustic mode, while peak 1 was thought to be due to the $l = -1$ folded longitudinal bulk acoustic phonon.

Table B.9: The θ_i value, the Brillouin spectrum collection date, and the observed phonon modes and corresponding frequencies obtained for sample PSi2.14A#1, a binary periodic multilayered π -Si film fabricated on 13/05/2009. The anodization times per cycle were $t_1 = 0.39130$ s and $t_2 = 0.52326$ s, the number of etch cycles is $\eta = 50$, the SL modulation wavelength deduced using the etch times and etch rates was $D = (113 \pm 3)$ nm, and the spectral position of the observed first-order optical Bragg peak was $w_1 = (2.01 \pm 0.01) \mu\text{m}^{-1}$.

θ_i	Collection Date	ν_{L_0}	ν_1
(deg.)		(GHz)	(GHz)
6	01/06/2009	37.24 ± 0.07	-
6	28/05/2009	-	4.35 ± 0.03

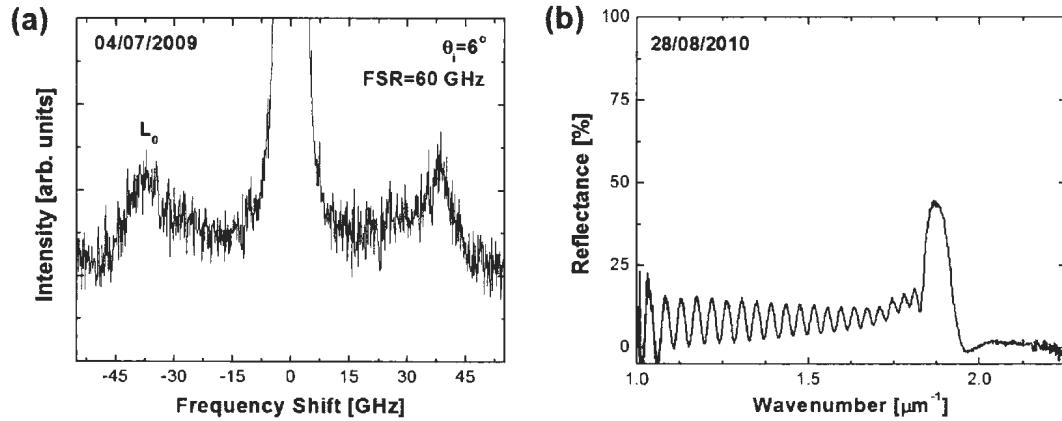


Figure B.10: (a) Near-normal incidence 180° -backscattering geometry Brillouin spectrum and (b) near-normal incidence broadband optical reflectance spectrum collected from sample PSi2.17#1, a binary periodic multilayered π -Si film. Brillouin peak L_0 was attributed to the zeroth-order folded longitudinal bulk acoustic mode

Table B.10: The θ_i value, the Brillouin spectrum collection date, and the observed phonon modes and corresponding frequencies obtained for sample PSi2.17#1, a binary periodic multilayered π -Si film fabricated on 25/06/2009. The anodization times per cycle were $t_1 = 0.41739$ s and $t_2 = 0.55813$ s, the number of etch cycles is $\eta = 42$, the SL modulation wavelength deduced using the etch times and etch rates was $D = (121 \pm 3)$ nm, and the spectral position of the observed first-order optical Bragg peak was $w_1 = (1.87 \pm 0.01) \mu\text{m}^{-1}$.

θ_i	Collection Date	ν_{L_0}
(deg.)		(GHz)
6	04/07/2009	37.1 ± 0.2

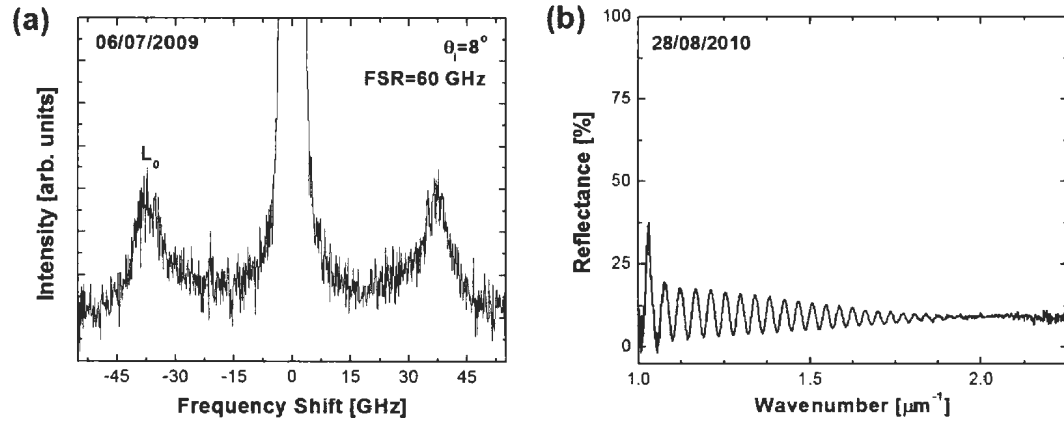


Figure B.11: (a) Near-normal incidence 180° -backscattering geometry Brillouin spectrum and (b) near-normal incidence broadband optical reflectance spectrum collected from sample PSi2.17#3, a binary periodic multilayered π -Si film. Brillouin peak L_0 was attributed to the zeroth-order folded longitudinal bulk acoustic mode

Table B.11: The θ_i value, the Brillouin spectrum collection date, and the observed phonon modes and corresponding frequencies obtained for sample PSi2.17#3, a binary periodic multilayered π -Si film fabricated on 25/06/2009. The anodization times per cycle were $t_1 = 0.17391$ s and $t_2 = 0.23256$ s, the number of etch cycles is $\eta = 100$, and the SL modulation wavelength deduced using the etch times and etch rates was $D = (50 \pm 1)$ nm.

θ_i	Collection Date	ν_{L_0}
(deg.)		(GHz)
8	06/07/2009	37.0 ± 0.1

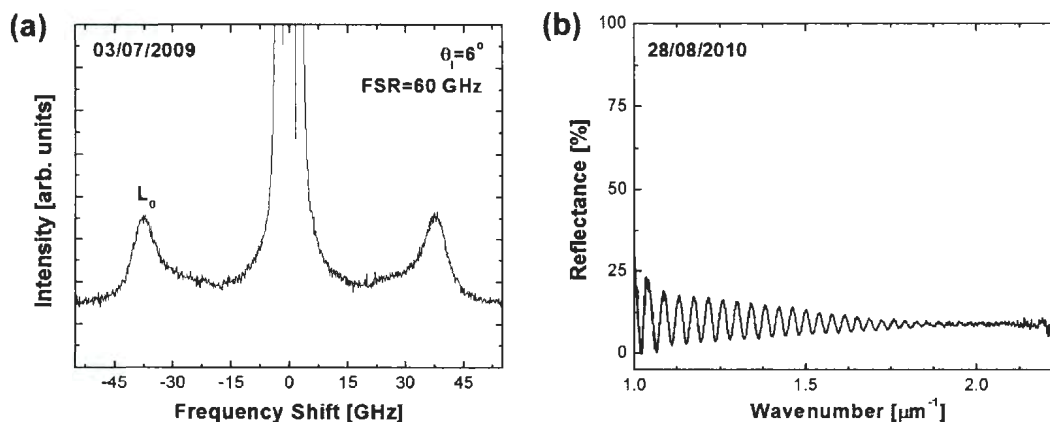


Figure B.12: (a) Near-normal incidence 180° -backscattering geometry Brillouin spectrum and (b) near-normal incidence broadband optical reflectance spectrum collected from sample PSi2.17#4, a binary periodic multilayered π -Si film. Brillouin peak L_0 was attributed to the zeroth-order folded longitudinal bulk acoustic mode

Table B.12: The θ_i value, the Brillouin spectrum collection date, and the observed phonon modes and corresponding frequencies obtained for sample PSi2.17#4, a binary periodic multilayered π -Si film fabricated on 25/06/2009. The anodization times per cycle were $t_1 = 0.13044$ s and $t_2 = 0.17442$ s, while the SL modulation wavelength deduced using the etch times and etch rates was $D = (38 \pm 1)$ nm.

θ_i	Collection Date	ν_{L_0}
(deg.)		(GHz)
6	03/07/2009	36.02 ± 0.06

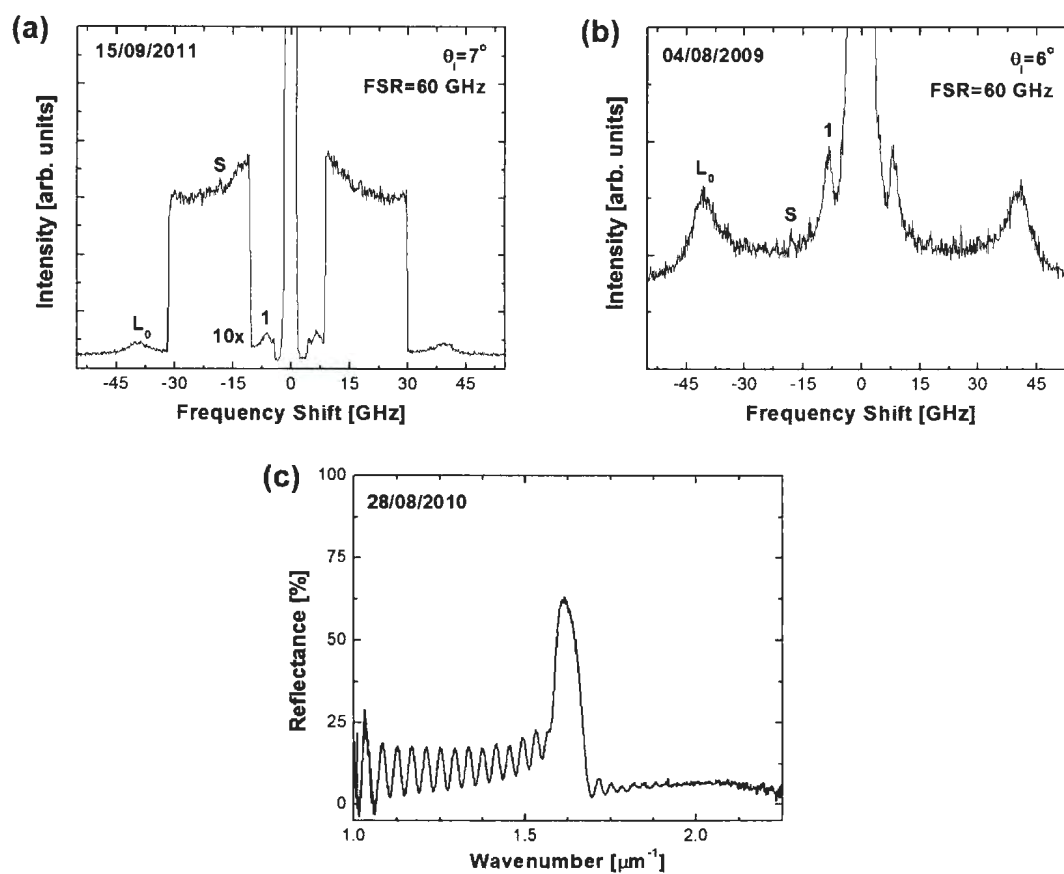


Figure B.13: (a)-(b) Near-normal incidence 180° -backscattering geometry Brillouin spectra and (c) near-normal incidence broadband optical reflectance spectrum collected from sample PSi2.18#12, a binary periodic multilayered π -Si film. Brillouin peaks L_0 and S were attributed to the zeroth-order folded longitudinal bulk acoustic mode and a surface-localized mode, respectively, while peak 1 was thought to be due to the $l = -1$ folded longitudinal bulk acoustic phonon.

Table B.13: The θ_i value, the Brillouin spectrum collection date, and the observed phonon modes and corresponding frequencies obtained for sample PSi2.18#12, a binary periodic multilayered π -Si film fabricated on 31/07/2009. The anodization times per cycle were $t_1 = 0.47432$ s and $t_2 = 0.64159$ s, the number of etch cycles is $\eta = 37$, the SL modulation wavelength deduced using the etch times and etch rates was $D = (138 \pm 4)$ nm, and the spectral position of the observed first-order optical Bragg peak was $w_1 = (1.62 \pm 0.01) \mu\text{m}^{-1}$.

θ_i	Collection Date	ν_{L_0}	ν_S	ν_1
(deg.)		(GHz)	(GHz)	(GHz)
7	15/09/2011	39.11 ± 0.09	18.08 ± 0.06	6.52 ± 0.05
6	04/08/2009	39.86 ± 0.08	18.0 ± 0.1	8.35 ± 0.04

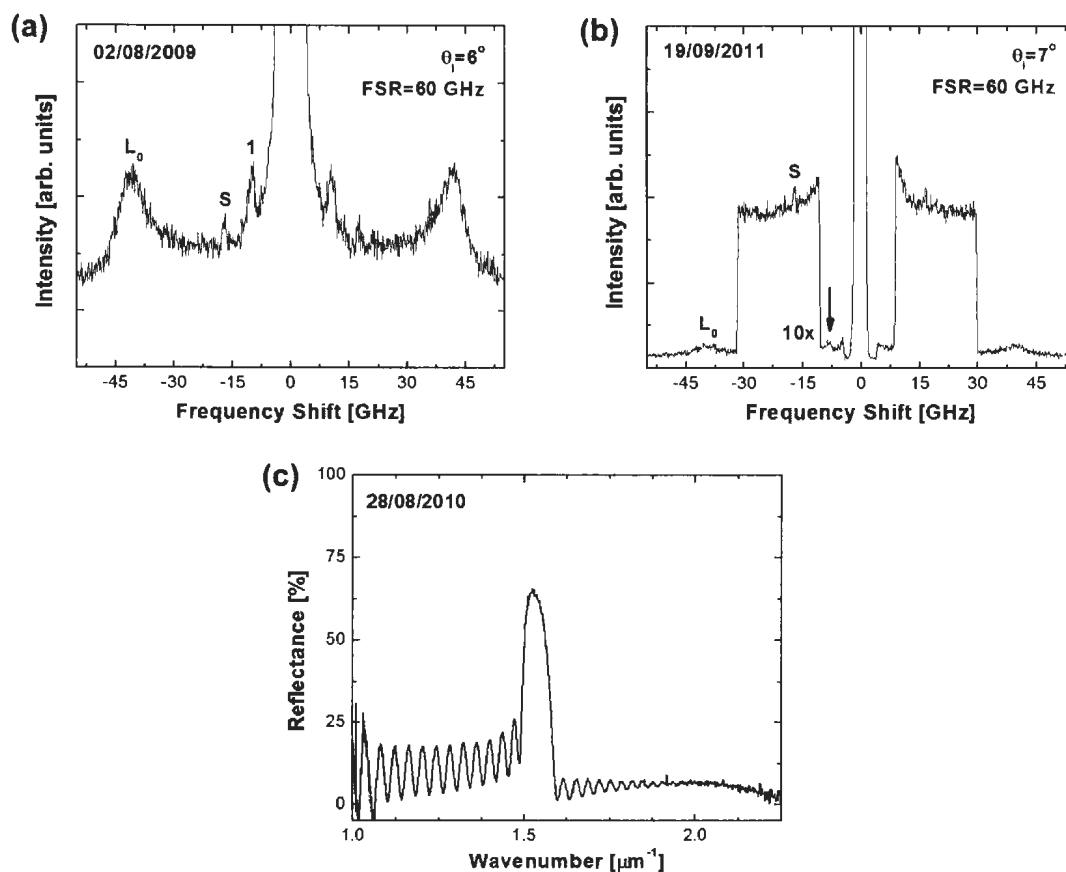


Figure B.14: (a)-(b) Near-normal incidence 180° -backscattering geometry Brillouin spectra and (c) near-normal incidence broadband optical reflectance spectrum collected from sample PSi2.18#13, a binary periodic multilayered π -Si film. Brillouin peaks L_0 and S were attributed to the zeroth-order folded longitudinal bulk acoustic mode and a surface-localized mode, respectively, while peak 1 was thought to be due to the $l = -1$ folded longitudinal bulk acoustic phonon. The arrow indicates a weak spectral feature that may be due to scattering from the $l = -1$ folded longitudinal bulk acoustic mode.

Table B.14: The θ_i value, the Brillouin spectrum collection date, and the observed phonon modes and corresponding frequencies obtained for sample PSi2.18#13, a binary periodic multilayered π -Si film fabricated on 31/07/2009. The anodization times per cycle were $t_1 = 0.49189$ s and $t_2 = 0.66535$ s, the number of etch cycles is $\eta = 36$, the SL modulation wavelength deduced using the etch times and etch rates was $D = (143 \pm 4)$ nm, and the spectral position of the observed first-order optical Bragg peak was $w_1 = (1.53 \pm 0.01) \mu\text{m}^{-1}$.

θ_i	Collection Date	ν_{L_0}	ν_S	ν_1
(deg.)		(GHz)	(GHz)	(GHz)
6	02/08/2009	40.9 ± 0.1	17.2 ± 0.1	10.19 ± 0.07
7	19/09/2011	39.2 ± 0.2	16.89 ± 0.06	-

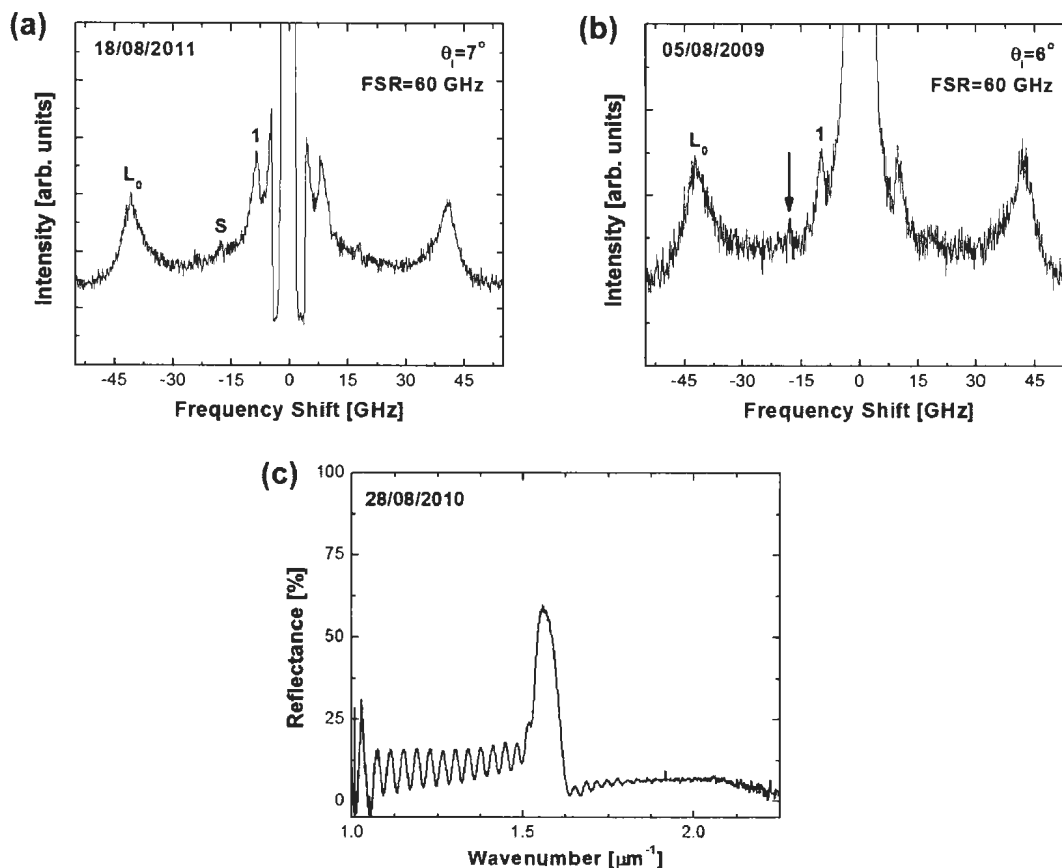


Figure B.15: (a)-(b) Near-normal incidence 180° -backscattering geometry Brillouin spectra and (c) near-normal incidence broadband optical reflectance spectrum collected from sample PSi2.18#14, a binary periodic multilayered π -Si film. Brillouin peaks L_0 and S were attributed to the zeroth-order folded longitudinal bulk acoustic mode and a surface-localized mode, respectively, while peak 1 was thought to be due to the $l = -1$ folded longitudinal bulk acoustic phonon. The arrow indicates a weak spectral feature that may be due to scattering from a surface-localized acoustic mode.

Table B.15: The θ_i value, the Brillouin spectrum collection date, and the observed phonon modes and corresponding frequencies obtained for sample P*Si*2.18#14, a binary periodic multilayered π -Si film fabricated on 31/07/2009. The anodization times per cycle were $t_1 = 0.45676$ s and $t_2 = 0.61782$ s, the number of etch cycles is $\eta = 39$, the SL modulation wavelength value deduced using the etch times and etch rates was $D = (133 \pm 4)$ nm, the SL modulation wavelength value deduced using cross-sectional scanning electron micrographs was $D = (150 \pm 1)$ nm, and the spectral position of the observed first-order optical Bragg peak was $w_1 = (1.56 \pm 0.01) \mu\text{m}^{-1}$.

θ_i	Collection Date	ν_{L_0}	ν_S	ν_1
(deg.)		(GHz)	(GHz)	(GHz)
7	18/08/2011	40.21 ± 0.07	17.8 ± 0.1	8.46 ± 0.04
6	05/08/2009	41.49 ± 0.09	-	9.93 ± 0.07

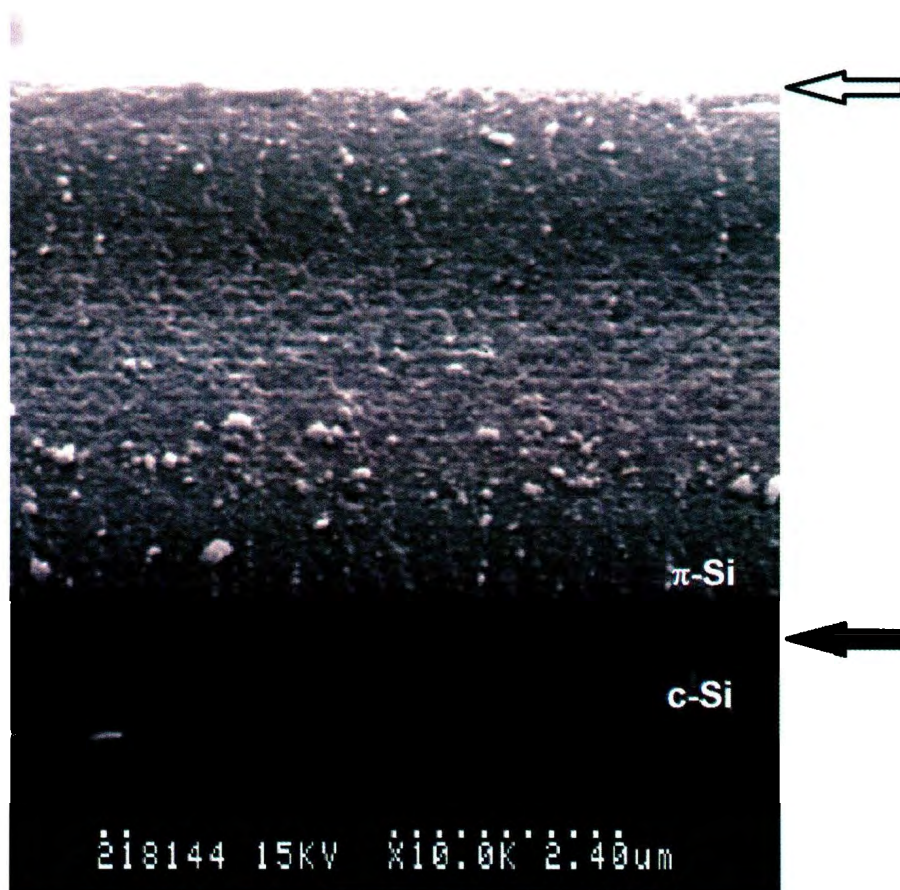


Figure B.16: Cross-sectional scanning electron micrograph of PSi2.18#14. There were 39 cycles of the current density. Overall thickness is $\sim 5.9 \mu\text{m}$. Empty(filled) arrows denote the film-air(substrate-film) interface.

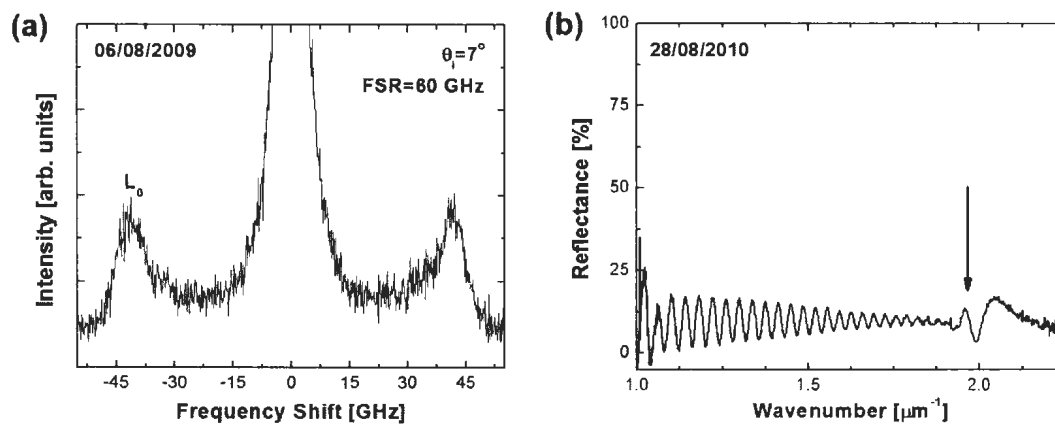


Figure B.17: (a) Near-normal incidence 180° -backscattering geometry Brillouin spectra and (b) near-normal incidence broadband optical reflectance spectrum collected from sample PSi2.18#15, a binary periodic multilayered π -Si film. Brillouin peak L_0 was attributed to the zeroth-order folded longitudinal bulk acoustic mode. The arrow indicates a weak spectral feature in the reflectance spectrum that may be a weak optical Bragg peak.

Table B.16: The θ_i value, the Brillouin spectrum collection date, and the observed phonon modes and corresponding frequencies obtained for sample PSi2.18#15, a binary periodic multilayered π -Si film fabricated on 31/07/2009. The anodization times per cycle were $t_1 = 0.34432$ s and $t_2 = 0.46574$ s, the number of etch cycles was $\eta = 51$, and the SL modulation wavelength deduced using the etch times and etch rates was $D = (100 \pm 3)$ nm.

θ_i	Collection Date	ν_{L_0}
(deg.)		(GHz)
7	06/08/2009	41.0 ± 0.1

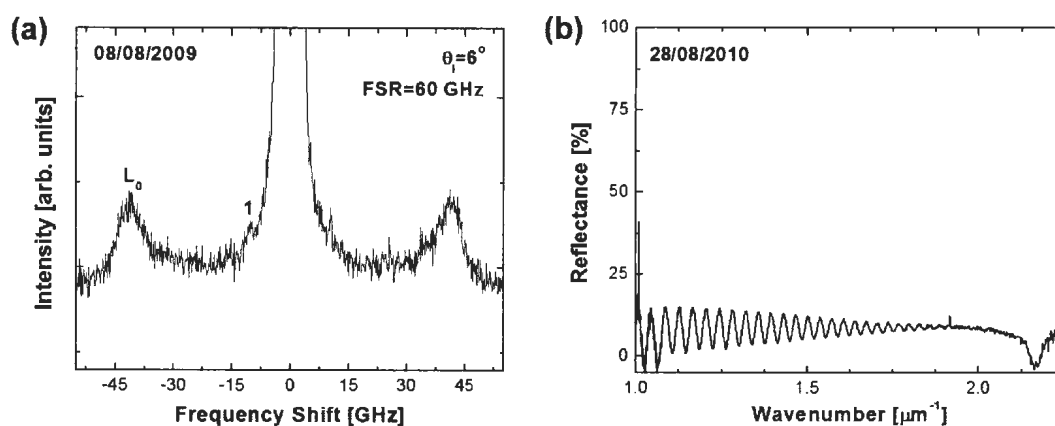


Figure B.18: (a) Near-normal incidence 180° -backscattering geometry Brillouin spectra and (b) near-normal incidence broadband optical reflectance spectrum collected from sample PSi2.18#17, a binary periodic multilayered π -Si film. Brillouin peak L_0 was attributed to the zeroth-order folded longitudinal bulk acoustic mode, while peak 1 was thought to be due to the $l = -1$ folded longitudinal bulk acoustic phonon.

Table B.17: The θ_i value, the Brillouin spectrum collection date, and the observed phonon modes and corresponding frequencies obtained for sample PSi2.18#17, a binary periodic multilayered π -Si film fabricated on 31/07/2009. The anodization times per cycle were $t_1 = 0.30216$ s and $t_2 = 0.40871$ s, the number of etch cycles was $\eta = 59$, the SL modulation wavelength value deduced using the etch times and etch rates was $D = (88 \pm 2)$ nm, and the SL modulation wavelength value deduced using cross-sectional scanning electron micrographs was $D = (98 \pm 1)$ nm.

θ_i	Collection Date	ν_{L_0}	ν_1
(deg.)		(GHz)	(GHz)
6	08/08/2009	40.8 ± 0.1	10.3 ± 0.2

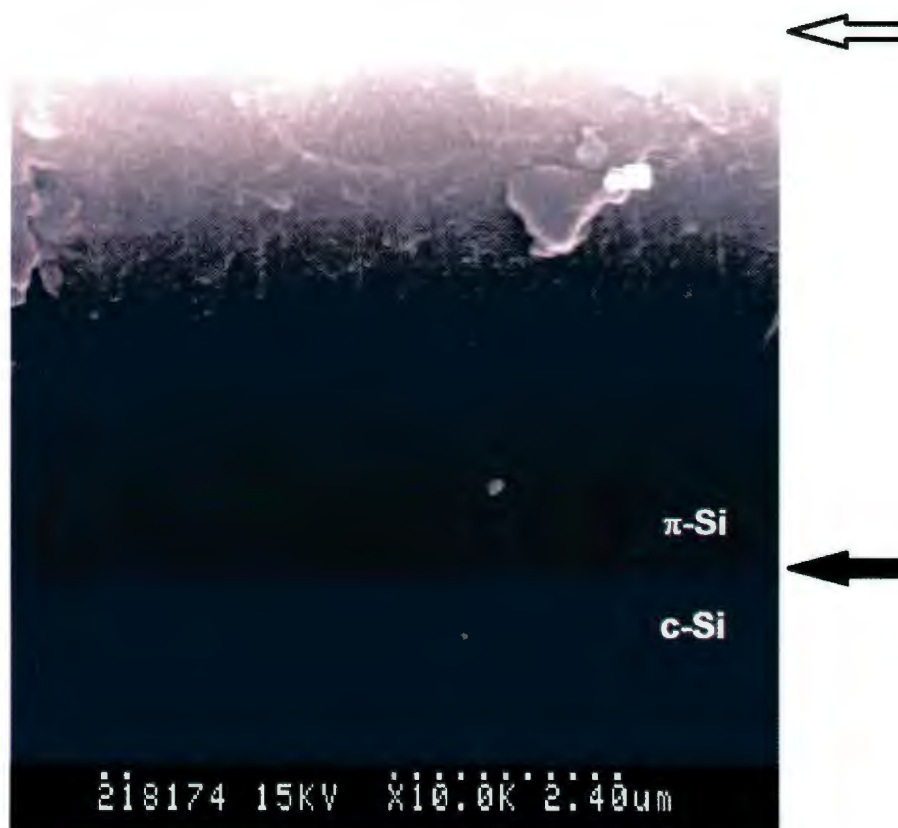


Figure B.19: Cross-sectional scanning electron micrograph of PSi2.18#17. There were 59 cycles of the current density. Overall thickness is $\sim 5.9\mu\text{m}$. Image contrast was adjusted for clarity. Empty (filled) arrows denote the film-air (substrate-film) interface.

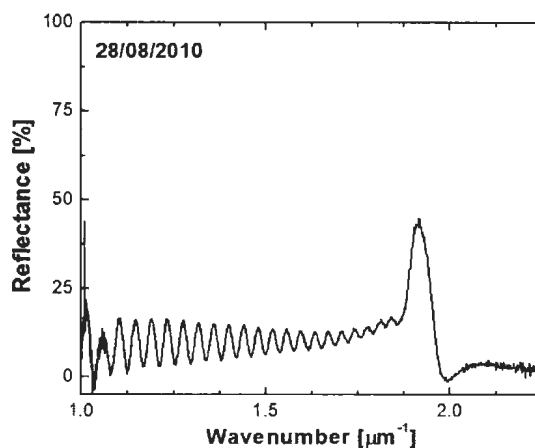


Figure B.20: Near-normal incidence broadband optical reflectance spectrum from sample PSi2.20#7, a binary periodic multilayered π -Si film fabricated on 14/08/2009. The anodization times per cycle were $t_1 = 0.39000$ s and $t_2 = 0.52753$ s, the number of etch cycles was $\eta = 45$, and the SL modulation wavelength value deduced using the etch times and etch rates was $D = (113 \pm 3)$ nm.

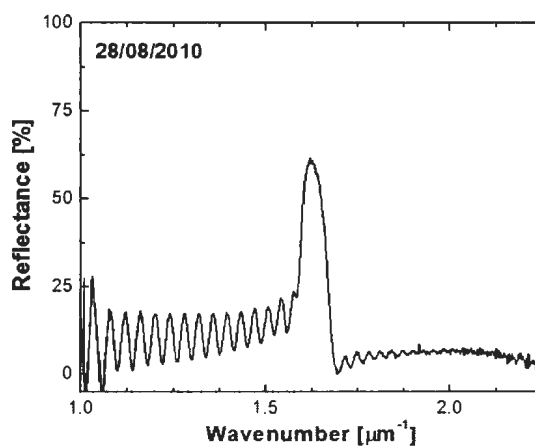


Figure B.21: Near-normal incidence broadband optical reflectance spectrum from sample PSi2.20#9, a binary periodic multilayered π -Si film fabricated on 14/08/2009. The anodization times per cycle were $t_1 = 0.45676$ s and $t_2 = 0.61782$ s, while the SL modulation wavelength value deduced using the etch times and etch rates was $D = (133 \pm 4)$ nm.

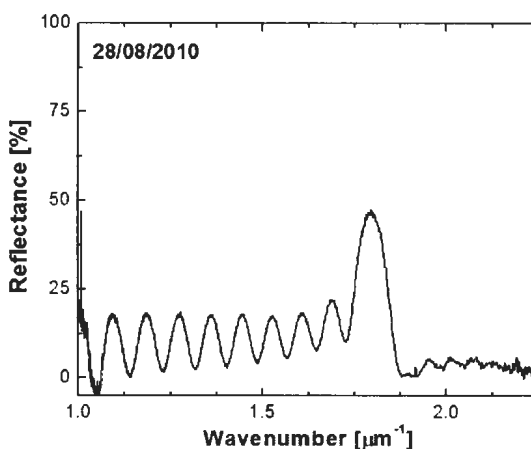


Figure B.22: Near-normal incidence broadband optical reflectance spectrum from sample PSi2.18#7, a binary periodic multilayered π -Si film fabricated on 21/07/2009. The anodization times per cycle were $t_1 = 0.41739$ s and $t_2 = 0.55813$ s, the number of etch cycles was $\eta = 20$, and the SL modulation wavelength value deduced using the etch times and etch rates was $D = (121 \pm 3)$ nm.

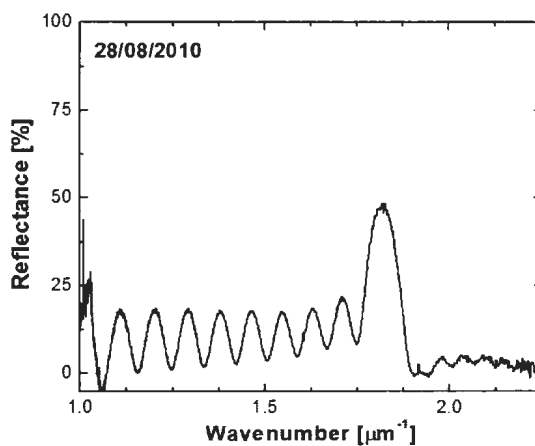


Figure B.23: Near-normal incidence broadband optical reflectance spectrum from sample PSi2.18#8, a binary periodic multilayered π -Si film fabricated on 21/07/2009. The anodization times per cycle were $t_1 = 0.41335$ s and $t_2 = 0.55272$ s, the number of etch cycles was $\eta = 20$, and the SL modulation wavelength value deduced using the etch times and etch rates was $D = (120 \pm 3)$ nm.

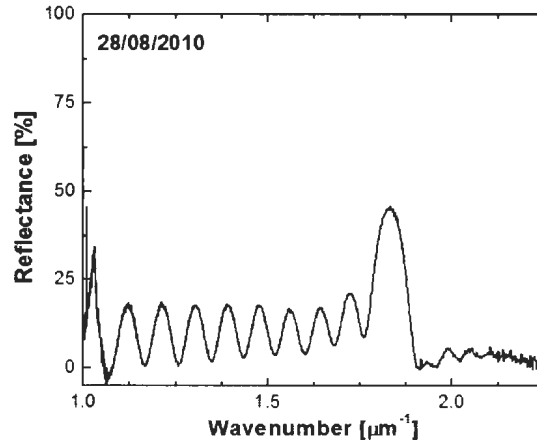


Figure B.24: Near-normal incidence broadband optical reflectance spectrum from sample PSi2.18#9, a binary periodic multilayered π -Si film fabricated on 21/07/2009. The anodization times per cycle were $t_1 = 0.40981$ s and $t_2 = 0.54799$ s, the number of etch cycles was $\eta = 20$, and the SL modulation wavelength value deduced using the etch times and etch rates was $D = (119 \pm 3)$ nm.

Table B.18: The anodization times per cycle, t_1 and t_2 , the SL modulation wavelength, D , and the spectral position of the observed first-order optical Bragg peak, w_1 , for a series of binary periodic multilayered π -Si films (see Figs. B.20 to B.24).

Sample	$t_1(t_2)$ (s(s))	D (nm)	w_1 (μm^{-1})
PSi2.20#7	0.39000(0.52753)	113 ± 3	1.91 ± 0.01
PSi2.20#9	0.45676(0.61782)	133 ± 4	1.62 ± 0.01
PSi2.18#7	0.41739(0.55813)	121 ± 3	1.80 ± 0.01
PSi2.18#8	0.41335(0.55272)	120 ± 3	1.82 ± 0.01
PSi2.18#9	0.40989(0.54799)	119 ± 3	1.83 ± 0.01

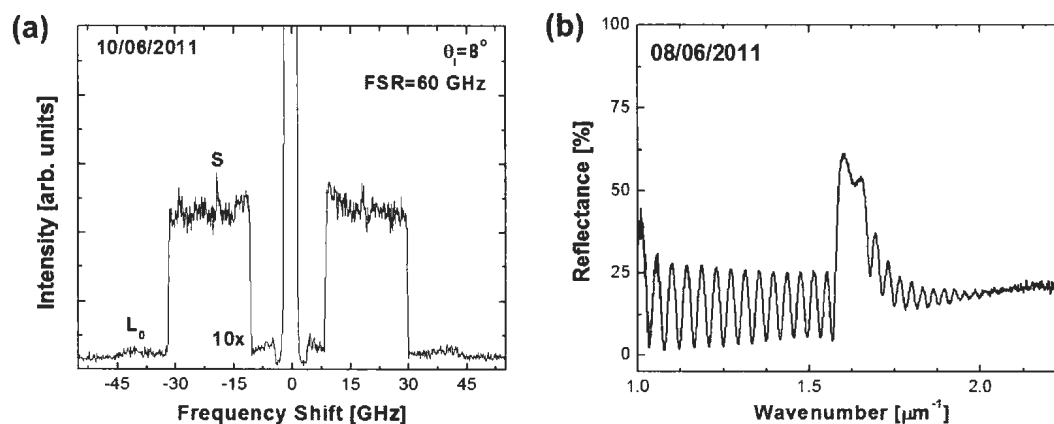


Figure B.25: (a) Near-normal incidence 180° -backscattering geometry Brillouin spectrum and (b) near-normal incidence broadband optical reflectance spectrum collected from sample P*Si*4.13#10, a binary periodic multilayered π -Si film with the higher porosity constituent layer at the air-film interface. Brillouin peaks L_0 and S were attributed to the zeroth-order folded longitudinal bulk acoustic mode and a surface-localized acoustic mode, respectively. The Brillouin spectrum was collected over 30,000 scans

Table B.19: The θ_i value, the Brillouin spectrum collection date, and the observed phonon modes and corresponding frequencies obtained for sample P*Si*4.13#10, a binary periodic multilayered π -Si film with the higher porosity constituent layer at the air-film interface. The sample was fabricated during June, 2011. The anodization times per cycle were $t_1 = 0.57046$ s and $t_2 = 0.77273$ s, the SL modulation wavelength value deduced using the etch times and etch rates was $D = (166 \pm 4)$ nm, and the spectral position of the observed first-order optical Bragg peak was $w_1 = (1.62 \pm 0.01) \mu\text{m}^{-1}$.

θ_i	Collection Date	ν_{L_0}	ν_S
(deg.)		(GHz)	(GHz)
8	10/06/2011	37.7 ± 0.3	18.69 ± 0.06

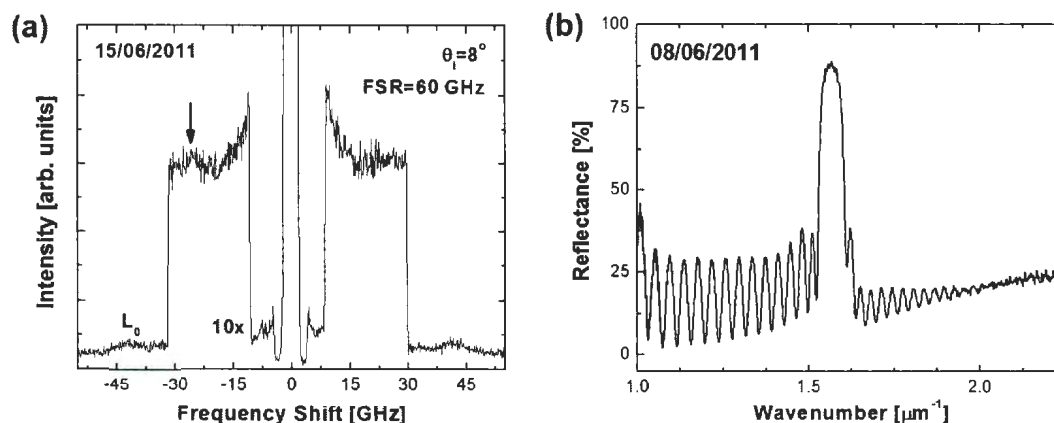


Figure B.26: (a) Near-normal incidence 180° -backscattering geometry Brillouin spectrum and (b) near-normal incidence broadband optical reflectance spectrum collected from sample PSi4.13#12, a binary periodic multilayered π -Si film with the lower porosity constituent layer at the air-film interface. Brillouin peak L_0 was attributed to the zeroth-order folded longitudinal bulk acoustic mode. The arrow indicates a relatively broad, weak feature at ~ 22 GHz which is thought to be due to scattering from the zeroth-order transverse bulk acoustic mode. The Brillouin spectrum was collected over 75,000 scans

Table B.20: The θ_i value, the Brillouin spectrum collection date, and the observed phonon modes and corresponding frequencies obtained for sample PSi4.13#12, a binary periodic multilayered π -Si film with the lower porosity constituent layer at the air-film interface. The sample was fabricated during June, 2011. The anodization times per cycle were $t_1 = 0.77273$ s and $t_2 = 0.57046$ s, the SL modulation wavelength value deduced using the etch times and etch rates was $D = (166 \pm 4)$ nm, and the spectral position of the observed first-order optical Bragg peak was $w_1 = (1.57 \pm 0.01) \mu\text{m}^{-1}$.

θ_i	Collection Date	ν_{L_0}
(deg.)		(GHz)
8	15/06/2011	41.5 ± 0.2

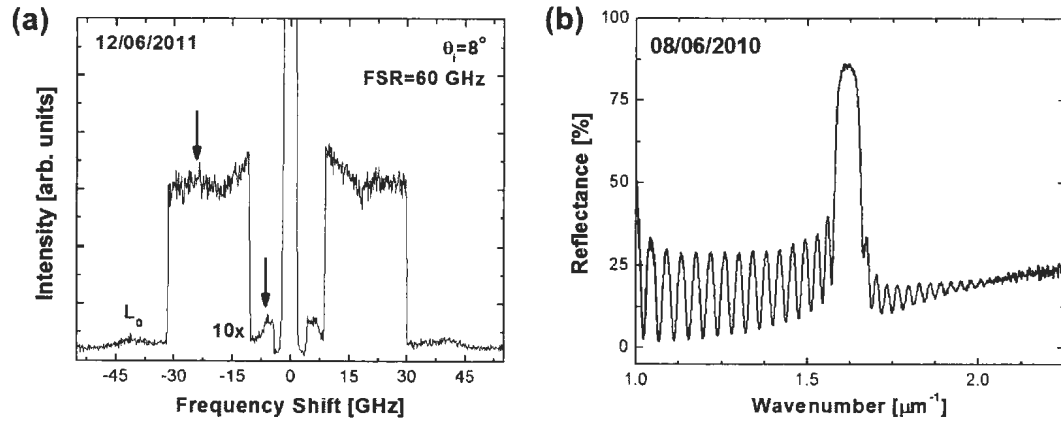


Figure B.27: (a) Near-normal incidence 180° -backscattering geometry Brillouin spectrum and (b) near-normal incidence broadband optical reflectance spectrum collected from sample P*Si*4.13#9, a binary periodic multilayered π -Si film with the lower porosity constituent layer at the air-film interface. Brillouin peak L_0 was attributed to the zeroth-order folded longitudinal bulk acoustic mode. The arrows indicate a relatively broad, weak feature at ~ 22 GHz which is thought to be due to scattering from the zeroth-order transverse bulk acoustic mode as well as spectral feature at ~ 6 GHz which may be due to the $l = -1$ folded longitudinal bulk acoustic mode. The Brillouin spectrum was collected over $\sim 58,000$ scans

Table B.22: The θ_i value, the Brillouin spectrum collection date, and the observed phonon modes and corresponding frequencies obtained for sample P*Si*4.13#9, a binary periodic multilayered π -Si film with the lower porosity constituent layer at the air-film interface. The sample was fabricated during June, 2011. The anodization times per cycle were $t_1 = 0.77273$ s and $t_2 = 0.57046$ s, the SL modulation wavelength value deduced using the etch times and etch rates was $D = (166 \pm 4)$ nm, and the spectral position of the observed first-order optical Bragg peak was $w_1 = (1.62 \pm 0.01) \mu\text{m}^{-1}$.

θ_i	Collection Date	ν_{L_0}
(deg.)		(GHz)
8	12/06/2011	40.1 ± 0.3

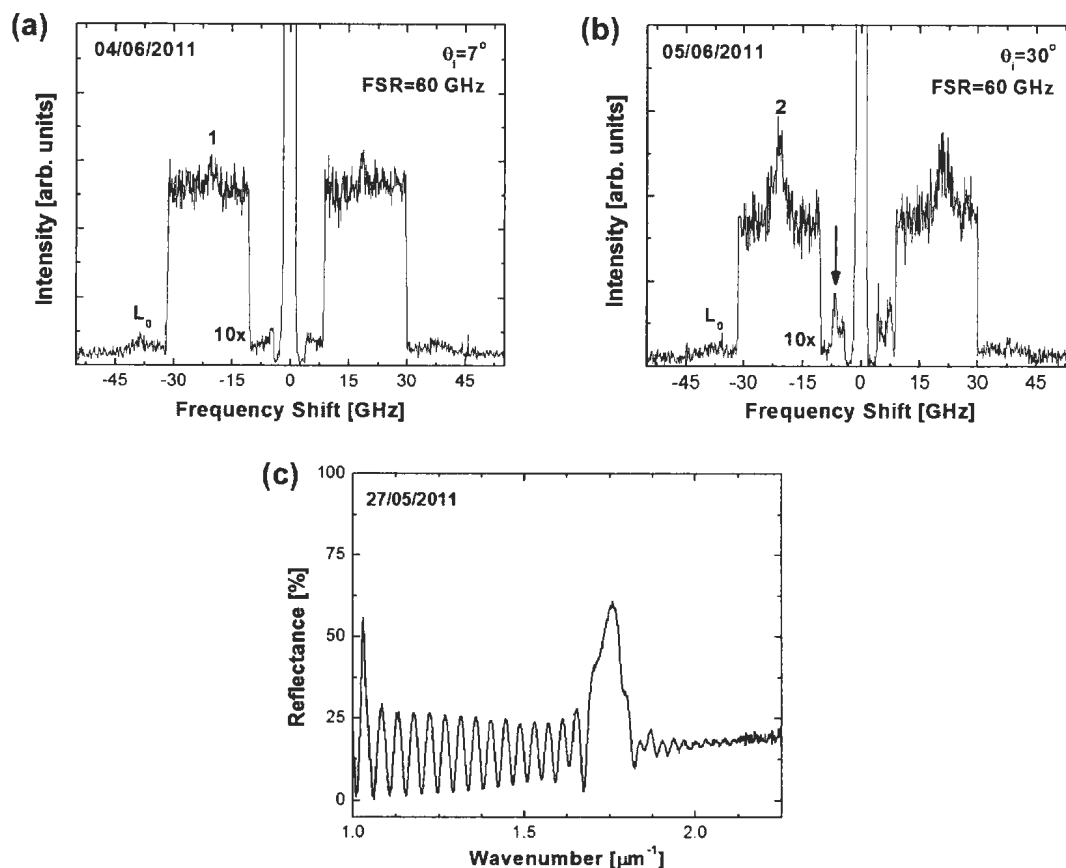


Figure B.28: (a) Near-normal incidence 180° -backscattering geometry Brillouin spectrum (collected over about 22,000 scans), (b) Oblique incidence 180° -backscattering geometry Brillouin spectrum (collected over about 7000 scans), and (c) near-normal incidence broadband optical reflectance spectrum collected from sample PSi4.13#2, a binary periodic multilayered π -Si film with the higher porosity constituent layer at the air-film interface. Brillouin peak L_0 was attributed to the zeroth-order folded longitudinal bulk acoustic mode. The arrow in the oblique incidence 180° -backscattering geometry Brillouin spectrum indicates a spectral feature which may be due to either the $l = -1$ folded longitudinal bulk acoustic mode or a surface-propagating mode. Peak 1 was thought to be due to a surface-localized mode, despite its relatively broad lineshape. Comparing the current near-normal incidence 180° -backscattering geometry Brillouin spectrum with those in Figs. B.25, B.26, and B.27, peak 1 has a signal to noise comparable to the S peak in Fig. B.25 and, furthermore, both spectra were collected for a similar number of scans. Peak 2 is attributed to the zeroth-order folded transverse bulk acoustic phonon.

Table B.23: The θ_i value, the Brillouin spectrum collection date, and the observed phonon modes and corresponding frequencies obtained for sample PSi4.13#2, a binary periodic multilayered π -Si film with the higher porosity constituent layer at the air-film interface. The sample was fabricated during June, 2011. The anodization times per cycle were $t_1 = 0.57047$ s and $t_2 = 0.77277$ s, the number of etch cycles was $\eta = 36$, the SL modulation wavelength value deduced using the etch times and etch rates was $D = (166 \pm 4)$ nm, and the spectral position of the observed first-order optical Bragg peak was $w_1 = (1.74 \pm 0.01) \mu\text{m}^{-1}$.

θ_i	Collection Date	ν_{L_0}	ν_1	ν_2
(deg.)		(GHz)	(GHz)	(GHz)
7	04/06/2011	37.9 ± 0.3	19.5 ± 0.2	-
30	05/06/2011	37 ± 2	-	21.1 ± 0.2

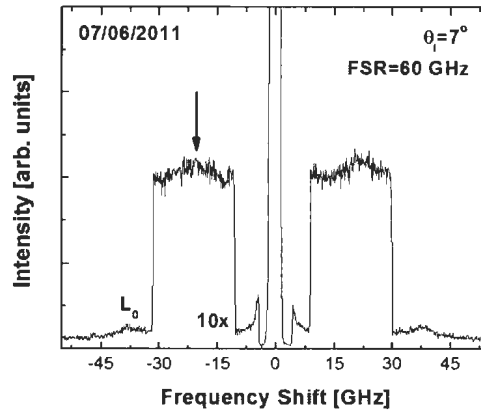


Figure B.29: Near-normal incidence 180° -backscattering geometry Brillouin spectrum collected from sample PSi4.13#5, a binary periodic multilayered π -Si film with the lower porosity constituent layer at the air-film interface. The spectrum was collected over about 65,000 scans. Brillouin peak L_0 was attributed to the zeroth-order folded longitudinal bulk acoustic mode. The arrow indicates a relatively broad, weak feature at ~ 22 GHz which is thought to be due to scattering from the zeroth-order transverse bulk acoustic mode.

Table B.24: The θ_i value, the Brillouin spectrum collection date, and the observed phonon modes and corresponding frequencies obtained for sample PSi4.13#5, a binary periodic multilayered π -Si film with the lower porosity constituent layer at the air-film interface. The sample was fabricated during June, 2011. The anodization times per cycle were $t_1 = 0.77277$ s and $t_2 = 0.57047$ s, the number of etch cycles was $\eta = 36$, and the SL modulation wavelength value deduced using the etch times and etch rates was $D = (166 \pm 4)$ nm.

θ_i	Collection Date	ν_{L_0}
(deg.)		(GHz)
7	07/06/2011	37.1 ± 0.2

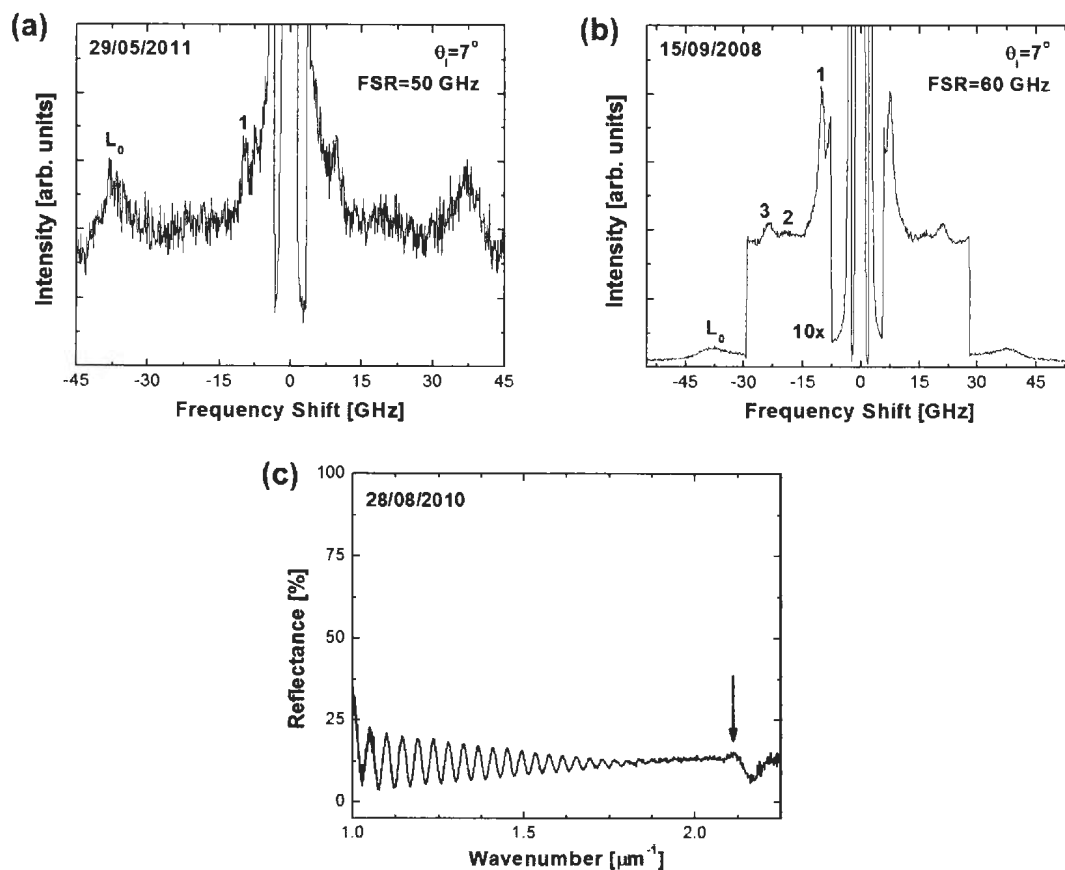


Figure B.30: (a)-(b) Near-normal incidence 180° -backscattering geometry Brillouin spectra and (c) near-normal incidence broadband optical reflectance spectrum collected from sample PSi2.12#5, a binary periodic multilayered π -Si film. Brillouin peak L_0 was attributed to the zeroth-order folded longitudinal bulk acoustic mode, while peaks 1 and 3 were thought to be due to the $l = -1$ folded longitudinal bulk acoustic phonon and the $l = 0$ folded transverse bulk acoustic phonon, respectively. Peak 2 was unassigned. The arrow indicates a spectral feature in the optical reflectance spectrum which may be due to a first-order optical Bragg peak.

Table B.25: The θ_i value, collection date, and the observed phonon modes and corresponding frequencies obtained for sample PSi2.12#5, a binary periodic multilayered π -Si film fabricated on 10/09/2008. The anodization times per cycle were $t_1 = 0.34783$ s and $t_2 = 0.46512$ s, the number of etch cycles was $\eta = 50$, the SL modulation wavelength value deduced using the etch times and etch rates was $D = (101 \pm 3)$ nm, the SL modulation wavelength value deduced using cross-sectional scanning electron micrographs was $D = (99 \pm 1)$ nm, and the spectral position of the observed first-order optical Bragg peak was $w_1 = (2.10 \pm 0.01) \mu\text{m}^{-1}$.

θ_i	Collection Date	ν_{L_0}	ν_1	ν_2	ν_3
(deg.)		(GHz)	(GHz)	(GHz)	(GHz)
7	29/05/2011	36.8 ± 0.1	9.4 ± 0.1	-	-
7	15/09/2008	37.40 ± 0.07	8.75 ± 0.02	18.3 ± 0.6	22.13 ± 0.05

Table B.26: Angle θ_i , angle θ_s , the corresponding θ_m value, the date of data collection, and the frequencies of the bulk acoustic phonons (ν_{T_0} , $\nu_{L_{-1}}$, and ν_{L_0}) probed in the pseudo-reflection geometry Brillouin scattering measurements taken from sample PSi2.12#5.

θ_i	θ_s	θ_m	Collection Date	ν_{T_0}	$\nu_{L_{-1}}$	ν_{L_0}
(deg.)	(deg.)	(deg.)		(GHz)	(GHz)	(GHz)
30	41	36	24/05/2011	21.26 ± 0.04	11.0 ± 0.2	36.57 ± 0.08
40	51	46	25/05/2011	20.52 ± 0.03	11.6 ± 0.1	35.23 ± 0.07
50	58	54	27/05/2011	20.49 ± 0.03	11.9 ± 0.1	35.32 ± 0.07

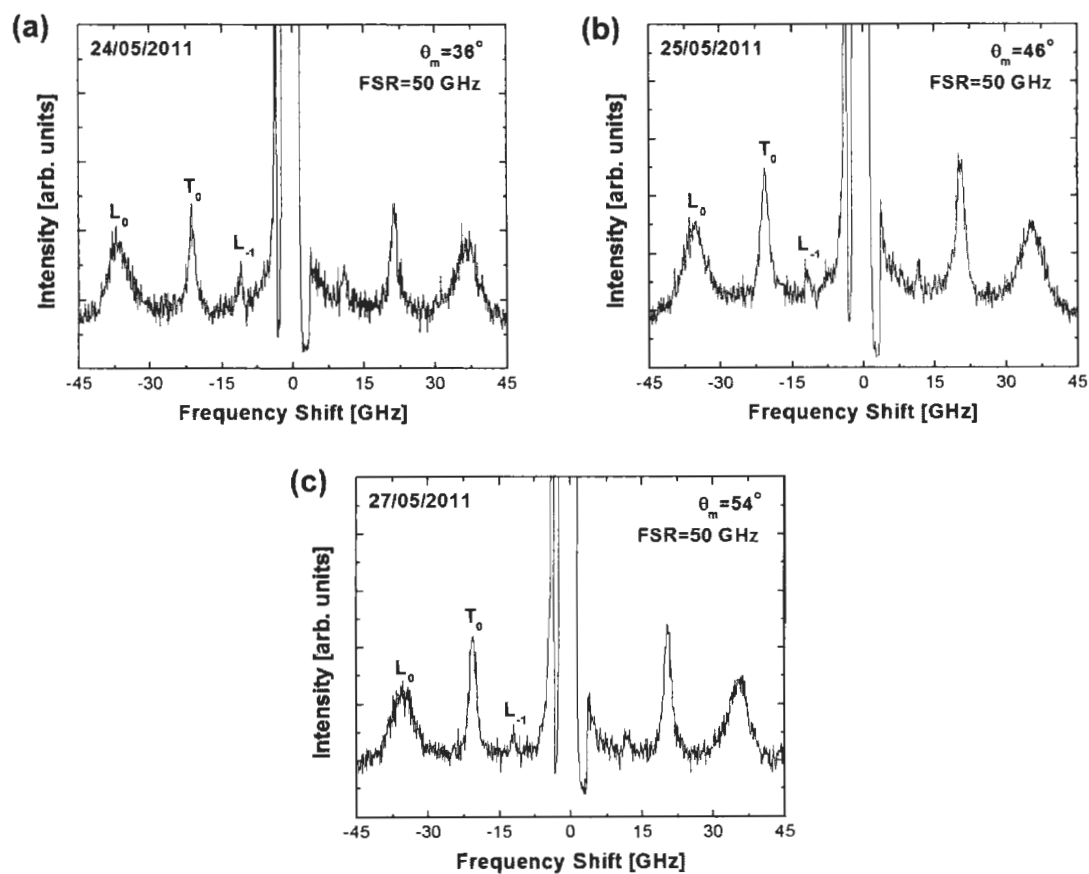


Figure B.31: Pseudo-reflection geometry Brillouin scattering spectra collected from sample PSi2.12#5, a binary periodic multilayered π -Si film. Peaks L_0 , L_{-1} , and T_0 were attributed to the $l = 0$ folded longitudinal bulk acoustic phonon, the $l = -1$ folded longitudinal bulk acoustic phonon, and the $l = 0$ folded transverse bulk acoustic phonon, respectively.

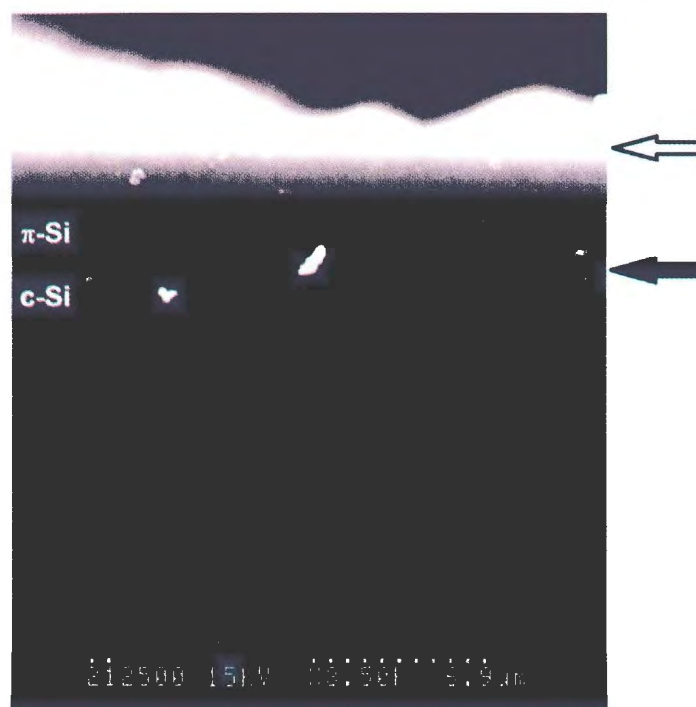


Figure B.32: Cross-sectional scanning electron micrograph of PSi2.12#15. There were 50 cycles of the current density. Overall thickness was $\sim 5\mu\text{m}$. Empty(filled) arrows denote the film-air(substrate-film) interface.

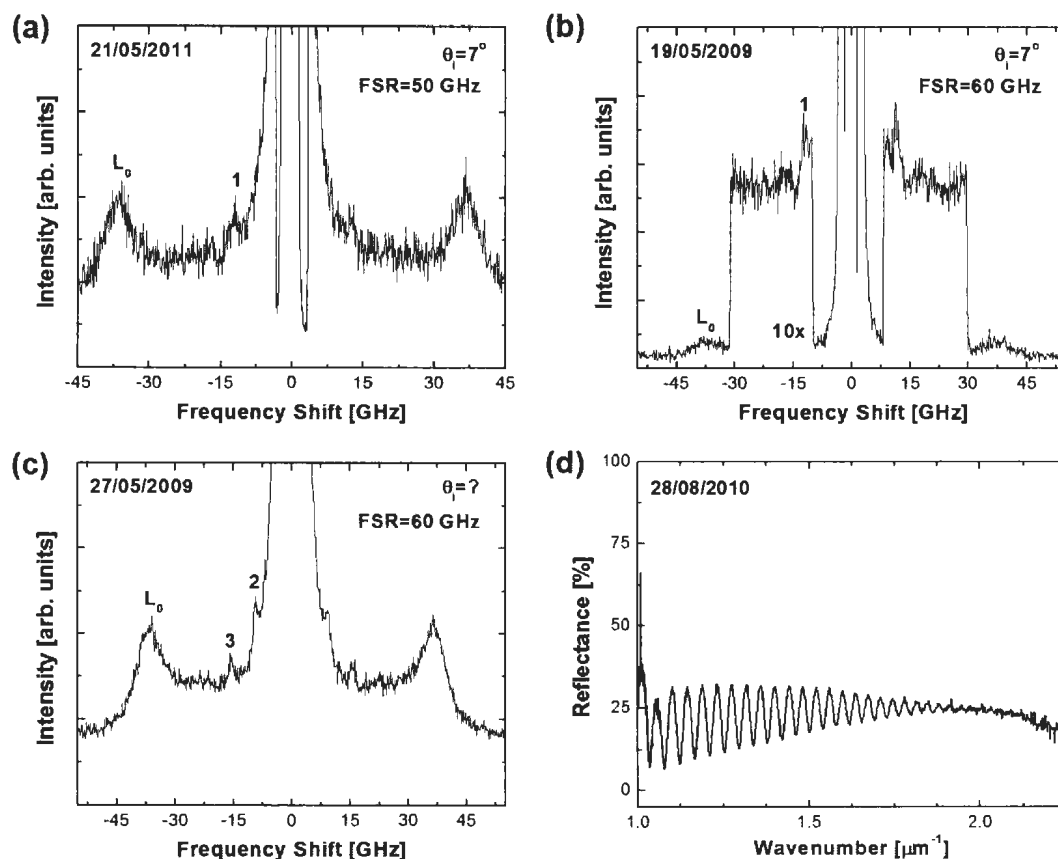


Figure B.33: (a)-(b) Near-normal incidence 180° -backscattering geometry Brillouin spectra, (c) 180° -backscattering geometry Brillouin spectrum collected at unknown angle, and (d) near-normal incidence broadband optical reflectance spectrum collected from sample PSi2.14A#2, a binary periodic multilayered π -Si film. Brillouin peak L_0 was attributed to the zeroth-order folded longitudinal bulk acoustic mode, while peak 1 was thought to be due to the $l = -1$ folded longitudinal bulk acoustic phonon. The results of the 180° -backscattering geometry Brillouin spectrum collected at an unknown value of θ_i were reported in the earliest study (see Chapter 4); the spectrum was originally considered to be collected at near-normal incidence. After failed attempts to reproduce the spectrum, it is now thought that the original spectrum was inadvertently collected at an oblique angle of incidence. Peaks 2 and 3 are unassigned.

Table B.27: The θ_i value, collection date, and the observed phonon modes and corresponding frequencies obtained for sample PSi2.14A#2, a binary periodic multilayered π -Si film fabricated on 13/05/2009. The anodization times per cycle were $t_1 = 0.30434$ s and $t_2 = 0.40698$ s, the number of etch cycles was $\eta = 60$, the SL modulation wavelength value deduced using the etch times and etch rates was $D = (88 \pm 2)$ nm.

θ_i (deg.)	Collection Date	ν_{L_0} (GHz)	ν_1 (GHz)	ν_2 (GHz)	ν_3 (GHz)
7	21/05/2011	36.4 ± 0.1	12.4 ± 0.1	-	-
7	19/05/2009	36.9 ± 0.2	11.7 ± 0.1	-	-
-	27/05/2009	36.17 ± 0.06	-	9.2 ± 0.3	15.64 ± 0.08

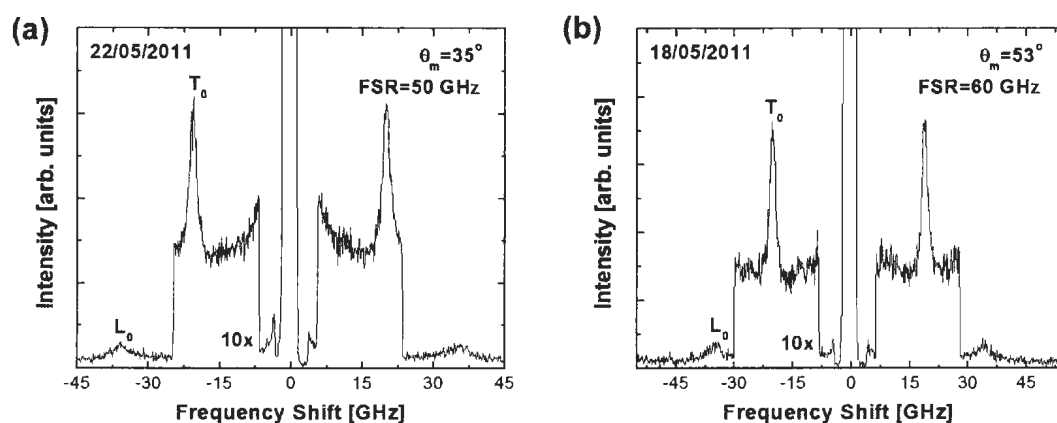


Figure B.34: Pseudo-reflection geometry Brillouin scattering spectra collected from sample PSi2.14A#2, a binary periodic multilayered π -Si film. Peaks L_0 and T_0 were attributed to the $l = 0$ folded longitudinal bulk acoustic phonon and the $l = 0$ folded transverse bulk acoustic phonon, respectively.

Table B.28: Angle θ_i , angle θ_s , the corresponding θ_m value, the date of data collection, and the frequencies of the bulk acoustic phonons (ν_{T_0} , $\nu_{L_{-1}}$, and ν_{L_0}) probed in the pseudo-reflection geometry Brillouin scattering measurements taken from sample PSi2.14A#2.

θ_i	θ_s	θ_m	Collection Date	ν_{T_0}	$\nu_{L_{-1}}$	ν_{L_0}
(deg.)	(deg.)	(deg.)		(GHz)	(GHz)	(GHz)
30	40	35	22/05/2011	20.34 ± 0.02	-	35.4 ± 0.2
58	68	63	18/05/2011	19.56 ± 0.03	-	34.4 ± 0.1

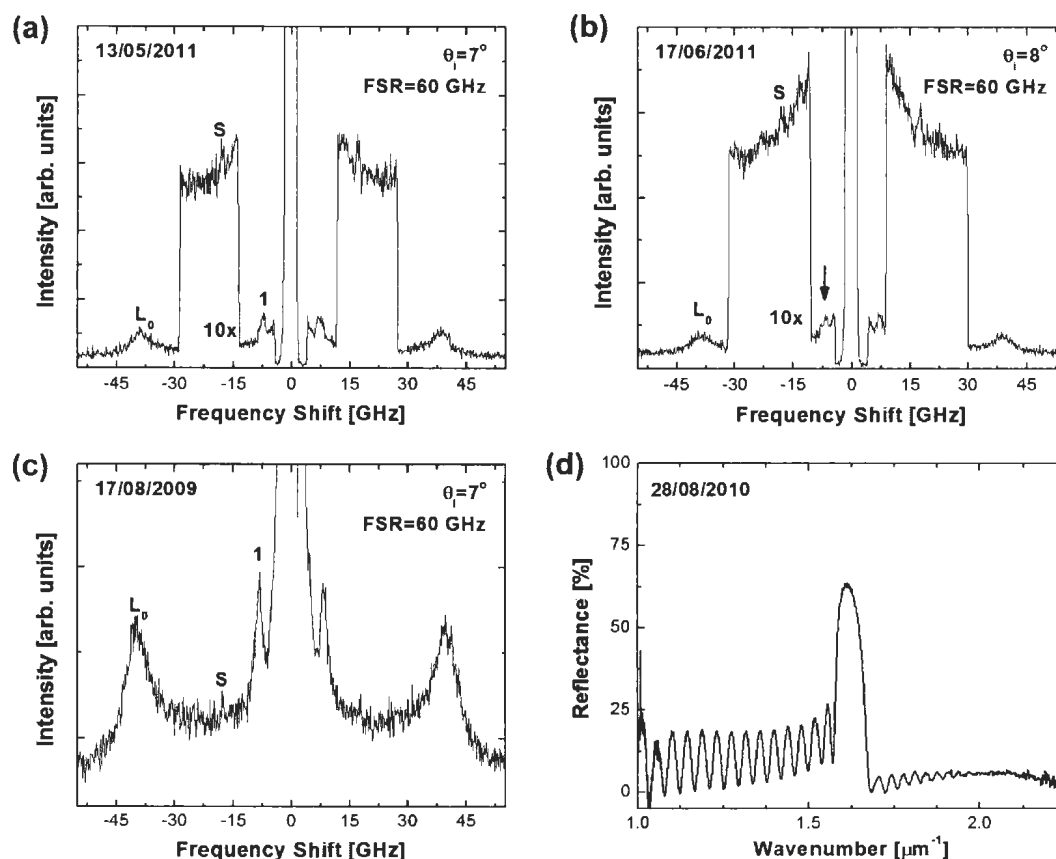


Figure B.35: (a)-(c) Near-normal incidence 180° -backscattering geometry Brillouin spectra and (d) near-normal incidence broadband optical reflectance spectrum collected from sample PSi2.20#8, a binary periodic multilayered π -Si film. Brillouin peaks L_0 and S were attributed to the zeroth-order folded longitudinal bulk acoustic mode and a surface-localized mode, respectively, while peak 1 was thought to be due to the $l = -1$ folded longitudinal bulk acoustic phonon. The arrow indicates a spectral feature which may be due to the $l = -1$ folded longitudinal bulk acoustic phonon.

Table B.29: The θ_i value, collection date, and the observed phonon modes and corresponding frequencies obtained for sample PSi2.20#8, a binary periodic multilayered π -Si film fabricated on 14/08/2009. The anodization times per cycle were $t_1 = 0.49189$ s and $t_2 = 0.66535$ s, the number of etch cycles was $\eta = 36$, the SL modulation wavelength value deduced using the etch times and etch rates was $D = (143 \pm 4)$ nm, the SL modulation wavelength value deduced cross-sectional scanning electron micrographs was $D = (145 \pm 1)$ nm, and the spectral position of the observed first-order optical Bragg peak was $w_1 = (1.61 \pm 0.01) \mu\text{m}^{-1}$.

θ_i	Collection Date	ν_{L_0}	ν_1	ν_S
(deg.)		(GHz)	(GHz)	(GHz)
7	13/05/2011	38.5 ± 0.1	7.27 ± 0.07	17.5 ± 0.1
8	17/06/2011	38.7 ± 0.1	-	17.7 ± 0.1
7	17/08/2009	39.38 ± 0.07	8.27 ± 0.04	17.8 ± 0.1

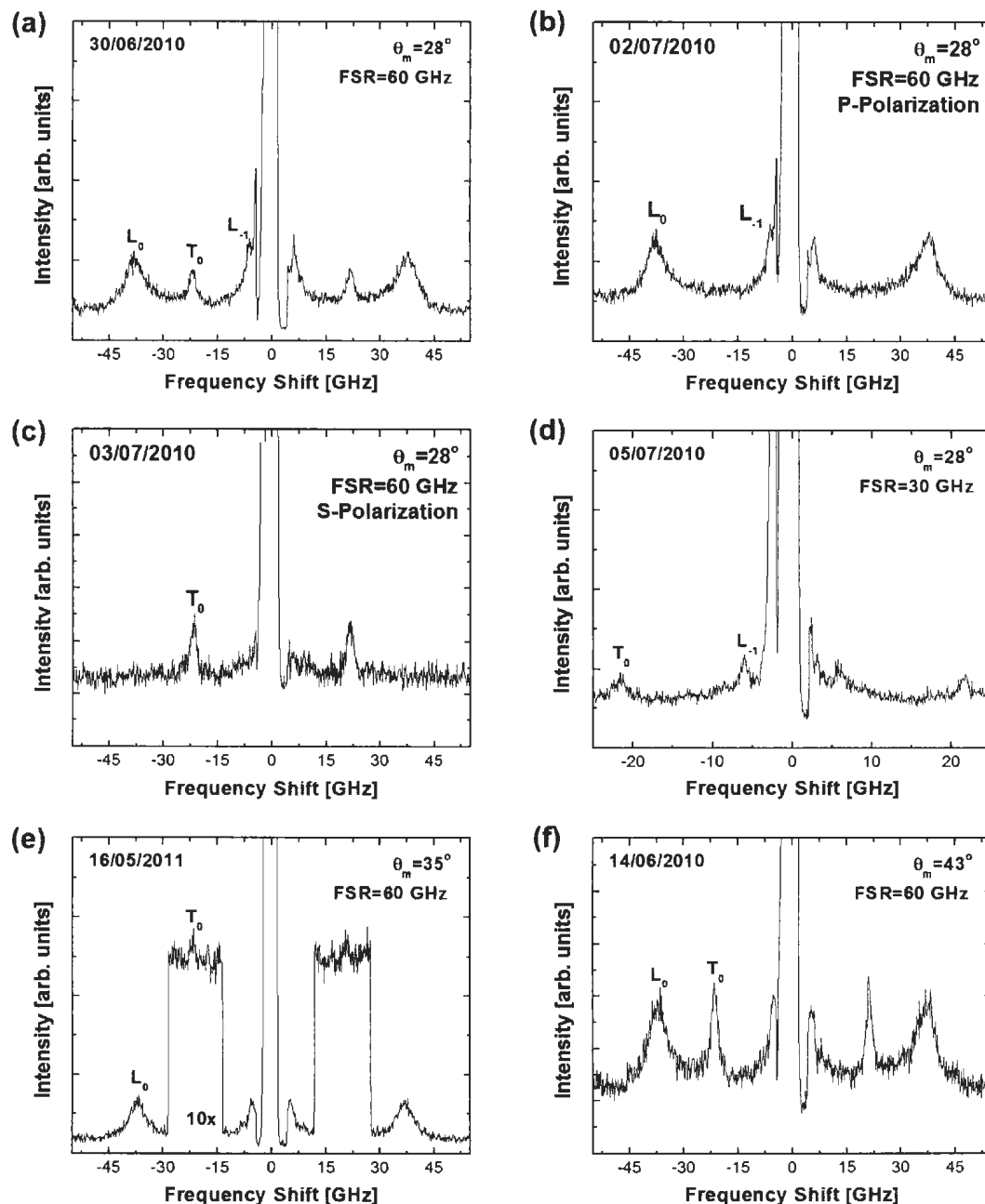


Figure B.36: A collection of pseudo-reflection geometry Brillouin scattering spectra collected from sample PSi2.20#8, a binary periodic multilayered π -Si film. Peaks L_0 and T_0 were attributed to the $l = 0$ folded longitudinal bulk acoustic phonon and the $l = 0$ folded transverse bulk acoustic phonon, respectively.

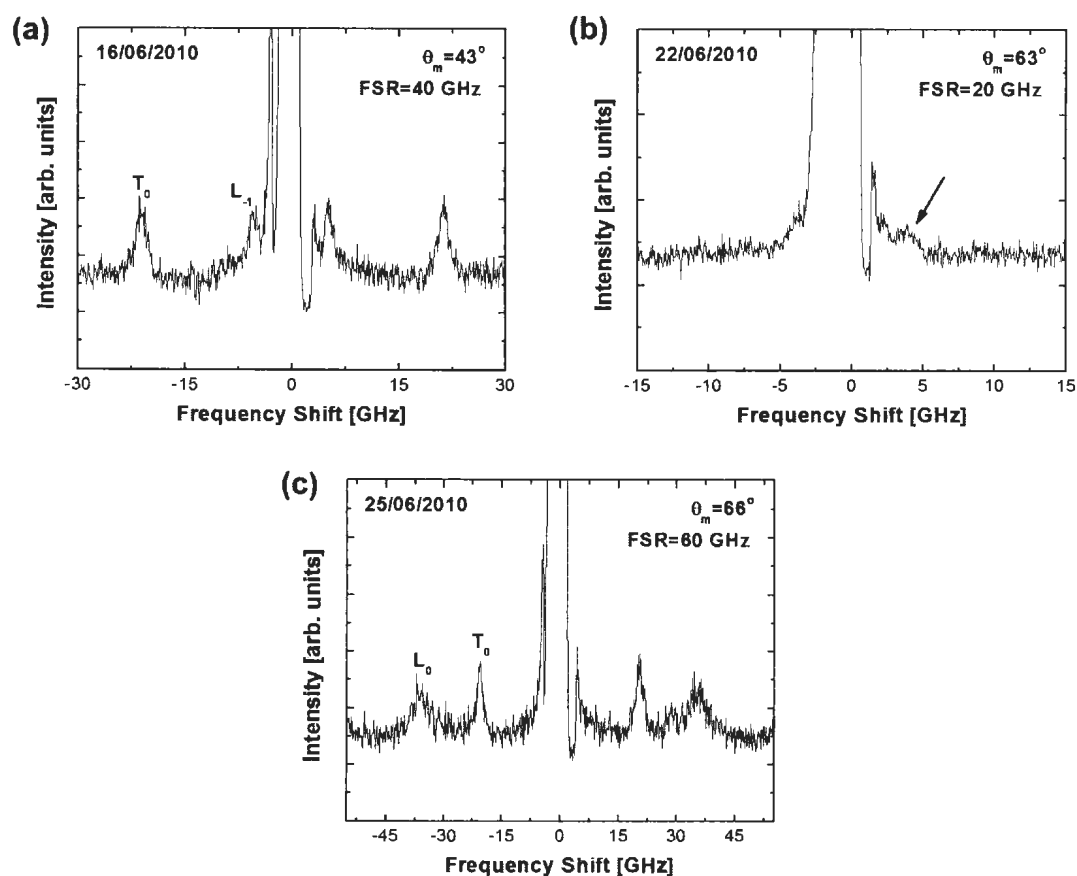


Figure B.37: Another collection of pseudo-reflection geometry Brillouin scattering spectra collected from sample PSi2.20#8, a binary periodic multilayered π -Si film. Peaks L_0 and T_0 were attributed to the $l = 0$ folded longitudinal bulk acoustic phonon and the $l = 0$ folded transverse bulk acoustic phonon, respectively. The arrow indicates a spectral feature thought to be due to the $l = -1$ folded longitudinal bulk acoustic mode; the Stokes component appears to be partially obscured by the center elastic peak.

Table B.30: Angle θ_i , angle θ_s , the corresponding θ_m value, the date of data collection, and the frequencies of the bulk acoustic phonons (ν_{T_0} , $\nu_{L_{-1}}$, and ν_{L_0}) probed in the pseudo-reflection geometry Brillouin scattering measurements taken from sample PSi2.20#8.

θ_i	θ_s	θ_m	Collection Date	ν_{T_0}	$\nu_{L_{-1}}$	ν_{L_0}
(deg.)	(deg.)	(deg.)		(GHz)	(GHz)	(GHz)
25	30	28	30/06/2010	21.8 ± 0.1	(6.22 ± 0.08)	37.44 ± 0.08
25	30	28	02/07/2010	-	(6.0 ± 0.1)	(37.41 ± 0.07)
25	30	28	03/07/2010	$(21.68 \text{ pm } 0.08)$	-	-
25	30	28	05/07/2010	(21.65 ± 0.06)	5.98 ± 0.08	-
30	40	35	16/05/2011	21.3 ± 0.2	-	36.92 ± 0.06
40	45	43	14/06/2010	21.37 ± 0.05	-	36.8 ± 0.1
40	45	43	16/06/2010	(21.25 ± 0.04)	5.3 ± 0.1	-
60	66	63	22/06/2010	-	(3.8 ± 0.1)	-
60	66	63	25/06/2010	20.53 ± 0.06	-	35.5 ± 0.2

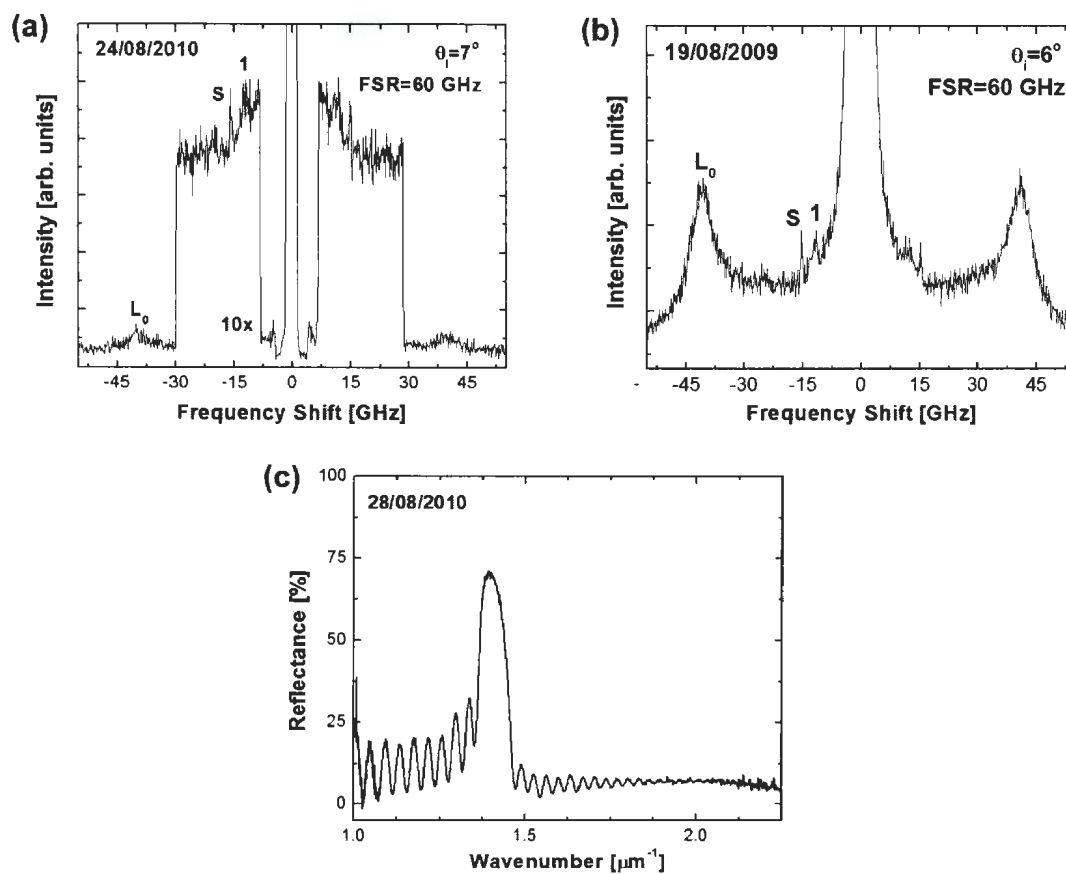


Figure B.39: (a)-(b) Near-normal incidence 180° -backscattering geometry Brillouin spectra and (c) near-normal incidence broadband optical reflectance spectrum collected from sample PSi2.20#10, a binary periodic multilayered π -Si film. Brillouin peaks L_0 and S were attributed to the zeroth-order folded longitudinal bulk acoustic mode and a surface-localized mode, respectively, while peak 1 was thought to be due to the $l = -1$ folded longitudinal bulk acoustic phonon.

Table B.31: The θ_i value, collection date, and the observed phonon modes and corresponding frequencies obtained for sample PSi2.20#10, a binary periodic multilayered π -Si film fabricated on 14/08/2009. The anodization times per cycle were $t_1 = 0.56216$ s and $t_2 = 0.76040$ s, the number of etch cycles was $\eta = 36$, the SL modulation wavelength value deduced using the etch times and etch rates was $D = (164 \pm 4)$ nm, the SL modulation wavelength value deduced cross-sectional scanning electron micrographs was $D = (166 \pm 2)$ nm, and the spectral position of the observed first-order optical Bragg peak was $w_1 = (1.40 \pm 0.01) \mu\text{m}^{-1}$.

θ_i	Collection Date	ν_{L_0}	ν_1	ν_S
(deg.)		(GHz)	(GHz)	(GHz)
7	24/08/2010	39.8 ± 0.3	11.7 ± 0.3	15.41 ± 0.03
6	19/08/2009	40.68 ± 0.06	11.6 ± 0.2	15.27 ± 0.07

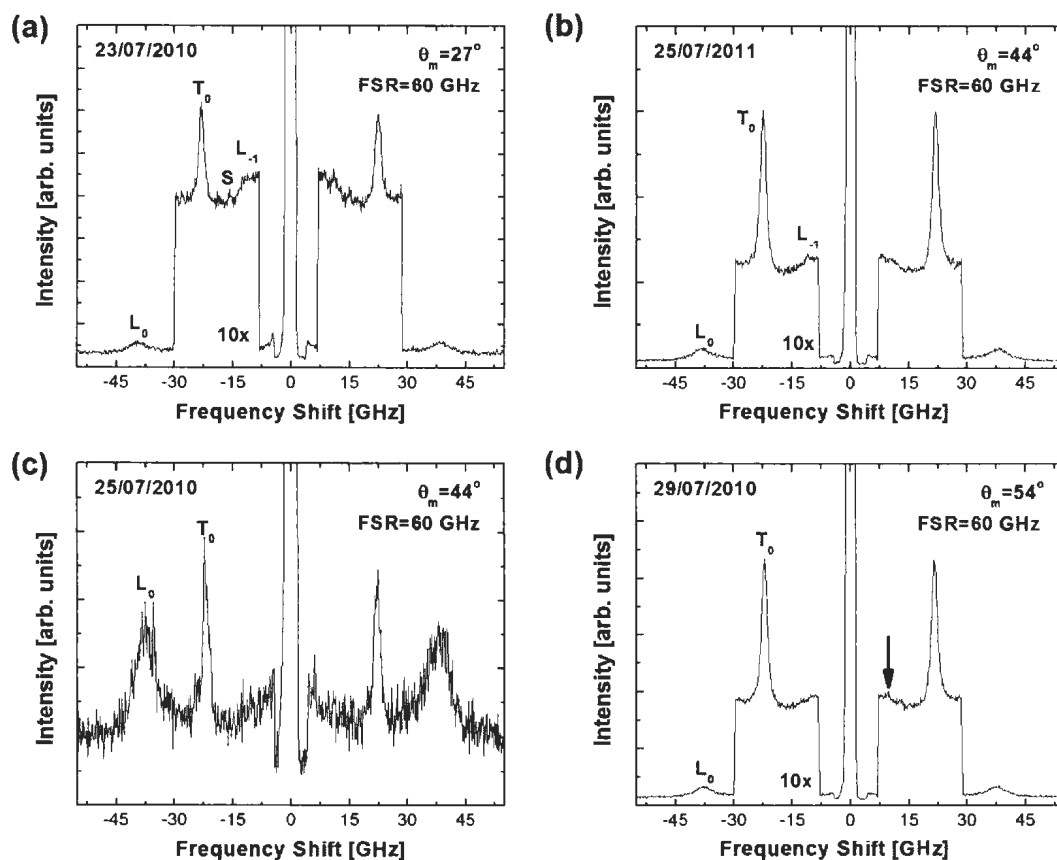


Figure B.40: A collection of pseudo-reflection geometry Brillouin scattering spectra collected from sample PSi2.20#10, a binary periodic multilayered π -Si film. Peaks L_0 , T_0 , and S were attributed to the $l = 0$ folded longitudinal bulk acoustic phonon, the $l = 0$ folded transverse bulk acoustic phonon, and a surface-localized mode, respectively. The arrow indicates a spectral feature that may be due to the $l = -1$ folded longitudinal bulk acoustic phonon.

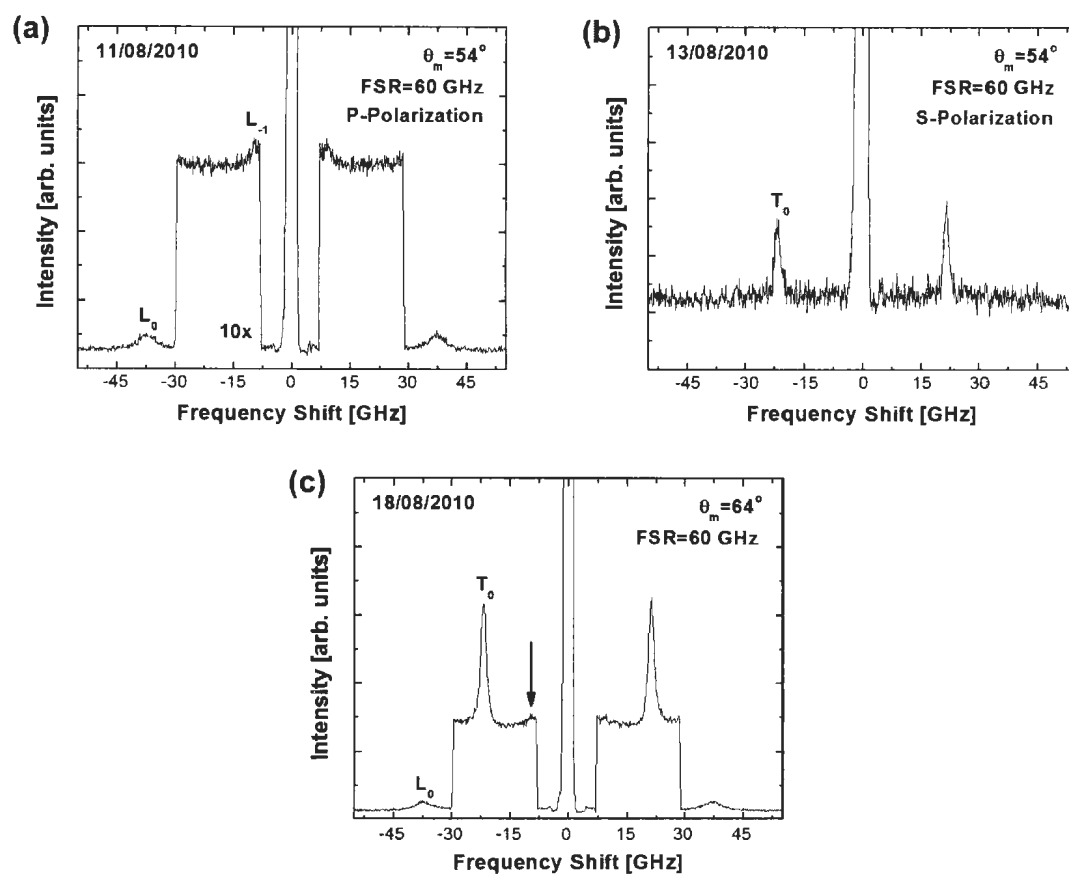


Figure B.41: Another collection of pseudo-reflection geometry Brillouin scattering spectra collected from sample PSi2.20#10, a binary periodic multilayered π -Si film. Peaks L_0 and T_0 were attributed to the $l = 0$ folded longitudinal bulk acoustic phonon and the $l = 0$ folded transverse bulk acoustic phonon, respectively. The arrow indicates a spectral feature that may be due to the $l = -1$ folded longitudinal bulk acoustic phonon.

Table B.32: Angle θ_i , angle θ_s , the corresponding θ_m value, the date of data collection, and the frequencies of the bulk acoustic phonons (ν_{T_0} , $\nu_{L_{-1}}$, ν_S , and ν_{L_0}) probed in the pseudo-reflection geometry Brillouin scattering measurements taken from sample PSi2.20#10.

θ_i	θ_s	θ_m	Collection Date	ν_{T_0}	$\nu_{L_{-1}}$	ν_{L_0}	ν_S
(deg.)	(deg.)	(deg.)		(GHz)	(GHz)	(GHz)	(GHz)
24	30	27	23/07/2010	22.73 ± 0.02	10.7 ± 0.2	38.9 ± 0.1	15.5 ± 0.1
41	47	44	25/07/2010	(22.16 ± 0.01)	10.7 ± 0.2	38.02 ± 0.05	-
41	47	44	25/07/2010	22.06 ± 0.04	-	(37.5 ± 0.1)	-
50	58	54	29/07/2010	(21.85 ± 0.01)	-	37.56 ± 0.04	-
50	58	54	11/08/2010	-	9.5 ± 0.1	(37.18 ± 0.08)	-
50	58	54	13/08/2010	21.66 ± 0.05	-	-	-
61	67	64	18/08/2010	21.55 ± 0.01	-	37.14 ± 0.06	-

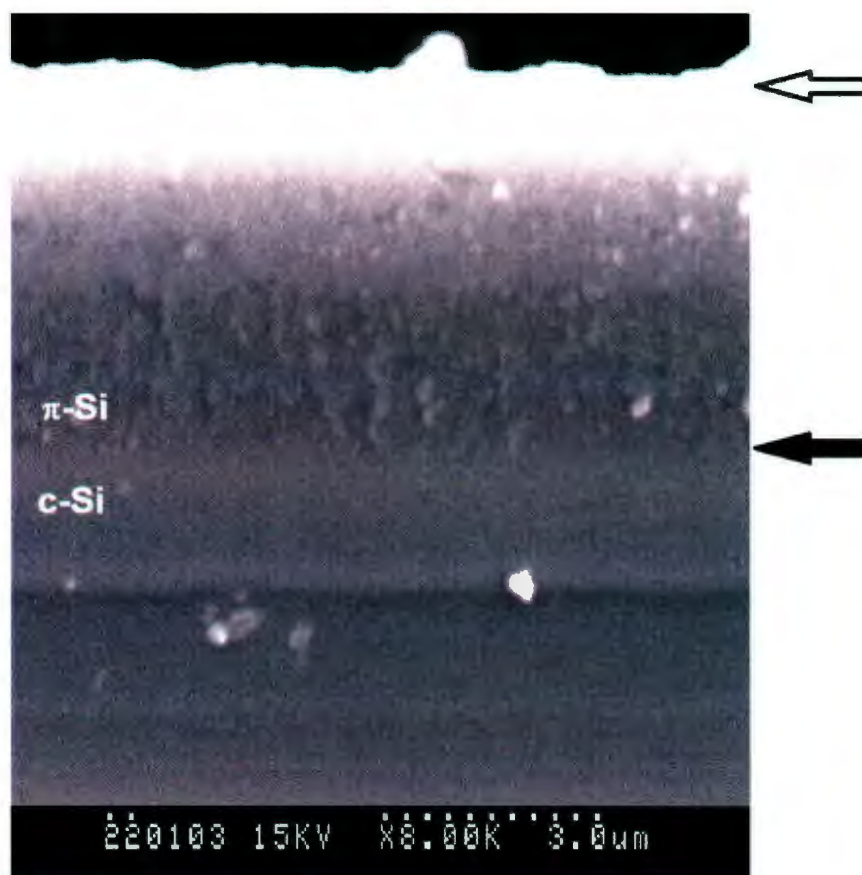


Figure B.42: Cross-sectional scanning electron micrograph of P-Si2.20#10. There were 36 cycles of the current density. Overall thickness was $\sim 6.0 \mu\text{m}$. Empty (filled) arrows denote the film-air (substrate-film) interface.

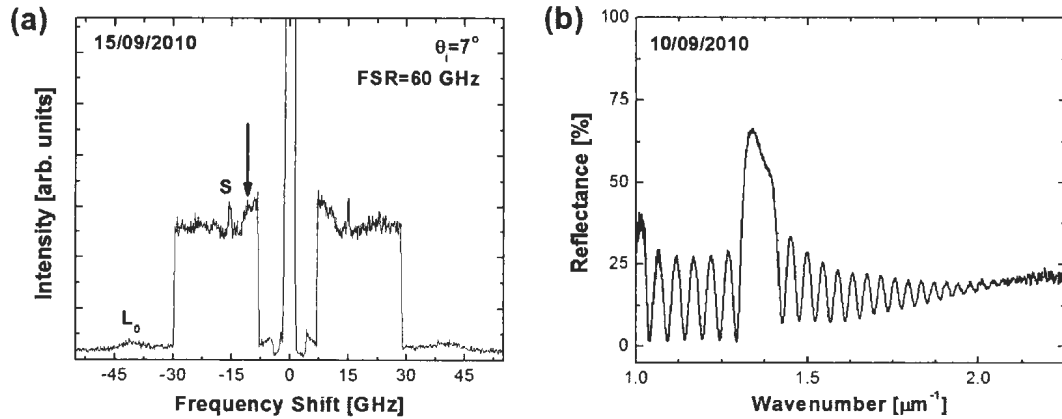


Figure B.43: (a) Near-normal incidence 180° -backscattering geometry Brillouin spectrum and (b) near-normal incidence broadband optical reflectance spectrum collected from sample PSi4.9#9, a binary periodic multilayered π -Si film. Brillouin peaks L_0 and S were attributed to the zeroth-order folded longitudinal bulk acoustic mode and a surface-localized mode, respectively. The arrow indicates a spectral feature that was thought to be due to the $l = -1$ folded longitudinal bulk acoustic phonon.

Table B.33: The θ_i value, collection date, and the observed phonon modes and corresponding frequencies obtained for sample PSi4.9#9, a binary periodic multilayered π -Si film fabricated on 09/09/2010. The anodization times per cycle were $t_1 = 0.66667$ s and $t_2 = 0.90909$ s, the number of etch cycles was $\eta = 25$, the SL modulation wavelength value deduced using the etch times and etch rates was $D = (195 \pm 5)$ nm, the SL modulation wavelength value deduced cross-sectional scanning electron micrographs was $D = (172 \pm 3)$ nm, and the spectral position of the observed first-order optical Bragg peak was $w_1 = (1.36 \pm 0.01) \mu\text{m}^{-1}$.

θ_i	Collection Date	ν_{L_0}	ν_S
(deg.)		(GHz)	(GHz)
7	15/09/2010	40.0 ± 0.2	15.32 ± 0.03

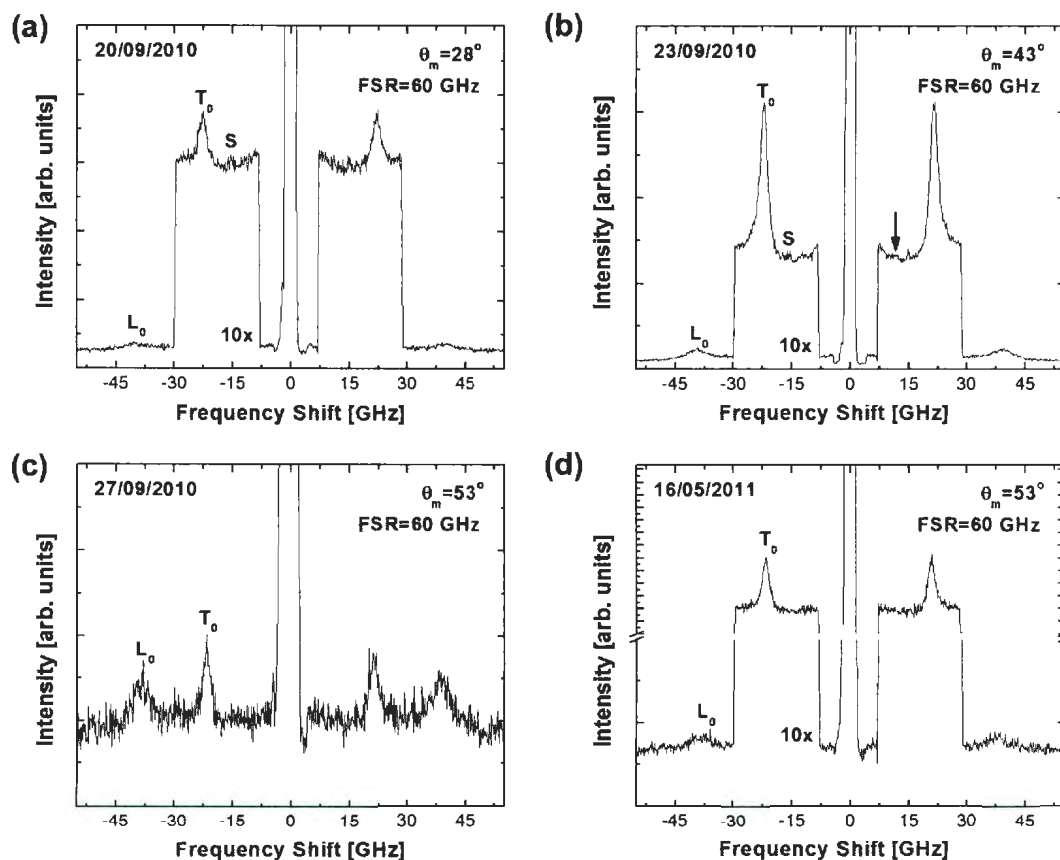


Figure B.44: A collection of pseudo-reflection geometry Brillouin scattering spectra collected from sample PSi4.9#9, a binary periodic multilayered π -Si film. Peaks L_0 , T_0 , L_{-1} , and S were attributed to the $l = 0$ folded longitudinal bulk acoustic phonon, the $l = 0$ folded transverse bulk acoustic phonon, the $l = -1$ folded longitudinal bulk acoustic phonon, and a surface-localized mode, respectively. The arrow indicates a spectral feature that may be due to the $l = -1$ folded longitudinal bulk acoustic phonon.

Table B.34: Angle θ_i , angle θ_s , the corresponding θ_m value, the date of data collection, and the frequencies of the bulk acoustic phonons (ν_{T_0} , $\nu_{L_{-1}}$, ν_S , and ν_{L_0}) probed in the pseudo-reflection geometry Brillouin scattering measurements taken from sample PSi4.9#9.

θ_i	θ_s	θ_m	Collection Date	ν_{T_0}	$\nu_{L_{-1}}$	ν_{L_0}	ν_S
(deg.)	(deg.)	(deg.)		(GHz)	(GHz)	(GHz)	(GHz)
25	30	28	20/09/2010	23.43 ± 0.04	-	39.6 ± 0.2	15.3 ± 0.1
40	46	43	23/09/2010	21.90 ± 0.02	12.0 ± 0.2	39.05 ± 0.06	15.27 ± 0.07
50	55	53	27/09/2010	21.60 ± 0.09	-	38.3 ± 0.2	-
50	55	53	04/10/2010	21.31 ± 0.03	-	38.0 ± 0.2	-

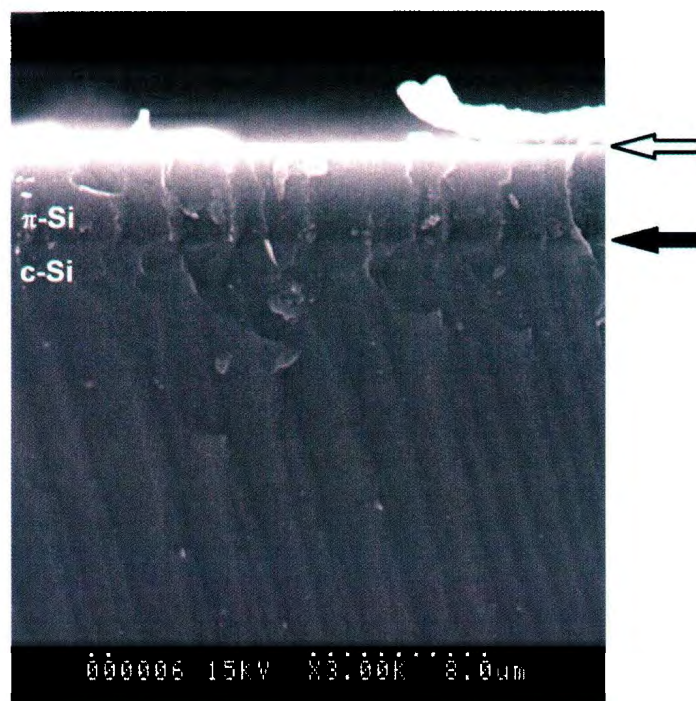


Figure B.45: Cross-sectional scanning electron micrograph of PSi4.9#9. There were 25 cycles of the current density. Overall thickness was $\sim 4.3 \mu\text{m}$. Empty(filled) arrows denote the film-air(substrate-film) interface.

Appendix C

Raw Data for Chapter 5

Pseudo-reflection geometry Brillouin scattering experiments were done on a high-porosity single-layer π -Si film (sample P*PSi*4.73), a low-porosity single-layer π -Si film (sample P*PSi*4.72), fused quartz, [100]-oriented gallium phosphide, and water. The single-layer π -Si films were fabricated using a 1:1 (49% wt. HF: 98% wt. ethanol) electrolyte. Figures C.1 to C.5 show Brillouin spectra collected from each sample; additional spectra were shown in Chapter 5. In addition, the near-normal incidence 180°-backscattering spectra, as well as the sample fabrication parameters, corresponding to the single-layer π -Si films were provided in Appendix A. The obtained Brillouin scattering data were tabulated in Tables C.1 to C.5. One should note that the near-normal incidence 180°-backscattering data corresponded to $\theta_s = \theta_i$ and $\theta_m = 0$.

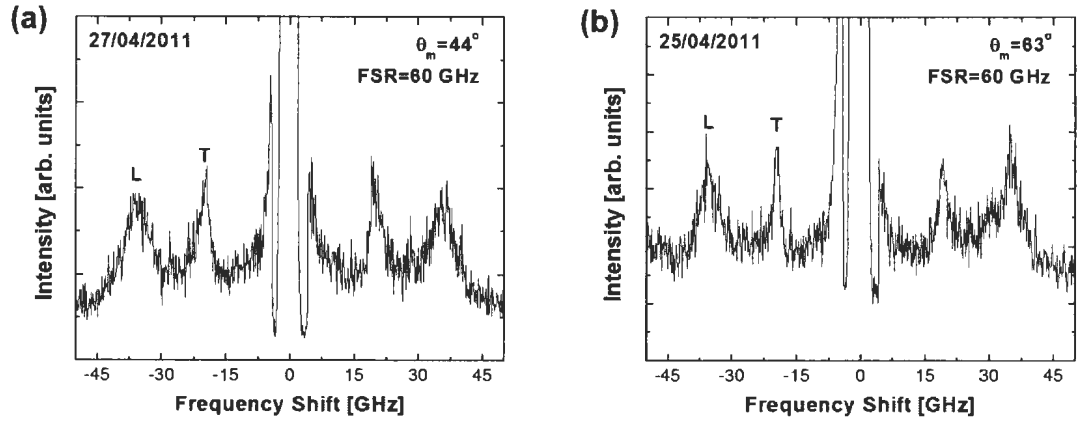


Figure C.1: Pseudo-reflection geometry Brillouin scattering spectra collected from sample P*Si*4.73, a single-layer π -Si film. Peaks L and T were attributed to the longitudinal bulk acoustic phonon and the transverse bulk acoustic phonon, respectively.

Table C.1: Angle θ_i , angle θ_s , the corresponding θ_m value, the date of data collection, and the frequencies of the bulk acoustic phonons (ν_T and ν_L) probed in the pseudo-reflection geometry Brillouin scattering measurements taken from sample P*Si*4.7#3.

θ_i	θ_s	θ_m	Collection Date	ν_T	ν_L
(deg.)	(deg.)	(deg.)		(GHz)	(GHz)
7	7	0	22/04/2011	-	37.3 ± 0.1
30	37	34	28/04/2011	20.2 ± 0.1	36.1 ± 0.2
40	48	44	27/04/2011	20.07 ± 0.07	35.4 ± 0.1
50	60	55	26/04/2011	19.41 ± 0.08	34.6 ± 0.1
60	66	63	25/04/2011	19.52 ± 0.08	35.0 ± 0.1

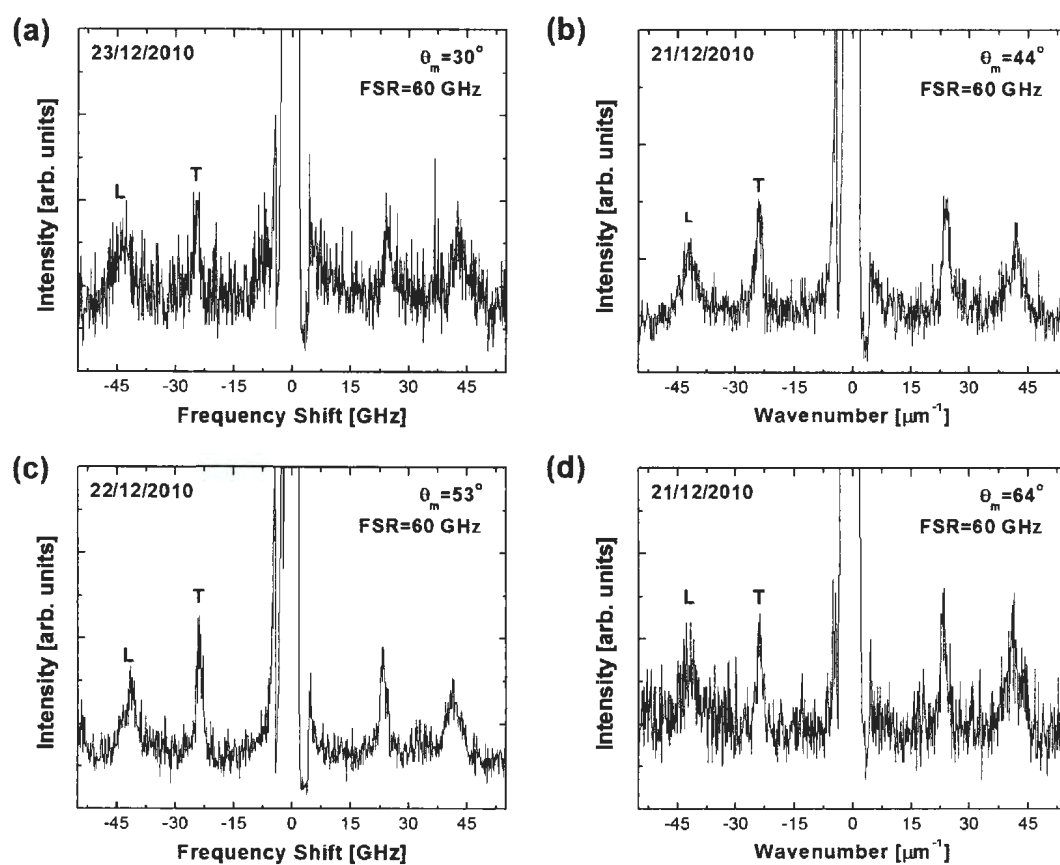


Figure C.2: Pseudo-reflection geometry Brillouin scattering spectra collected from sample PSi4.72, a single-layer π -Si film. Peaks L and T were attributed to the longitudinal bulk acoustic phonon and the transverse bulk acoustic phonon, respectively.

Table C.2: Angle θ_i , angle θ_s , the corresponding θ_m value, the date of data collection, and the frequencies of the bulk acoustic phonons (ν_T and ν_L) probed in the pseudo-reflection geometry Brillouin scattering measurements taken from sample PSi4.7#2.

θ_i	θ_s	θ_m	Collection Date	ν_T	ν_L
(deg.)	(deg.)	(deg.)		(GHz)	(GHz)
7	7	0	21/12/2010	-	43.3 ± 0.1
25	35	30	23/12/2010	24.6 ± 0.1	43.1 ± 0.2
40	48	44	23/12/2010	24.04 ± 0.04	41.8 ± 0.1
50	55	53	22/12/2010	23.63 ± 0.04	41.3 ± 0.1
60	67	64	22/12/2010	23.51 ± 0.07	41.4 ± 0.2

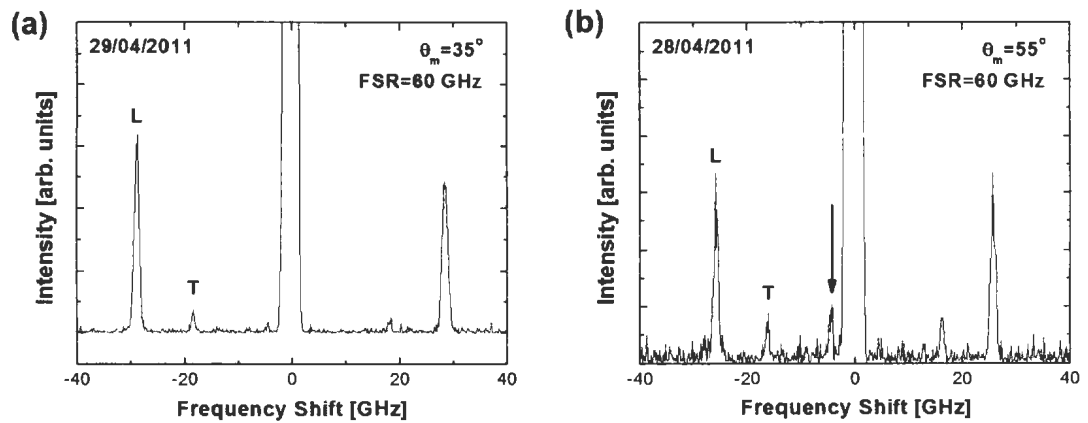


Figure C.3: Pseudo-reflection geometry Brillouin scattering spectra collected from a sample of fused quartz. Peaks L and T were attributed to the longitudinal bulk acoustic phonon and the transverse bulk acoustic phonon, respectively. The arrow indicates a feature that is due to a portion of the center elastic peak that is outside the shuttered spectral region.

Table C.3: Angle θ_i , angle θ_s , the corresponding θ_m value, the date of data collection, and the frequencies of the bulk acoustic phonons (ν_T and ν_L) probed in the pseudo-reflection geometry Brillouin scattering measurements taken from a sample of fused quartz.

θ_i	θ_s	θ_m	Collection Date	ν_T	ν_L
(deg.)	(deg.)	(deg.)		(GHz)	(GHz)
7	7	0	28/04/2011	-	31.98 ± 0.01
30	40	35	29/04/2011	18.3 ± 0.2	28.72 ± 0.02
40	48	44	29/04/2011	17.4 ± 0.1	27.46 ± 0.02
50	60	55	28/04/2011	16.25 ± 0.06	25.73 ± 0.02
61	67	64	28/04/2011	15.87 ± 0.02	24.97 ± 0.01

Table C.4: Angle θ_i , angle θ_s , the corresponding θ_m value, the date of data collection, and the frequencies of the bulk acoustic phonons (ν_T and ν_L) probed in the pseudo-reflection geometry Brillouin scattering measurements taken from a sample of gallium phosphide.

θ_i	θ_s	θ_m	Collection Date	ν_T	ν_L
(deg.)	(deg.)	(deg.)		(GHz)	(GHz)
7	7	0	22/06/2011	53.26 ± 0.01	76.01 ± 0.01
30	38	34	22/06/2011	52.14 ± 0.04	75.38 ± 0.03
40	50	45	22/06/2011	51.67 ± 0.05	74.66 ± 0.03
50	59	55	22/06/2011	51.40 ± 0.04	74.12 ± 0.02
60	69	65	22/06/2011	51.27 ± 0.03	73.69 ± 0.02

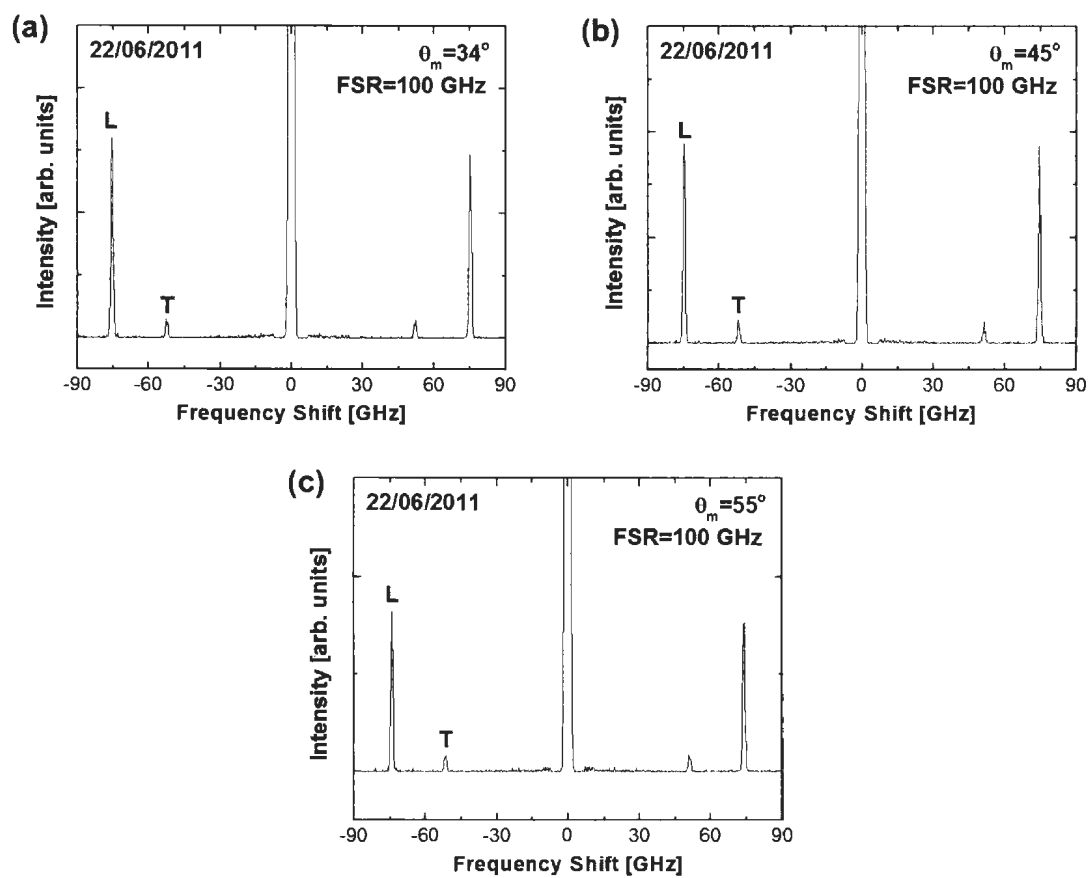


Figure C.4: Pseudo-reflection geometry Brillouin scattering spectra collected from a sample of gallium phosphide. Peaks L and T were attributed to the longitudinal bulk acoustic phonon and the transverse bulk acoustic phonon, respectively.

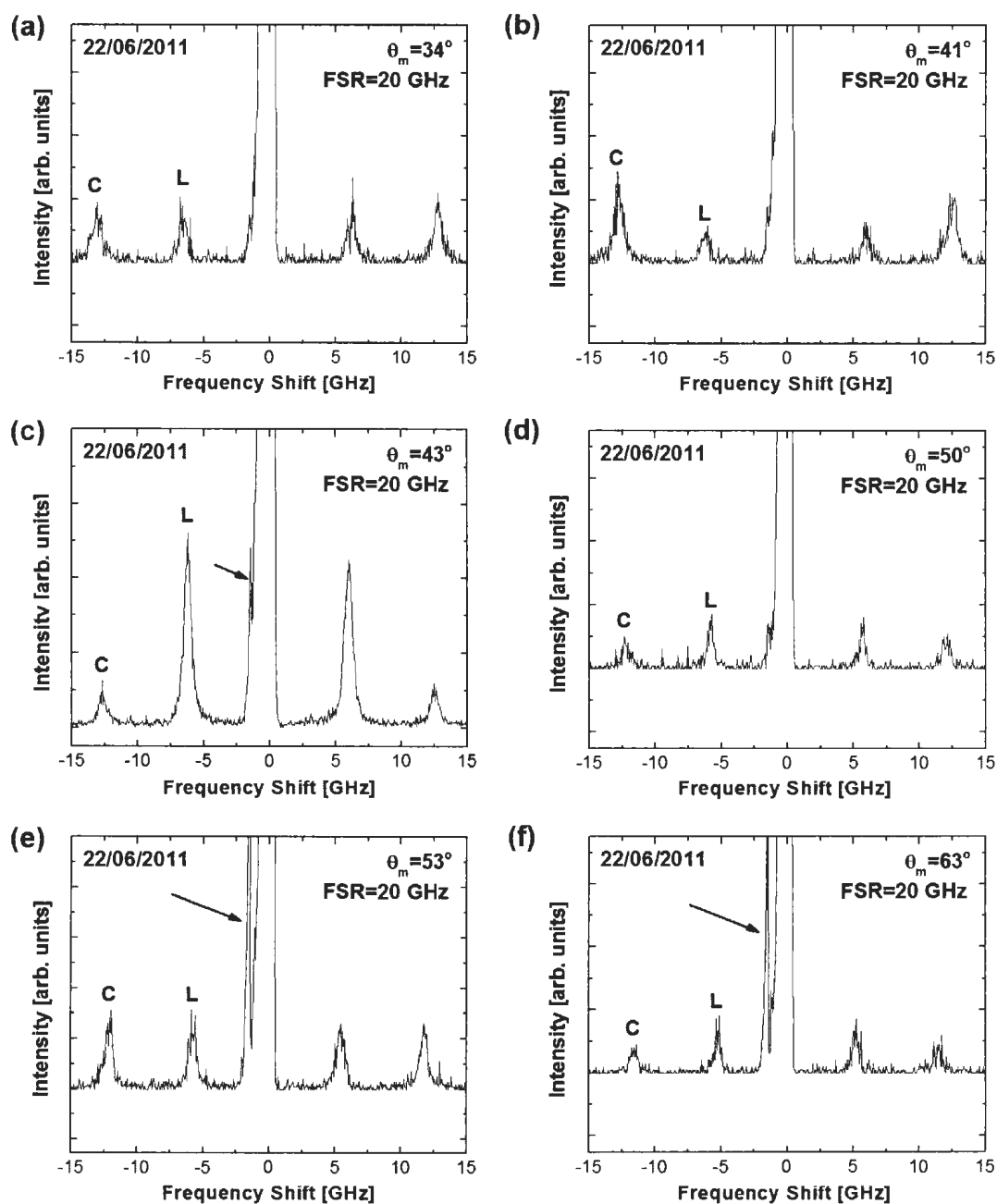


Figure C.5: Pseudo-reflection geometry Brillouin scattering spectra collected from sample a sample of water. Peaks L and C were attributed to the longitudinal bulk acoustic wave of water and the longitudinal bulk acoustic phonon of the clear plastic case that held the water, respectively. The arrows indicate a feature that is due to a portion of the center elastic peak that is outside the shuttered spectral region.

Table C.5: Angle θ_i , angle θ_s , the corresponding θ_m value, the date of data collection, and the frequencies of the bulk acoustic phonons probed in the pseudo-reflection geometry Brillouin scattering measurements taken from a sample of water. In particular, peaks L and C were attributed to the longitudinal bulk acoustic wave of water and the longitudinal bulk acoustic phonon of the clear plastic case that held the water, respectively. That is, with the probing laser beam focused at a water-plastic interface, a portion of the incident light interacted with the plastic holder.

θ_i	θ_s	θ_m	Collection Date	ν_L	ν_C
(deg.)	(deg.)	(deg.)		(GHz)	(GHz)
7	7	0	22/06/2011	7.50 ± 0.01	-
30	38	34	22/06/2011	6.41 ± 0.02	12.91 ± 0.02
36	45	41	22/06/2011	6.08 ± 0.03	12.66 ± 0.01
40	45	43	22/06/2011	6.11 ± 0.01	12.59 ± 0.04
45	54	50	22/06/2011	5.76 ± 0.01	12.12 ± 0.02
50	56	53	22/06/2011	5.60 ± 0.02	11.94 ± 0.02
60	66	63	22/06/2011	5.22 ± 0.01	11.52 ± 0.02

Appendix D

Raw Data for Chapter 7

Both optical reflectance measurements and Brillouin scattering experiments were done on two binary periodic porous silicon films made using a 1:1:1 (water: 49% wt. HF: 98% wt. ethanol) electrolyte. In particular, sample PSi2.3#15 (labeled Sample 1 in Chapter 7) and sample PSi2.6#4 (labeled Sample 1 in Chapter 7) were characterized. Figures D.1 to D.6 show the Brillouin spectra collected from sample PSi2.3#15, while Figs. D.8 to D.11 contain the Brillouin spectra collected from sample PSi2.6#4; additional spectra were shown in Chapter 5. Tables D.5 to D.12 compile the corresponding Brillouin scattering data, while Tables D.1 to D.4 contain the collected optical reflectance data. One should keep in mind that the near-normal incidence 180°-backscattering data corresponded to $\theta_s = \theta_i$ and $\theta_m = 0$. A number of cross-sectional scanning micrographs were collected from each SL. Figures D.7 and D.12 display example scanning electron micrographs collected from sample PSi2.3#15 and sample PSi2.6#4, respectively. In an effort to emphasize the film-substrate in-

Table D.1: Spectral positions of the first-order optical Bragg peaks observed for samples PSi2.3#15 and PSi2.6#4. In particular, the peak positions for air-filled pores, w_1^{air} , and ethanol-filled pores, $w_1^{ethanol}$, are considered.

Sample	w_1^{air}	$w_1^{ethanol}$
	$(\pm 0.01 \mu\text{m}^{-1})$	$(\pm 0.01 \mu\text{m}^{-1})$
PSi2.315	2.31	2.26
PSi2.64	2.18	2.12

terface, the digitized scanning electron micrographs were processed and, specifically, adjustments were made to the image contrast and brightness. One should note that white, irregular features in the SEM images correspond to dirt and debris on the samples.

Table D.2: A set of incident angle-dependent optical reflectance data, R_{ob} , collected from sample PSi2.315, a binary periodic multilayered π -Si film. Measurements were taken with both s- and p- polarized light. The optical wavelength was $\lambda_o = 532$ nm.

Incident Angle (s-polarization) ($\pm 0.5^\circ$)	R_{ob} (s-polarization)	Incident Angle (p-polarization) ($\pm 0.5^\circ$)	R_{ob} (p-polarization)
11.5	18.9	16.5	15.9
15.5	19.2	20.5	14.8
19.5	19.5	24.5	13.5
23.5	20.1	28.5	12.8
27.5	20.9	31.0	9.5
31.5	21.5	35.0	9.8
35.5	22.5	39.0	10.1
39.5	23.8	42.5	7.8
43.5	25.6	43.0	9.3
47.5	27.3	46.5	6.4

Table D.3: Another set of incident angle-dependent optical reflectance data, R_{ob} , collected from sample PSi2.315, a binary periodic multilayered π -Si film. Measurements were taken with both s- and p- polarized light. The optical wavelength was $\lambda_o = 532$ nm.

Incident Angle (s-polarization) ($\pm 0.5^\circ$)	R_{ob} (s-polarization)	Incident Angle (p-polarization) ($\pm 0.5^\circ$)	R_{ob} (p-polarization)
51.5	30.2	47.0	7.0
55.5	34.9	50.5	5.1
59.5	38.4	51.0	5.1
63.5	43.5	54.5	3.9
67.5	47.1	55.0	3.2
-	-	58.5	2.3
-	-	62.5	1.3
-	-	66.5	0.9
-	-	70.5	1.7
-	-	74.5	5.0

Table D.4: Incident angle-dependent optical reflectance data, R_{ob} , collected from sample PSi2.64, a binary periodic multilayered π -Si film. Measurements were taken with both s- and p- polarized light. The optical wavelength was $\lambda_o = 532$ nm.

Incident Angle (s-polarization) ($\pm 0.5^\circ$)	R_{ob} (s-polarization)	Incident Angle (p-polarization) ($\pm 0.5^\circ$)	R_{ob} (p-polarization)
12.0	17.8	12.0	16.0
16.0	18.0	16.0	15.5
20.0	18.2	20.0	14.7
24.0	18.2	24.0	13.5
28.0	18.6	28.0	12.1
32.0	19.3	32.0	11.0
36.0	20.4	36.0	9.7
40.0	22.1	40.0	8.7
44.0	23.7	44.0	7.4
48.0	26.3	48.0	6.2
52.0	28.8	52.0	4.7
56.0	31.5	56.0	3.4
60.0	35.8	60.0	2.1
64.0	38.8	64.0	1.6
68.0	44.0	68.0	2.1
72.0	52.3	72.0	4.4
74.0	56.0	74.0	6.3

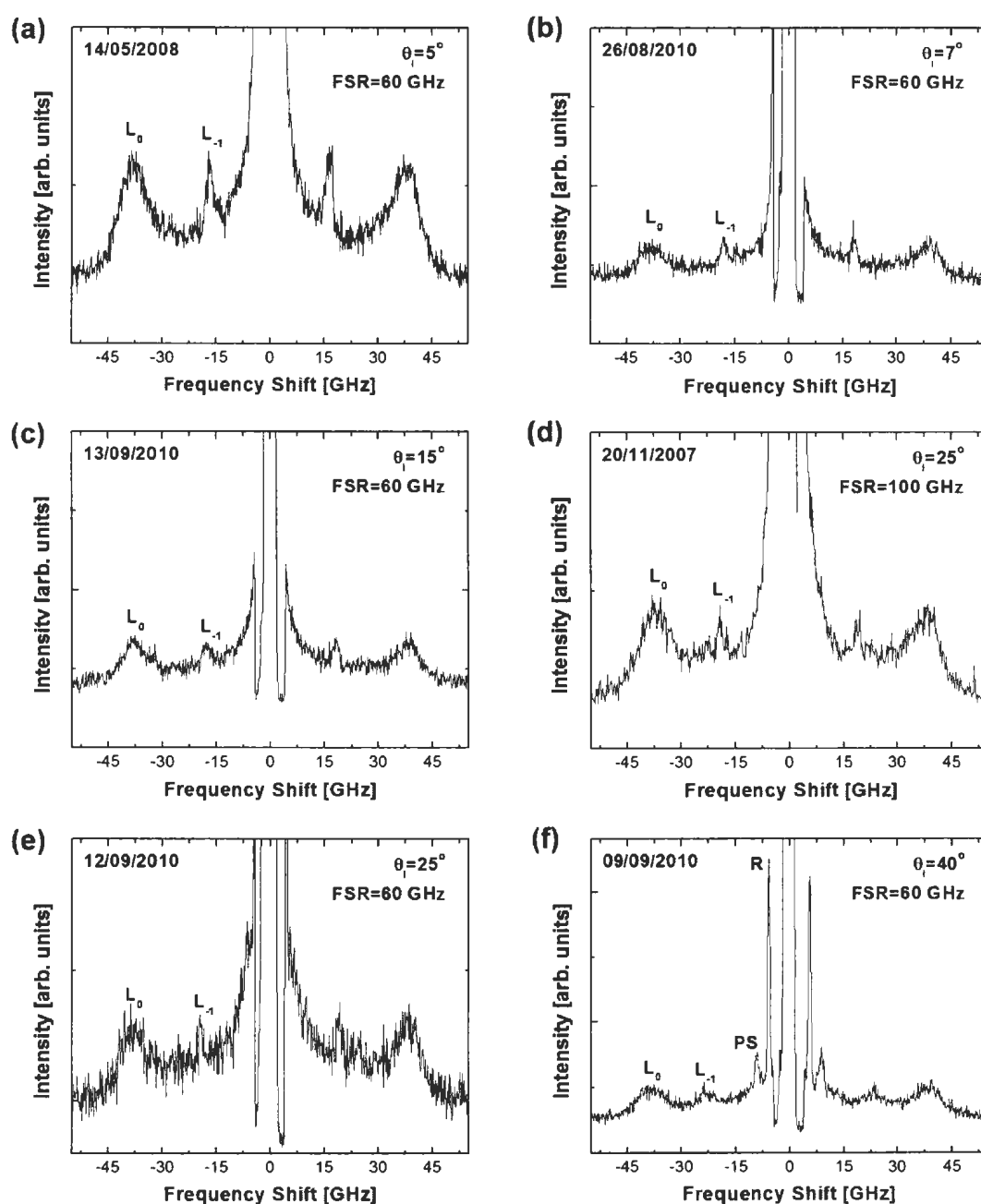


Figure D.1: A collection of oblique incidence 180° -backscattering geometry Brillouin spectra collected from sample PSi2.3#15, a binary periodic multilayered π -Si film. Brillouin peaks L_0 , L_{-1} , R, and PS were attributed to the $l = 0$ folded longitudinal bulk acoustic mode, the $l = -1$ folded longitudinal bulk acoustic mode, the Rayleigh surface mode, and a pseudo-surface mode, respectively.

Table D.5: The θ_i value, collection date, and the observed phonon modes and corresponding frequencies obtained for sample PSi2.3#15, a binary periodic multilayered π -Si film fabricated on 08/08/2007. The anodization times per cycle were $t_1 = 1.568$ s and $t_2 = 4.703$ s, while the number of etch cycles was $\eta = 76$.

θ_i	Collection Date	ν_R	ν_{PS}	ν_{L-1}	ν_{T_0}	ν_{L_0}
(deg.)		(GHz)	(GHz)	(GHz)	(GHz)	(GHz)
5	14/05/2008	-	-	16.56 ± 0.07	-	37.42 ± 0.09
7	26/08/2010	-	-	17.9 ± 0.2	-	38.0 ± 0.2
15	13/09/2010	-	-	18.0 ± 0.2	-	37.5 ± 0.1
25	20/11/2007	-	-	19.0 ± 0.2	-	36.9 ± 0.2
25	12/09/2010	-	-	19.3 ± 0.1	-	37.7 ± 0.2
40	09/09/2010	5.70 ± 0.01	9.03 ± 0.08	23.6 ± 0.4	-	37.9 ± 0.1

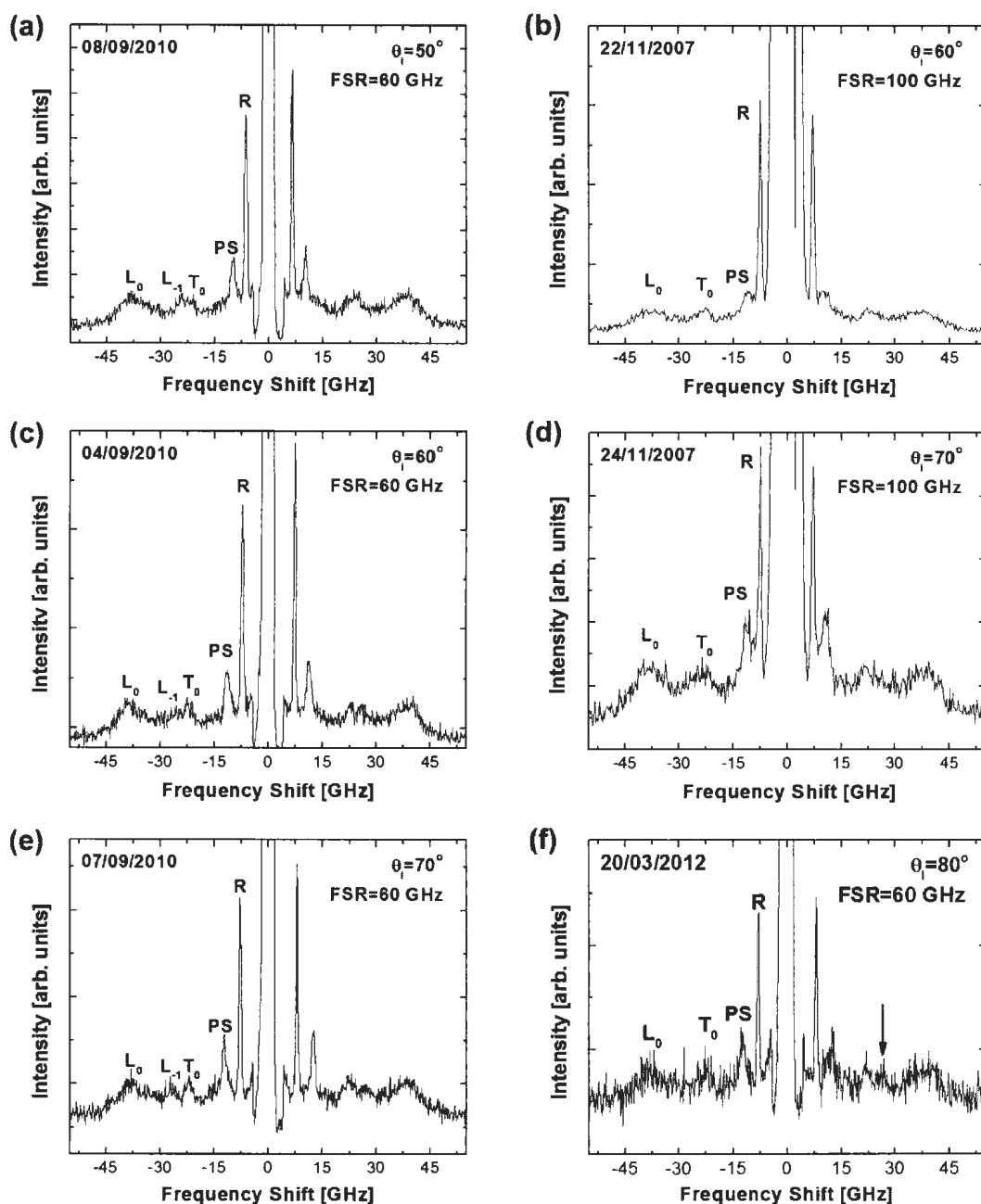


Figure D.2: Another collection of oblique incidence 180° -backscattering geometry Brillouin spectra collected from sample PSi2.3#15, a binary periodic multilayered π -Si film. Brillouin peaks L_0 , L_{-1} , T_0 , R, and PS were attributed to the $l = 0$ folded longitudinal bulk acoustic mode, the $l = -1$ folded longitudinal bulk acoustic mode, the $l = 0$ folded transverse bulk acoustic mode, the Rayleigh surface mode, and a pseudo-surface mode, respectively. The arrow indicates the expected spectral position of the L_{-1} peak in $\theta_i = 80^\circ$ spectrum.

Table D.6: The θ_i value, the collection date, and the observed phonon modes and corresponding frequencies obtained for sample PSi2.3#15 in the second set of 180°-backscattering geometry Brillouin measurements.

θ_i (deg.)	Collection Date	ν_R (GHz)	ν_{PS} (GHz)	ν_{L-1} (GHz)	ν_{T_0} (GHz)	ν_{L_0} (GHz)
50	08/09/2010	6.48 ± 0.01	10.15 ± 0.07	24.3 ± 0.2	21.5 ± 0.3	37.4 ± 0.1
60	22/11/2007	7.31 ± 0.01	11.0 ± 0.1	-	22.7 ± 0.4	37.6 ± 0.3
60	04/09/2010	7.29 ± 0.01	11.40 ± 0.06	25.7 ± 0.3	22.6 ± 0.1	38.1 ± 0.1
70	24/11/2010	7.33 ± 0.01	10.82 ± 0.08	-	22.8 ± 0.4	38.3 ± 0.3
70	07/09/2010	7.92 ± 0.01	12.41 ± 0.05	27.2 ± 0.3	22.2 ± 0.2	37.5 ± 0.2
80	20/03/2012	8.08 ± 0.02	12.3 ± 0.2	-	22.3 ± 0.3	37.7 ± 0.4

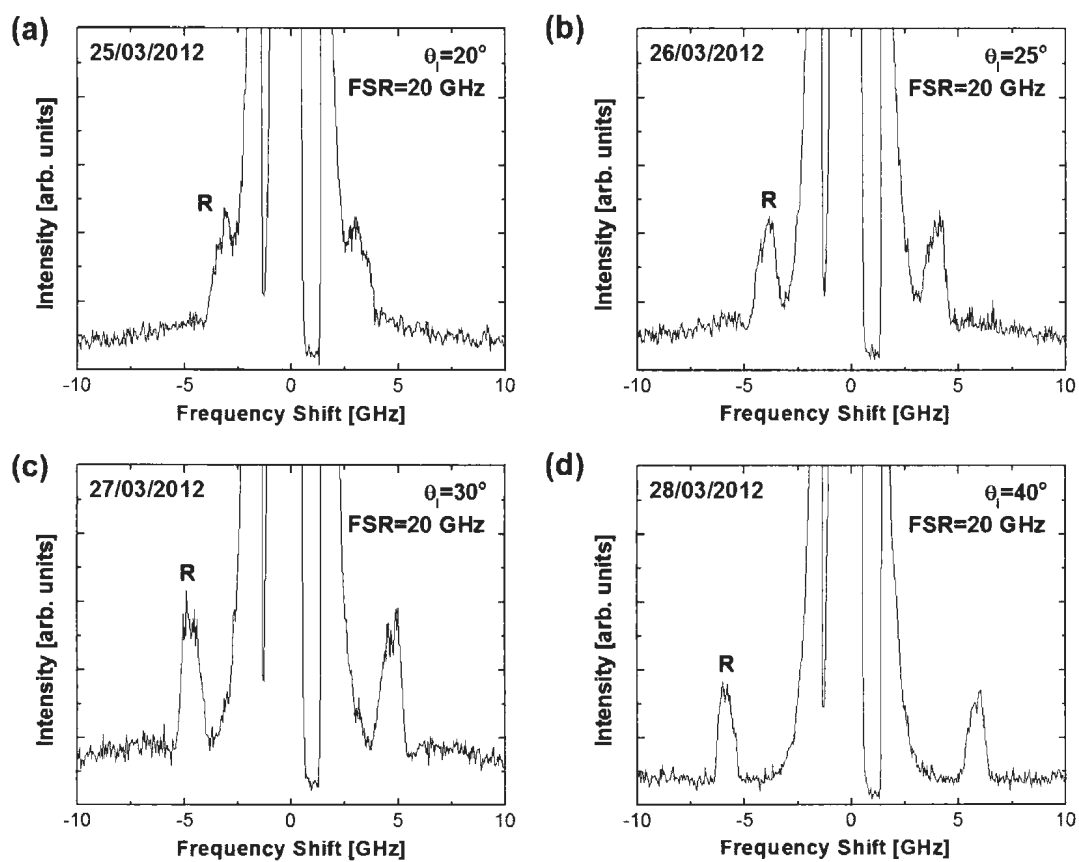


Figure D.3: A third collection of oblique incidence 180° -backscattering geometry Brillouin spectra collected from sample P*Si*2.3#15, a binary periodic multilayered π -Si film. Brillouin peak R was attributed to the Rayleigh surface mode.

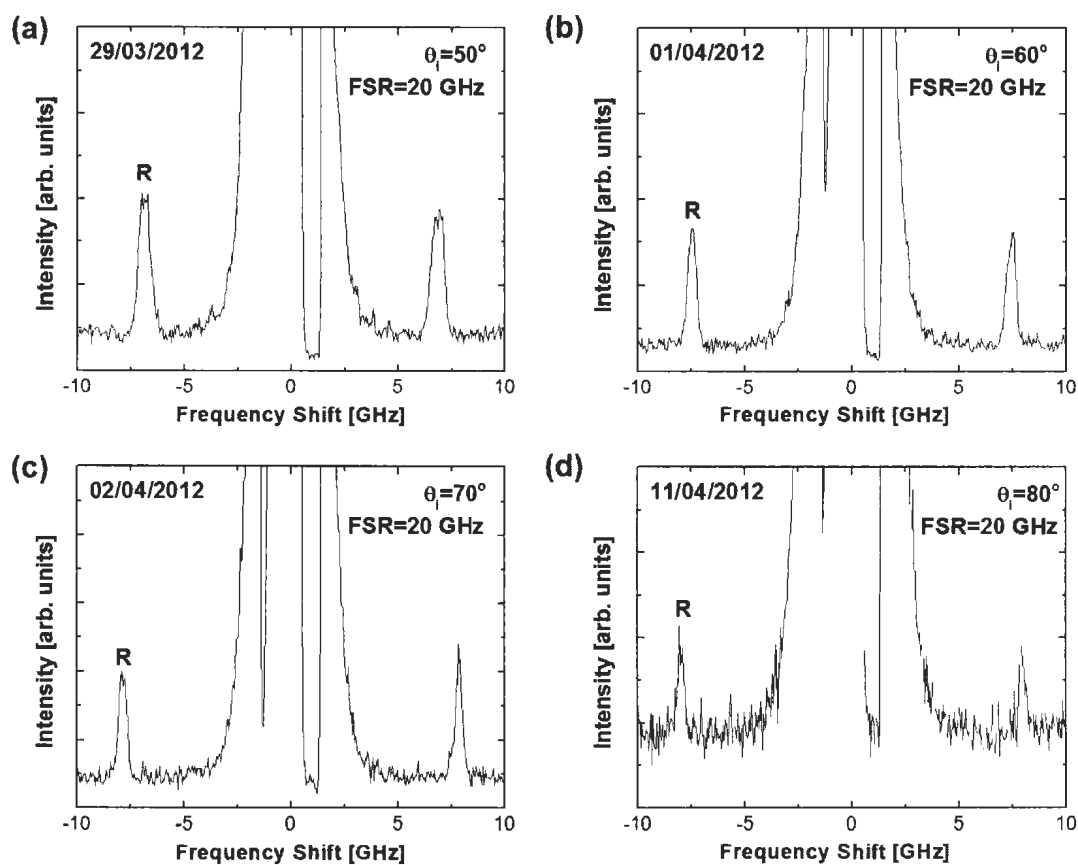


Figure D.4: A fourth collection of oblique incidence 180° -backscattering geometry Brillouin spectra collected from sample PSi2.3#15, a binary periodic multilayered π -Si film. Brillouin peak R was attributed to the Rayleigh surface mode.

Table D.7: The θ_i value, the collection date, and the observed phonon modes and corresponding frequencies obtained for sample P*Si*2.3#15 in the third and fourth sets of 180°-backscattering geometry Brillouin measurements.

θ_i (deg.)	Collection Date	ν_R (GHz)
20	25/03/2012	3.01 ± 0.05
25	26/03/2012	3.92 ± 0.02
30	27/03/2012	4.68 ± 0.02
40	28/03/2012	5.84 ± 0.01
50	29/03/2012	6.86 ± 0.01
60	01/04/2012	7.46 ± 0.01
70	02/04/2012	7.86 ± 0.01
80	11/04/2012	7.98 ± 0.02

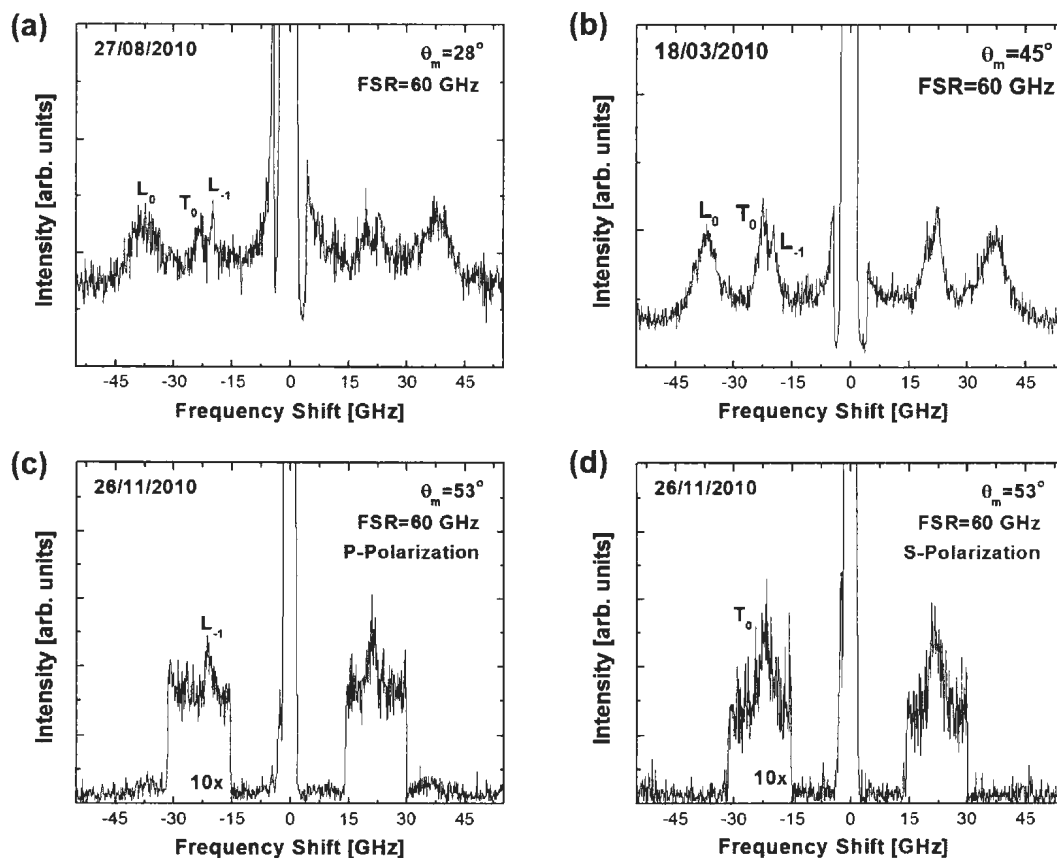


Figure D.5: A collection of pseudo-reflection geometry Brillouin scattering spectra collected from sample PSi2.3#15, a binary periodic multilayered π -Si film. Peaks L_0 , L_{-1} , and T_0 were attributed to the $l = 0$ folded longitudinal bulk acoustic phonon, the $l = -1$ folded longitudinal bulk acoustic phonon, and the $l = 0$ folded transverse bulk acoustic phonon, respectively.

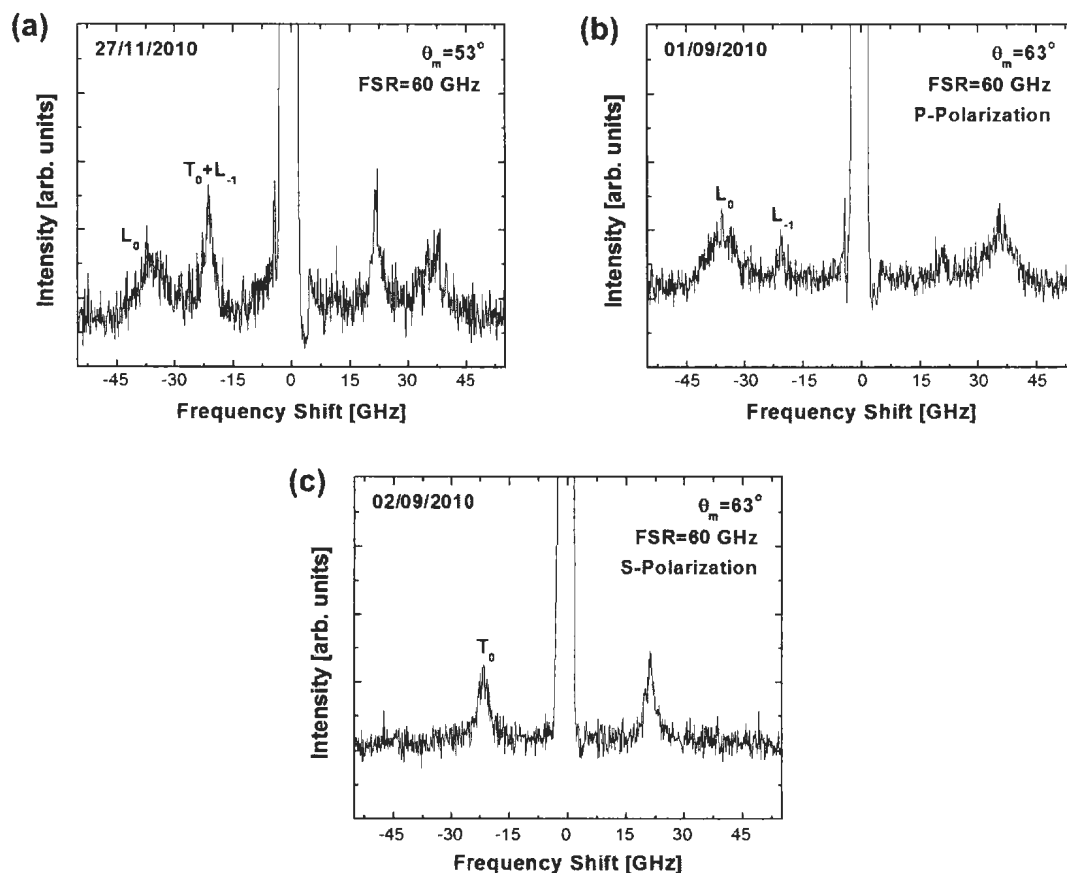


Figure D.6: Another collection of pseudo-reflection geometry Brillouin scattering spectra collected from sample PSi2.3#15, a binary periodic multilayered π -Si film. Peaks L_0 , L_{-1} , and T_0 were attributed to the $l = 0$ folded longitudinal bulk acoustic phonon, the $l = -1$ folded longitudinal bulk acoustic phonon, and the $l = 0$ folded transverse bulk acoustic phonon, respectively. Spectral feature $T_0 + L_0$ is attributed to the sum of scattering from the $l = 0$ folded transverse bulk acoustic phonon and the $l = -1$ folded longitudinal bulk acoustic phonon.

Table D.8: Angle θ_i , angle θ_s , the corresponding θ_m value, the date of data collection, and the frequencies of the bulk acoustic phonons (ν_{T_0} , $\nu_{L_{-1}}$, and ν_{L_0}) probed in the pseudo-reflection geometry Brillouin scattering measurements taken from sample PSi2.3#15.

θ_i	θ_s	θ_m	Collection Date	ν_{T_0}	$\nu_{L_{-1}}$	ν_{L_0}
(deg.)	(deg.)	(deg.)		(GHz)	(GHz)	(GHz)
25	31	28	27/08/2010	23.2 ± 0.2	19.5 ± 0.2	37.4 ± 0.3
40	50	45	18/03/2012	22.3 ± 0.2	19.9 ± 0.3	36.89 ± 0.08
50	55	53	26/11/2010	-	21.1 ± 0.1	-
50	55	53	26/11/2010	21.8 ± 0.2	-	-
50	55	53	27/11/2010	(21.51 ± 0.08)	-	36.0 ± 0.2
60	65	63	01/09/2010	-	20.7 ± 0.2	35.6 ± 0.2
60	65	63	02/09/2010	21.77 ± 0.07	-	-

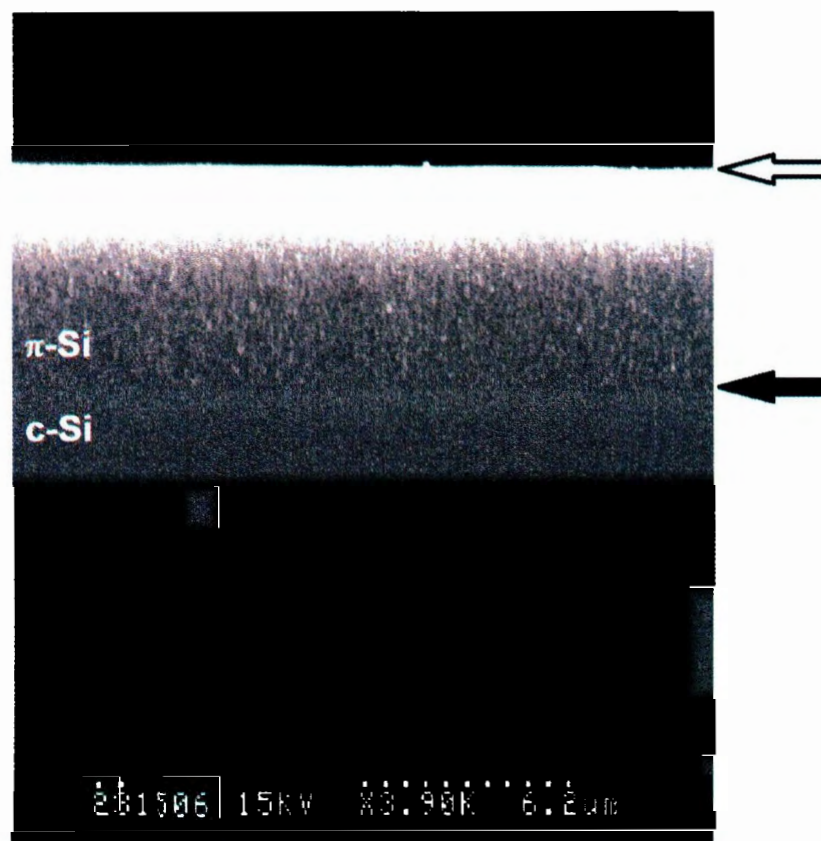


Figure D.7: Cross-sectional scanning electron micrograph of PSi2.3#15. There were 76 cycles of the current density. Overall thickness was $\sim 6.6 \mu\text{m}$. Empty(filled) arrows denote the film-air(substrate-film) interface.

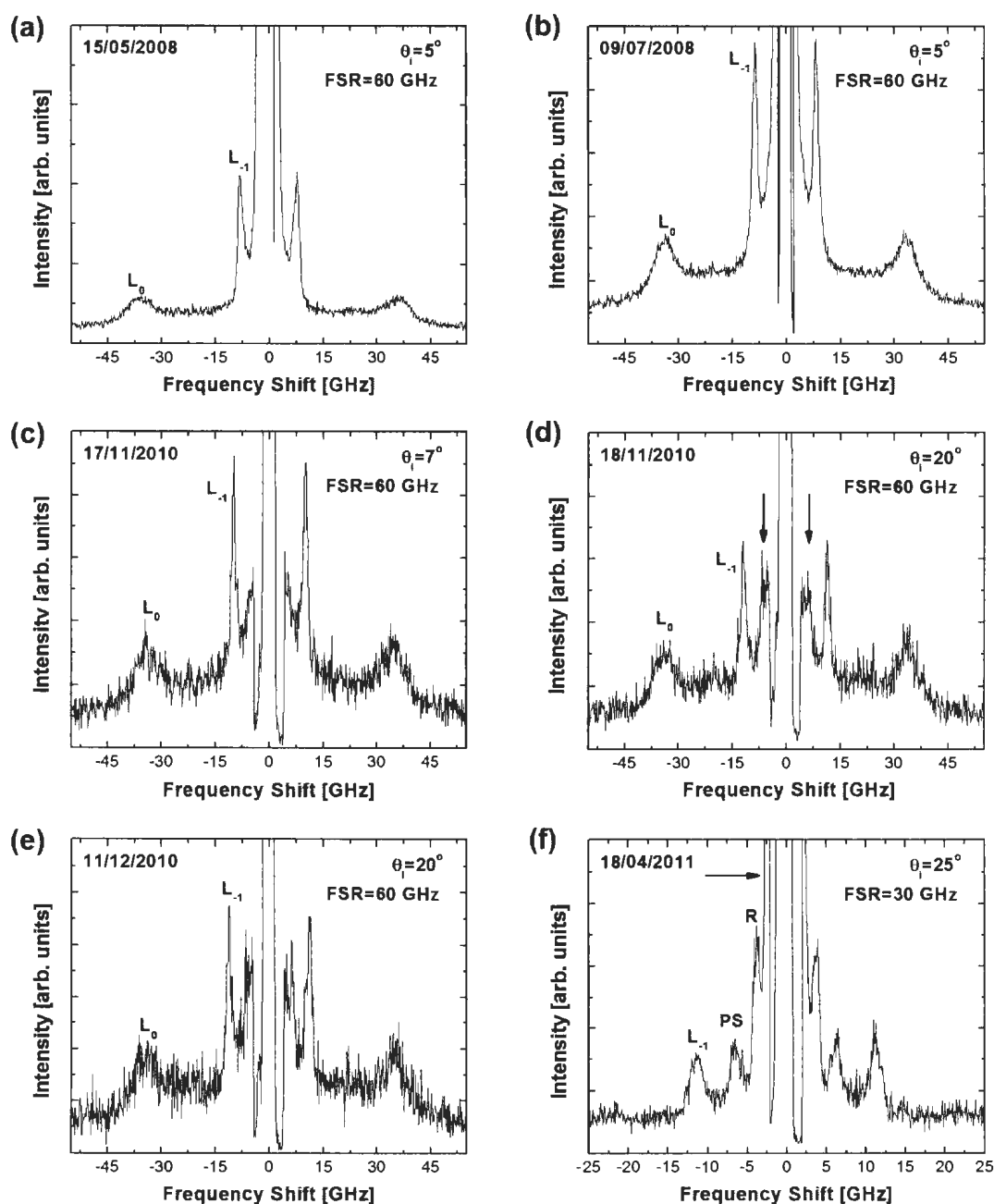


Figure D.8: A collection of oblique incidence 180° -backscattering geometry Brillouin spectra collected from sample PSi2.6#4, a binary periodic multilayered π -Si film. Brillouin peaks L_0 , L_{-1} , T_0 , R , and PS were attributed to the $l = 0$ folded longitudinal bulk acoustic mode, the $l = -1$ folded longitudinal bulk acoustic mode, the $l = 0$ folded transverse bulk acoustic mode, the Rayleigh surface mode, and a pseudo-surface mode, respectively. The vertical arrows indicate spectral features that may be attributable to a pseudo-surface mode, while the horizontal arrow indicates a feature that is due to a portion of the center elastic peak that is outside the shuttered spectral region.

Table D.9: The θ_i value, collection date, and the observed phonon modes and corresponding frequencies obtained for sample PSi2.6#4, a binary periodic multilayered π -Si film fabricated on 14/05/2008. The anodization times per cycle were $t_1 = 2.0588$ s and $t_2 = 6.1765$ s, while the number of etch cycles was $\eta = 70$.

θ_i	Collection Date	ν_R	ν_{PS}	ν_{L-1}	ν_{T_0}	ν_{L_0}
(deg.)		(GHz)	(GHz)	(GHz)	(GHz)	(GHz)
5	15/05/2008	-	-	8.01 ± 0.05	-	35.4 ± 0.1
5	09/07/2008	-	-	8.46 ± 0.02	-	33.17 ± 0.06
7	17/11/2010	-	-	9.96 ± 0.04	-	33.8 ± 0.2
20	18/11/2010	-	-	11.65 ± 0.05	-	33.5 ± 0.1
20	11/12/2010	-	-	11.10 ± 0.06	-	34.4 ± 0.2
25	18/04/2010	3.66 ± 0.02	6.45 ± 0.05	11.26 ± 0.05	-	-

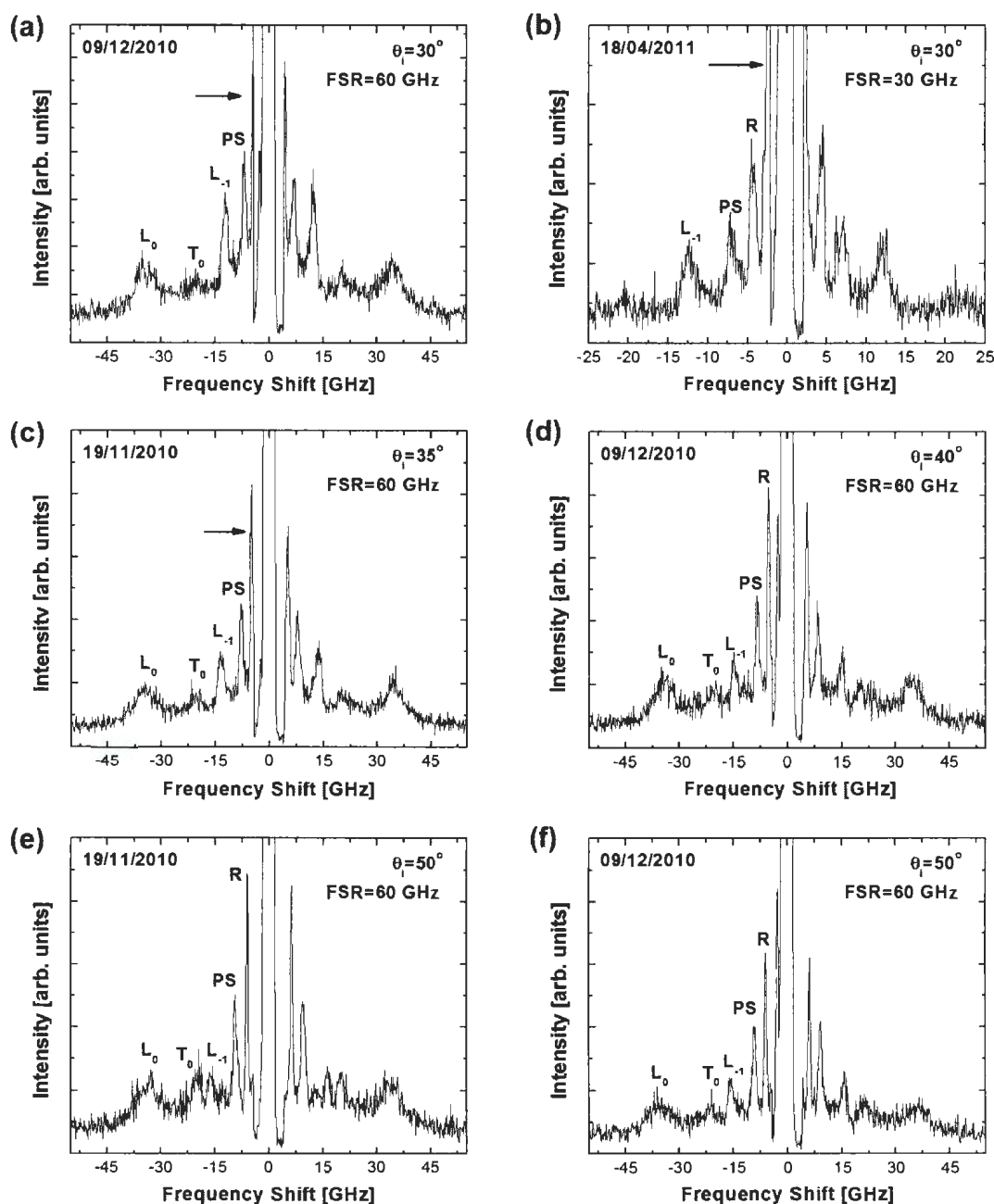


Figure D.9: Another collection of oblique incidence 180° -backscattering geometry Brillouin spectra collected from sample PSi2.6#4. Brillouin peaks L_0 , L_{-1} , T_0 , R , and PS were attributed to the $l = 0$ folded longitudinal bulk acoustic mode, the $l = -1$ folded longitudinal bulk acoustic mode, the $l = 0$ folded transverse bulk acoustic mode, the Rayleigh surface mode, and a pseudo-surface mode, respectively. The horizontal arrows indicate a feature that may be due to either a portion of the center elastic peak that is outside the shuttered spectral region or an edge of the Rayleigh mode peak.

Table D.10: The θ_i value, the collection date, and the observed phonon modes and corresponding frequencies obtained for sample PSi6#4 in the second collection of 180°-backscattering Brillouin measurements.

θ_i	Collection Date	ν_R	ν_{PS}	ν_{L-1}	ν_{T_0}	ν_{L_0}
(deg)		(GHz)	(GHz)	(GHz)	(GHz)	(GHz)
30	09/12/2010	-	6.85 ± 0.04	12.16 ± 0.04	20.7 ± 0.5	34.3 ± 0.2
30	18/04/2011	4.29 ± 0.02	7.02 ± 0.05	12.17 ± 0.08	-	-
35	19/11/2010	-	7.82 ± 0.03	13.41 ± 0.05	21.0 ± 0.3	34.5 ± 0.2
40	09/12/2010	5.29 ± 0.02	8.44 ± 0.05	14.85 ± 0.08	20.3 ± 0.2	34.3 ± 0.1
50	19/11/2010	6.14 ± 0.01	9.45 ± 0.03	16.2 ± 0.2	20.0 ± 0.2	33.4 ± 0.2
50	09/12/2010	6.07 ± 0.01	9.18 ± 0.03	15.4 ± 0.1	22.0 ± 0.3	35.4 ± 0.3

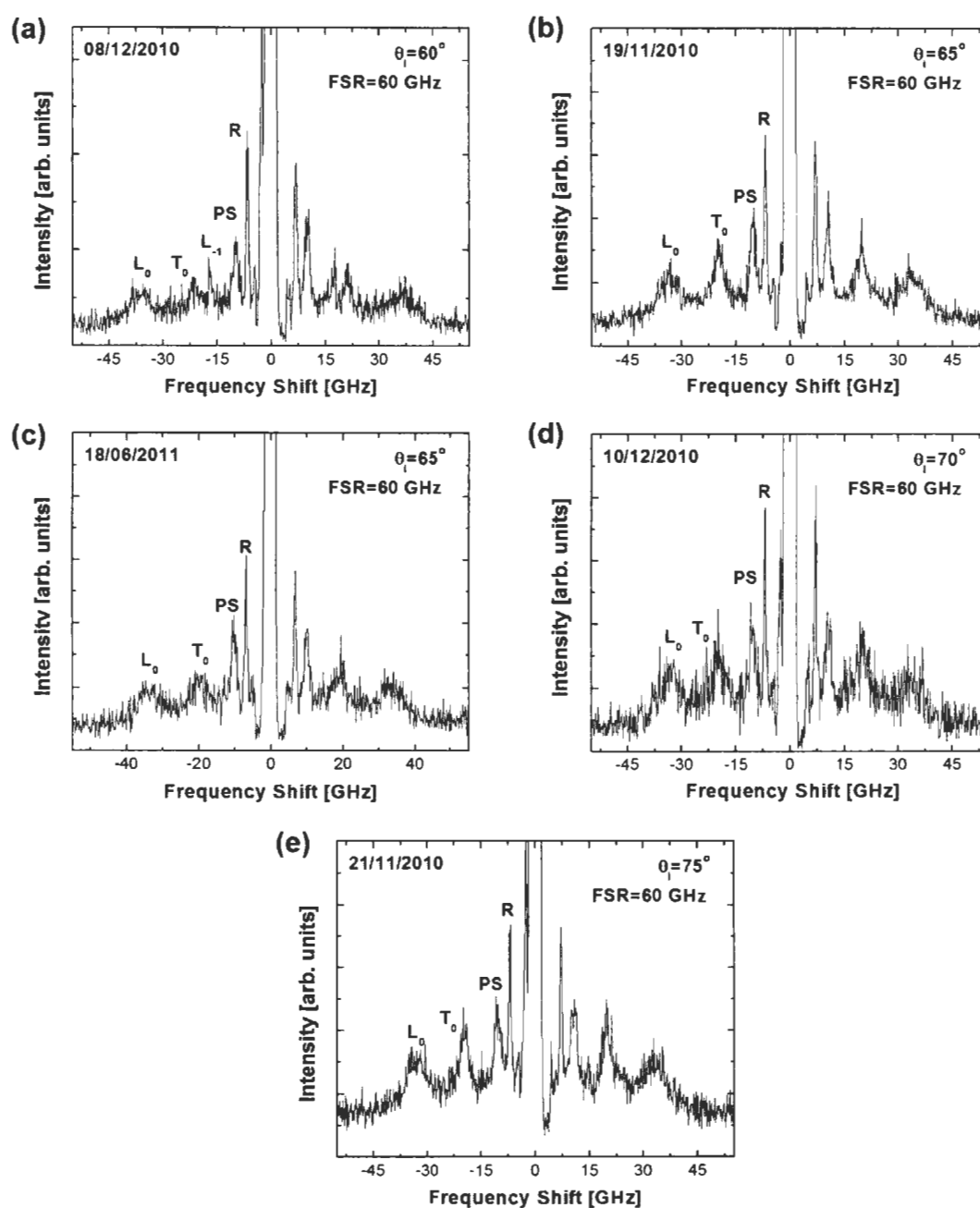


Figure D.10: A third collection of oblique incidence 180° -backscattering geometry Brillouin spectra collected from sample PSi2.6#4. Brillouin peaks L_0 , L_{-1} , T_0 , R, and PS were attributed to the $l = 0$ folded longitudinal bulk acoustic mode, the $l = -1$ folded longitudinal bulk acoustic mode, the $l = 0$ folded transverse bulk acoustic mode, the Rayleigh surface mode, and a pseudo-surface mode, respectively.

Table D.11: The θ_i value, the collection date, and the observed phonon modes and corresponding frequencies obtained for sample PSi6#4 in the third collection of 180°-backscattering Brillouin measurements.

θ_i	Collection Date	ν_R	ν_{PS}	ν_{L-1}	ν_{T_0}	ν_{L_0}
(deg)		(GHz)	(GHz)	(GHz)	(GHz)	(GHz)
60	08/12/2010	6.71 ± 0.02	9.99 ± 0.06	17.1 ± 0.1	21.1 ± 0.2	35.9 ± 0.3
65	19/11/2010	6.93 ± 0.01	10.39 ± 0.04	-	19.7 ± 0.1	33.4 ± 0.2
65	18/06/2011	6.83 ± 0.02	10.12 ± 0.05	-	19.2 ± 0.2	33.7 ± 0.2
70	10/12/2010	7.01 ± 0.02	10.45 ± 0.08	-	19.8 ± 0.2	33.4 ± 0.3
75	21/11/2010	7.09 ± 0.02	10.55 ± 0.06	-	19.9 ± 0.1	32.8 ± 0.2

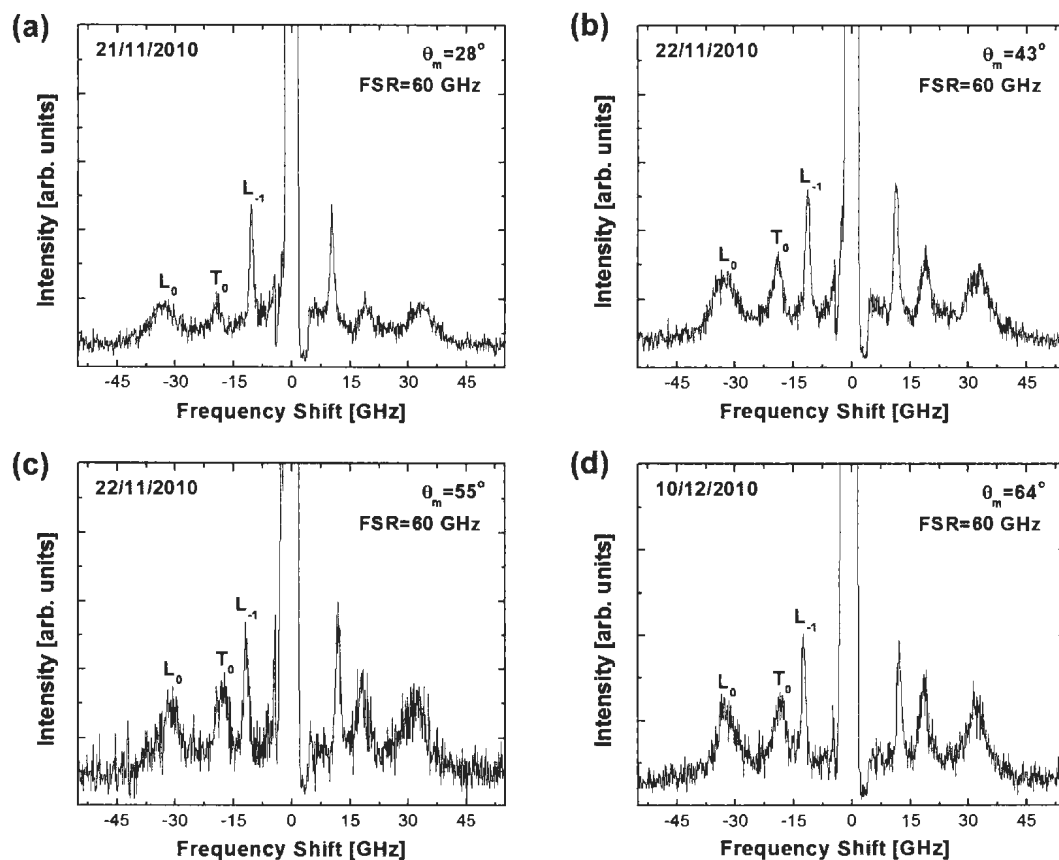


Figure D.11: A collection of pseudo-reflection geometry Brillouin scattering spectra collected from sample PSi2.6#4, a binary periodic multilayered π -Si film. Peaks L_0 , L_{-1} , and T_0 were attributed to the $l = 0$ folded longitudinal bulk acoustic phonon, the $l = -1$ folded longitudinal bulk acoustic phonon, and the $l = 0$ folded transverse bulk acoustic phonon, respectively.

Table D.12: Angle θ_i , angle θ_s , the corresponding θ_m value, the date of data collection, and the frequencies of the bulk acoustic phonons (ν_{T_0} , $\nu_{L_{-1}}$, and ν_{L_0}) probed in the pseudo-reflection geometry Brillouin scattering measurements taken from sample PSi2.6#4.

θ_i	θ_s	θ_m	Collection Date	ν_{T_0}	$\nu_{L_{-1}}$	ν_{L_0}
(deg)	(deg)	(deg)		(GHz)	(GHz)	(GHz)
25	30	28	21/11/2010	19.2 ± 0.2	10.38 ± 0.02	33.1 ± 0.2
40	46	43	22/11/2010	19.04 ± 0.07	11.36 ± 0.02	32.5 ± 0.1
50	59	55	22/11/2010	18.0 ± 0.1	11.81 ± 0.04	31.4 ± 0.2
60	67	64	10/12/2010	18.54 ± 0.08	12.28 ± 0.03	32.0 ± 0.1

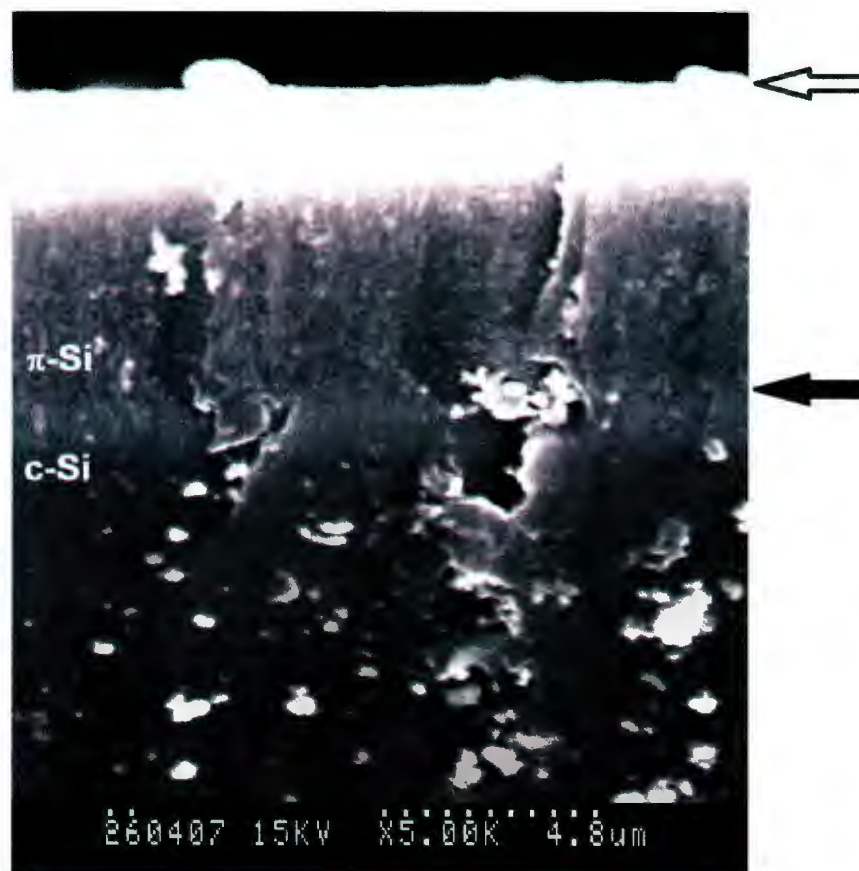


Figure D.12: Cross-sectional scanning electron micrograph of PSi2.6#4. There were 70 cycles of the current density. Overall thickness was $\sim 7.2 \mu\text{m}$. Empty(filled) arrows denote the film-air(substrate-film) interface.

